UNDERSTANDING DRUG RESPONSE DYNAMICS

IN BRAF-MUTATED MELANOMA CELLS

By

BUDDHI BISHAL PAUDEL

Dissertation

Submitted to the Faculty of the

Graduate School of Vanderbilt University

in partial fulfillment of the requirements

for the degree of

DOCTOR OF PHILOSOPHY

in

Chemical and Physical Biology

February 28, 2018

Nashville, Tennessee

Approved:

Sandra S. Zinkel, MD, PhD

Carlos F. Lopez, PhD

Gregor Neuert, PhD

Thomas E. Yankeelov, PhD

Kimberly B. Dahlman, PhD

Vito Quaranta, MD

DEDICATION

To my Grandmother and my Family,

For raising me to believe that nothing is impossible,

For instilling in me the value of hard-work,

For lifting me up when I gave up at times.

Thank you so much for all you have sacrificed for me.

के हो ठुलो जगतमा ?' 'पसिना विवेक'
'उद्देश्य के लिनु ?' 'उडि छुनु चन्द्र एक ।'
--Laxmi Prasad Devkota

ACKNOWLEDGEMENTS

This work would not have been possible without the financial support from US National Institutes of Health (U54 CA113007, VQ; CAU01174706, VQ), CTSA Award No. UL1TR000445 from the National Center for Advancing Translational Sciences (VICTR #VR16721, #VR16721.1, BBP) and Vanderbilt International Scholars Program (BBP).

I am extremely grateful to my advisor, Dr. Vito Quaranta, for taking me into his group in 2012 and letting me explore numerous interesting research questions. From my initial curiosity to understand motility of cancer cells to response dynamics of melanoma cells, he has been supportive, kind and extremely patient with me. At times, when I found myself overwhelmed with complexities of data, he has taught me to keep it simple, to think clearly, and to follow the data. I felt I was in the “cloud” on multiple occasions, but never felt I was alone. He has taught me to be bold and courageous to approach difficult and complex research questions.

My thesis committee members Dr. Sandra Zinkel, Dr. Gregor Neuert, Dr. Kim Dahlman, Dr. Carlos Lopez and Dr. Tom Yankeelov have all been instrumental in providing me valuable suggestions both in my research projects, and career development. Your comments and insights have helped me tremendously to grow as a scientist and an independent researcher.

At Vanderbilt, I have enjoyed and learnt from my interaction with other brilliant scientists. I would like to acknowledge Dr. Ann Richmond, Dr. Jeff Sosman and Dr. Doug Johnson for their help and suggestions. Dr. Josh Fessel was instrumental in helping me develop the second part of my dissertation on *NOX5* and *PGC1α*. I would also like to sincerely thank Patty Mueller, Dr. Bruce Damon for their assistance and help; Amanda Connolly and Dr. Kathy Gould for helping me transition to graduate school through Vanderbilt International Scholars Program (VISP).

In between Lopez Lab and Quaranta Lab, I have enjoyed my interaction with fellow students, post-docs and appreciate the opportunities to learn science in an interdisciplinary environment. In Dr. Leonard Harris, I found my second mentor and a great resource in learning the concepts of mathematical modeling and attractor landscape theory. He has inspired me to ask thought-stimulating questions at the interface of biology and mathematics, and to pay attention to details. I would also like to thank Dr. Darren Tyson for helping me get started in melanoma projects and his valuable suggestions throughout. My sincere thanks to previous lab members Dr. Peter Frick, Dr. Akshata Udyavar, Shawn Garbett, Dr. Lourdes Estrada for helping me transition in the lab. Dr. Jing Hao has been very helpful and supportive throughout my graduate school journey. Much of what we do in Quaranta Lab would not be possible without her. Other graduate students: David Wooten, Erin Shockley, Christian Meyer, Corey Hayford have been excellent to discuss potential research questions and ideas. I especially want to thank Dr. Matthew McKenna and Dr. Keisha Hardeman for making my time enjoyable, providing encouragement, and for helping me keep sane. From Matthew, I have not only learnt a lot on mathematical models, but also benefitted discussing interesting research ideas, questions and their applications. Last but not least, I would like to thank Keisha for being an awesome friend, co-author and lab-mate. You have been like a family to me and have helped me keep sane both on personal level and in my scientific pursuit. Through our discussions, I have not only appreciated the scientific outlook, but also developed a unique perspective in life.

My journey wouldn't have been exciting and fun-filled without the presence of some interesting people in my life in Nashville and beyond. My little brother in Nashville Ashwin Joshi has been there for me at all times. I am grateful for support and friendship I have received from members of Nashville Nepali Community: Ayush Giri and Siddhida Acharya, Anup Aryal,

Ashish Satyal and Diksha Satyal, Upendra, Parashar, Surabhya, and Bikki. My friends Sundar Ranabhat and Sailesh Thapa always listened to my frustrations and offered their most genuine support throughout.

My parents Manahari Paudel and Sita Devi Paudel, have always been supportive of my academic journey and have been a constant source of love and inspiration. You have sacrificed a lot for me and I could not be more proud to be your son. Nobody deserves more credit than you two for all I have achieved over the years. My sisters, Meena, Bishnu, Seema and Sabita have always encouraged me throughout. My journey would have been much more arduous if I didn't have you all in my life. Most of all, I would like to thank my wife, Neeru Panthee for loving me and encouraging me at all times. Past three years have been nothing but magical. Your unconditional love and support made it easier for me to make it this far. You believed in me more than I believed in myself and always pushed me to keep moving even when times were tough.

“If you don't fight for what you want, don't cry for what you lost.”—Bhagwat Geeta

LIST OF PUBLICATIONS

1. Frick PL, **Paudel BB**, Tyson DR, Quaranta V. Quantifying heterogeneity and dynamics of clonal fitness in response to perturbation. J. Cell. Physiol. 2015;230:1403–12.

2. Harris LA, Frick PL, Garbett SP, Hardeman KN, **Paudel BB**, Lopez CF, et al. An unbiased metric of antiproliferative drug effect in vitro. Nat. Methods. 2016;13:497–500.

3. Hardeman KN, Peng C, **Paudel BB**, Meyer CT, Luong T, Tyson DR, et al. Dependence On Glycolysis Sensitizes *BRAF*-mutated Melanomas For Increased Response To Targeted *BRAF* Inhibition. Sci. Rep. 2017;7:42604.

4. **Paudel BB**, Harris LA, Hardeman KN, Abugable AA, Hayford CE, Tyson DR, & Quaranta, V. A Non-Quiescent "Idling" State in Drug-Treated *BRAF*-mutated Melanoma Cell Populations. (2018) *Biophysical Journal*. (*in press*).

5. **Paudel BB**, Hardeman KN, Meyer CM, Harris LA, Tyson DR, Fessel JP, & Quaranta, V. NADPH Oxidase Inhibition Sensitizes *BRAF*-mutated Melanoma Cells to *BRAF*-inhibition. (*manuscript in preparation*).

TABLE OF CONTENTS

LIST OF TABLES

Page

LIST OF FIGURES

LIST OF ABBREVIATIONS

AA	Activity Area
ABC	ATP-Binding Cassette
ACS	American Cancer Society
ALDH	Aldehyde Dehydrogenase
ALK	Anaplastic Lymphoma Kinase
An	Anisomycin
ATCC	American Type Culture Collection
ATP	Adenoside Triphosphate
AUC	Area Under Curve
BCC	Basal Cell Carcinoma
BCR-ABL	BCR-ABL fusion protein or “Philadephia chromosome”
BRAF	v-Raf murine sarcoma viral oncogene homolog B
*BRAF*i	v-Raf murine sarcoma viral oncogene homolog B inhibitor
CCLE	Cancer Cell Line Encyclopedia
cDNA	complementary DNA
cFP	Clonal Fractional Proliferation
CML	Chronic Myeloid Leukemia
CR	Complete Response
CRAF	V-Raf-1 Murine Leukemia Viral Oncogene Homolog 1
CSC	Cancer Stem Cell
CTLA4	cytotoxic T-lymphocyte antigen 4
CyTOF	Cytometry by Time of Flight
DIP	Drug-Induced Proliferation
DMEM	Dulbecco's Modified Eagle's Medium
DMSO	Dimethyl sulfoxide
DS	Discrete Subline
DTP	Developmental Therapeutics Program
EC50	Half maximal Effective concentration
ECAR	Extracellular Acidification Rate
ECM	Extracellular Matrix
EGFR	Epidermal Growth Factor Receptor
EMT	Epithelial-Mesenchymal Transition
EOE	End of Experiment
ERK	Extracellular-signal Related Kinases
FACS	Fluorescence-activated cell sorting
FAK	Focal Adhesion Kinase
FDA	Food and Drug Administration
FUCCI	Fluorescence Ubiquitination Cell Cycle Indicator
GDSC	Genomics of Drug Sensitivity in Cancer

GIST	Gastrointestinal
GRN	Gene Regulatory Network
H2B-mRFP	Histone H2B monomeric Red Fluorescent Protein
HER2	Human Epidermal Growth Factor Recepter 2
HGF	Hepatocyte Growth Factor
IC50	Half maximal Inhibitory Concentration
IGF1-R	Insulin Like Growth Factor 1 Receptor
KEGG	Kyoto Encyclopedia of Genes and Genomes
lm	linear model
mAG	monomeric Azami Green
MAPK	Mitogen-activated protein kinases
MCMC	Monte Carlo Markov Chain
MEK1/2	Mitogen-Activated Protein Kinase Kinases 1/2
MEKi	MEK inhibitor
mRNA	messenger Ribonucleic Acid
NAD	Nicotinamide adenine dinucleotide
NAMPT	Nicotinamide phosphoribosyltransferase
NCI	National Cancer Institute
NF1	Neurofibromin 1
NMN	Nicotinamide Mononucleotide
NOX	NADPH Oxidase
NOX5	NADPH Oxidase 5
NOXi	NADPH Oxidase Inhibitor
NRAS	Neuroblastoma RAS Viral (V-Ras) Oncogene Homolog
NRG	Neuregulin 1
NSCLC	Non-Small Cell Lung Carcinoma
OCR	Oxygen Consumption Rate
ODE	Ordinary Differential Equations
PBS	Phosphate Buffered Saline
PCA	Principal Component Analysis
PD	Progressive Disease
PDGFRα	Platelet-derived growth factor receptor alpha
PDX	Patient-Derived Xenografts
PEA	Partial Equilibrium Assumption
PLX	plexxikon
PR	Partial Response
qPCR	quantitative Polymerase Chain Reaction
RECIST	Response Evaluation Criteria in Solid Tumors
RNA-FISH	Ribonucleic Acid--Fluorescent in situ hybridization
RNASeq	Ribonucleic Acid Sequencing
ROS	Reactive Oxygen Species
RPMI	Roswell Park Memorial Institute medium

RTK	Receptor Tyrosine Kinases
SB	SB2033580
SC	Subclone
SCC	Squamous Cell Carcinoma
SD	Standard Deviation
SD	Stable Disease
SEM	Standard Error Mean
siRNA	small interfering RNA
TGFβ	Transforming Growth Factor Beta
UV	Ultraviolet
WT	Wild Type

CHAPTER 1

TARGETED THERAPY AND PERSONALIZED MEDICINE IN CANCER

Targeted Therapy in Cancer

Cancer is one of the leading causes of death in the world [1] and in the United States [2]. The incidence of cancer is on rise in the last few decades owing to recent advancements in cancer screening and diagnosis. In the next decade, the new cancer cases worldwide are projected to increase by 50% [3]. In the United States alone, 1.6 million new cancer cases and 600,920 cancer deaths are projected to occur in 2017 [2]. These numbers are staggering worldwide [1]. Significant percentage of cancer incidence and mortality occur in developing countries in Asia, Africa and South America [3].

Recent progress in basic translational science has added more treatment options for cancer patients; however, cancer still remains as largely untreatable disease. Traditionally, cytotoxic chemotherapy and radiation therapy have been the standards of care for different cancers [4]. In early decade of 2000, a genomic revolution [5] led to a massive genomic characterization of tumors. This characterization steered treatment options from cytotoxic chemotherapies to more specific gene directed therapy. These “Targeted therapies” refer to a class of drugs that interfere with specific molecular targets that have a significant role in tumor progression and maintenance [6]. In contrast to chemotherapy which targets all dividing cells, targeted therapy is more specific to cancer cells with a distinct gene aberration. The scope and research interest in targeted therapy have increased considerably after the early success of imatinib in chronic myeloid leukemias (CML) and gastrointestinal stromal tumors (GIST).

The rationale for using targeted inhibitors of specific proteins or kinases relies on the idea of "oncogene addiction," [7] which posits that cancer cells, despite having multiple genetic and epigenetic alterations, depend on a few genes for rendering different hallmarks of cancers and are often susceptible to impairment of such oncogenes [8]. Experimental evidence of oncogene addiction has been obtained in diverse systems: genetically engineered mouse models, mechanistic studies on human cancer cell lines, and clinical trials [9]. With the use of transgenic mice, researchers found that expression of *c-myc* oncogene in the hematopoietic cells led to the tumor growth, while its inhibition led to growth arrest and apoptosis [10]. Colomer *et. al.* used *erbB-2* antisense oligonucleotides and inhibited the proliferation of human breast cancer cell lines with an amplified *erbB-2*, providing support for the dependence of breast cancer cells on this oncogene [11]. The use of targeted inhibition of oncogenes either through antibodies or drugs has significantly improved patient outcomes, further validating the importance of such oncogenes in tumor maintenance [12,13].

Translation of this dependence to therapeutic exploit has not always been easy because of pleiotropic distribution and action of some of these oncogenes. The earliest clinical targeting of oncogene addiction came in the form of trastuzumab (monoclonal antibody targeting *HER2*) for treatment of patients with *HER2* amplified breast cancer [12,14–16]. Human epidermal growth factor receptor (*HER2*) is overexpressed in 20-30% of breast cancers, and trastuzumab improved progression free survival in both the adjuvant and metastatic settings [12,17]. Fast-track Food and Drug Administration (FDA) approval of multi-kinase inhibitor imatinib in treating CML [18–20] subsequently led to the approval of imatinib (in *KIT*-mutated GIST) [21,22], erlotinib [23] and gefitinib [24,25] (in *EGFR*-mutated Non-Small Cell Lung Cancer (NSCLC)), vemurafenib (in *BRAF*-mutated melanoma) [26,27] and crizotinib (in *ALK*-fusion positive NSCLC) [28,29]. Currently, there are numerous targeted agents

available to treat different cancers (Table 1.1). This list is expected to increase in the next few years as our understanding of the molecular basis of cancer becomes clearer. Current targeted therapies can broadly be categorized into two types: (i) Monoclonal antibodies & (ii) Small molecules. Monoclonal antibodies are designed specifically against extracellular proteins or cell surface proteins, whereas small molecules, because of their ability to get into cells, target intracellular proteins or kinases.

Table 1.1: FDA-Approved Targeted Therapies in Oncogene-Addicted Cancers.

Drug	Molecular target	Cancer Type	Category
Imatinib	*BCR-ABL*^{mutant}	CML[1]	Small Molecule
Trastuzumab	*HER2*^{amplification}	Breast cancer	Monoclonal Antibody
Erlotinib	*EGFR*^{mutant}	NSCLC[2]	Small Molecule
Gefitinib	*EGFR*^{mutant}	NSCLC	Small Molecule
Vemurafenib	*BRAF*^{mutant}	Melanoma	Small Molecule
Crizotinib	*ALK*^{fusion}	NSCLC	Small Molecule
Dabrafenib	*BRAF*^{mutant}	Melanoma	Small Molecule
Afatinib	*EGFR*^{mutant}	NSCLC	Small Molecule
Olaratumab	*PDGFRα*	Soft tissue sarcoma	Monoclonal Antibody

Melanoma Biology and Therapy: Current Options and Challenges

Skin cancer is the most common form of cancer in the United States and is broadly categorized into two groups: (i) Non-Melanomas and (ii) Melanomas [2,30]. Non-melanomas

[1] Chronic myeloid leukemia (CML)
[2] Non-small cell lung cancer (NSCLC)

are comprised of Basal Cell Carcinoma (BCC) and Squamous Cell Carcinoma (SCC) based on their cell of origin. Non-melanoma skin cancers are considered curable, mostly through surgical resection [2]. In contrast, melanoma is the most lethal form of skin cancer. Although it accounts for less than 3% of new skin cancer cases, melanoma is responsible for the vast majority (~80%) of skin cancer related deaths. The American Cancer Society (ACS) estimates 87,100 new cases of melanoma diagnoses (~5% of total cancer cases) and 9,730 cancer deaths in 2017 [2]. Based on the recent statistics published by ACS, melanoma is among the top seven cancers in the United States among both male and female [2]. Over the years, among the top seven cancers in the United States, melanoma is the only cancer whose incidence is increasing at an alarming rate, partly due to better screening and diagnosis.

Melanoma arises from melanocytes, pigment producing cells that are mostly found in the skin and eyes. Melanocytes originate from motile neural-crest progenitors that migrate to skin and eyes during embryonic development. Their function and homeostasis are regulated by keratinocytes, a cell type in the skin epidermis [31]. Melanomas are sub-divided into three groups based on their anatomical location: (i) Mucosal, (ii) Ocular and (iii) Cutaneous. Mucosal melanoma originates from melanocytes that line the epithelia of the nasal cavity, oropharynx, and gastrointestinal tract, and is a rare subtype of melanoma accounting for only 1-2% of total melanoma cases [32]. Ocular melanoma is the second most common type of melanoma, and accounts for about 5% of all melanoma cases and originates from melanocytes that line conjunctival membrane and uveal tract of the eye [32,33]. In contrast, cutaneous melanoma, also called melanoma of the skin accounts for a large portion of melanoma, representing >90% or more cases [32]. If diagnosed early, melanoma can be surgically removed. However, most melanomas are discovered after they have already metastasized, making metastatic

melanoma difficult to treat, with a dismal 5-year survival rate of less than <20%, depending on location [34].

Up until the early 2000s, metastatic melanoma diagnosis essentially depended on pathology—which divided melanoma into four main clinical subtypes based on their growth pattern and associated risk factors: superficial spreading melanoma, nodular melanoma, lentigo maligna melanoma and acral lentiginous melanoma [35]. After the discovery of *BRAF*-mutated melanoma in 2002 [36], different genomic subgroups of cutaneous melanoma have been identified. Recent molecular profiling and integrative analyses of genomic alterations show melanoma to be a heterogeneous group of malignancies driven by distinct patterns of oncogenic mutation. These studies have categorized melanoma into four groups: *BRAF, NRAS, NF1* and Triple Wild-Type, based on their genotypes and known mutations mostly in *MAPK* signaling cascade [37]. Activating *BRAF* mutations are the most frequent genetic alterations in cutaneous melanoma, reported in 50% of all malignant tumors (7-8% of cancers) [36–38], about 80-90% of which involve the substitution of valine at codon 600 by glutamic acid ($BRAF^{V600E}$) [39]. Mutations in *NRAS* comprise of the second major group, accounting for 30% of all cutaneous melanoma. The third most commonly observed mutations in melanoma samples is loss of function mutation in *NF1*, observed in 15% of all tumor samples. The remaining tumor samples, which lacked mutations in *BRAF*, *NRAS* and/or *NF1* defined the Triple-WT subtype [37]. This classification did not only set the stage for accurate subtyping of cutaneous melanoma, but also has ignited plethora of research in development of targeted drugs for specific groups.

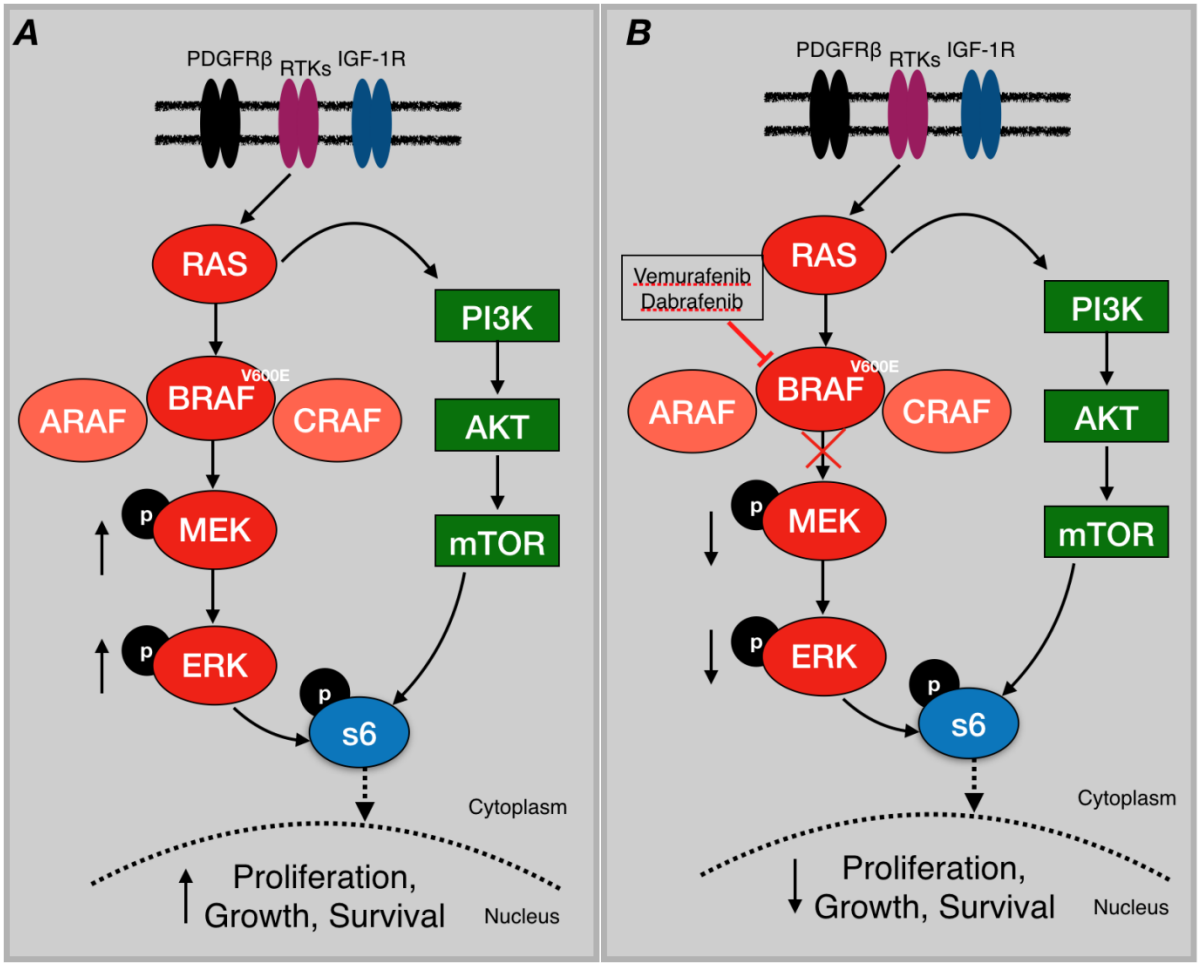

Figure 1.1: Deregulated MAPK signaling pathway in *BRAF*-mutated melanoma cells. (A) Missense mutations in *BRAF* lead to its constitutive activation, leading to enhanced phosphorylation of MEK, ERK and ultimately increased cell survival, proliferation and growth. (B) Small molecule inhibitors of *BRAF* (i.e. vemurafenib, dabrafenib) inhibit mutant-*BRAF* and its activity, leading to decrease in cellular proliferation and survival.

Current Options: Success story so far

The year 2011 marked an end to "dark ages" of melanoma as the FDA approved a targeted therapy for melanoma patients [27]. Before that, metastatic melanoma was considered largely incurable, and only FDA approved treatment options for melanoma were dacarbazine and high dose interleukin-2 [40]. Dacarbazine is the only FDA approved chemotherapy for metastatic melanoma; however, it has low response rates and poor progression free survival [26]. In contrast, interleukin-2 offers longer durable responses, but only benefits a minority of patients and is often associated with high toxicity [41]. The

identification of an activating missense mutation (V600E) in the *BRAF* kinase in majority of primary and metastatic melanoma has provided an attractive target for targeted therapy [36–38].

Because a majority of melanomas harbor an activating missense mutation (V600) in the *BRAF* kinase [36], they have an activated MAPK signaling pathway. MAPK signaling pathway that consists of RAS-RAF-MEK-ERK signaling axis has a key role in regulating cellular responses to growth signals (Figure 1.1). Activating mutations in *BRAF* kinase involve missense mutations, approximately 90% of which involve the substitution of valine at codon 600 by glutamic acid (V600E), although other mutations are also known (for example V600K, V600D, V600R) [36,38]. These missense *BRAF* mutations lead to constitutive activation of downstream signaling through *MEK* and *ERK*, leading to enhanced cell growth and proliferation [42]. Because of the importance of oncogenic *BRAF* in driving tumorigenesis in melanoma models [42], small molecule inhibitors were developed to specifically target activated *BRAF*. PLX4720 showed greater specificity and preferentially inhibited $BRAF^{V600E}$ compared to other broad kinases leading to cell cycle arrest and apoptosis exclusively in $BRAF^{V600E}$ positive melanoma cells (Figure 1.1) [43]. Subsequent studies led to the discovery of vemurafenib (PLX4032), structurally similar but with better pharmacokinetics properties, as inhibitor of mutated *BRAF* in melanoma models [13]. The approval of vemurafenib changed the treatment paradigm in melanoma [27]. Vemurafenib resulted in tumor regression and improved both overall and progression free survival in patients harboring *BRAF* mutations compared to dacarbazine [26,44,45]. The estimated median progression-free survival was reported to be 5.3 months in the vemurafenib group and 1.6 months in the dacarbazine group [26].

Despite exhibiting an improved clinical efficacy in patients with $BRAF^{V600E}$ mutations, vemurafenib resulted in adverse cutaneous side effects, especially the development of

cutaneous squamous cell carcinoma (SCC), keratocanthoma or both in 18% of patients [26,45]. Following the initial success of vemurafenib, the FDA approved second small molecule inhibitor dabrafenib as single agent therapy which showed higher specificity against activated *BRAF* compared to wild-type *BRAF* and *CRAF* [46,47] and lower cutaneous adverse effects compared to vemurafenib [26,45]. Because of an improved progression-free and overall survival compared to chemotherapy, trametinib, a selective *MEK1/MEK2* inhibitor, was also granted FDA approval for metastatic melanoma in 2013 first as single agent [48–51]. Although trametinib resulted in inferior response rates compared to vemurafenib, it did not result in cutaneous squamous cell carcinomas, commonly observed adverse effects in vemurafenib and dabrafenib [50]. However, both preclinical and clinical evidences led to conclude that combination of *BRAF*i with *MEK*i showed higher response rates, and better clinical efficacy compared to single agents [52–54]. This combination soon replaced single agents as the preferred treatment regimen for patients with metastatic melanoma harboring $BRAF^{V600}$ mutations [52,54,55].

Concurrent to targeted therapies, immunotherapy also has had some success in melanoma patients. High-dose interleukin-2 (IL-2) was the first immune therapy that was granted FDA approval for metastatic melanoma [40]. Although high-dose interleukin-2 benefited only a small fraction of melanoma patients, it produced durable partial and complete responses leading to long-term survival [41]. There is a considerable interest in melanoma immunotherapy because of length of durable responses observed in responding patients. Ipilimumab, a human monoclonal antibody specific for human cytotoxic T lymphocyte-associated antigen 4 (CTLA4) showed improved median overall survival (10.1 months) compared to glycoprotein 100 (gp100) peptide vaccine (6.4 months) in patients with metastatic melanoma regardless of their genetic mutation [56] and was granted FDA approval in 2011.

This was followed by the approval of Pembrolizumab, antibody against human anti-programmed-death-receptor-1 in 2014 [57,58]. Later studies showed Pembrolizumab to have higher overall survival and less toxic effects compared to ipilimumab [59]. Options in targeted therapies, immunotherapies and chemotherapies have significantly improved clinical care for patients with metastatic melanoma (Table 1.2). In recent years, immunotherapies are preferred as the first-line therapy for melanoma patients [60]. However, targeted therapies still show greater promise because of its higher response rates in patients with *BRAF* oncogenic mutations. Therapeutic failure to targeted therapies is attributed to tumor heterogeneity which will be discussed in detail in subsequent sections. The following section discusses the challenges in current targeted therapy in melanoma with development of various resistance mechanisms in both clinical and preclinical experimental system.

Table 1.2: A list of current FDA approved therapies for metastatic melanoma

Drugs	Class of Drugs	Approved
Dacarbazine	Chemotherapy	1975
High-dose Interferon Alfa-2b	Immunotherapy	1986
Interleukin-2	Immunotherapy	1998
Ipilimumab	Immunotherapy	2011
Peginterferon Alfa-2b	Immunotherapy	2011
Vemurafenib	Targeted Therapy	2011
Dabrafenib	Targeted Therapy	2013
Trametinib	Targeted Therapy	2013
Pembrolizumab	Immunotherapy	2014
Nivolumab	Immunotherapy	2014
Talimogene laherparepvec “T-Vec”	Immunotherapy	2015
Trametinib + dabrafenib	Targeted Therapy	2015
Cobimetinib + vemurafenib	Targeted Therapy	2015
Nivolumab +Ipilimumab	Immunotherapy	2016

Challenges: Resistance Mechanisms

Targeted small molecule inhibitors of *BRAF* show remarkable, short-term efficacy in melanoma patients with tumors harboring $BRAF^{V600}$ mutations. However, clinical responses are variable (Figure 1.2), short-lived, and relapse is almost inevitable within few months of therapy initiation. Rapid acquisition of drug resistance still remains a major challenge for successful melanoma therapy. This treatment failure has subdued the excitement that targeted

therapies once brought to the field of melanoma and cancer in general. Broadly, the common resistance mechanism to targeted kinase inhibitors constitutes: (i) alterations in the target gene, (ii) dependence on the targeted pathway, (iii) activation of alternative pathway(s), and (iv) resistance mediated by the microenvironment. A list of known resistance mechanisms in *BRAF*-mutated melanomas is provided in Table 1.3.

(i) Alterations in the target gene

The most common resistance mechanism to ATP-competitive targeted kinase inhibitors constitutes the acquisition of second "gatekeeper" mutations in the target gene. While gatekeeper mutations have been discovered for imatinib [61] (T315I in *BCR-ABL* in CML), erlotinib [62] (T790M in *EGFR* in NSCLC), and trametinib [63] (Q60P in *MEK2* in melanoma), no such mutation has yet been identified for *BRAF*-inhibitors (*BRAF*i). In addition to secondary mutations, amplification of the target gene can also confer resistance to targeted inhibitors. Villanueva *et. al.* [63] identified *BRAF* amplification in xenograft tumor model derived from patients resistant to the combination of dabrafenib and trametinib. Poulikakos *et. al.* [64] showed that cells resistant to vemurafenib expressed splice isoforms of $BRAF^{V600E}$ that dimerized in a *RAS*-independent manner. Although different from gatekeeper mutations, both target gene amplification and splice variants underscore the reliance of cancer cells on the targeted oncogenic pathway.

(ii) Dependence on the targeted pathway

Because of their increased dependence on the targeted pathway, cancer cells reactivate the signaling axis under targeted inhibition through either modification of the target gene or alterations in downstream or upstream effectors of the signaling cascade. Some of the known resistance mechanisms under *BRAF*i that reactivate MAPK signaling pathway include:

elevated expression of *CRAF* [65], *BRAF* amplification [63,66], *BRAF* kinase domain duplication [67], expression of *COT* [68], upregulation of *NRAS* or RTK [69], mutations in *MEK1/2* [70,71].

(iii) Activation of alternative pathway(s)

Cancer cells can also bypass the dependence on the targeted pathway by activating alternative pathway(s). In melanoma, upregulation of receptor tyrosine kinases (RTKs) as well as activation of parallel PI3K-AKT signaling pathways have been shown to confer resistance to *BRAF*i. Nazarian *et. al.* [69] showed elevated expression of *PDGFRβ* in patients whose tumors regressed on *BRAF*i. Villanueva *et. al.* [72] demonstrated increased expression of *IGF-1R* and pAKT level thus enhancing the signaling through PI3K-AKT signaling in *BRAF* inhibitor resistant human melanoma samples [72]. The role of PI3K-PTEN-AKT signaling pathway in acquired resistance to *BRAF*i was further corroborated from several recent studies [73–76].

(iv) Resistance mediated by the microenvironment

The models of drug resistance discussed above are cell-autonomous. However, given the complexity of cancer, it is appreciated that cancer is not just the collection of cells. It is becoming increasingly clear that cancer cells work symbiotically with their environment, other cell types, and neighboring cells to tolerate external perturbations. A number of recent studies have suggested that the tumor microenvironment contributes to resistance to targeted therapies by creating a “safe heaven” for cancer cells. A systematic analysis of interactions between tumors and the microenvironment by Straussman *et. al.* uncovered the role of hepatocyte growth factor (HGF) secreted by stromal cells in conferring an innate/intrinsic resistance to *BRAF*i [77]. The study showed that HGF secreted by stromal cells, particularly fibroblasts, confer resistance to *BRAF*-inhibition in *BRAF*-mutated melanoma cells by activating MET, and downstream MAPK and PI3K/AKT signaling cascades. Subsequent

studies revealed the role of extracellular matrix (ECM) and cell adhesion molecules in facilitating resistance to *BRAF*i. Hirata *et. al.* showed that melanoma cells "paradoxically" activate fibroblasts and remodel their extracellular matrix by activating integrin β1/FAK/Scr signaling to survive *BRAF*-inhibition [78]. Fedorenko *et. al.* in a series of papers underscored the role of fibroblasts-mediated drug resistance in melanoma cells undergoing *BRAF*-inhibition. Vemurafenib-treated melanoma cells released transforming growth factor-β (*TGFβ*) which led to enhanced fibronectin deposition, upregulation of neuregulin (*NRG*) [79]. Mechanistically, it was shown that enhanced fibronectin remodeled a protective niche through integrin $\alpha_5\beta_1$ and elevated signaling through PI3K/AKT pathway [80]. Together, increasing evidence suggests that melanoma cells cooperate with their microenvironment, other cell types and neighboring cells either through secretome or through ECM remodeling to survive drug exposure.

Table 1.3 Diversity of Known Resistance Mechanisms in *BRAF*-mutated Melanoma Cells Against *BRAF*i.

Resistance Mechanism Type	Mechanisms	References
Alterations in the target gene	*BRAF* Splice Variants	[64]
	BRAF Amplification	[63,81]
	BRAF kinase domain duplication	[67]
Dependence on the targeted pathway	Elevated *CRAF* Expression	[65]
	COT Expression	[68]
	NRAS up-regulation	[69]
	MEK1/2 mutations	[70,71]
Activation of Parallel Pathways	Elevated RTK expression	[69]
	Signaling via PI3K/AKT	[73,74]
Mediated by Microenvironment	HGF Secretion	[77]
	FAK/Scr signaling	[79,80]
	ECM remodeling	[78]

Heterogeneity: The Source of Tumor Recurrence

It is now well appreciated that cancer is not one disease, rather a collection of multiple diseases. There is substantial variability among cancer cells in both their genetic and functional features. These differences (both genetic and phenotypic) exist not only between tumors (inter-tumor heterogeneity) but also within single tumors (intra-tumor heterogeneity). Inter- and intra-tumor heterogeneity have direct implications not only in the choice of biomarkers to guide treatment, but also on the outcome of cancer treatments. While some lesions undergo dramatic initial responses to therapy, other lesions in the same patient

continue to progress. Even within the same tumor, despite an impressive early regression, tumors invariably recur within a few months of therapy initiation. This partial or incomplete response observed in seemingly identical oncogene-driven tumors points to tumor heterogeneity responsible for tumor recurrence. In this subsection, I will discuss heterogeneity between tumors (inter-tumor) and within tumors (intra-tumor) and its implications for therapy.

Inter-tumor Heterogeneity

Tumors, depending on their tissue of origin or cell types, vary in their genomic landscapes. Tumors originating in different tissues exhibit varying degrees of mutational frequencies of oncogenes and tumor suppressor genes [82]. In addition, cell-intrinsic differences also affect the tumor composition which affect the therapeutic response of tumors to anti-cancer drugs. For instance, *BRAF*i are much more effective in *BRAF*-mutated melanoma cells than in *BRAF*-mutated colorectal cancer cells [83]. Recent experimental evidence suggests that diminished efficacy of vemurafenib in *BRAF*-mutated colorectal cancer is due to reactivation of epidermal growth factor receptor (*EGFR*) signaling in response to vemurafenib [84]. Mechanistically, *BRAF*i cause rapid feedback activation of *EGFR*, which supports continued proliferation even in the presence of *BRAF*-inhibition [84,85]. Since basal phospho-*EGFR* levels are higher in *BRAF*-mutated colorectal cancer cells than in *BRAF*-mutated melanoma cells, colorectal cancer cells utilize *EGFR*-mediated resistance to vemurafenib [86]. Therefore, cellular context and inherent nature of cancer cells are highly relevant to therapeutic efficacy. However, considerable variation is also seen in genomic features of tumors that originate from the same tissue and cell type [87].

Even with tumors harboring common $BRAF^{V600}$ mutations, melanoma patients respond differently to vemurafenib, a potent small molecule inhibitor of mutated *BRAF*. The clinical responses are variable and differ from patient-to-patient in metrics such as time to response,

initial reduction in tumor size, progression-free survival and overall survival (Figure 1.2) [26,45]. This widespread patient-to-patient variability has led to increased efforts in identification of biomarkers to guide treatment options. Some strategies include identifying subset of patients that are likely to respond to particular therapy—an effort which not only maximizes treatment outcomes, but also saves time and resources.

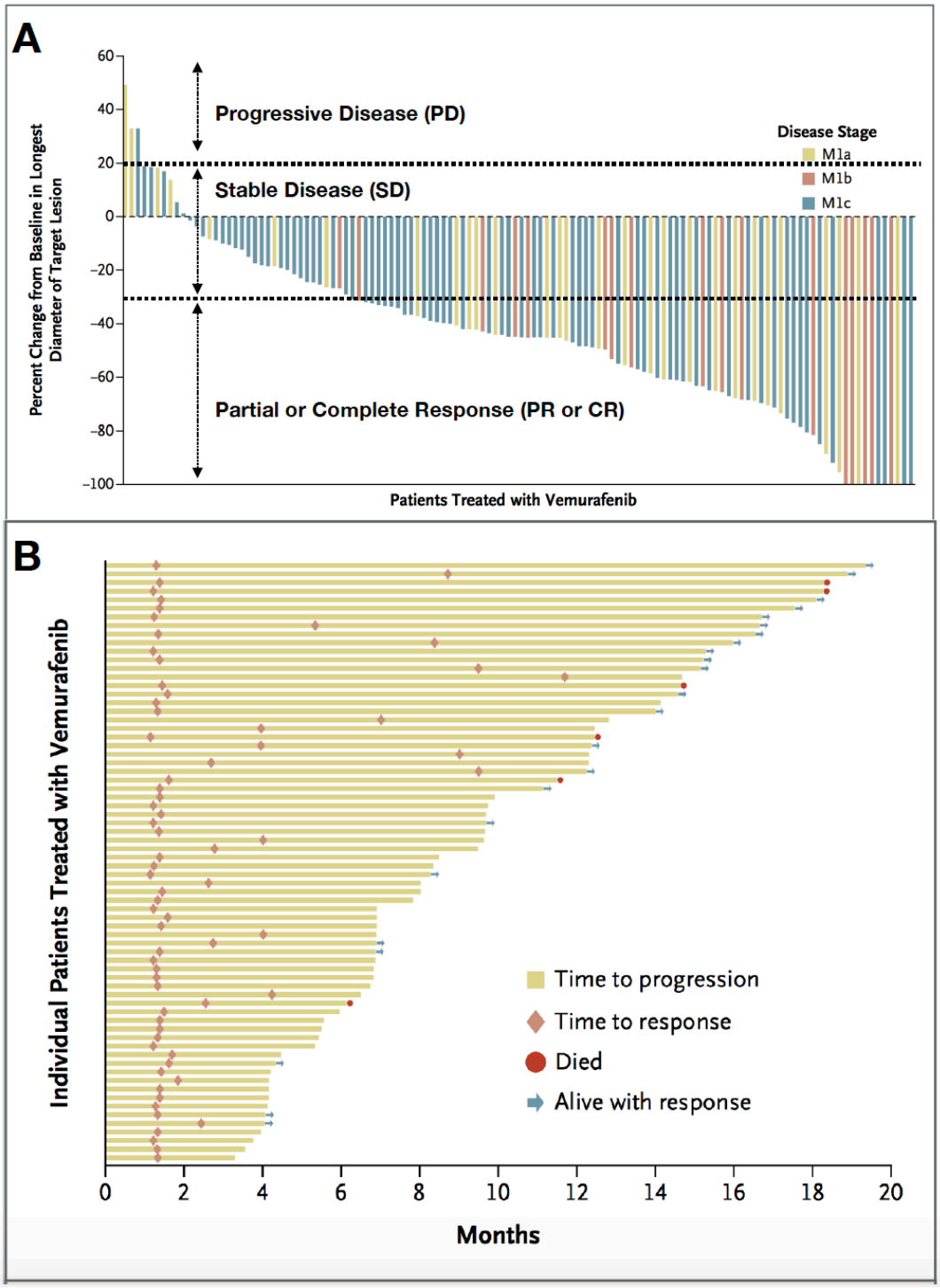

Figure 1.2: Patient-to-patient variability in *BRAF*-mutated Melanomas. (A) Waterfall plot showing objective tumor responses with vemurafenib; RECIST criteria used to categorize patient clinical responses. A decrease of at least 30% is defined as Partial Response (PR), 100% decrease—Complete Response (CR), an increase of 20% and more is Progressive Disease (PD), and tumor response between -30% and 20% is Stable Disease (SD). (B) Times to response (in months) and progression among 69 patients treated with vemurafenib. Reproduced with permission from Sosman *et. al.* NEJM. (2012), Copyright Massachusetts Medical Society.

Intra-tumor Heterogeneity

Cancer cells within a tumor display profound variability in characteristics such as size, morphology, invasive and metastatic ability, mutations and mutant-oncogene expression [88,89]. Indeed, it is widely accepted now that at a fine-enough resolution, cancer cells will display widespread phenotypic differences [90]. It is, therefore, not surprising that cancer cells from seemingly identical cell populations or a uniform genetic lineage or a single tumor also exhibit differential sensitivity to anti-cancer drugs [91–93]. Thus, one challenge in biology is not to demonstrate that cancer cells are heterogeneous, rather to understand the origins of such variability. Broadly, the origins of intra-tumor heterogeneity can be traced to either genetic- or non-genetic sources.

Genetic Sources

Malignant tumors, at a given time, are expected to consist of numerous somatic mutations and are speculated to evolve over time. This idea of tumor evolution dates back to seminal work by Peter Nowell in 1976 which laid the foundation for evolutionary principles in cancer [94]. Tumors evolve through acquisition of a series of mutations over time as a result of high genomic instability broadly either through “linear” or “branched” evolution. In linear evolution, tumor progression is thought to result from acquired genetic alterations in a dominant clone which is selected over time leading to emergence of more aggressive tumors. While in branched evolution, multiple clones arise simultaneously and survive leading to co-existence of heterogeneous mutations [95]. Regardless of the origin, the existence of clonal differences within a tumor provides a basis for Darwinian selection—which posits that fitter clones are “passively” selected over time under perturbations. The model assumes that while most clones die out under treatment, fitter clones because of their advantageous mutations survive an initial treatment, and expand during therapy leading to tumor recurrence.

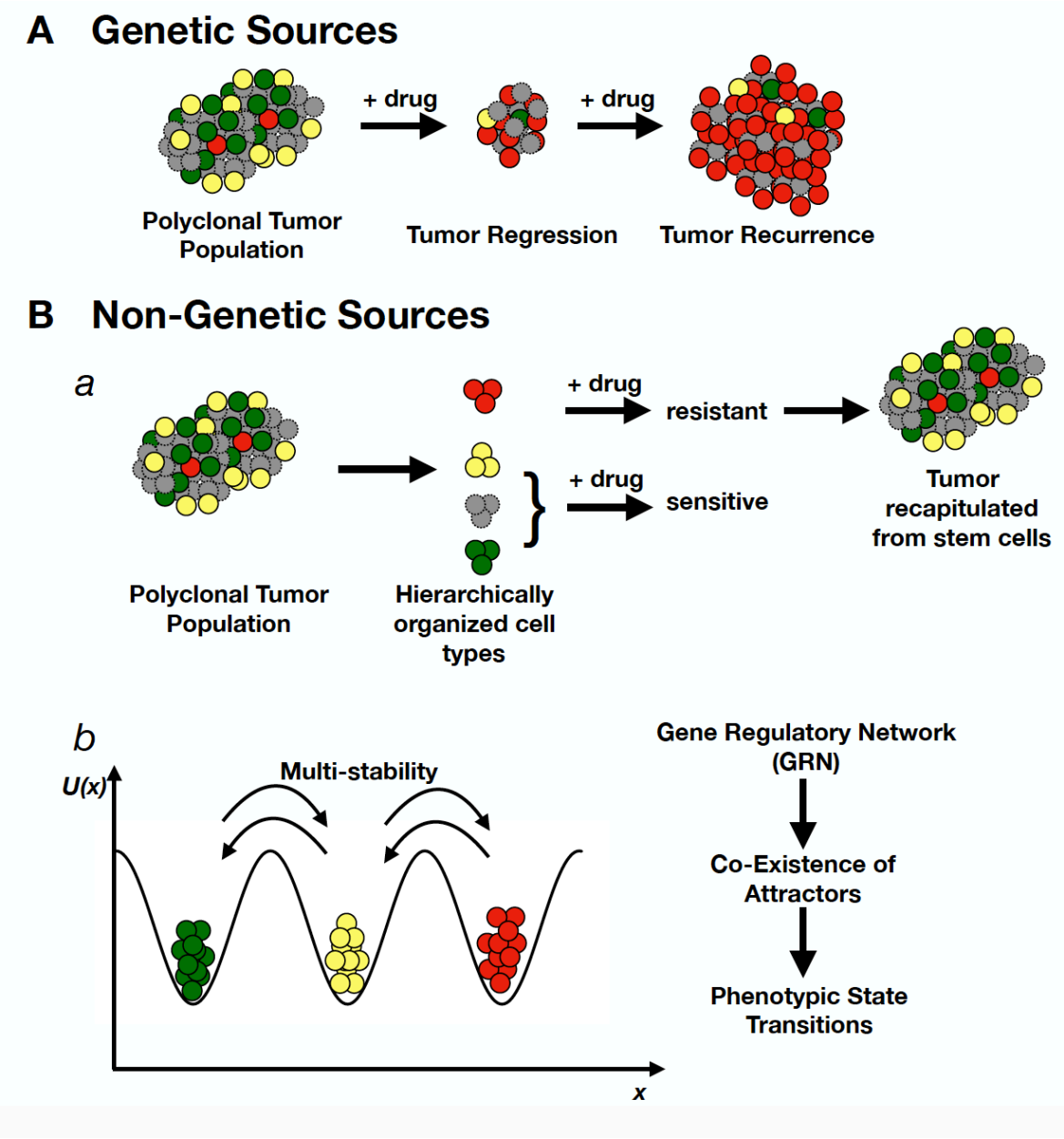

Figure 1.3: Sources of Tumor Heterogeneity. Tumor heterogeneity arises from either genetic sources or non-genetic sources. (A) Genetic sources usually refer to the clonal selection model; (B) While non-genetic sources encompass cancer stem cell hypothesis (*B.a*), stochastic process and epigenetic landscape and attractor theory (*B.b*), here *U(x)* represents quasi-potential energy and *x* is the reaction coordinate, arrows represent phenotypic state transitions between subpopulations.

This type of intra-tumor heterogeneity forms the basis for intrinsic or innate resistance, where pre-existing genetic differences among cancer cells are speculated to contribute to treatment failure (Figure 1.3a). For instance, pre-existing amplifications of *EGFR* [96],

mutations in *RAC1* [97], and *MEK1/MEK2* mutations [98] were identified in drug-naïve tumors of *BRAF*-mutated melanoma patients, albeit in small frequency. With innovation in large-scale genetic screens, we are likely to find many more such alterations in drug naïve tumors that correlate to tumor recurrence. The central idea of Darwinian principle is that tumors undergo irreversible changes under perturbations such as drug selection such that subpopulations with advantageous mutations dominate the tumor size. This would require that cancer cells selected under treatment would be highly resistant to similar treatments in subsequent times. However, both preclinical and clinical evidence show that cancer cells can become re-sensitized to therapy after an initial treatment [81,99–101]. Combination therapies have been proposed based on the nature of pre-existing or acquired mutations in tumors, with implications of co-targeting multiple pathways to achieve durable responses. However, combination therapies offer only modest improvements compared to monotherapies. This coupled with reversibility of drug-sensitivity observed in tumors suggest that genetic sources cannot explain the entire degree of variability seen in cancer cells.

Non-Genetic Sources

Accumulating evidence suggests that non-mutational processes play a significant role in the response of cancer cells to drugs [102–105]. Cancer cells employ a dynamic survival strategy governed by epigenetic alterations to survive lethal drug exposure [106,107]. Epigenetic alterations depend on the amount of drugs used—as the drug-tolerant state in cancer cell populations were reported in high concentrations [106,108]. In addition, the nature of alterations vary over different time scales—short-term changes involving histone (de-) modification dynamics, while long-term changes involving intrinsic differences due to cell division [109,110]. These strategies are reminiscent of survival strategies observed in bacterial cell populations [111,112]. Non-genetic sources, in broad terms, trace their origin to: (i)

Stochastic Processes, (ii) Differentiation Hierarchies, and (iii) Epigenetic Landscape and Attractor Theory. With the right use of high-throughput and high-content single-cell analyses and lineage construction assays, it may be possible to characterize and quantify the contribution of each of these non-genetic sources [93,102,113–115]. Non-genetic changes are reversible as compared to genetic clonal evolution model which is irreversible. Although they explain two different types of tumor progression, they are not mutually exclusive.

(i) Stochastic Processes

The stochastic model assumes that cancer cells within a clonal subpopulation are identical, and heterogeneity in their behaviors is influenced by stochasticity in both cell-intrinsic and extrinsic factors [116]. Cell intrinsic factors constitute random fluctuations in biochemical reactions within cells, transcriptional burst leading to cell-to-cell variation in mRNA and protein concentrations, cell fate decisions [102,117,118]. Similarly, cell extrinsic factors such as tumor microenvironment, growth factors, immune response also result in randomness among cells in expression of cell surface markers, tumor initiation capacity, and cell fate decisions. Irrespective of the nature of origin, stochastic model suggests that the cellular phenotype is not heritable and all cells are prone to such stochastic influences. All cancer cells in stochastic view of heterogeneity possess similar tumorigenic, invasive, metastatic potential.

(ii) Differentiation Hierarchies

In contrast, hierarchy model postulates that heterogeneity in cancers reflects differentiation hierarchies that exist in normal tissues. Within this view, cancer cells are hierarchically organized into majority of non-tumorigenic and small subpopulation of tumorigenic cells [119–121]. In other words, tumors are composed of stem- and non-stem cells. Stem-ness is then referred to as an enhanced tumorigenicity and self-propagating capacity. Only cancer stem cells (CSCs) maintain their tumorigenic potential and can recapitulate initial tumor

heterogeneity even when the bulk of non-tumorigenic cancer cells die out under perturbations (Figure 1.3b). Numerous studies have described diagnostic markers to identify cancer stem cell populations. High expression of ABC transporters [122], ALDH expression [123,124], CD271 expression [125,126] are some well-described markers. Cancer stem cell hypothesis differs from stochastic model in terms of the fraction of tumor cells capable of self-renewal. While stochastic model assumes all cancer cells are capable of self-renewal, CSC model assumes only a minority of cells have tumorigenic potential. However, it is still controversial whether cancer exhibits such a hierarchy; therefore, tumorigenic cells are often described as cancer-stem-cell-like cells.

(iii) Epigenetic Landscape and Attractor Theory

Within genetically similar cancer cells, a network of genes can give rise to multiple metastable cellular phenotypes (Figure 1.3b) [127–131]. This is defined in terms of gene regulatory networks (GRN), where genetically distinct cell type possesses the same underlying GRN. The idea dates back to Waddington and his seminal essay which described cellular differentiation as a dynamical trajectory through an epigenetic landscape [132]. Kauffman formalized Waddington's epigenetic landscape and linked phenotypic variability to a multidimensional dynamical-systems theory. He showed that given a network architecture, most random gene networks will ultimately settle into few stable basins of attraction called "attractors" [127]. Attractors represent distinct stable phenotypes in an epigenetic landscape. Epigenetic landscape is defined mathematically in terms of a quasi-potential energy surface [133], described with concepts from physical chemistry using either Arrhenius equation (for equilibrium systems or one-dimensional non-equilibrium systems) [134] or large deviations theory (for multidimensional non-equilibrium systems) [135]. Local minima or basins of attraction, within the potential surface constitute cell types and the relative stability of cell types

depends on the depths of the basins. Within this landscape, cells can transition between basins with rates dependent on the heights of local maxima or energy barriers separating basins. Within this framework, a cellular differentiation hierarchy is a special type of epigenetic landscape where transitions down a series of basins are more probable than up, although reverse transitions or dedifferentiation, are theoretically possible [136]. This framework allows for co-existence of multiple metastable phenotypes of comparable stability. A population of genetically similar cancer cells then driven by both intrinsic and extrinsic factors can transition in and out of these available phenotypes thus altering the proportions of cells that each state occupies. This phenotypic "drift" is postulated to be the source of non-genetic heterogeneity in cancer, which is known to influence therapeutic response [93,129]. Therefore, at a given time, cancer cells respond differently depending on the perturbations and fitness of each state.

Approaches to Study Heterogeneity

The rapid advancement in "omics" technology has made it possible to delineate inter- and intra-tumor heterogeneity. Heterogeneity, by its definition, refers to differences within a cell population with respect to specific features or properties. The degree of phenotypic heterogeneity is typically measured with respect to some trait X of individual cells. Heterogeneity is often defined with respect to gene expression (genomics), transcription factors, surface markers, protein expression (proteomics), and signaling. Recent studies have also demonstrated differences in how cancer cells respond to perturbations both in cell fates and clonal fitness [91,92,103]. Based on temporal information, current approaches applied to study heterogeneity can be classified into two types: *stationary* and *dynamic*.

Methods that provide population snapshots and their variation at a given point in time fall under *stationary* approaches. High throughput flow cytometry and similar techniques such as mass cytometry/CyTOF provide an extensive phenotypic characterization of cancer cells

both at the cell surface and intracellular levels (signaling). While these techniques provide quantitative assessments of proteins or markers' abundance, imaging-based tools such as immunofluorescence provide information on both the abundance and subcellular localization. Single cell RNA sequencing (scRNASeq) techniques also decipher intra-tumor heterogeneity within tumors [137–139]. Similarly, RNA-FISH (fluorescent *in situ* hybridization), although limited in number of probes, yields highly accurate RNA counts and localization data [140,141]. Highly multiplexed single-molecule RNA-FISH resolves numerous RNA species in different cellular context [140,142–145].

Because tumors evolve over time, a single population snapshot, such as seen with *stationary* approaches will provide an incomplete and often, an inaccurate representation of phenotypic heterogeneity. Therefore, *dynamic* tools are employed to monitor expression of markers in individual cells over time. Usually, tools to infer dynamic information involve time-lapse imaging which has been successfully used to examine live-cell reporters of signaling, transcription factor activity, and cell cycle phases [118,146,147]. Potential applications include single-cell tracking of cell fates and cell-lineage construction [148]. In addition, an extension of flow cytometry technology, FACS (fluorescence-activated cell sorting) can be used to sort cell populations into distinct subtypes and monitor their distributions and phenotypes over time to get dynamic insights. Existence of distinct subtypes within cell population, can be a biological strategy for adaptation to stressful environments. Heterogeneity within cell population can have profound effect on the cellular response to perturbations [149]. Recently, we proposed a high-throughput approach called clonal Fractional Proliferation (cFP) assay to measure clonal fitness and cell fate heterogeneity in cancer cells during drug treatment [92]. Since clonal fitness is defined in terms of drug-induced proliferation rate, difference between rates of division and death within a clonal lineage, it provides a dynamic metric to study how cancer

cells change under perturbations. Furthermore, multiple single-cell derived clones can be isolated from within a genetically identical cell population [92]. These clones mimic the pre-existing heterogeneity within cell populations and can be used to probe for molecular differences [92]. Additionally, these molecular differences could be correlated with their drug response dynamics and clonal fitness.

Summary and Purpose of this study

Targeted cancer therapies for melanoma show great promise because of their high response rates in *BRAF*-mutated tumors. As a result, mutant *BRAF* still remains an attractive target for melanoma treatment due to its oncogenic properties. However, the problems of treatment-refractory patient responses and drug resistance limit optimal drug efficacy. A tremendous amount of work has been done to understand a range of acquired resistance mechanisms in *BRAF*-mutated melanomas. Some of these studies have paved the way for combination therapies, currently the standard of care in clinic. However, even the current combination therapies offer only modest improvements over monotherapy, and clinical benefits remain transient and unpredictable. One of the main limitations in our knowledge in melanoma is that our understanding of tumor recurrence or resistance comes from post-resistant tumors or cells, and very little is known about what happens to tumor or cell populations during the early phase of response leading up to resistance. Traditional end-point assays often used to assess the drug's action lead to incomplete and misleading information since cancer is highly heterogeneous and adaptive in nature.

As part of my dissertation, I explored drug response variability within melanoma cell populations and quantified the range of clonal variation with recently proposed Drug-Induced Proliferation (DIP) rate [92,150]. The purpose of examining drug response variability at the clonal level is to probe the role of non-genetic differences in response dynamics, correlate

them with distinct molecular signals and identify the possible sources of variability within cell population. The fundamental goal of this study is to test the hypothesis that non-mutational variability among melanoma cells contributes to differential drug responses. Therefore, I employed a hybrid of experimentation and mathematical modeling, in a classical systems biology approach, to delineate the possible sources of cell-to-cell response variability. For this, I used *BRAF*-mutated human melanoma cell lines as model systems and a repertoire of live-cell imaging, single-cell cloning, RNA sequencing and mathematical modeling to understand the drug response dynamics. In the following chapters, I describe a novel metric and a method to quantify dynamics of cellular fitness and heterogeneity within cell populations (CHAPTER 2), link therapeutic response variability with glycolytic reserve (CHAPTER 3), provide a unifying view and a framework for short- and long-term melanoma sensitivity to targeted drugs in terms of combined processes of clonal competition and phenotypic state transitions (CHAPTER 4), identify potential determinants of drug-response variability among isogenic clonal sublines (CHAPTER 5). On-going experiments and future directions will steer this project to find potential drug targets and combinations (CHAPTER 6).

CHAPTER 2

A NOVEL METRIC TO QUANTIFY DYNAMICS OF CELLULAR FITNESS AND HETEROGENEITY IN RESPONSE TO PERTURBATION

Adapted from:

1. Frick PL, **Paudel BB**, Tyson DR, Quaranta V. Quantifying heterogeneity and dynamics of clonal fitness in response to perturbation. J. Cell. Physiol. 2015;230:1403–12.
2. Harris LA, Frick PL, Garbett SP, Hardeman KN, **Paudel BB**, Lopez CF, Quaranta V, Tyson DR. An unbiased metric of antiproliferative drug effect in vitro. Nat. Methods. 2016;13:497–500.

Summary

Cellular response to drug can be confounded by many complexities such as time dependency in measurements and heterogeneity within cell populations. The biases in exponential growth, delay in drug effect stabilization, differences in the cell division rates and clonal heterogeneity within cell populations could lead to erroneous conclusions about sensitivities of cells to drugs. In this chapter, I will describe two such approaches that take into account the differences in inter and intra-cell lines' fitness under perturbation and how that fitness changes over time. These methods comprise a novel metric of measuring the anti-proliferative effects of different perturbations and a high-throughput way of measuring pre-existing heterogeneity within parental cell populations. My contributions in both the referenced manuscripts included experimental data collection and analyses in *BRAF*-mutated melanoma cells.

Abstract

In vitro cell proliferation assays are widely used in pharmacology, molecular biology and drug discovery. Using theoretical modeling and experimentation, we show that current metrics of anti-proliferative small molecule effect suffer from time-dependent bias, leading to inaccurate assessments of parameters such as drug potency and efficacy. We propose the drug-induced proliferation (DIP) rate, the slope of the line on a plot of cell population doublings versus time, as an alternative, time-independent metric. Using the DIP rate to quantify the heterogeneous dynamics of clonal lineages within a cell population, we propose, for the first time, a method that enables a dynamic, global picture of clonal fitness within a mammalian cell population. This novel assay allows facile comparison of the structure of clonal fitness in a cell population across many perturbations. By utilizing high-throughput imaging, our methodology provides ample statistical power to define clonal fitness dynamically and to visualize the structure of perturbation-induced clonal fitness within a cell population. We envision that this technique will be a powerful tool to investigate heterogeneity in biological processes involving cell proliferation, including development and drug response.

Introduction

Evaluating anti-proliferative drug activity of cells *in vitro* is a widespread practice in basic biomedical research [151–153] and discovery of therapeutic molecules [154,155]. Typically, quantitative assessment relies on exposing cells to drugs over a range of concentrations and constructing dose-response curves from number of viable cells measured directly [147] or indirectly. The *de facto* standard metric is the number of viable cells 72 h after drug addition [152,156,157]. Being a single-time point measurement, we refer to this as a “static” drug effect metric. The data is then fit to the Hill equation [158], a four parameter log-logistic function, to produce a sigmoidal dose-response curve that summarizes the relationship between drug

effect and concentration. Parameters extracted from these curves include the maximum effect (E_{max}), the half-maximal effective concentration (EC_{50}), the half-maximal inhibitory concentration (IC_{50}), area under the curve (AUC) and activity area (AA) [152,156,157]. These are useful for quantitatively comparing various aspects of drug activity across drugs and cell lines.

We contend that dose-response curves constructed using current standard metric of drug potency and effect can result in erroneous and misleading values of drug-activity parameters, skewing data interpretation. This is because of many complexities such as time-dependent bias and pre-existing heterogeneity within cell populations. Time-dependent bias is when the metric value varies with the time point chosen for experimental measurement. We identify two specific sources of time-dependent bias: (i) exponential growth, and (ii) delays in drug effect stabilization. The former can lead to erroneous conclusions, e.g., that a drug is increasing in effectiveness over time, while the later requires shifting the window of evaluation to only include data points after stabilization has been achieved. Complementary to this idea, a recent report also highlights the bias due to different number of cell divisions during the course of an assay in various treatment conditions [159].

Another important aspect that confounds the traditional metrics is the heterogeneity that exists within cell populations. Historically, each data point in most *in vitro* assays is the average of the proliferative response of thousands of cells in a perturbagen-treated well, at single or few time points, in comparison to untreated control. However, it is becoming increasingly clear that heterogeneity within a cell population can have profound influence on outcomes [149]. It is well established that polyclonal cell populations, display variable fitness at the clonal level in certain microenvironments [94,160] and provides a mechanism for how cell populations adapt to stress. Heterogeneity itself, built in a cell population, can be a biological

strategy for adaptation to stressful environments. Well known cases include clonal subpopulations of tumor cells evading therapy [161], or bet-hedging bacteria [162]. These differences in clonal fitness could lead to a period of complex, non-linear dynamics (brief regression followed by rebound) observed for cell lines that exhibit wide variability in clonal responses. This kind of response behavior further corroborates the time-dependent bias in measuring the drug sensitivity in cell populations. However, differences in clonal fitness have also generally been considered in qualitative terms, relative to the size of the population. Thus, studies of clonal fitness variation would benefit from an approach that quantitatively assesses clonal differences over time, that is the dynamics and heterogeneity of polyclonal responses.

The proliferation of a cell population (at both clonal and population level) describes, at its most basic level, the process of cell numbers changing over time. Thus, accurate metrics to quantify proliferation are essential to understanding perturbation-induced cellular responses. Since proliferation is a dynamic process that, by its very nature, would be best quantified as a rate (for example population doublings per unit of time). To this end, we propose as an alternative drug effect metric the drug-induced proliferation (DIP) rate, defined as the steady-state rate of proliferation of a cell population in the presence of a given concentration of drug. Here, we show that DIP rate is an ideal metric of anti-proliferative drug effect because it naturally avoids the bias afflicting traditional metrics, it is easily quantified as the slope of the line on a plot of cell-population doublings versus time for both at the cell-population and clonal level. This metric facilitates the study of two key aspects of cell proliferation: heterogeneity and dynamics. To probe heterogeneity, we developed the clonal Fractional Proliferation (cFP), a high-throughput imaging method, and using the DIP rate as metric of drug response, we directly quantified the clonal fitness within a cell population as a rate of proliferation in response to perturbation. This approach builds on our previous studies that determine the

relative contribution of different cell fates to overall population dynamics [147]. We demonstrate that, by sparse plating and high-throughput measurements of colony size, cFP effectively captures clonal dynamics in a single novel metric of fitness, the drug-induced proliferation (DIP) rate. It is easily interpretable biologically as the rate of regression or expansion of a cell population or a clonal subpopulation. Measured in bulk, the DIP rate distributions reveal perturbation-induced changes to the structure of clonal fitness across various conditions.

Materials and Methods

Mathematical Model of Drug Action

We propose a simple two state model of drug action on an exponentially proliferating cell population. We assume that cells can exist in two states, a 'no-drug' and a 'drug-saturated' state, and that cells in each state can experience two fates, division and death with kinetic rate constants that are characteristics of the state, i.e. reflecting the effect of the drug. In the presence of drug, cells can transition from the no-drug to drug-saturated state at a rate proportional to the concentration of drug. Reverse transitions occur at a rate independent of drug. If *Cell* is the number of cells in the no-drug state and *Cell** is the number of cells in the drug-saturated state, then the temporal dynamics of the drug-treated cell population are described by the following pair of coupled ordinary differential equations,

$$\frac{dCell}{dt} = (k_{div} - k_{death} - k_{on}Drug) * Cell + k_{off} * Cell^* \quad (1)$$

$$\frac{dCell^*}{dt} = \left(k_{div^*} - k_{death^*} - k_{off}\right) * Cell^* + k_{on} * Drug * Cell \quad (2)$$

where $k_{div}(k_{div^*})$ and $k_{death}(k_{death^*})$ are the rate constants for cellular division and death respectively, in the no-drug and drug-saturated state; $Drug$ is the drug concentration; k_{on} is

the rate constant for the transition from the no-drug to the drug-saturated state; and k_{off} is the rate constant for the reverse transition.

At a given drug concentration, a population of cell will eventually reach a dynamic equilibrium in terms of number of cells in each state. The effective Drug-Induced Proliferation (DIP) rate of a cell population is then the weighted average of the net proliferation rates (the difference between the division- and death rate constants). With increasing drug concentration, the equilibrium shifts increasingly toward the drug-saturated state, asymptotically approaching 100% occupancy. The result is a sigmoidal dose-response relationship between DIP rate and drug concentration. Dynamic equilibrium between states is achieved immediately upon drug addition if the rate constants of interconversion between states are large. This is known as the partial equilibrium assumption (PEA) [163]. Mathematically, the PEA asserts that

$$k_{on} * Drug * Cell = k_{off} * Cell^{*} \quad (3)$$

Under this assumption, an analytical solution for the total number of cells, $Cell_T = Cell + Cell^{*}$, can be obtained as a function of time,

$$\because n\frac{Cell_T(t)}{Cell_T(0)} = \frac{\frac{k_{off}}{k_{on}}(k_{div}-k_{death})+Drug(k_{div^{*}}-k_{death^{*}})}{\frac{k_{off}}{k_{on}}+Drug} \times t \quad (4)$$

where $Cell_T(0)$ is the initial number of cells.

The DIP rate is defined as the slope of the line on a semi-log2 plot of cell number vs time. Therefore, under the PEA, the DIP rate of our model is

$$DIP = \frac{1}{ln2} \times \frac{\frac{k_{off}}{k_{on}}(k_{div}-k_{death})+Drug(k_{div^{*}}-k_{death^{*}})}{\frac{k_{off}}{k_{on}}+Drug} \quad (5)$$

At zero drug concentration, equation (5) reduces to

$$DIP_0 = \frac{1}{ln2} \times (k_{div} - k_{death}) \quad (6)$$

At maximum drug concentration, equation (5) reduces to

$$DIP_{max} = \frac{1}{ln2} \times (k_{div^*} - k_{death^*}) \quad (7)$$

Cell lines and Reagents

The PC9 cell line was gift from William Pao (Vanderbilt University, Nashville, TN). WM115 cells were from Meenhard Herlyn (Wistar Institute, Philadelphia, PA). All other cell lines were obtained from American Type Culture Collection (ATCC) (http://www.atcc.org). PC9, MDA-MB-231, HCC1954 cells were cultured in RPMI 1640 (obtained from ATCC, Manassas, VA) media supplemented with 10% fetal bovine serum (FBS). All other cell lines were cultured in DMEM media (Gibco, Grand Island, NY) supplemented with 10% FBS. All cells were cultured in CO_2, temperature-controlled and humidified incubators. Cells were confirmed mycoplasma negative before use. Cycloheximide was obtained from Sigma (Sigma-Aldrich, St. Louis, MO). Trametinib, SB2033580, and PLX4720 were obtained from Selleckchem (Houston, TX). Anisomycin was obtained from Abcam (Cambridge, MA). All reagents were solubilized in DMSO at a stock concentration of 10 mM and stored at -20^{o}C until further use.

Time-lapse Fluorescence Microscopy

To facilitate automated image processing, cells were engineered to express fluorescent fusion proteins histone 2B monomeric red fluorescent protein (H2BmRFP; Addgene plasmind#18982) and geminin-monomeric azami green [164] using replication-incompetent recombinant lentiviral particles. Fluorophores integrated cells were flow sorted for highest 20% intensity. For cell population level studies, cells were seeded at ~2,500 cells per well in 96-well imaging plates (BD Biosciences) and fluorescent nuclei are imaged using a BD Pathway 855 with a 20x objective in 3x3 montaged images per well. Alternatively, fluorescent cell nuclei are imaged twice daily using a Synentec Cellavita High End with a 20x objective and tiling of nine images.

clonal Fractional Proliferation (cFP) Assay

Sub-confluent cells were split and seeded at optimized single-cell density into 96-well cell culture imaging plates. For PC9, the ideal conditions are 40 cells seeded per well in a final volume of 100 µL growth media. For A375 cells, ~20 cells are seeded per well in a final volume of 200 µL growth media. Plates are kept in tissue culture incubators for 6 days to allow single cells to expand into single cell-derived colonies. After this period, all wells are imaged and the experimental perturbation is added immediately thereafter. The plates are returned to the tissue culture incubators and all wells of the plates are imaged daily or twice daily until the end of the experiment.

Image Registration and Processing

To prepare raw images for analysis, images are sequentially organized into spatially organized image montages, and temporally assembled into stacks using the freely-available ImageJ [165] software (http://imagej.nih.gov/ij). Subsequent image processing scripts were applied on a per-colony basis.

Statistical Analysis

All statistical analyses were performed using the R statistical software (R-project.org). DIP rates were obtained as slope of a linear model of $\log_2$(cell number) ~time for time points greater than the observed delay. Linear model fits were performed using the *lm* function applied to the data points. Adjusted R^2 values were calculated from the *lm* function. Pearson correlation coefficients were calculated using cor.test.

Results

Theoretical Illustration of Time-Dependent Bias

To theoretically illustrate the consequences of time-dependent bias in standard drug

effect metrics, we constructed a simple mathematical model of cell proliferation that exhibits the salient features of cultured cell dynamics in response to drugs. The model assumes that cells experience two fates: division and death, and that the drug modulates the difference between the rates of these two processes, i.e., the net rate of proliferation. Drug action may occur immediately or gradually over time, depending on the chosen parameter values. In all cases, a stable DIP rate is eventually achieved, and when calculated over a range of drug concentrations a sigmoidal dose-response relationship emerges (Figure 2.1).

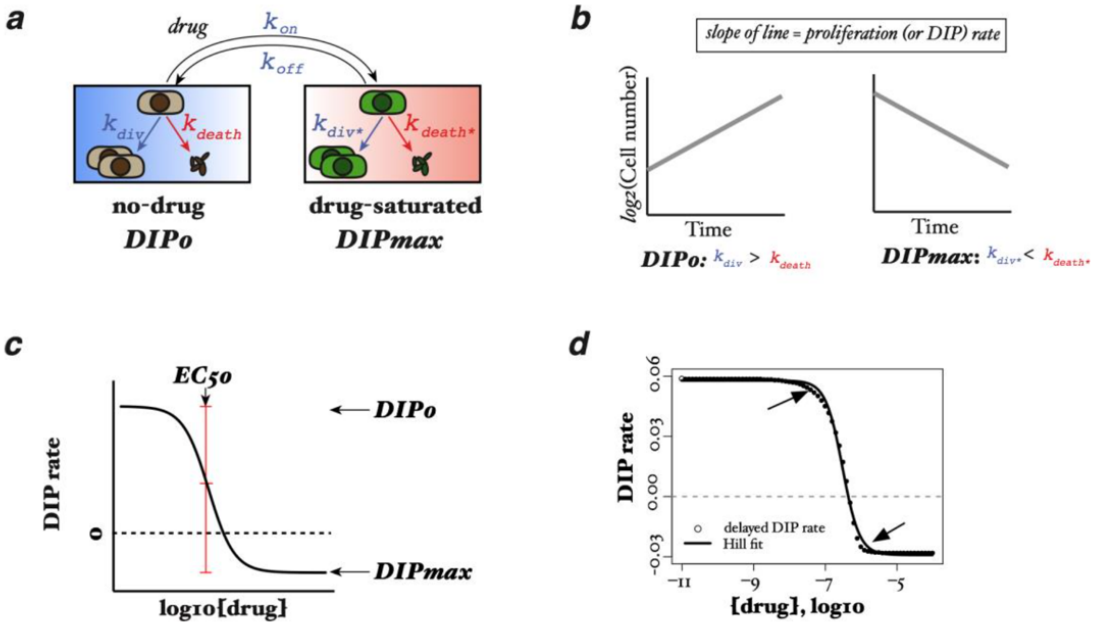

Figure 2.1: Two-State Model of Fractional Proliferation. Two-state model of fractional proliferation predicts a sigmoidal relationship between proliferation rate and drug concentration (a) The model assumes two states, a drug-naïve state and a drugged state, each with its own characteristics rate of proliferation (DIP_0 and DIP_{max}, respectively), which is the difference between the rates of cell division and death. The rate of transition from the drug-naïve state to the drugged state depends on the concentration of drug, while the reserve transition does not. Hence, as the concentration of drug increases, the dynamic equilibrium between states shifts increasingly in favor of the drugged state. (b) Since of the action of an anti-proliferative drug is to reduce, and perhaps reverse, the rate of proliferation of a cell population, we assume that the proliferation rate of the drug-naïve state is positive and greater than that of the drugged state (which may be positive or negative). The DIP rate of the drugged state (DIP_{max}) is assumed to negative because we assume that in each case the drug is cytotoxic at saturating drug concentrations (i.e., causes regression of the cell population). (c) An example of dose-response curve predicted by the two-state model under the partial equilibrium assumption (PEA). The curve was generated from equation with EC_{50} = $1e^{-8}$ M, DIP_0 = 0.06*ln(2) h^{-1}, and DIP_{max} = -0.03*ln(2) h^{-1}. (d) An example dose-response curves predicted by the two-state model in conditions where the PEA does not hold. The curve was generated by numerical integration of equations.

We model three scenarios: treatment of a fast-proliferating cell line with a fast-acting drug (Figure 2.2a), a slow-proliferating cell line with a fast-acting drug (Figure 2.2b) and a fast-proliferating cell line with a delayed-action drug (Figure 2.2c,Figure 2.3). In each case, we generate simulated growth curves in the presence of increasing drug concentrations (Figure 2.2, columns 1 and 2) and from these produce static dose-response curves by taking cell counts at single time points between 12h and 120h (Figure 2.2, column3). As expected, in each scenario the shape of the dose-response curves varies depending on the time of measurement. Consequently, parameter values extracted from these curves (EC_{50} and AA) also vary (Figure 2.2, columns 4 and 5). In contrast, DIP rates, being the slope of a line, is independent of measurement time. Using it as the drug effect metric gives a single dose-response curve (Figure 2.2, columns 3 and 6) and single values of the extracted drug-activity parameters *(*Figure 2.2, columns 4 and 5). Similar results are obtained for an alternative drug effect metric proposed by the U.S. National Cancer Institute's Development Therapeutics Program (DTP) (Figure 2.3) [166].

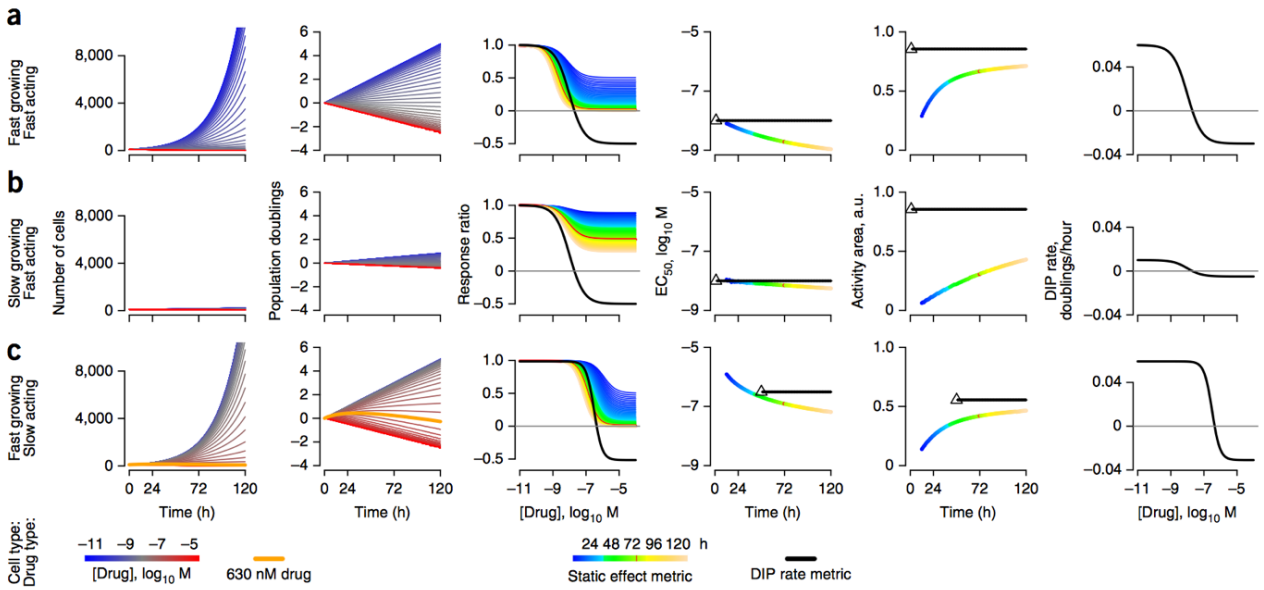

Figure 2.2: Theoretical Illustration of Bias in Dose-response Curves Based on Static Metrics of Drug Effect. Theoretical illustration of bias in dose-response curves based on static metrics of drug effect. Shown are computational simulations of the effects of drugs on (a) a fast-growing cell line treated with a fast-acting drug, (b) a slow-growing cell line treated with a fast-acting drug, and (c) a fast-growing cell line treated with a slow-acting drug. In all cases, in silico growth curves, plotted in linear (column 1) and $\log_2$ (column 2) scale, are used to generate static- (column 3) and DIP-rate-based (columns 3 and 6) dose-response curves, from which EC_{50} (column 4) and AA (column 5) values are extracted. For DIP-rate-based values of EC_{50} and AA, the black triangle denotes the first time point used to calculate the DIP rate (i.e., after the drug effect has stabilized) and the trailing black line signifies that the value remains constant for all subsequent time points.

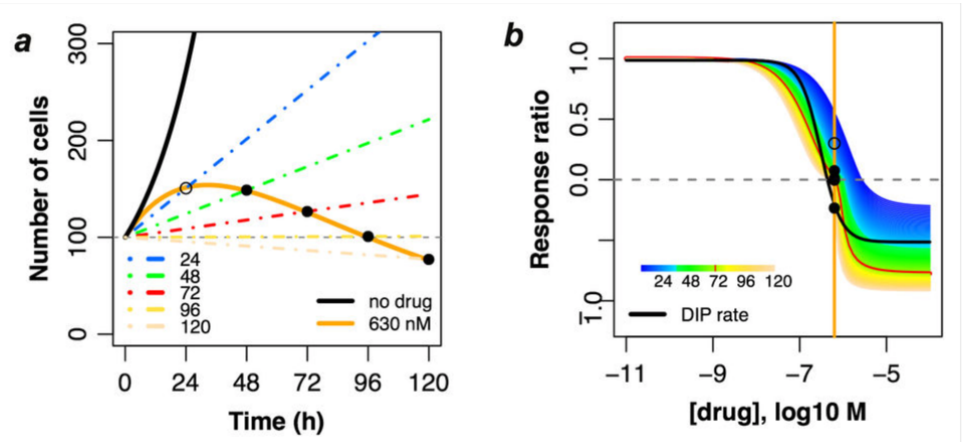

Figure 2.3: Growth Curves for the Theoretical Fast-Growing Cell Line with Delayed Drug Effect. (a) Growth curves in the absence and presence of 630 nM drug for the theoretical fast-growing cell line with delayed drug effect (related to Fig. 2.2c). Dash-dotted lines are a visual illustration of the NCI DTP dynamic metric and the time-dependent bias that it harbors. Depending on when cell count measurements are taken, the NCI DTP metric can indicate that the drug is partially cytostatic (<96 h), fully cytostatic (96 h), or cytotoxic (>96 h) at this concentration. (b) Comparison of dose-response curves for this cell line and drug type based on the NCI DTP dynamic effect metric and DIP rate. The vertical orange line corresponds to 630 nM drug concentration; circles correspond to those in part (a).

Experimental Illustration of Time-Dependent Bias in Drug-Treated Cancer Cells

As a first confirmation of our theoretical findings, we subjected triple-negative breast cancer cells (MD-MB-231) to the metabolic inhibitors rotenone (Figure 2.4a) and phenformin (Figure 2.4b). Using fluorescence microscopy time-lapse imaging [92,147,167], we quantified changes in cell number over time for a range of drug concentrations. For both drugs, we observe a rapid stabilization of the drug effect (<24 h delay) and stable exponential proliferation thereafter, reminiscent of the growth dynamics of the theoretical cell lines treated with fast-acting drugs (Figure 2.2). We generated dose-response curves from these data using the standard static effect metric and DIP rate for various drug exposure times. Consistent with our theoretical results, the shape of the static-based dose-response curve strongly depends on the time point at which cell counts are taken, an illustration of time-dependent bias. The DIP rate, on the other hand, is free of time-dependent bias and produces a single dose-response curve in both cases.

These DIP rate-based dose-response curves produce interesting insights (Figure 2.4a, b). For example, they indicate that while rotenone is much more potent than phenformin (EC_{50} = 8.5 nM vs 25 μM), phenformin is more effective (E_{max}/E_0 = -0.1 versus 0.1). The ordering of potencies (rotenone >> phenformin) could have been garnered from the static dose-response curves, but not the ordering of efficacies i.e., the static drug effect metric obscures the crucial fact that at saturating concentrations phenformin is cytotoxic (causes cell population regression) while rotenone is partially cytostatic (cell populations continue to expand slowly). This information is obviously critical to studies assessing drug mechanism of action. This example illustrates the perils of biased drug effect metrics and the ability of DIP rate to produce reliable dose-response curves from which accurate quantitative and qualitative assessments of anti-proliferative drug activity can be made.

To illustrate the confounding effects that a delay in the stabilization of the drug effect can have, we examined single-cell derived clones of the lung cancer cell line PC9, which is known to be hypersensitive to erlotinib [168], an epidermal growth factor receptor (*EGFR*) kinase inhibitor. Consistent with our previous report [147], three drug-sensitive PC9-derived clones (DS3, DS4, DS5) each respond to 3 μM erlotinib with nonlinear growth dynamics over the first 48-72 h, followed by stable exponential proliferation thereafter (Figure 2.4c). These dynamics are reminiscent of those for the theoretical fast-proliferating cell line with a delayed-action drug (Figure 2.2c). Due to the delay in drug action, all three clones have nearly identical population sizes 72 h after drug addition for all concentrations considered. The static 72 h metric thus produces essentially identical dose-response curves for all clones. In contrast, dose-response curves based on DIP rate make a clear distinction between the clones in terms of their long-term response to drug i.e., erlotinib is cytotoxic (negative DIP rate) for two of the clones but partially cytostatic (positive DIP rate) for the other (c). We then investigated the effects of erlotinib and lapatinib (a dual *EGFR*/human *EGFR 2* (*HER2*) kinase inhibitor) on HER2-positive breast cancer cell lines (HCC1954; delay ~48 h; Figure 2.4d). In each case, DIP rate-based dose-response curves produce EC_{50} values more than five-fold larger than their static counterparts, i.e., by the static drug effect metric the drugs appear significantly more potent than they actually have. Taken together with the PC9 results (Figure 2.4c), these data illustrate the importance of accounting for delays in drug action when assessing antiproliferative drug activity and further emphasize the ability of the DIP rate metric to produce accurate drug-activity parameters and qualitative conclusions about drug-response dynamics.

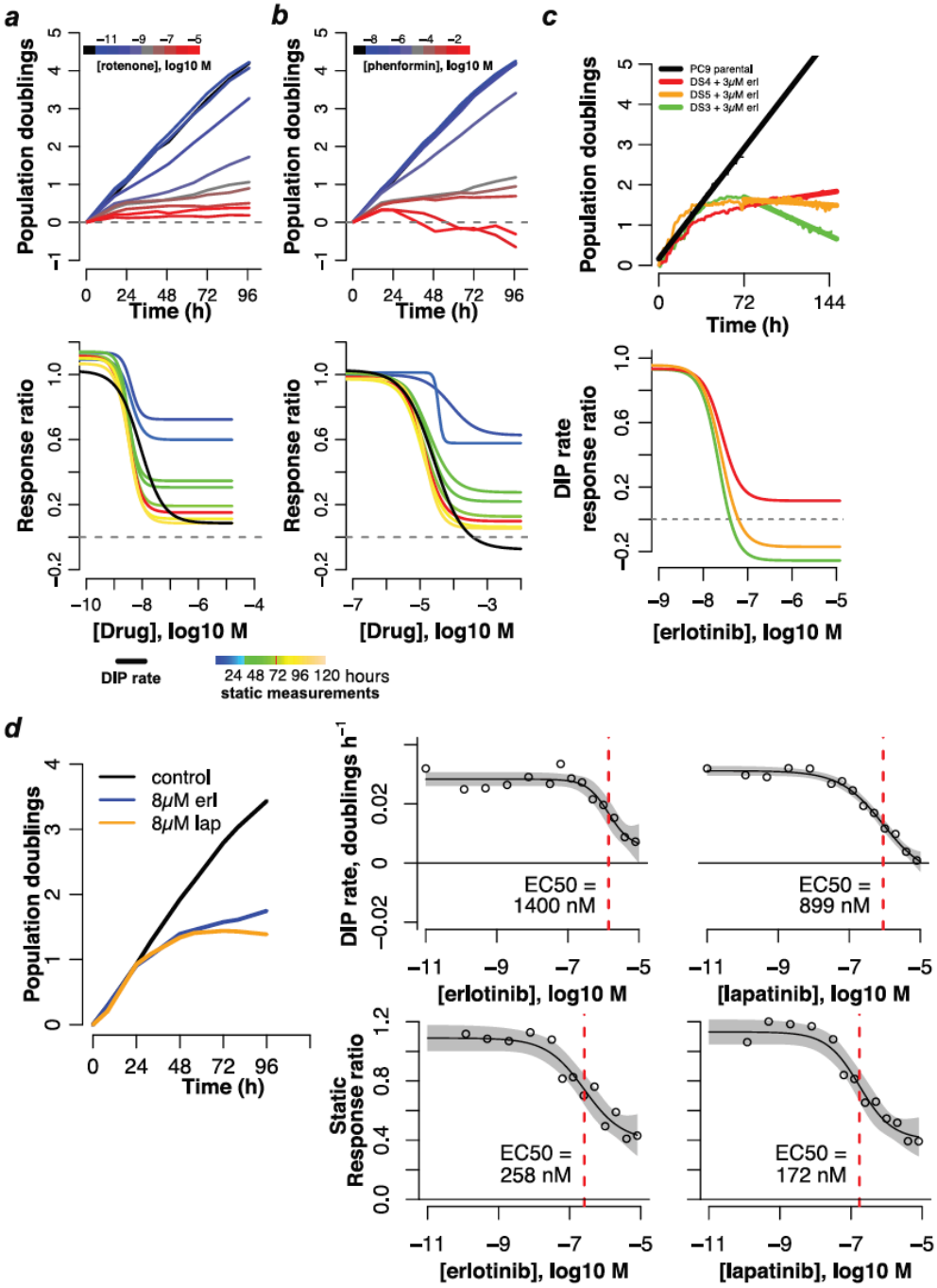

Figure 2.4: Experimental Illustration of Time-Dependent Bias in Dose-Response Curves for Drug-Treated Cancer Cells. Population growth curves ($\log_2$ scaled) and derived dose-response curves (static- and/or DIP rate-based) for (a) MDA-MB-231 triple negative breast cancer cells treated with rotenone; (b) MDA-MB-231 cells treated with phenformin; (c) three single-cell derived drug-sensitive (DS) clones for the *EGFR* mutant-expressing lung cancer cell line PC9 treated with erlotinib; (d) HCC1954 *HER2*-positive breast cancer cells treated with erlotinib and lapatinib. Data for (a) and (b) are from single experiments with technical duplicates; data in (c) are from individual wells for two experiments containing technical duplicates (growth curves) and from a single experiment with technical duplicates (dose-response curves; data in (d) are sums of technical duplicates from a single experiments (growth curves) and mean values (circles) with 95% confidence intervals (gray shading) on the log-logistic model fit (dose-response curves; n=4, 6 for erlotinib and lapatinib, respectively).

DIP Rate Overcomes Time-Dependent Biases in Drug Potencies

Within the last several years, a number of studies have been published reporting drug responses for hundreds of cell lines to a large panel of drugs [156,169]. To investigate bias in these datasets, we treated four *BRAF*^{V600} expressing melanoma cell lines with various concentrations of the *BRAF*-targeted agent PLX4720, an analog of vemurafenib. We produced experimental growth curves (Figure 2.5a), static- and DIP rate-based dose-response curves (Figure 2.5b), and extracted IC_{50} values for each cell line and compared these to IC_{50} values obtained from CCLE and GDSC data sets (Figure 2.5c). In all cases, our IC_{50} values correspond closely to the value from at least one of the public data sets. While in three cases the static- and DIP rate-based IC_{50} values correspond within an order of magnitude, in one case (A375) they differ by nearly two orders of magnitude. This discrepancy can be traced to a period of complex, non-linear dynamics (brief regression followed by rebound) observed for this cell line between 24 h and 72 h post-drug addition (Figure 2.5a). This result is particularly intriguing because it shows that, based on DIP rate, this cell line is not much different in terms of drug sensitivity than the other three. Using the biased static drug effect metric, however, one would be led to the incorrect conclusion that it is significantly more sensitive. It is very likely that cases like this abound within these and other similar data sets [170,171] and illustrates the critical need for new anti-proliferative drug effect metrics.

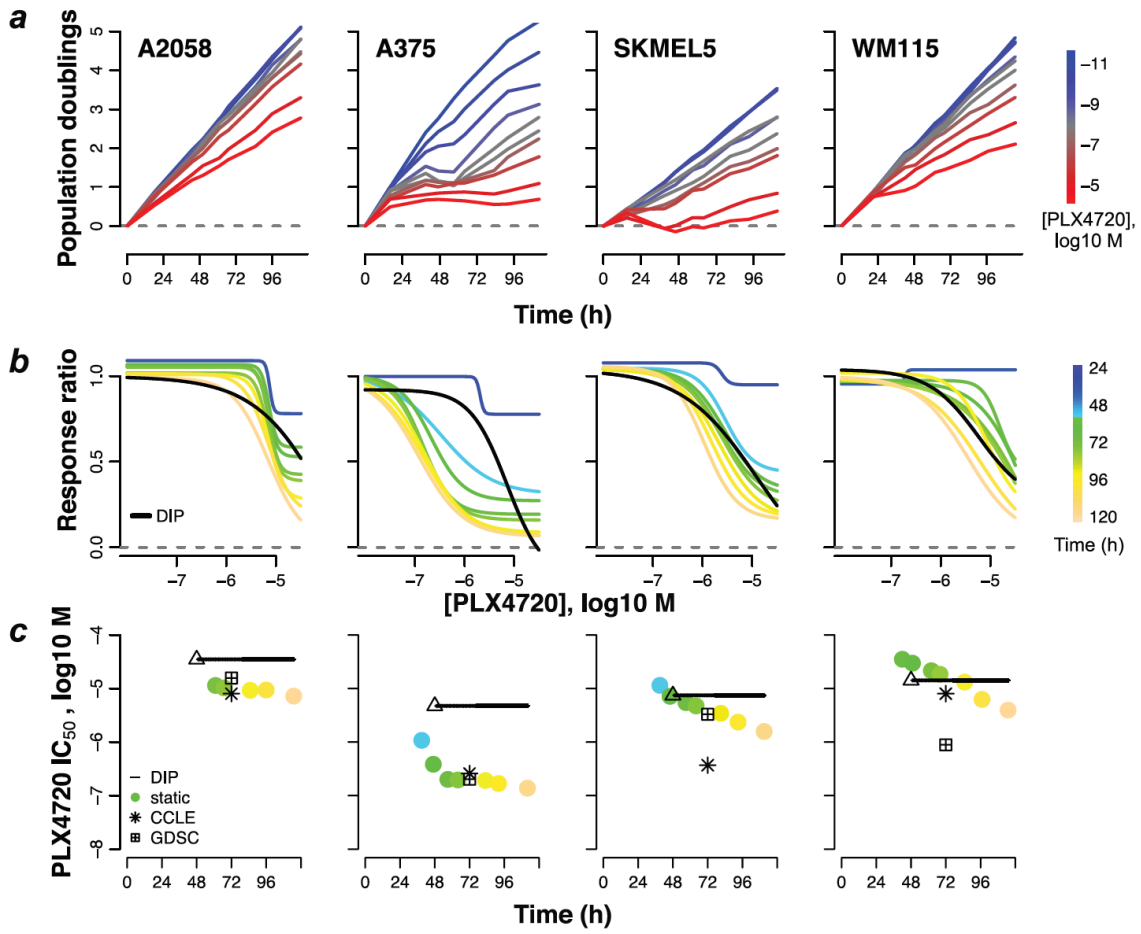

Figure 2.5: Bias in Potency Metrics from Publicly Available Data Sets. (a) Population growth curves (log_2 scaled) for four selected *BRAF*-mutated melanoma cell lines treated with various concentrations of the *BRAF* inhibitor PLX4720; (b) dose-response curves based on the static effect metric (colored lines) and DIP rate (black line; (c) static- (circles) and DIP rate-based (triangle + line) estimates of IC_{50} for each measurement time point. IC_{50} values obtained from public data sets (CCLE: Cancer Cell Line Encyclopedia; GDSC: Genomics of Drug Sensitivity in Cancer), based on the static 72 h drug effect metric, are included for comparison. The triangle denotes the first time point used in calculating the DIP rate and the black line signifies that the value remains constant for all subsequent time points. Data shown are from a single experiment with technical duplicates. Experiment has been repeated at least twice with similar results.

Mean Cell Seeding Density Does Not Affect DIP Rate Estimates

To examine how random variations in mean seeding density affect the measured values of drug effect metrics, we treated populations of a *BRAF*-mutated melanoma cell line, SKMEL5 with 8 µM of the *BRAF* inhibitor PLX4720 for 150 h and calculated DIP rates based on all data points >72 h. Four time courses were obtained at each seeding density ranging from 312 to 10,000 cells/well (Figure 2.6). As expected, the mean values are statistically indistinguishable

across seeding densities (p=0.47), however, the variance in the calculated DIP rates decreases with increasing seeding density (Levene's test p =0.0082). These results indicate that reliable estimates of DIP rate can be obtained even at low seeding densities.

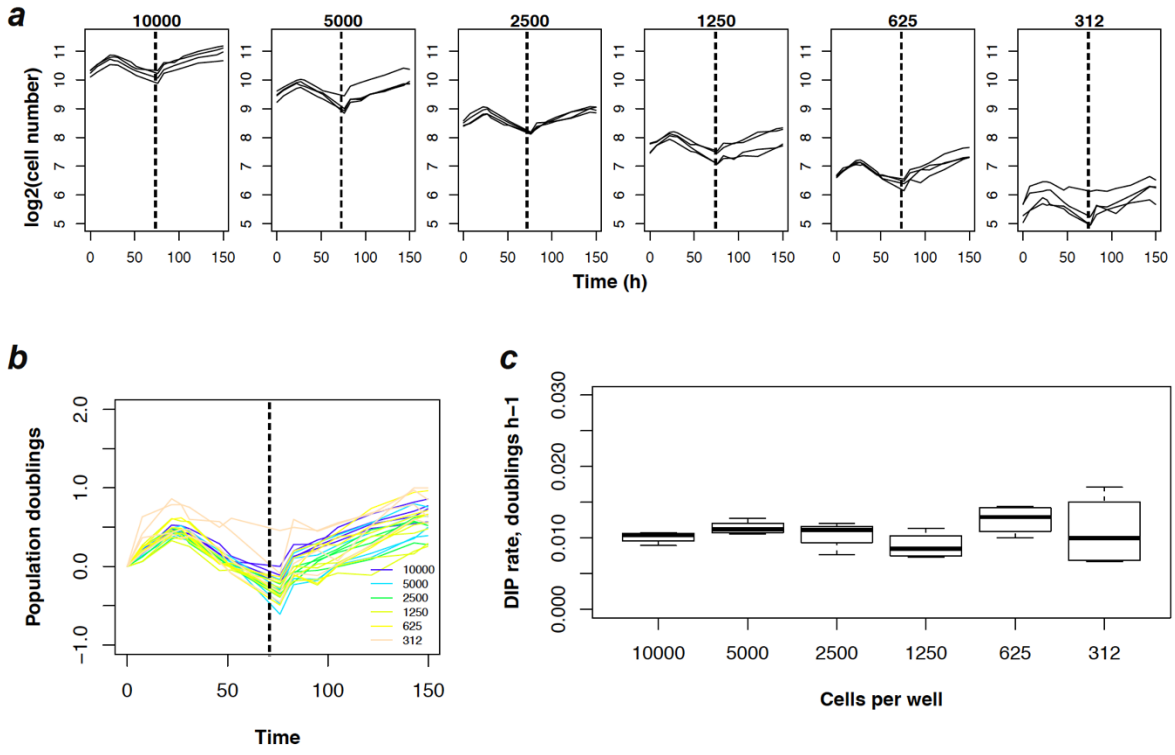

Figure 2.6: Effects of Variations in Mean Cell Seeding Density on DIP Rate Estimation. (a) Population growth curves (log_2 scaled) for each seeding density considered (n=4; seeding density is listed above each plot.) Vertical dashed line corresponds to ~72 h, the hand-chosen stabilization time; data to the right of this point were used to estimate DIP rate. (b) Population growth curves from part (a) normalized to the number of cells for each well at the first time point. Vertical dashed line corresponds to ~72 h. (c) Boxplots of estimated DIP rates (n=4) at each seeding density. Mean values were statistically indistinguishable across all seeding density (p=0.47); variances were not (Levene's test, p=0.0082).

High-Throughput Assay to Probe Clonal Heterogeneity

Since cell lines exhibited a period of complex, non-linear dynamics (brief regression followed by rebound) for a period of 24 h to 72 h post-drug addition, we wondered whether all cells within a cell population respond uniformly to drug or whether the population level response is a composite of clonal subpopulation responses. To quantify clonal fitness globally

within a cell population, we devised the clonal Fractional Proliferation (cFP) assay, which tracks, in parallel, clonal proliferation in response to perturbation (Figure 2.7). We chose to represent clonal fitness by the proliferation of single-cell derived colonies, because this yields a dynamic metric based on direct measurements of clonal behavior using methods described elsewhere [147,167]. In setting up the cFP assay, we aimed to balance several prerequisites. We reasoned that if the cell population response to a perturbation is composed of clones with variable fitness, then it is imperative to quantify as many clones as feasible per experiment in order to obtain a representative sample of the range and frequency (or diversity) of clonal fitness. Additionally, individual colonies must contain a sufficiently high number of cells prior to treatment in order to minimize error introduced by small cell number counts, especially if the perturbation induces a decline in cell number within a clone. However, to ensure that colonies are in fact clonally derived, the cell population must be sparsely plated and the assay terminated prior to colony confluence or mixing. On balance, we found that using a 96-well plate format (Figure 2.7), and plating ~20-40 cells/well are optimal initial conditions to obtain single-cell derived colonies. After plating, the colonies are allowed to grow for ~6-7 days in complete growth media, and subsequently subjected to a continuous experimental perturbation, during which the entire well is imaged daily or twice daily for ~7-10 days. Plating efficiency is sufficiently high so that information on ~100-150 colonies per experimental condition can be obtained from 10-15 replicate wells.

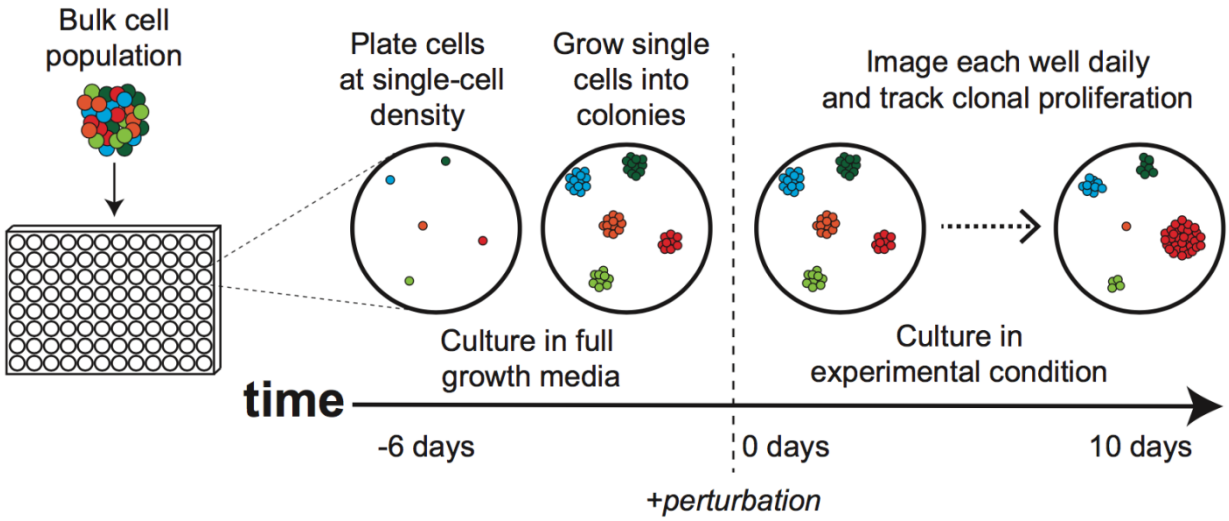

Figure 2.7: Schematic of Clonal Fractional Proliferation Experimental Workflow. Cells are seeded at single-cell density into microtiter imaging plates. Single cells are allowed to proliferate for ~6-7 days in full growth media to expand into colonies. Once colonies have reached an optimal size, cells are imaged and then the experimental perturbation is immediately added. Sequentially, each well is imaged daily until the end of the experiment.

Tracking of colonies throughout the duration of the perturbation requires that images must be both spatially and temporally registered (Figure 2.8). To this end, we use the freely available ImageJ [165] software (http://imagej.nih.gov/ij/, version 1.48i) to generate time-series image montages of individual wells. First, the subset of all images belonging to a single well at a single time point is considered. Then, images are spatially ordered based on acquisition time and converted to a stitched image montage of the entire well. This step is repeated for all time points and all the montages are ordered by acquisition time, resulting in an image stack of wells over the course of the experimental treatment (Figure 2.8).

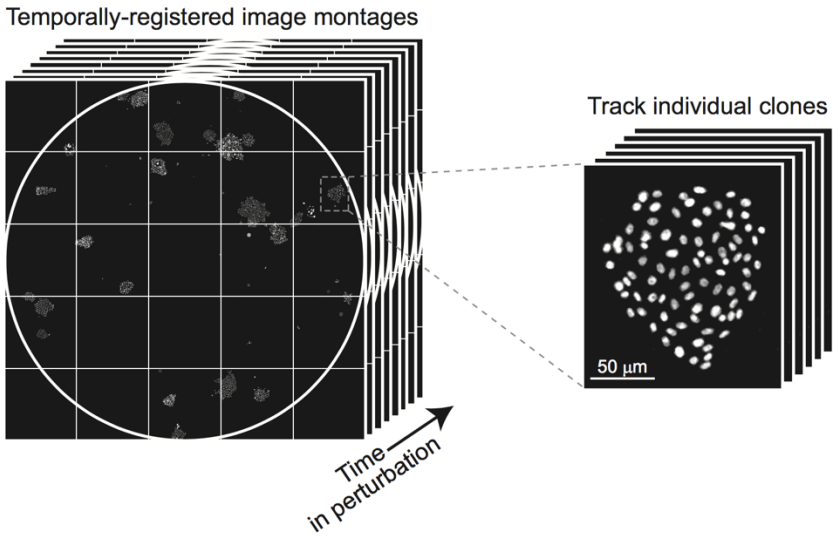

Figure 2.8: Spatially- and Temporally Registered Images Facilitate Tracking of Individual Colonies. Time-ordered stacks of image montages allow sequential measurements of colony cell numbers during drug treatment.

To quantify the proliferation dynamics of individual clones, we developed an image processing workflow using ImageJ to count the total number of cell nuclei at each time point from registered image stacks (Methods). Fluorescence intensity masks were generated for each colony by applying a use-defined threshold to the pixel intensity histogram computed from all images unique to that colony. These masks show that fluorescence from cell nuclei is sufficiently high above background to detect cells. However, colonies remain under-segmented, compared to manual counting. To correct for this, the watershed segmentation algorithm was implemented to distinguish nearby nuclei. Then the “analyze particles” command scans the image stack for elements with optimized morphological parameters and returns the number of identical cell nuclei and the corresponding images (Figure 2.9).

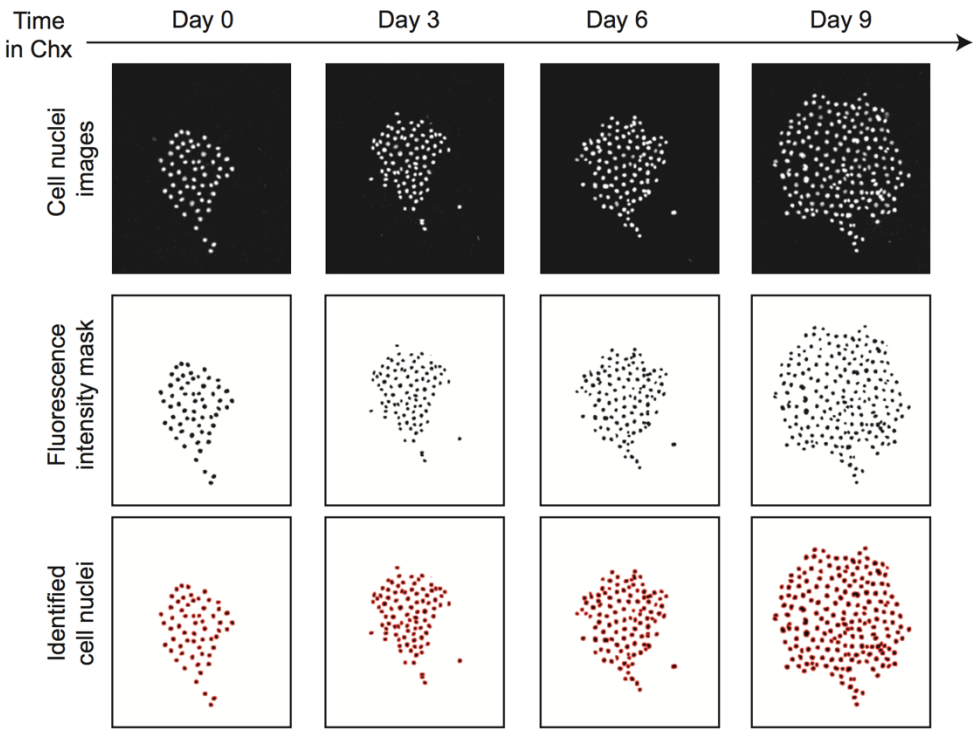

Figure 2.9: Validation of cFP Image Processing. (a) Top row: Images of a representative colony throughput cycloheximide (Chx, 500 ng/ml) treatment at the indicated days. Middle row: Binary mask generated in ImageJ using the same intensity threshold at all time points. Bottom row: Identified cells after image processing.

This technique was used to serially identify cell nuclei throughout a representative experiment. To quantify how well the automated image segmentation represented the actual cell number at each time point, we manually counted the total cell nuclei per colony at 219 total time points. The manual counts are highly correlated (adjusted $R^2 = 0.99$) with the automated cell counts (Figure 2.10,left) showing that automated cell counting is an efficient and faithful representation of changes in colony cell number. Additionally, the residual errors of the linear model fit do not show evidence of bias (Figure 2.10,right) and the standard deviation of the residuals is over fifty times smaller than the smallest cell number of any colony.

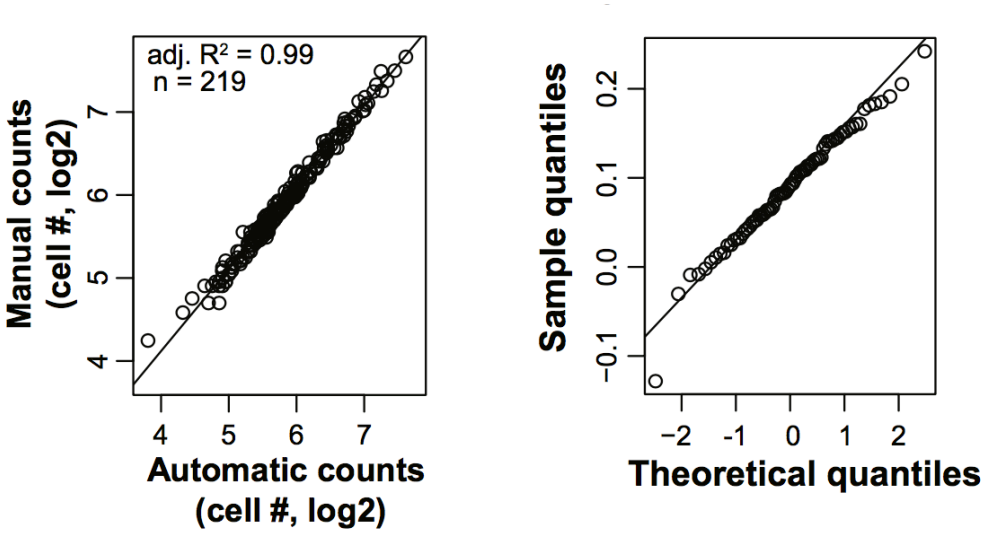

Figure 2.10: Automated Counting of Cell Nuclei Appropriately Quantifies Colony Cell Number. (left) Manual cell counts from colony from colony images at various time points (n=219) are used as a reference to validate the automatically measured colony cell numbers. The superimposed line represents the linear model fit for the data, with the corresponding adjusted R-squared value (adj. R2); (right) Q-Q plot of the residuals of the linear model fit used, there is insufficient bias to conclude that automated image analysis is inappropriate for colonies of certain size.

Having validated the ability to quantify colony size by cFP, we set out to measure the clonal fitness variability within a population in response to drug treatments. We used drug-induced proliferation (DIP) rate as an absolute metric for the fitness of clones in the presence of a perturbation, independent of comparison to untreated control. Because the DIP rate estimates the overall ability of a clonal lineage to survive, or perish, and expand, or regress, in size over time, it can be considered as a metric of clonal fitness. An advantage of using a single parameter to describe clone behavior is that it enables an easy display of the clonal variability within a cell population. In response to cycloheximide (Figure 2.11), clonal DIP rates within PC9 cells are well approximated by a skew-normal distribution (Kolmogorov-Smirnov test p=0.99; high p-value indicates insufficient statistical power to reject the fit), described by three parameters, μ, σ, α. Because cFP was designed to measure clonal variability within a cell population, we interpret μ as the average clonal fitness of the population, whereas σ and α

represent the variability of clonal fitness. Taken together, we interpret the distribution of DIP rates as the structure of clonal fitness of a cell population in the presence of a given perturbation.

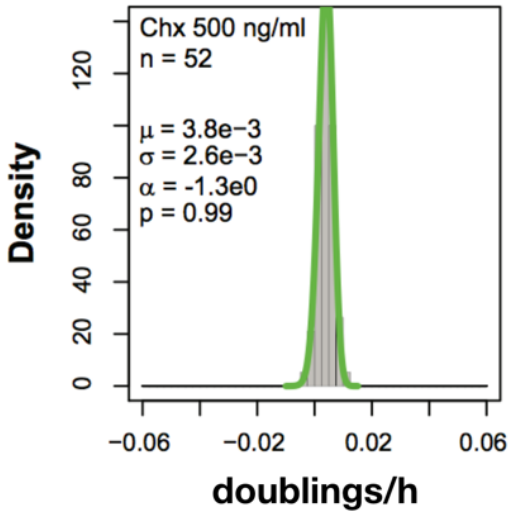

Figure 2.11: Histograms of DIP Rates for PC9 Colonies Treated with 500 ng/ml cycloheximide. Curves represent the estimated skew-normal probability distribution with the indicated values. Kolmogorov-Smirnov test p-values are shown.

To visualize the changes in shape of clonal DIP rates directly, we overlaid the distribution fits for different perturbations. By comparing the fits alone, the effects of the DIP rate distribution shape can be easily seen relative to other conditions. The progressive decrease in both the clonal DIP rate mean and variability induced by increasing cycloheximide, Trametinib (trm), a *MEK* inhibitor, SB203580 (SB), and anisomycin (An) concentrations are evident by the DIP rate distribution shifting to the left and becoming narrower (Figure 2.12).

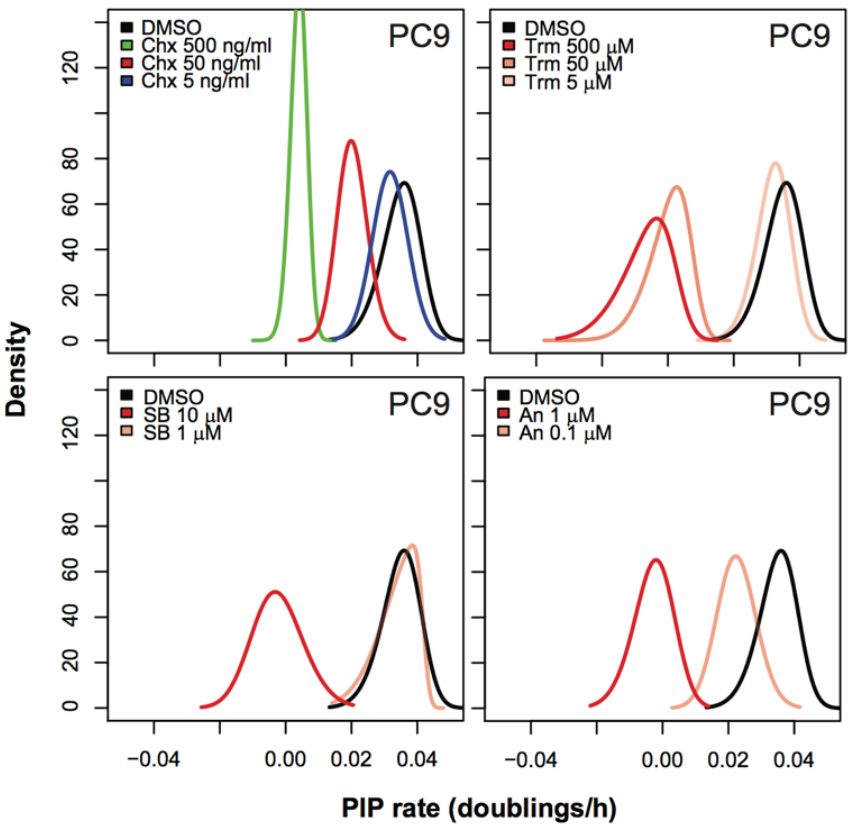

Figure 2.12: Skew-Normal Fits of Histograms of DIP Rates for PC9 Colonies. Histograms of DIP rates for PC9 colonies treated with different cycloheximide (Chx), Trametinib (Trm), SB203580 (SB) and Anisomycin (An) concentrations.

Similar trends were observed in *BRAF*-mutated melanoma cell line, A375 when treated with either PLX4720, a specific *BRAF* kinase inhibitor [43] or ABT-737 [172], a BH3 mimetic that sequesters pro-survival Bcl2 family member proteins (Figure 2.13). Thus, comparing the shapes of DIP rate distributions quickly summarizes how perturbations shape the clonal fitness profile within a cell population.

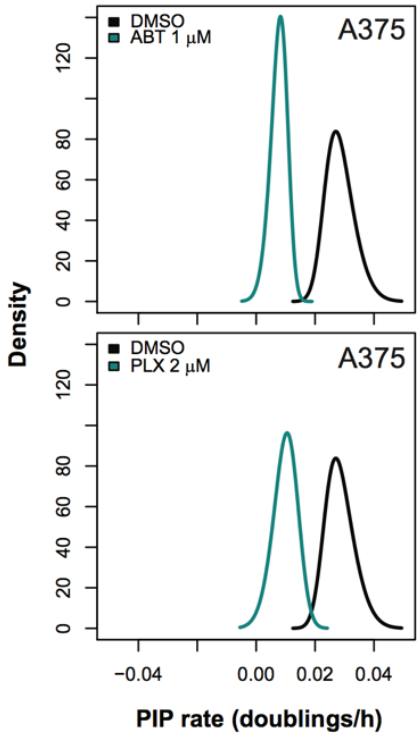

Figure 2.13: Skew-normal fits of histograms of DIP rates for A375 colonies treated with either ABT-737 (ABT) or PLX4720 (PLX).

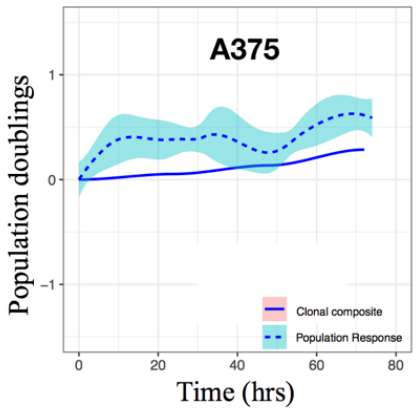

Figure 2.14: Aggregate of clonal responses qualitatively matches population level response. The clonal composite (sum of cell counts from all colonies at each time point) closely corresponds to the short-term population-level response; mean shown as solid or dashed lines, 95% confidence intervals as shaded regions.

Furthermore, the aggregate of the clonal responses qualitatively matches the short-term population level response (Figure 2.14). This suggests that the population level response is composite of multiple clonal responses—which can be quantified in terms of DIP rates. Moreover, it also informs about the nature of clonal drug-response behaviors within the cell populations. For instance, an early regression indicates that the contribution of regressing clones is larger, whereas a rebound suggests positively expanding clones dominate the population size.

Discussion

Together, we present here a novel metric, Drug-Induced Proliferation (DIP) rate, which overcomes biases in traditional measure of drug sensitivities in cancer cells. From cellular response dynamics, we show that complex drug-response behaviors can be inferred. DIP rates faithfully encompass, within a single value, the long-term effect of a drug at cell population level. Using DIP rates to quantify cellular behavior, we present here a high-throughput assay to monitor clonal fitness under perturbations. cFP assay captures pre-existing heterogeneity within a cell population and with DIP rate, it is biologically interpretable.

Current protocols for cell proliferation assays are based on informal 'rules of thumb," for example, counting cells at 72 h of treatment to ameliorate the impact of complex dynamics and delays in drug response. However, these de facto standards have no theoretical basis, and as demonstrated here, suffer from many complexities such as time-dependent bias and pre-existing heterogeneity within cell populations. These factors lead to erroneous conclusions to cancer cells' sensitivities to anti-cancer drugs. In light of the widespread applications of cell proliferation assays in oncology, pharmacology, and basic biomedical science [173], it is imperative that the quality of the metric for anti-proliferative assays be improved. Toward this end, we have proposed DIP rate as a viable, unbiased alternative anti-proliferative drug-effect

metric. DIP rate overcomes time-dependent bias by log-scaling cell count measurements to account for exponential proliferation and by shifting the time window of evaluation to accommodate lag in the action of a drug, changes that do not substantially alter experimental design. Moreover, DIP rate is an intuitive, biologically interpretable metric with a sound basis in theoretical population dynamics, and it faithfully captures, within a single value, the long-term effect of a drug of a cell population.

Another important factor to consider while evaluating drug sensitivities in cancer cells is heterogeneity. Existence of diverse subpopulations within a cell type ensures that the cell population exhibits complex, non-linear drug response dynamics. Using DIP rate to quantify cellular responses, we devised a high-throughput clonal Fractional Proliferation (cFP) assay to measure the structure of clonal fitness of a cell population in response to perturbation. Heterogeneity can be observed at the single cell level—where individual cells exhibit multiple cell fates in response to perturbations. Tyson *et. al.* previously showed that live-cell microscopy can be used to resolve heterogeneous cell behavior dynamically. With method called Fractional Proliferation, they unveiled how multiple cell fates contribute to changes in population size over time. However, this approach cannot be easily employed to follow many individual clonal subpopulations nor to assess their fitness over longer time scales. By generating clonal subpopulations essentially from single cells and quantifying their clonal proliferation rates, cFP overcomes both of these limitations. This allows us to monitor dynamic colony growth, unravel the structure of clonal fitness that exists in a cell population, and how that changes across many conditions. The distribution of clonal fitness is key to understanding how a cell population will evolve under drug perturbations. Because clonal fitness is presented as rates, the output should be amenable to mathematical models of population dynamics [174] and studies of clonal competition. Since the obtained clonal fitness reflects the pre-existing

differences among subpopulations, it will help identify whether rare subpopulations exist within a cell population. In such scenario, the distribution will essentially be bimodal, one representing the rare clones with advantageous mutations, and the other sensitive subpopulations. A normal distribution implies that there is no clear hierarchy among subpopulations, and both non-genetic and stochastic processes might modulate the drug response behaviors. Distribution may also give insight into the adaptation of a cell population to stress and also informative to linking molecular signaling gradients to its shape.

In summary, we describe a novel metric of measuring the anti-proliferative effects of different perturbations and a high-throughput way of measuring pre-existing heterogeneity within parental cell populations. The structure and distribution of clonal fitness reveal how multiple clonal subpopulations contribute to changes in population size over time.

CHAPTER 3

GLYCOLYTIC RESERVE CORRELATES WITH DRUG RESPONSE VARIABILITY IN *BRAF*-MUTATED MELANOMA CELLS

Adapted from:

Hardeman KN, Peng C, **Paudel BB**, Meyer CT, Luong T, Tyson DR, Young JD, Quaranta V, Fessel JP. Dependence On Glycolysis Sensitizes *BRAF*-mutated Melanomas For Increased Response To Targeted *BRAF* Inhibition. Sci. Rep. 2017;7:42604.

Summary

BRAF-mutated melanoma cells exhibit variability in response to targeted therapies. This heterogeneity mimics response variability seen in clinic. Recent studies link dysregulated metabolism to therapeutic resistance through activation of compensatory signaling. In this chapter, I will describe an approach of linking drug response variability among cancer cells with their metabolic phenotype measured by Seahorse flux analyzer and immunostaining of mitochondria in cells. My contributions in the above referenced manuscript included experimental data collection and analyses in quantifying drug response differences among melanoma cells and also in relating therapeutic response with metabolic phenotype.

Abstract

Dysregulated metabolism can broadly affect therapy resistance by influencing compensatory signaling and expanding proliferation. Given that many *BRAF*-mutated melanoma patients experience disease progression with targeted *BRAF*i, we hypothesized that therapeutic response is related to tumor metabolic phenotype, and that altering tumor metabolism could change therapeutic outcome. We demonstrated the proliferative kinetics of

BRAF-mutated melanoma cells treated with the *BRAF*i, PLX4720, fall along a spectrum of sensitivity providing a model system to study the interplay of metabolism and drug sensitivity. We discovered a relationship between glucose utilization and sensitivity to *BRAF* inhibition through characterization of metabolic phenotypes using a nearly a dozen metabolic parameters in Principal Component Analysis. Our results indicate metabolic vulnerability of melanoma cancer cells and may suggest ways to rationalize combination therapies of targeted therapies and metabolic inhibitors.

Introduction

Melanoma is the most malignant form of skin cancer, and roughly 50% of clinical isolates have a mutation in the *BRAF*-kinase of the mitogen-activated protein kinase (MAPK) pathway (Figure 1.1) [36,175]. Ninety percent of those *BRAF* mutations are missense mutations that change the valine at position 600 to glutamic acid (V600E) or aspartic acid (V600D) [176]. The mutation confers constitutive activation of the *BRAF* kinase and drives oncogenic signaling through *MEK* phosphorylation. Targeted therapies against mutant *BRAF* have prolonged progression-free survival and overall survival in Phase III clinical trials [26]. Unfortunately, most patients will exhibit some degree of disease progression while treated with a *BRAF* inhibitor, with nearly 50% of patients progressing after only 6 to 7 months of initial treatment (Figure 1.2) [177]. There have been a variety of mechanisms that underlie initial and acquired drug resistance described in the literature (Table 1.3). Generally, mechanisms of resistance to anti-*BRAF* therapies are put into *MEK*-dependent and *MEK*-independent categories. *MEK*-dependent mechanisms include mutations in *NRAS, MEK1* and *MEK2* [69], loss of *RAS* regulation by NF1 [178,179], *COT* overexpression driving *MEK* signaling [68], and genetic alterations in *BRAF* itself, such as truncation or amplification [64]. *MEK*-independent

mechanisms of resistance include receptor tyrosine kinase protein and ligand overexpression such as c*MET*, *IGF1R* and *PDGFRβ* [69], and signaling through *PI3K* [180]. Unfortunately, more than 40% of the resistance found in patients who progressed on targeted therapy cannot be attributed to any of these mechanisms (CHAPTER 1) [75]. One of the features common to all of the known pathways that contribute to resistance is that they exert direct or indirect control of multiple cellular metabolic pathways—contributing to the single "hallmark" of metabolic reprogramming.

Dysregulated metabolism in cancer has been shown to affect treatment outcome via multiple pathways, including the activation of compensatory receptor tyrosine kinase signaling to bypass molecular targeted therapies, the repression of pro-apoptotic signaling, and limitation of drugs' access to molecular targets through active and passive mechanisms [181]. Recently, it has been shown in *BRAF*-mutated melanoma that chronic treatment with a *BRAF* inhibitor induces glutamine dependence that correlates with drug resistance [182,183]. We wanted to examine whether the molecular landscape of any individual tumor has any relationship to its sensitivity to targeted therapies. Although metabolic pathways have been targets in *BRAF*-mutated melanomas, a consensus of the major metabolic programs exhibited by *BRAF*-mutated melanomas is lacking. *BRAF*-mutated melanomas have been characterized as exhibiting primarily aerobic glycolysis [184] or oxidative phosphorylation [185,186]. However, the relationship between metabolic program and therapeutic response in *BRAF*-mutated melanomas is poorly understood. As a result, we set out to probe the phenotypic relationship of metabolism and responses to the *BRAF*-inhibitor vemurafenib.

In the present study, we used a panel of human *BRAF*-mutated melanoma cell lines to demonstrate *in vitro* variability in response to PLX4720, a *BRAF* inhibitor analogue of

vemurafenib. Utilizing drug-induced proliferation (DIP) rates as metrics of anti-proliferative effect under various treatment conditions [150], we ordered cell lines on a continuum of sensitivity to PLX4720. We also quantified metabolic profiles of our panel of *BRAF*-mutated melanomas for both their baseline glycolysis and oxidative metabolism. Our results show a relationship between reliance on glycolysis and sensitivity to PLX4720 and may suggest metabolic vulnerability of melanoma cancer cells.

Materials and Methods

Reagents

PLX4720 (Cat# S1152) was obtained from Selleckchem. Glycolysis Stress Test and Mitochondrial Stress Test kits were obtained from Seahorse Biosciences and used according to manufacturer instructions. Dulbecco's Modified Eagle Media (Cat# 11965-092) was obtained from Sigma.

Cell Culture

Cells were grown and cultured in DMEM media containing 2 mM glutamine, 4.5 g/L glucose, 10% FBS and no sodium pyruvate (Cat#11965-092), except where specified otherwise. Cells were split and seeded at ratios that allowed for splitting 1-2 times per week. For drug-response experiments, cells were plated the night before, then reagents/drug were prepared in fresh media and added to the cells immediately before the start of the experiment.

Proliferation Assays

Cells were labeled with a fluorescent, nuclear tag (Histone 2B monomeric Red Fluorescent Protein, H2BmRFP from Addgene), and flow sorted. Only top 10% bright cells were kept for further experiments. Cells were seeded onto 96-well plates (1000-5000 cells per well) and drug treatments applied the following day, including the DMSO or PBS control (all

concentrations contained equal percentage of DMSO or PBS solvent to be consistent). Images were taken every 8-12 hours with sufficient image alignment (montaging) in order to capture about 25-100 cells per well/treatment. Direct measurement of cell counts was made using Cellavista image processing software and ImageJ macros. Proliferation was $\log_2$ transformed and normalized to cell counts to time zero.

Seahorse Metabolic Assays

For measurement of Oxygen Consumption and Extracellular Acidification Rates, cells were plated onto 96-well plates (Seahorse Biosciences, Billerica, MA) at a density of 25,000-40,000 cells/well before analysis on the Seahorse XFe extracellular flux analyzer. Mitochondrial Oxygen Consumption was quantified using the Mito Stress Test kit, and glycolytic rate quantified using the Glycolysis Stress Test kit, each according to manufacturer's instructions. Briefly, assay medium was unbuffered DMEM containing either 10 mM Glucose, 2 mM Glutamine, and 1 mM Sodium Pyruvate (Mito Stress Test) or none of the aforementioned (Glyco Stress Kit). No FBS was used in assay medium.

Principal Component Analysis (PCA) and Linear Regressions

Metabolic parameters were extracted for nine cell lines from two representative experiments, a glycolytic function experiment (Glyco Stress Test) and a mitochondria function experiment (Mito Stress Test) according to schematic shown. Bioenergetic Health Index was calculated as previously described by Chacko *et. al.* Pearson Correlation was used to estimate correlation between metabolic parameter and IC_{50}. Before principal component analysis (PCA), each extracted parameter was Z-score normalized to minimize variation due to the different parameter scales. The first principal component was calculated using all possible combinations of parameters and each combination was correlated with the measured IC_{50} for nine cell lines in panel.

Generation of Single-Cell-Derived Subclones

Single-cell derived subclones from SKMEL5 were isolated by seeding single-cell into 96-well and expanded in complete media until frozen stocks were made. Each subclone was grown in each media for at least two weeks before treating them with PLX4720 (CHAPTER 4).

Statistical Analyses

Data are presented as either an average of 3+ separate experiments or a representative example; error bars are means+ or –SD and p-values were obtained using unpaired t-test.

Results

BRAF-mutated Melanoma Cell Lines Exhibit Varying Sensitivity to BRAF-inhibition

To examine whether the variability in response to mutant *BRAF*-inhibition in patients could be modeled in vitro, we measured the cell lines' proliferative responses to *BRAF*-inhibition. We quantified the proliferative kinetics of the cell lines in the presence of PLX4720 using our previously described metric of anti-proliferative drug effect, drug-induced proliferation (DIP) rates [150]. Based on DIP rates calculated at an intermediate concentration of PLX4720 (8 μM) across the cell lines, *BRAF*-mutated melanoma cell lines fall along a response spectrum or a continuum (Figure 3.1a), from highly sensitive cell line (i.e. WM164) to largely insensitive (i.e. A2058). Similarly, we used the estimated DIP rates at each drug concentration and fitted a log-logistic curve to obtain the IC_{50} metric (Figure 3.1b), which termed DIP IC_{50}, and observed that cell lines ranked along a similar spectrum (Figure 3.1c).

We next confirmed that the measured variability in response to PLX4720 treatment was not due to phenotypic selection of drug-resistant subclones during the short 4-5-day time-frame of our experiments. We leveraged a fluorescent ubiquitin-dependent cell cycle indicator (FUCCI; mAG-gem1-110) to detect cells that have committed to cell division (i.e. passed the

G1/S transition). Our hypothesis was if intrinsically resistant clones exist within the population, they would be enriched in cells that continue to proliferate in the presence of PLX4720 and would remain resistant after isolation. To test this possibility, we treated the *BRAF*-mutated melanoma lines with PLX4720 or DMSO for 72 hours and sorted actively divided FUCCI+ cells from both cells. We re-challenged the flow-sorted cells with PLX4720 after a drug holiday of 24 hours, and observed that the proliferative responses of the two groups were essentially the same, indicating that PLX4720 does not appear to select for resistant populations in the short-term (Figure 3.2). Similar results were obtained with FUCCI- cells when re-challenged with PLX4720 (Figure 3.2).

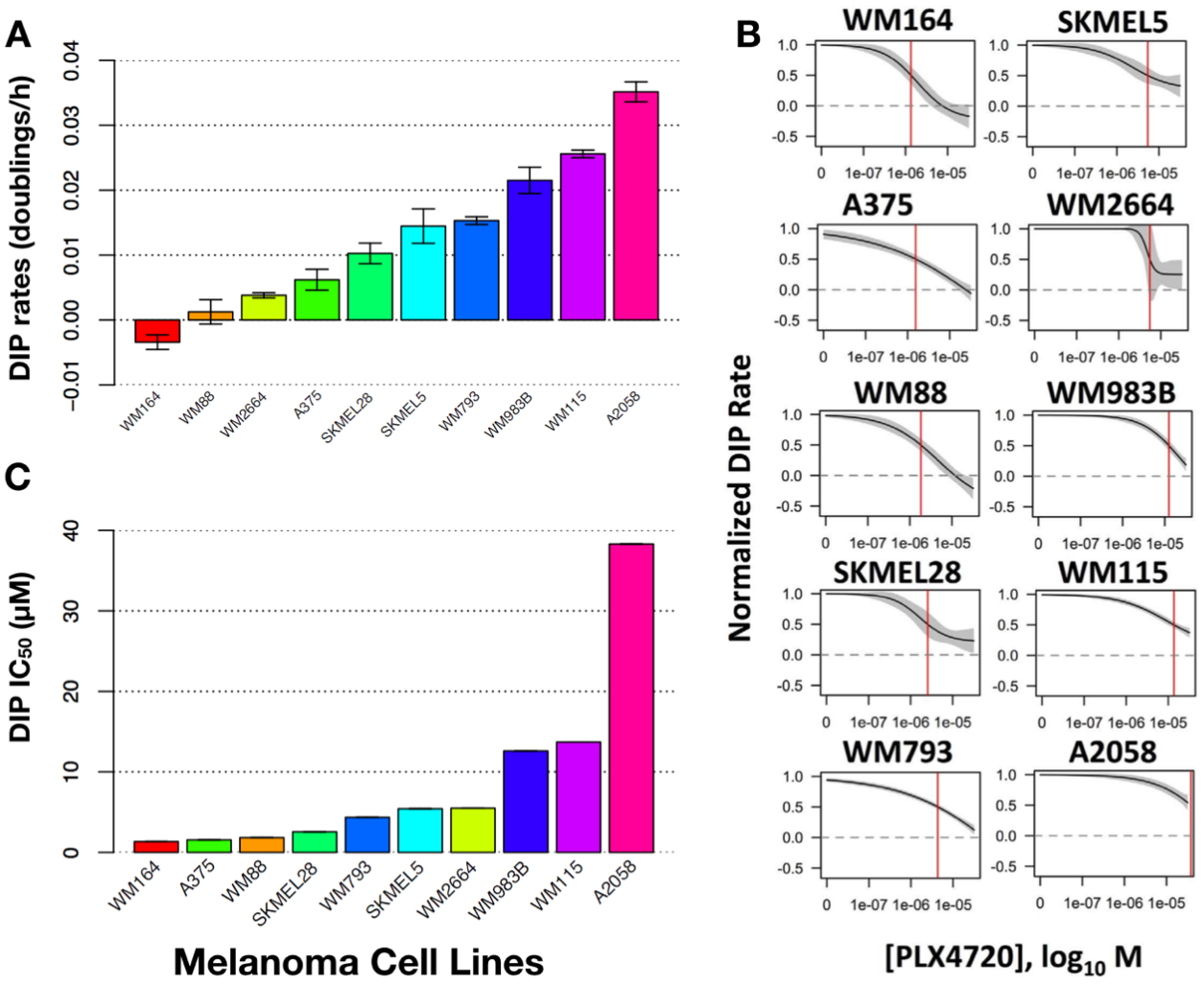

Figure 3.1: *BRAF*-mutated Melanoma Cells Exhibit Varying Sensitivities to *BRAF*-inhibition. (A) Drug-Induced Proliferation (DIP) rates are calculated as the slope of the line fitted to the $\log_2$ normalized population curve after 48 h in 8 μM PLX4720. Bar plot shows the mean ±SEM; data shown are from >4 technical duplicates. (B) Dose-response curves are generated using a 2-fold dilution of PLX4720 from 32 μM down to zero (DMSO). Log-logistic curve is then fitted to Drug-Induced Proliferation (DIP) rates calculated as the slope of the line fitted to the $\log_2$ normalized population curve at each concentration after 48 h. (C) IC_{50} metric is extracted by fitting log-logistic curve is fitted to Drug-Induced Proliferation (DIP) rates calculated over a range of concentrations of PLX4720.

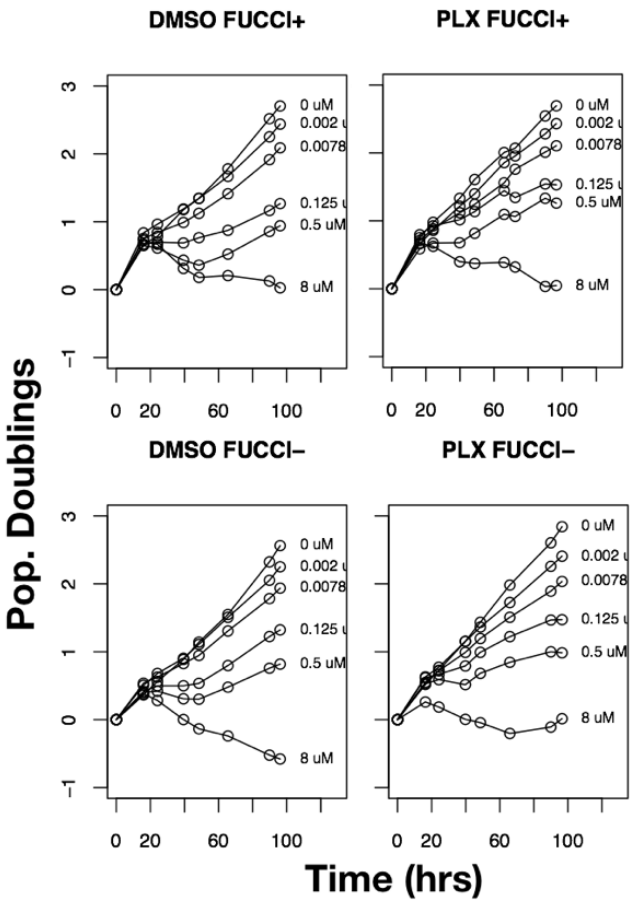

Figure 3.2: Response Variability is not Due to Phenotypic Selection of Drug-Resistant Subpopulations. Population growth curves (log_2 normalized; 3+ replicates) for SKMEL5 cells pre-treated with PLX4720 and sorted for their FUCCI status with varying concentrations of PLX4720. SKMEL5 cells were pre-treated with 8 μM PLX4720 for 72 h and flow-sorted based on their FUCCI status. Both FUCCI+ and FUCCI- cell populations were re-treated with different concentrations of PLX4720.

BRAF-mutated Melanoma Cell Lines Exhibit Heterogeneous Metabolic Features

To determine metabolic features exhibited by our panel of *BRAF*-mutated melanoma cell lines, we quantified lactate-producing glycolysis and mitochondrial oxidative metabolism using the Seahorse extracellular flux analyzer platform. Using a panel of 10 *BRAF*-mutated melanoma cell lines, we observed that most cells can variably utilize glucose and consume oxygen as part of mitochondrial respiration (Figure 3.3a). Notably, most cells have minor glycolytic reserve after the addition of oligomycin, indicating that most of the melanoma cells are functioning at or near their glycolytic capacity (Figure 3.3b). The basal respiration and

oxygen consumption also varied across cell lines. The subsequent decreases in oxygen consumption rate (OCR) after the addition of oligomycin (Figure 3.3a) suggest varying dependencies on ATP-linked respiration across the cell lines. Taken together, our data indicates that there is broad, intrinsic metabolic heterogeneity across *BRAF*-mutated melanoma cell lines.

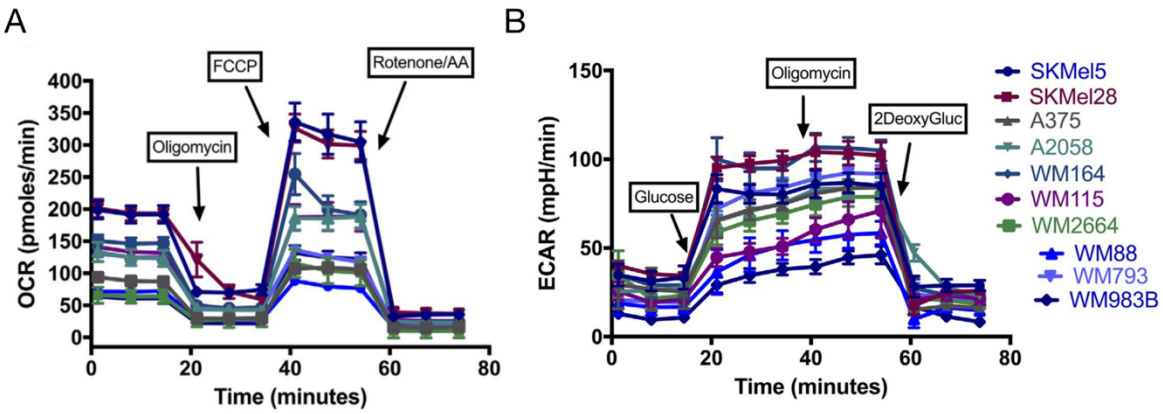

Figure 3.3: Metabolic Heterogeneity Among *BRAF*-mutated Melanoma Cells. (a) Oxygen consumption rates (OCR) indicative for oxidative metabolism for the cell lines indicated with sequential additions of oligomycin (1 µM), FCCP (1 µM) and Rotenone/Antimycin (0.5 µM). (b) Extracellular acidification rate (ECAR) indicative of glycolysis for the cell lines with sequential additions of glucose (10 mM), oligomycin (1 µM) and 2-deoxyglucose (0.5 µM).

Metabolic Phenotype Variability Correlates with Variability in Response to PLX4720

Given the observed heterogeneity in sensitivities to PLX4720, and variabilities in the metabolic features of our panel of *BRAF*-mutated melanoma cell lines, we sought to examine more closely whether a direct relationship exists between metabolism and drug response. To quantify the relationship between the metabolic program of *BRAF*-mutated melanoma cell lines and their response to PLX4720, we extracted eleven metabolic parameters from measurements of mitochondrial oxygen consumption rate (OCR) and glycolytic function curves

for nine cell lines (parameters described in Figure 3.4). Each metabolic parameter was independently tested for correlation with the measured DIP IC_{50} for PLX4720 for each cell line (Figure 3.5). Of all the metabolic parameters, we observed that glycolytic reserve shows moderate positive correlation (Corr: 0.605) whereas, glycolysis showed an inverse correlation with DIP IC_{50} values (corr: -0.495). This suggests that increased glycolysis among *BRAF*-mutated melanoma cell lines is indicative of greater sensitivity to *BRAF*-inhibition (lower DIP IC_{50}). Conversely, higher glycolytic reserve is indicative of lesser sensitivity to *BRAF*-inhibition (higher DIP IC_{50}).

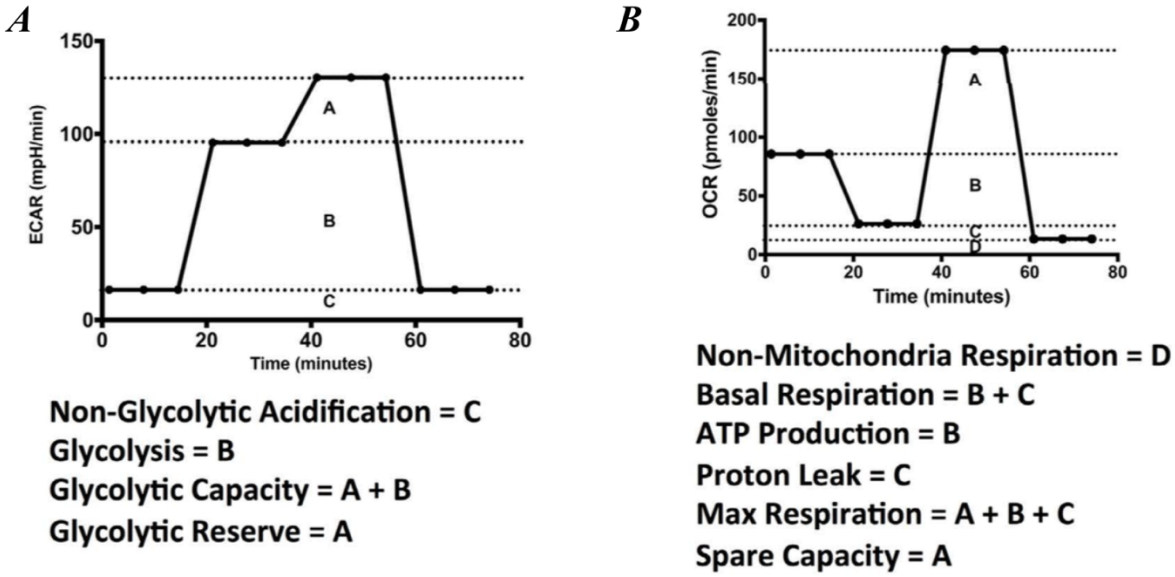

Figure 3.4: Schematic Diagram Describing the Components and Metrics from Seahorse Metabolic Assays used in the Principal Component Analysis (PCA). (A) Schema for example Glyco Stress Test Parameters. (B) Schema for example Mito Stress Test parameters.

Next, we determined how different combinations of the metabolic parameters correlated with drug sensitivity using Principal Component Analysis (PCA). Of all possible combinations

of parameters, our results indicated that of a linear combination of glycolysis and glycolytic reserve accounts for ~70% of the variance in the parameter ensemble across the cell lines used (Figure 3.6). Since glycolysis inversely correlated with DIP IC_{50}, while glycolysis reserve showed positive correlation, taken together, our data suggests that increasing the rate of glycolysis while depleting glycolytic reserve would sensitize *BRAF*-mutated melanoma cells to *BRAF*-inhibition (lower IC_{50} values).

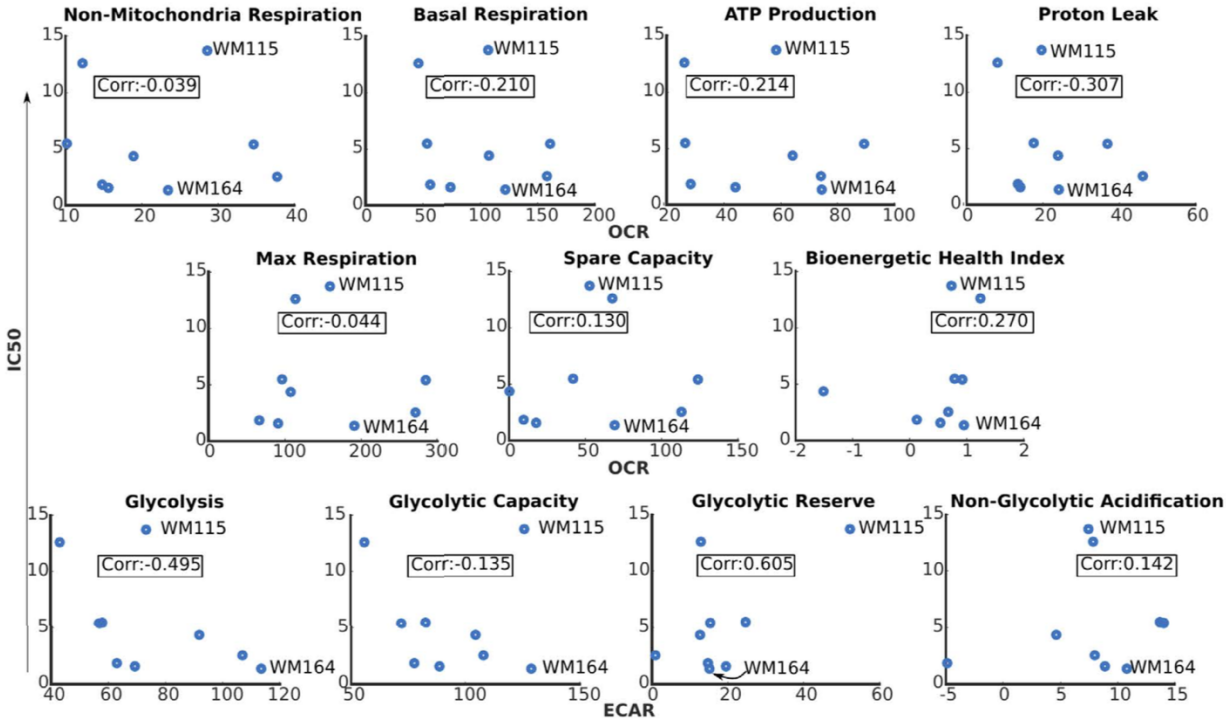

Figure 3.5: Metabolic heterogeneity correlates with sensitivity to *BRAF*-inhibition. Statistical test for correlation (Pearson) between metabolic parameters individually against sensitivity to *BRAF*-inhibition measured as DIP IC_{50} of the panel of *BRAF*-mutated melanoma cells.

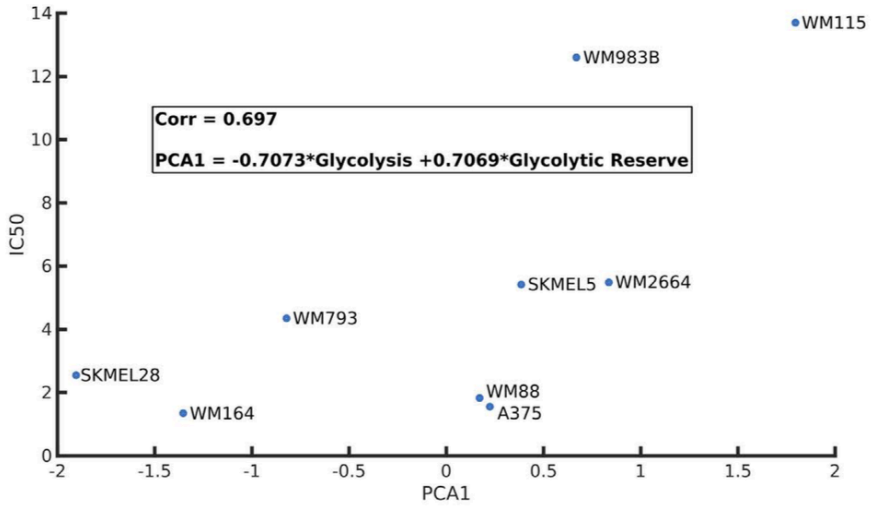

Figure 3.6: Glucose Utilization Strongly Correlates with Sensitivity to *BRAF*-inhibition. Principal Component of a linear combination of glycolysis and glycolytic reserve (Glucose utilization) correlates well with DIP IC_{50} in the panel of *BRAF*-mutated melanoma cells.

Glucose Availability Enhances the Effect of BRAF Inhibition on BRAF-mutated Melanoma Cells

To determine how glucose availability affects drug responses, we subjected *BRAF*-mutated melanoma cells grown on three different growth conditions to varying concentrations of PLX4720. For this, we utilized three single-cell derived subclones of SKMEL5—SC01, SC07 and SC10. We grew each subclone on three different growth media (DMEM, DMEM/F12 and F12), each with varying concentrations of glucose. While DMEM is high glucose containing media (4.5 g/L glucose), DMEM/F12 (3.15 g/L glucose) and F12 (1.80 g/L glucose) have low glucose concentrations. We grew each subclone in different media at least two weeks prior to subjecting them to drug treatment. For each subclone, we observed cells grown in high glucose (DMEM) media were consistently more sensitive to PLX4720, while cells grown in low glucose (F12) media were the least sensitive (Figure 3.7). Taken together, our results suggest that the effect of *BRAF*-inhibition is enhanced with increase in glucose availability in *BRAF*-mutated melanoma cells, consistent with our results from Principal Component Analysis.

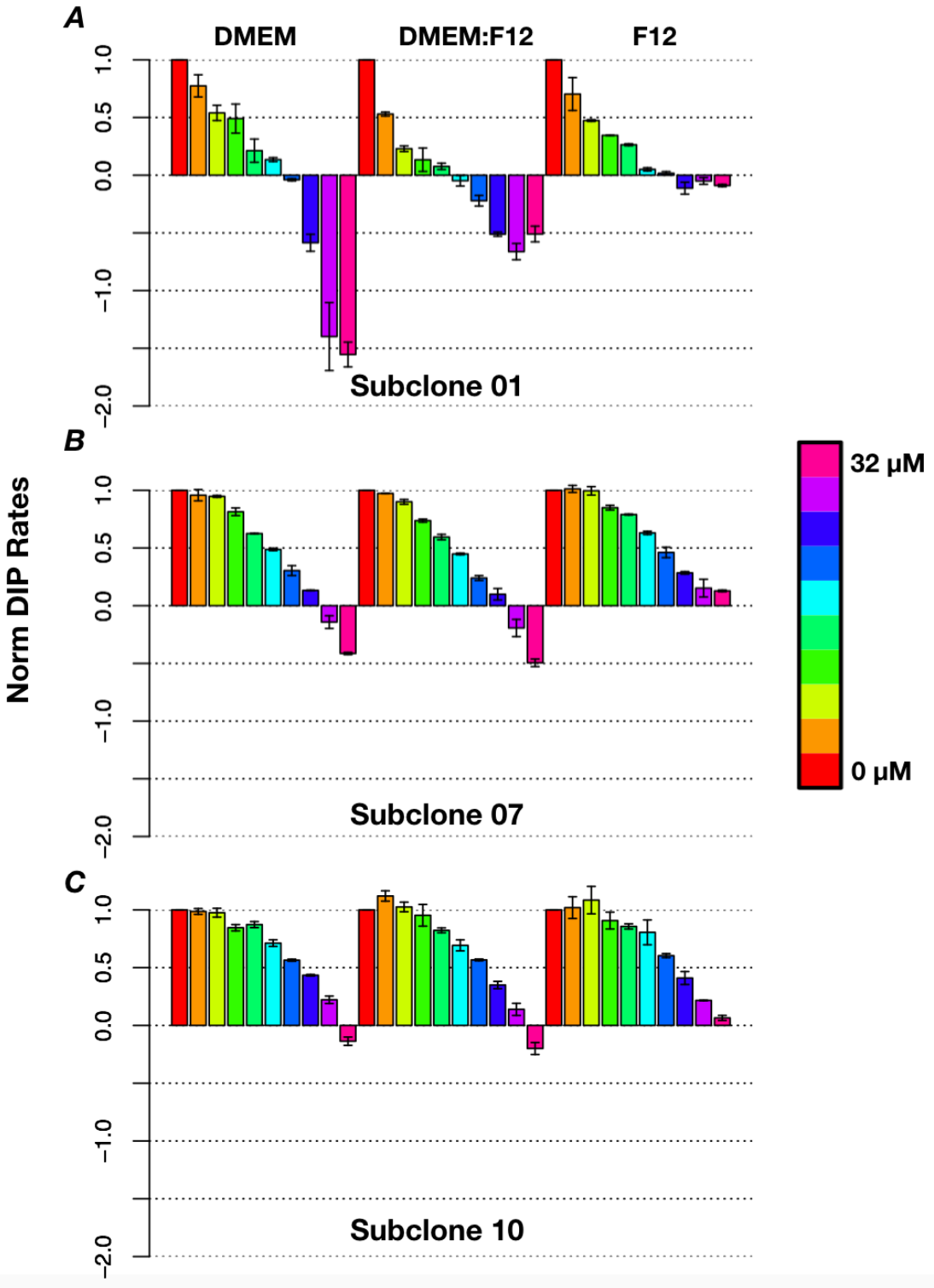

Figure 3.7: Glucose Availability Enhances the Effect of *BRAF*-Inhibition on *BRAF*-mutated Melanoma Cells. Drug-Induced Proliferation (DIP) rates calculated as the slope of the line fitted to the $\log_2$ normalized population curves for cells grown in three different media (DMEM, DMEM/F12 and F12) treated with varying concentrations of PLX4720 (32 µM and 2-fold-down). (A) SC01, (B) SC07 and (C) SC10. Color bars represent different concentrations of PLX4720 (32 µM and 2-fold-down).

Discussion

All cells, both normal and tumor cells, have basic energy and metabolic needs for survival and proliferation. Cellular responses—such as adaptation, differentiation, proliferation and signal transduction—are inherently complex and dynamic in nature. Therefore, sustained proliferation in the presence of targeted therapies is likely shaped by a cells' dynamic metabolic constraints. In this study, we investigated whether there exists a direct link between overall metabolic program and sensitivity to targeted *BRAF* inhibition. Our results indicate that over-reliance on glycolysis can sensitize *BRAF*-mutated melanoma cells to targeted *BRAF* inhibitor treatment. This finding is in agreement with earlier reports [184–186] suggesting *BRAF*-mutated melanoma cells undergo metabolic reprogramming under *BRAF*-inhibition and enhance their mitochondrial respiration.

Melanoma patients harboring *BRAF*V600 mutations experience heterogeneous drug responses with *BRAF*-inhibition. Using a relatively large panel of *BRAF*-mutated melanoma cell lines and examining their drug sensitivities, we modeled such heterogeneity. With the use of DIP rates [92,150], a metric recently introduced by our group which overcomes time-dependent bias prevalent in traditional end-point assays (CHAPTER 2), we categorized melanoma cells and their PLX4720 sensitivity on a continuum (Figure 3.1). Drug response variability in our melanoma panel is not due to selection of pre-existing resistant subpopulations (Figure 3.2), often attributed as the source of intrinsic or acquired resistance in cancer cells [94,187]. Because recent studies have highlighted the role of dysregulated metabolism in driving therapeutic response, we probed for metabolic phenotypes in our panel of melanoma cells. Although recent reports suggested that melanoma cells undergo metabolic reprogramming under *BRAF*-inhibition, questions remain about what physiological role glycolysis, oxidative phosphorylation, or mitochondria play for *BRAF*-mutated melanoma, in the

context of drug-treatment. Cancer cells, because of their high proliferative capacity, are glycolytic in nature, a phenomenon often termed as “Warburg effect.”[188] Clinical evidence suggests that *BRAF*-mutated melanoma tumors under targeted therapies exhibit reduced glucose uptake [189]. We used a systems approach to find correlation between several metabolic parameters and DIP rates of melanoma cells. Our analysis, for the first time, shows that over-reliance on glycolysis sensitizes melanoma cells to *BRAF*-inhibition. Specifically, dependence on glycolysis is defined in two terms which relate to how well the cells utilize glucose: glycolysis and glycolytic reserve. We show that sensitive melanoma cells (WM88, WM164) have high glycolysis and low glycolytic reserve. Consistent with relationship inferred from PCA, we observed cells grown in high glucose media were highly sensitive compared to cells grown in low glucose media. It is still to be determined what glycolytic reserve means in the context of cellular metabolism. Future experiments should focus on unraveling the molecular determinants of metabolic variability which will provide rational combination strategies for maximal therapeutic efficacy of *BRAF*i.

CHAPTER 4

A NON-QUIESCENT "IDLING" STATE IN DRUG-TREATED *BRAF*-MUTATED MELANOMA CELL POPULATIONS

Adapted from:

Paudel BB, Harris LA, Hardeman KN, Abugable AA, Hayford CE, Tyson DR, & Quaranta, V. (2017). A Non-Quiescent "Idling" State in Drug-Treated *BRAF*-mutated Melanoma Cell Populations. *Biophysical Journal*. (*in revision*).

Summary

While many resistance mechanisms to *BRAF*i have been identified, very little is known about what happens to tumor or cell populations during the early phase of response that precede resistance. In this chapter, I use mathematical modeling coupled to experimentation to describe drug response dynamics of *BRAF*-mutated melanoma cells within the theoretical framework of epigenetic landscape and phenotypic state transitions. We propose that the observed population-level dynamics are the result of a re-equilibration process across the basins of attraction within a drug-modified phenotypic landscape, resulting in the emergence of a novel, non-quiescent idling state of balanced division and death under sustained *BRAF*-inhibition. Our approach provides a generalizable approach to study drug response dynamics and a unifying view of how *BRAF*-mutated melanomas respond to continued *BRAF*-inhibition.

Abstract

Targeted therapy is an effective standard of care in *BRAF*-mutated malignant melanoma. However, tumor remission varies unpredictably among patients and relapse is

almost inevitable. In this chapter, we monitor the responses of several *BRAF*-mutated melanoma cell lines, including isogenic sublines, to *BRAF*i. We observe complex response dynamics across cell lines, with short-term responses (<100 h) varying from cell line to cell line. In the long term, however, we observe transition of all cell populations into a non-quiescent state of balanced death and division, which we term "idling." To our knowledge, the idling state has not been previously reported. Using mathematical modeling, we propose that the observed population-level dynamics are the result of a reequilibration of the cell population across basins of attraction within a drug-modified phenotypic landscape. Each basin is associated with a drug-induced proliferation (DIP) rate, a recently introduced metric that quantifies the dynamics of cell population responses to drugs. The idling state represents a new dynamic equilibrium in which cells are distributed across the landscape such that the population achieves zero net-growth. By fitting our model to experimental drug-response data, we infer the phenotypic landscapes of all considered cell lines and provide a unifying view of how *BRAF*-mutated melanomas respond to *BRAF* inhibition. We hypothesize that residual disease observed in patients following therapy may comprise a significant number of idling cells. Thus, quantifying the molecular determinants of the phenotypic landscape that idling cells occupy may lead to the development of novel therapies based on rational modification of the landscape to favor basins with greater drug susceptibility.

Introduction

Targeted small molecule inhibitors of *BRAF* [190] show remarkable, short-term efficacy in melanoma patients with tumors harboring $BRAF^{V600}$ mutations [26,44]. However, clinical responses are variable, short-lived, and tumor recurrence is almost universal within a few months of therapy initiation [26,45]. Analyses of post-resistant tumors or cells provide most of our current knowledge of tumor recurrence in melanoma [75], which is usually attributed to

rare, resistance-conferring genetic alterations that either preexist [94,187,191] or develop during therapy [73,192]. However, accumulating evidence suggests that non-mutational processes play a significant role in the response of cancer cells to drugs [102–105]. For example, there is preclinical and clinical evidence that cancer cells can become re-sensitized to therapy after a brief “drug holiday” [81,99–101]. It has also been suggested that cancer cells employ a dynamic survival strategy governed by epigenetic alterations to survive lethal drug exposure [106,107], similar to strategies seen in bacterial cell populations [111,112].

Recently, the idea that networks of genes can give rise to multiple metastable cellular phenotypes has received considerable interest [127–131]. The idea dates back to Waddington [132], who posited that cellular differentiation can be conceptualized as a dynamical trajectory through an “epigenetic landscape.” Borrowing concepts from physical chemistry [134], the epigenetic landscape is defined mathematically in terms of a quasi-potential energy surface [133]. Local minima, or basins of attraction, within this surface constitute cell types and the relative stability of cell types depends on the depths of the basins. Cells can transition between basins with rates dependent on the heights of local maxima, or energy barriers, separating basins. Within this framework, a cellular differentiation hierarchy is a special type of epigenetic landscape where transitions down a series of basins are more probable than up, although reverse transitions, or dedifferentiation, are theoretically possible, as has been confirmed experimentally [136]. The concept of the epigenetic landscape has recently been extended to cancer cells [128,131,161]. In contrast to normal cellular development, a clear hierarchy of cell types is not generally believed to exist for many cancers [191,193]. Rather, multiple metastable phenotypes of comparable stability can coexist and a population of cancer cells, driven by both intrinsic (e.g., gene expression) [102] and extrinsic [103] stochastic forces, will tend to spread out across these available phenotypes [194,195]. This phenotypic “drift” is postulated to be the

source of non-genetic heterogeneity in cancer, which is known to influence therapeutic response [93,129].

Here, we experimentally quantify drug-induced proliferation dynamics in *BRAF*-mutated melanoma cell lines at the cell population, clonal, and single-cell levels. We show that in all cases examined, treatment with *BRAF*i induces entry into a previously unrecognized, non-quiescent state of balanced death and division, which we refer to as "idling." To understand the nature of the idling state, we build a simple three-state model of cellular proliferation in terms of our recently proposed drug-induced proliferation (DIP) rate metric [92,150]. The model posits that the addition of drug alters the epigenetic landscape that melanoma cells inhabit. As a result, the cell population begins to re-equilibrate within the new, drug-modified landscape. Complex population-level dynamics observed immediately following drug addition reflects the re-equilibration process and the idling state represents the final, equilibrated state where cells are distributed across the landscape such that the population exhibits zero net growth. By calibrating the model to time-lapse imaging data, we infer the topographies of the drug-modified landscapes for multiple *BRAF*-mutated melanoma cell lines and show that differential short-term dynamics from cell line to cell line can be explained in terms of slight topographical variations. Our analysis thus provides a simple theoretical explanation for the wide range of responses observed for different *BRAF*-mutated melanomas to *BRAF* inhibition. We discuss the potential clinical relevance of idling cancer cells as well as the possibility for novel therapies based on rational modification of the epigenetic landscape using therapeutic agents.

Materials and Methods

Reagents

PLX4720 (Cat# S1152) and vemurafenib (Cat# S1267) were obtained from Selleckchem (Houston, TX). Dabrafenib (Cat# HY-14660) was obtained from MedChem

Express (Monmouth Junction, NJ) and solubilized in dimethyl sulfoxide (DMSO) at a stock concentration of 10 mM. BKM120 (Cat# S2247, buparlisib) was obtained from Selleckchem (Houston, TX) and solubilized in DMSO at a stock concentration of 10 mM. Trametinib (Cat# T-8123) and BEZ235 (Cat# N-4288) were obtained from LC Laboratories (Woburn, MA) and solubilized in DMSO at stock concentrations of 1 mM. Cisplatin (Cat# 479306, cis-Diamineplatinum(II) dichlorine) was obtained from Sigma-Aldrich and solubilized in phosphate buffered saline (PBS) at a stock concentration of 12.5 mM. All drugs were aliquoted and stored at -20°C until use except for cisplatin, which was stored at -80°C. Phospho-*MEK1/2* antibodies (Cat#9121) were obtained from Cell Signaling (Danvers, MA).

Cell culture

BRAF-mutated melanoma cells (SKMEL5, A375, WM793, SKMEL19, SKMEL28, WM164, WM88, A2058) were grown and cultured in Dulbecco's modified Eagle's medium and Ham's F-12 medium (DMEM:F12, 1:1, Cat# 11330-032). Media were obtained from Gibco (Grand Island, NY) and supplemented with 10% FBS. All cells were cultured in CO_2, temperature-controlled (37°C), and humidified incubators. Cells were tested for mycoplasma before use and confirmed negative. Cells were passaged 1–2× per week and maintained as exponentially growing cultures for a maximum of less than 20 passages. Unless otherwise indicated, cells were seeded ~16–24 h prior to treatment to allow cells to adhere to culture plates. Reagents/drugs were prepared in complete medium immediately prior to adding to cells by replacement.

Fluorescent imaging

To facilitate automated image processing, cells were engineered to express fluorescent fusion proteins histone 2B monomeric red fluorescent protein (H2BmRFP; Addgene plasmid# 18982) and geminin1–110 monomeric azami green [164] using replication-incompetent

recombinant lentiviral particles, as previously described [147,167]. Cells were seeded at 1000–5000 cells per well in 96-well culture imaging plates (BD Biosciences, product# 353219). DMSO and PBS were used as vehicle controls, as appropriate. Images were acquired through a 10× or 20× objective with a CellaVista High End Bioimager (SynenTec Bio Services, Münster, Germany) every 6–12 hours as 3×3 or 5×5 montages for approximately two weeks. Media containing matching concentrations of drug or vehicle in each well were replaced every three days. Image processing to obtain counts of cell nuclei at each time point was performed as previously described [147,150]. SKMEL5 (including all clonal derivatives), A375, WM88, SKMEL19 and A2058 were all treated with 8μM *BRAF* inhibitor (*BRAF*i; PLX4720 unless otherwise stated); SKMEL28 was treated with 16μM *BRAF*i; WM164 and WM793 were treated with 32 μM *BRAF*i. Drug-naïve and post-idling (pre-treated with 8 μM *BRAF*i for two weeks followed by a brief 24 h drug holiday) cell populations of the SKMEL5 sublines SC01, SC07, and SC10 were treated with 1 μM trametinib, 5 μM cisplatin, 1 μM BKM120, and 2 μM BEZ-235. In all cases, population growth curves are plotted as the ratio of cell counts to the initial cell counts (at the time of drug addition), in $\log_2$ scale (i.e., population doublings).

clonal Fractional Proliferation assay

Clonal Fractional Proliferation (cFP) was done as previously described (CHAPTER 2) [92]. Briefly, subconfluent cells are seeded at low density (~10–20 cells per well) in 96-well culture imaging plates. Plates are kept in humidified and CO_2-controlled incubators for approximately one week with medium replacement every three days to allow single cells to expand into colonies of approximately 50 cells. Medium is then replaced with drug- or vehicle-containing medium and cells are imaged every ~8–12 hours until the end of the experiment, with drug replacement every three days. Images are processed as previously described [92]. Raw images are sequentially organized into spatially registered montages and temporally

assembled into image stacks. Cell counts per colony were obtained using the freely-available ImageJ software (https://imagej.nih.gov/ij/) with a custom-written macro, as described previously [92]. Colony drug response was quantified in terms of DIP rate, obtained as the slope of a linear fit to the $\log_2$-scaled growth curve [92,150].

Single cell-derived sublines

Sixteen SKMEL5 sublines were derived from single cells by serial dilution. Briefly, cells were serially diluted to less than 1 cell per well in 96-well imaging plates and imaged to identify wells containing a single cell. Cells were expanded in complete growth medium (in the absence of *BRAF*i) and sequentially transferred to 48-, 24-, and 6-well plates until sufficient numbers of cells were available for cryopreservation. All sublines were tested for their sensitivity to *BRAF*i prior to cryopreservation.

Time-lapse single cell tracking

Fluorescence images of cellular nuclei were obtained as previously described [167]. Briefly, images were acquired using a BD Pathway 855 in (spinning disk) confocal mode with a 20× (0.75NA) objective in a CO_2- and temperature-controlled environment every 20 min for 260 h from the time of first drug addition. Medium was replaced with freshly prepared drug every three days. Images from each well were organized into stacks of time series. Fluorescent nuclei were manually tracked across sequential images to obtain cell lifespans and resultant cell fates (death or division), as previously described [147]. “Birth time” denotes the time at which a mitotic event occurred, resulting in two sister cells. “Lifetime” denotes the duration of single cell viability until the cell either died or underwent mitosis. End of Experiment (EOE) represents the cells that were born in drug but did not exhibit any cell fate during the remaining observation time. Data is displayed as two-dimensional plots of birth time vs. lifetime with death, division, and EOE signified with different markers.

Mathematical modeling and parameter calibration

We consider three cell subpopulations, defined in terms of their net proliferation rates: *R* (regressing), *S* (stable), and *E* (expanding). Cells within each subpopulation can divide, die, or transition into "adjacent" subpopulations. The ordinary differential equations (ODEs) describing the temporal dynamics of the system are

$$\frac{dN_R}{dt} = \left(k_{pR} - k_{rs}\right)N_R + k_{sr}N_S \quad (1)$$

$$\frac{dN_S}{dt} = \left(k_{pS} - k_{sr} - k_{se}\right)N_S + k_{rs}N_R + k_{es}N_E \quad (2)$$

$$\frac{dN_E}{dt} = \left(k_{pE} - k_{es}\right)N_E + k_{se}N_S \quad (3)$$

where N_R, N_S, and N_E are the numbers of cells in subpopulations *R*, *S*, and *E*, respectively; k_{pR}, k_{pS}, and k_{pE} are the DIP (net-proliferation) rates of subpopulations *R*, *S*, and *E*, respectively; k_{rs} and k_{sr} are the forward and reverse transition rate constants between subpopulations *R* and *S*, respectively; and k_{se} and k_{es} are the forward and reverse transition rate constants between subpopulations *S* and *E*, respectively. DIP rates were set to $k_{pR} = -0.055\ \mathrm{h}^{-1}$, $k_{pS} = 0\ \mathrm{h}^{-1}$, and $k_{pE} = 0.015\ \mathrm{h}^{-1}$ and a total initial cell population of 10,000 was assumed (see Supplementary Information). The remaining six parameters [k_{rs}, k_{sr}, k_{se}, k_{es}, and the initial cell proportions R_0 and S_0 (≥0 and ≤1)] were determined by calibrating to experimental data (see below). The model was encoded in R (https://www.r-project.org/) and ODE simulations were performed using the *ode* function of the R package 'deSolve' [196].

Parameter calibration was performed using Markov chain Monte Carlo (MCMC) sampling [197,198] (10^5 iterations) using the *modMCMC* function of the R package 'FME' [199]. Goodness of fit was quantified using the cost function

$$Cost = \sum_{i=1}^{n} \frac{(M_i - L_i)^2}{\sigma_i} \quad (4)$$

where n is the number of measured time points and M_i, O_i, and σ_i are the model prediction, experimentally observed value, and standard experimental error (automatically determined by *modMCMC*) at time point i, respectively. For the SKMEL5 cell line, the model was calibrated against an experimental time course for a 1:1:1 clonal mixture of three single cell-derived sublines (SC01, SC07, and SC10). Predictions for the dynamics of the SKMEL5 parental line and sublines were then made by selecting 1000 random parameter sets from the last 50% of iterations (accounting for burn-in) in the MCMC-generated parameter ensemble. Specifically, for each of the 1000 parameter sets, we recalibrated the model using MCMC keeping the transition rate constants (k_{rs}, k_{sr}, k_{se}, k_{es}) fixed at the values for that particular iteration and allowing the initial cell proportions (R_0 and S_0) to vary as free variables. For other *BRAF*-mutated melanoma cell lines (WM88, WM164, SKMEL28, SKMEL19, A375, WM793), model calibration was performed against experimental time courses for the parental lines. In all cases, we plot simulated time courses as one-standard-deviation envelopes around the mean from 1000 random samples of the MCMC-generated parameter ensemble. Additional details of the model and the MCMC calibration procedure, including MCMC-generated parameter distributions, are provided in the Appendix.

Inferring quasi-potential energy landscapes

We assume that the probability that a cell transitions from subpopulation X to Y follows Arrhenius' equation [200,201]. Within this view, each subpopulation constitutes a basin of attraction within a quasi-potential energy landscape and transitions between subpopulations require traversal of an energy barrier separating adjacent basins. The height of this barrier, delU_{xy}, is proportional to the negative logarithm of the transition rate constant, i.e.,

$$\Delta U_{xy} \sim -\ln\ k_{xy} \qquad (5)$$

Intuitively, the higher the barrier the less probable is the transition. For each cell line considered, we randomly select 2000 parameter sets from the MCMC-generated parameter ensemble (see above) and estimate barrier heights between basins for each set using Eq. (5). A pictorial representation of the inferred quasi-potential energy landscape is then generated as a one-standard-deviation envelope around the mean barrier heights from the 2000 sampled parameter sets.

Results

BRAF-mutated melanoma cell populations exhibit balanced death and division upon long-term exposure to BRAF inhibition

To investigate the effects of *BRAF* inhibition on *BRAF*-mutated melanoma, we subjected populations of numerous *BRAF*-mutated human melanoma cell lines to the small molecule *BRAF*i PLX4720 for a period of approximately two weeks (~350 h; Figure 4.1a and Figure 4.2a). The proliferation dynamics immediately following drug addition (<100 h) varied from cell line to cell line, with some populations continuing to slowly expand while others experienced significant cell death (Figure 4.1a). Over longer time periods, however, all cell populations eventually settled into a state of near-zero net growth (Figure 4.1a). For the expanding cell populations, we confirmed that the zero-net-growth state is not trivially due to confluency (Figure 4.2b). Moreover, we observed that ~5-15% of cells continue to divide during this period, as indicated by an exogenous marker of the S, G2, and M cell cycle phases [164] (Figure 4.1b and Figure 4.2c). Cell death was also observed, as indicated by early nuclear morphological changes associated with apoptosis [202] (Figure 4.2d). Because cells continue to turnover (die and divide) during this period, but the cell population maintains a constant level, we refer to this state as “idling.” Other *BRAF*s (dabrafenib and vemurafenib) also caused idling, as did the combination of *BRAF*i and trametinib, an inhibitor of *MEK* (a downstream

target of *BRAF* in the *MAPK* signaling cascade; Figure 4.2e). Interestingly, we also observed that idling cells resume normal exponential proliferation when switched to drug-free media and exhibit similar drug-response dynamics when re-challenged with *BRAF*i (Figure 4.1c). The reversibility of the phenotype suggests that the idling state is non-mutational in nature [128]. Taken together, these results demonstrate that the idling state is drug-induced, reversible, and a common response of *BRAF*-mutated melanoma cell populations to continued, long-term *MAPK* pathway inhibition.

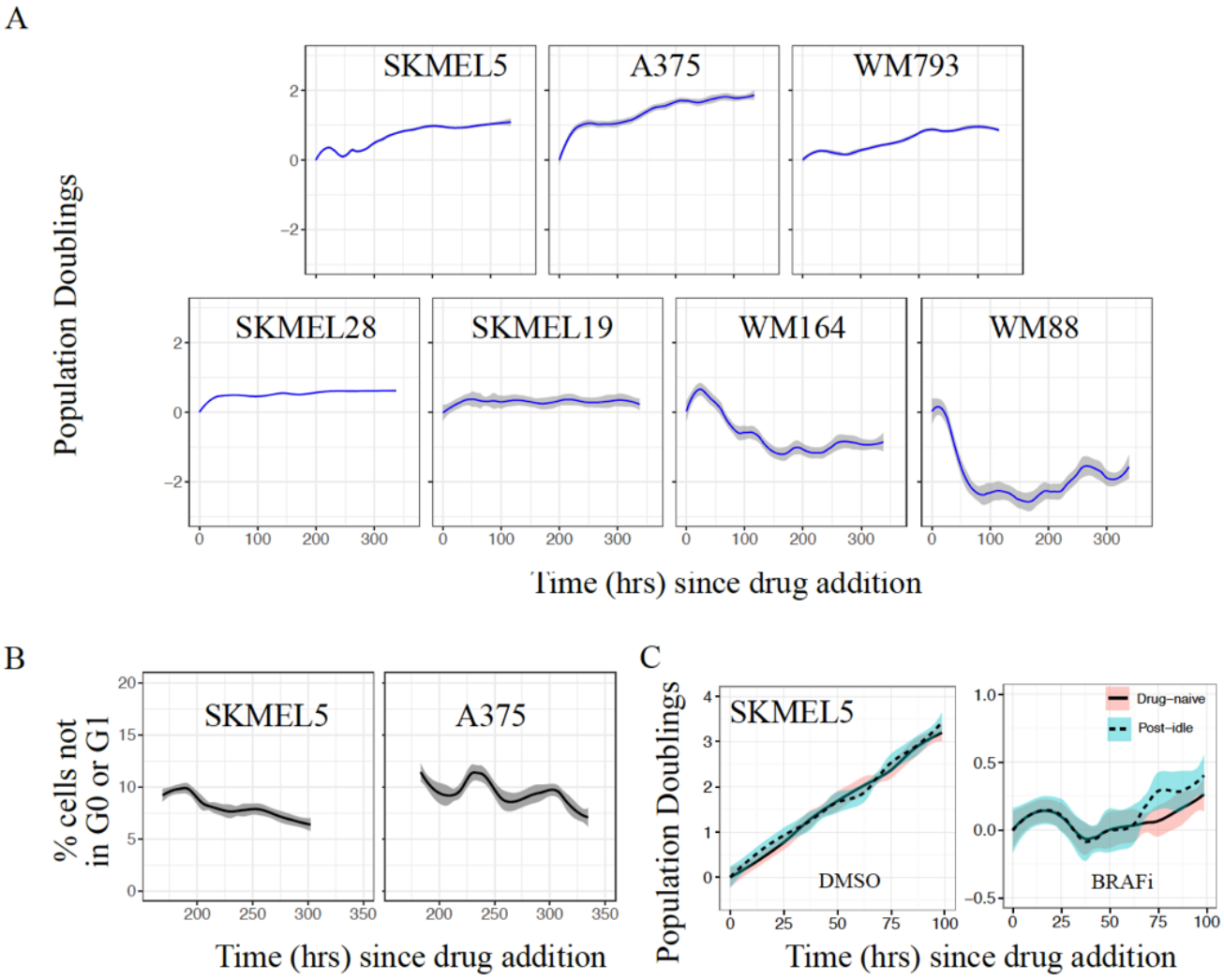

Figure 4.1: *BRAF*-Mutated Melanoma Cell Populations Idle Under Continued *BRAF* Inhibition. (a) Population growth curves (log_2 normalized; 3+ technical replicates) for seven *BRAF*-mutated melanoma cell lines treated with saturating concentrations of *BRAF*i. (b) Percentage of FUCCI-positive cells (an indicator of cellular commitment to division) during 168-350 h of *BRAF*i treatment for the SKMEL5 and A375 cell lines. (c) Idling cells return to normal, pre-drug function after a 24 h drug holiday: (*left*) drug-naive and post-idling cells (SKMEL5) expand at equal rates in complete-growth media; (*right*) drug-naïve and post-idling cells respond almost identically to *BRAF*i (mean responses are shown as solid lines, 95% confidence intervals as shaded regions).

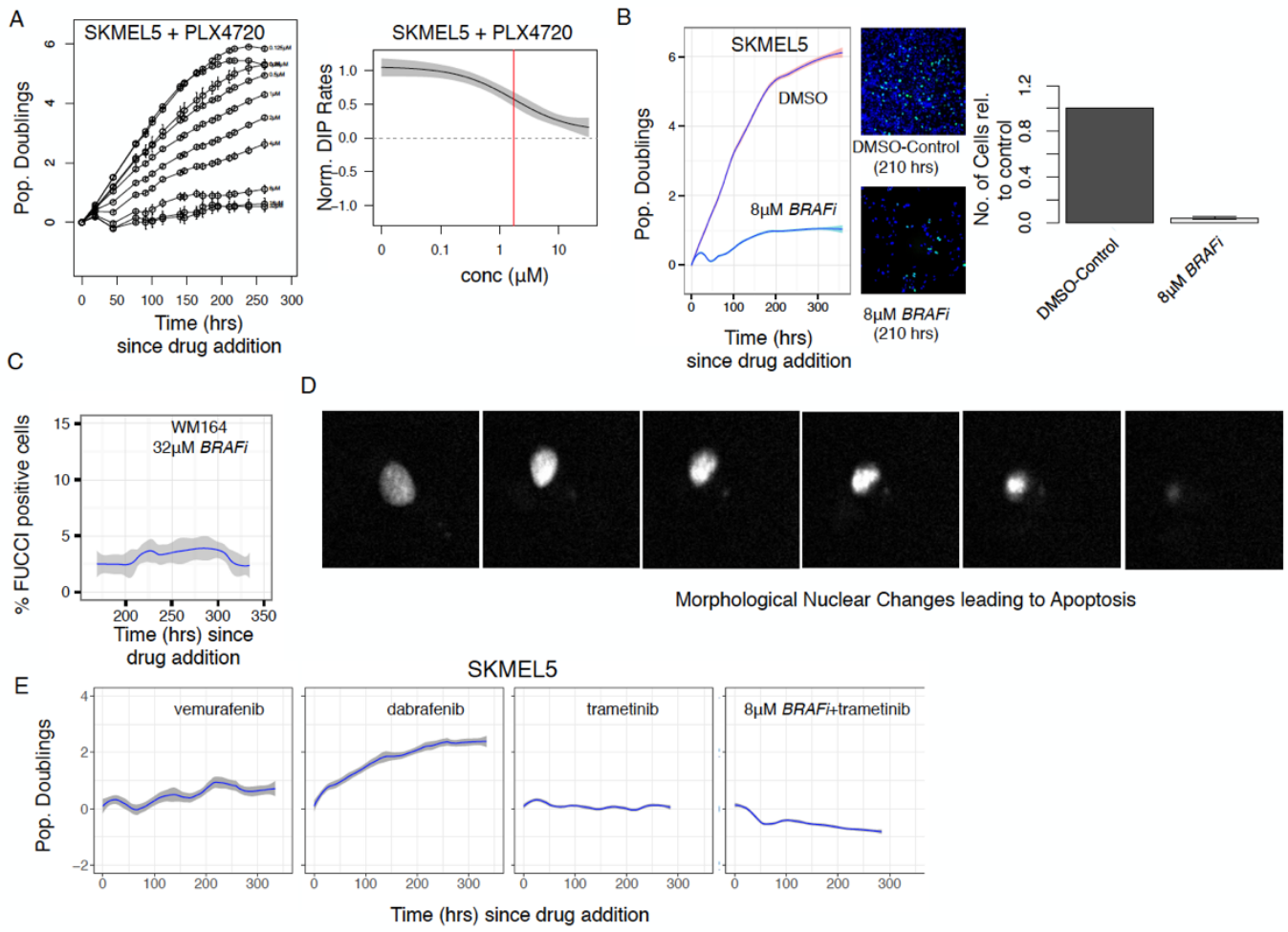

Figure 4.2: *BRAF*i-Induced Responses of *BRAF*-Mutated Melanoma Cell Populations. (a) (left) Population growth curves (log_2 normalized) for SKMEL5 parental cells treated with varying concentrations of *BRAF*i; (right) DIP rate-based dose–response curve (red line is the EC_{50}). (b) The idling state is not trivially due to confluence: (left) comparison of population growth curves (log_2 normalized) for SKMEL5 cells treated with *BRAF*i and DMSO control; (right) representative images at 210 h post *BRAF*i treatment (nuclei are shown in blue, FUCCI-positive (cycling) cells in green). (c) Percentage of FUCCI-positive WM164 cells between 168-350 h of treatment with 32 μM *BRAF*i. (d) Nuclear morphological changes leading to apoptosis observed in *BRAF*i-treated SKMEL5 cells. (e) Population growth curves (log_2 normalized) for SKMEL5 parental cells treated with 16 μM vemurafenib, 4 μM dabrafenib, 0.125 μM trametinib, and a combination of 8μM *BRAF*i and 0.125 μM trametinib (mean responses are shown as solid lines, 95% confidence intervals as shaded regions).

Short-term drug response reflects pre-existing clonal heterogeneity

We investigated more closely the short-term drug response dynamics in the SKMEL5 cell line by tracking ~200 single cell-derived colonies, or “clones” (~110 cells per clone), treated with *BRAF*i using the clonal Fractional Proliferation (cFP) assay (see Materials and Methods) [92]. Because the idling phenotype is reversible (Figure 4.1c), we assume that these

clones are *non-mutational* in nature, i.e., their differences are not based on genetic alterations (this differs from the conventional use of the term “clone,”. [203]. Drug responses were quantified in terms of DIP rate [150] and varied from clone to clone, encompassing a broad range of behaviors from expanding to regressing (Figure 4.3, a and b). Similar results were obtained for other drug concentrations (Figure 4.4a) and other *BRAF*-mutated melanoma cell lines (Figure 4.4b). We observed that the proliferation rate of a clonal lineage prior to treatment does not correlate to its DIP rate in *BRAF*i (Figure 4.3c), indicating a non-trivial relationship between drug-free and drug-induced proliferation (i.e., “fast” proliferators in the absence of drug are not necessarily fast proliferators in drug, etc.). Furthermore, the aggregate of the clonal responses qualitatively matches the short-term population-level response (Figure 4.3d). This suggests that the short-term dynamics is due to clonal competition [94], i.e., clones with negative DIP rates die out while clones with positive DIP rates expand and ultimately drive the population-level response. Thus, these results indicate that *BRAF*-mutated melanoma cell lines contain pre-existing, *hidden* non-mutational clonal heterogeneity that is only revealed upon drug exposure and drives the short-term drug response.

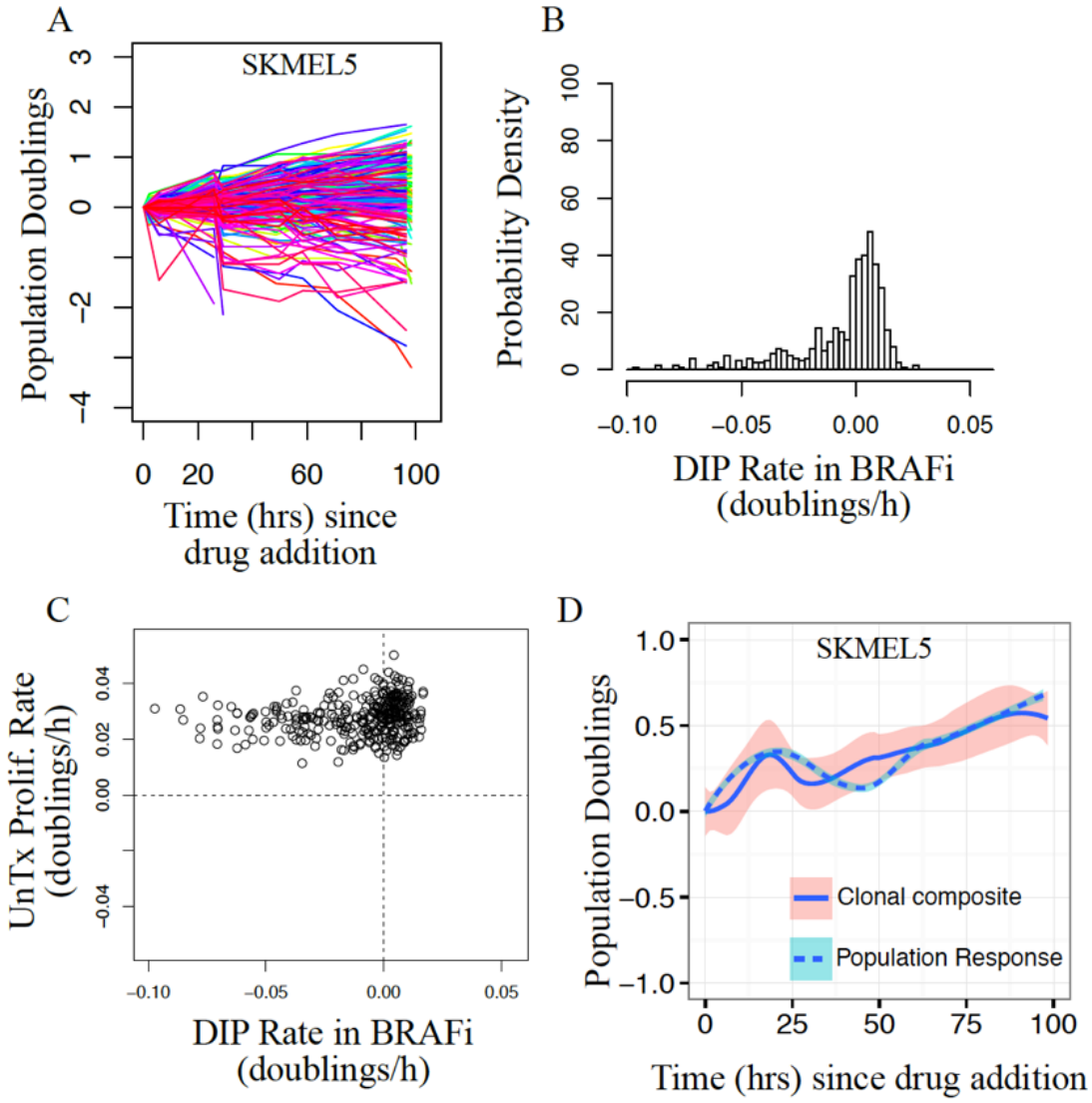

Figure 4.3: Short-Term Drug Response Dynamics Reveals Pre-existing Clonal Heterogeneity. (a) Population growth curves (log_2 normalized) for *BRAF*i-treated SKMEL5 single cell-derived colonies (n=203) obtained using the cFP assay. (b) Distribution of clonal drug-induced proliferation (DIP) rates (doublings/h), obtained by linear fits to the growth curves. (c) Colony DIP rates do not correlate with untreated proliferation rates. (d) The clonal composite (sum of cell counts from all colonies at each time point) closely corresponds to the short-term population-level response (same data as in Fig. 1*A*; means are shown as solid or dashed lines, 95% confidence intervals as shaded regions).

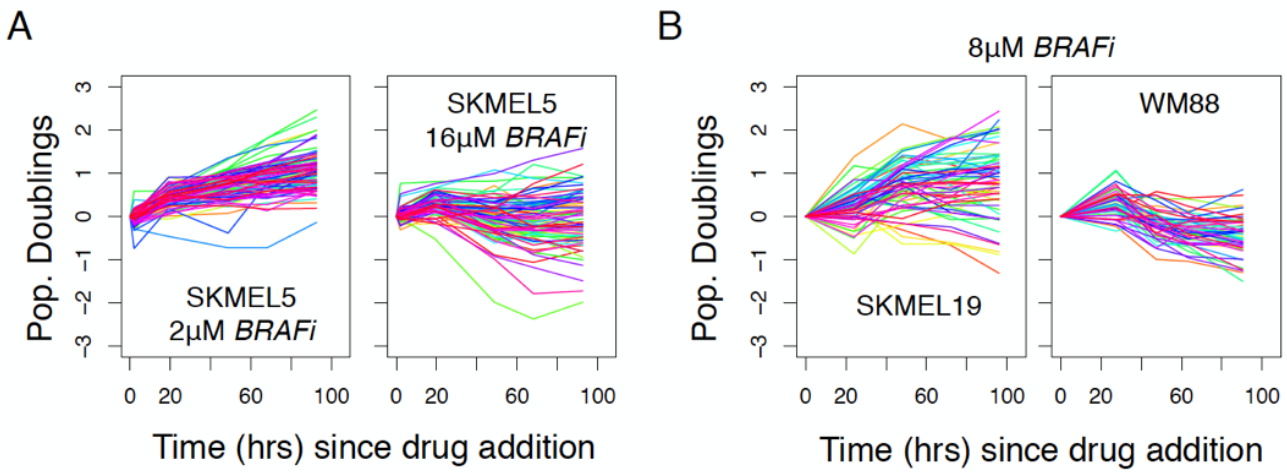

Figure 4.4: Clonal Responses of Multiple *BRAF*-mutated Melanoma Cell Lines to Various Concentrations of *BRAF*i (a) Population growth curves (log_2 normalized) obtained using the cFP assay for SKMEL5 single cell-derived colonies treated with 2 μM *BRAF*i (n=106) and 16 μM *BRAF*i (n=95). (b) Population growth curves (log_2 normalized) obtained using the cFP assay for single cell-derived colonies of SKMEL19 (n=60) and WM88 (n=55) treated with 8 μM *BRAF*i.

Idling occurs within single cell-derived sublines with varying short-term drug sensitivities

To reconcile the long-term population-level response (Figure 4.1, Figure 4.2) with the observed clonal heterogeneity (Figure 4.3, Figure 4.4), we sought to determine whether each clonal lineage enters an idling state independently or if the phenomenon is limited to select clones. To distinguish between these possibilities, we isolated 16 single cell-derived sublines from the SKMEL5 cell line (Figure 4.5a; Materials and Methods). As in the cFP assay (Figure 4.3,Figure 4.4), upon exposure to *BRAF*i the short-term dynamics (<100 h) varied significantly across the clonal sublines, with some expanding, some regressing, and some maintaining a stable population (Figure 4.5b and Table 4.1). We selected three sublines representative of the range of observed short-term responses for further experimentation: SC01 (regressing), SC07 (stable), and SC10 (expanding). Upon prolonged exposure to *BRAF*i, despite their initial divergent responses, both SC01 and SC10 converged to near-zero DIP rates, while SC07

maintained its initial zero-net-growth response (Figure 4.6a). Similar results were obtained for three other SKMEL5 sublines (Figure 4.5c). As before, we confirmed that entry into the idling state is not due to confluence (Figure 4.5d). Furthermore, by manually tracking the fates of multiple individual cells over time, we determined that all three clonal sublines experience death and division while in the idling state (Figure 4.6b), confirming that idling is not due to quiescence but rather due to balanced rates of death and division. These results suggest, therefore, that the idling state is a characteristic feature of *BRAF*-mutated melanoma that is accessible, in the continued presence of *BRAF* inhibition, to all clonal populations regardless of their initial sensitivities.

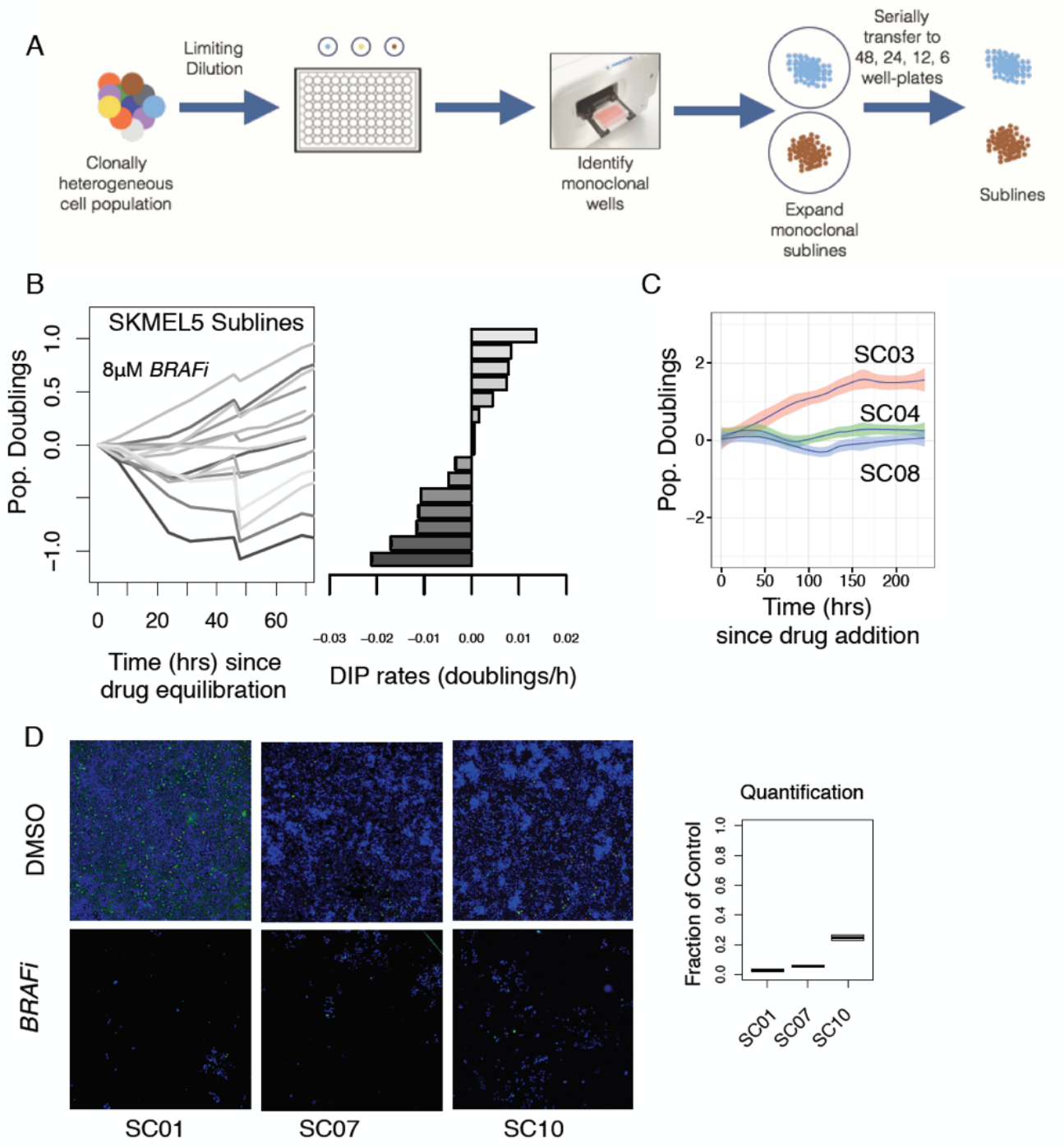

Figure 4.5: Responses of Single Cell-Derived SKMEL5 Clonal Sublines Treated with *BRAF*i (a) Schematic of single-cell-cloning technique used to isolate single cell-derived sublines. (b) 16 single cell-derived SKMEL5 sublines treated with 8μM *BRAF*i: (left) population growth curves ($\log_2$ normalized); (right) bar-plot of *BRAF*i-treated subline DIP rates calculated as linear fits to the growth curves. (c) Three additional SKMEL5 single cell-derived sublines (SC03, SC04, SC08) idle after prolonged exposure to *BRAF*i. (d) (left) Representative images at 190 h post drug addition of populations of SKMEL5 sublines SC01, SC07, and SC10 in DMSO and treated with *BRAF*i; (right) cell fractions in *BRAF*i relative to DMSO control.

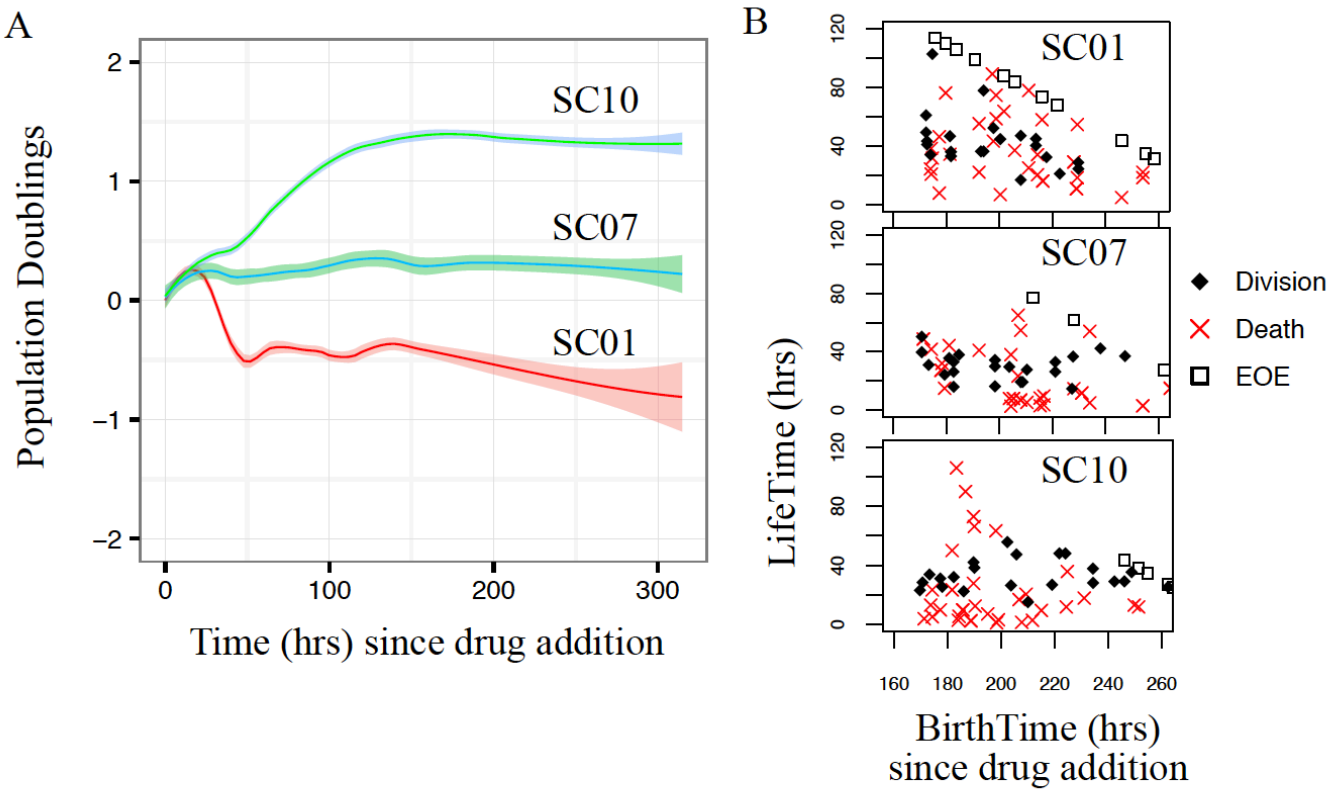

Figure 4.6: Single Cell-Derived Clonal Sublines Idle Independent of Short-Term Drug Sensitivity. (a) Population growth curves (log_2 normalized) for three single cell-derived SKMEL5 sublines treated with *BRAF*i (3+ technical replicates; means are shown as solid lines, 95% confidence intervals as shaded regions). (b) Single cell lifespans vs. birth times (time of first mitotic event) for the three sublines after a week in *BRAF*i (cells born during the experiment but reaching the end of the experiment (EOE) without a second mitotic event are plotted along the diagonal).

Table 4.1: Drug-Induced Proliferation (DIP) Rates for Single-Cell derived SKMEL5 sublines[3].

Subline	Prolif. rate (doublings/h)	Std. deviation
SC01	-2.13E-02	1.07E-02
SC02	4.20E-03	N/A
SC03	1.05E-02	1.48E-03
SC04	-6.51E-03	1.24E-03
SC05	9.00E-04	N/A
SC06	7.10E-03	N/A
SC07	1.53E-03	3.53E-03
SC08	-2.81E-03	3.65E-03
SC10	1.16E-02	4.16E-04
SC11	1.14E-02	N/A
SC12	1.20E-03	N/A
SC13	-2.40E-03	N/A
SC15	-1.90E-03	N/A
SC16	-2.50E-03	N/A

BRAFi-induced idling cells are not multi-drug resistant and have reduced metabolic profiles

Multi-drug resistance is the ability of cancer cells to withstand the effects of anticancer drugs and compounds that are structurally and/or functionally unrelated [204–206]. Recently, it was reported that when exposed to sub-lethal drug concentrations for multiple weeks, melanoma cells transition into a multi-drug-resistant state [207]. To determine whether our *BRAF*i-induced idling cells are multi-drug resistant, we re-challenged idling cell populations ("post-idling") of three SKMEL5 clonal sublines (SC01, SC07, and SC10) with trametinib (a

[3] SC refers to sublines of SKMEL5; Drug-Induced Proliferation (DIP) rates for each subline are calculated from drug response dynamics between 24 h to 96 h in 8 μM PLX4720.

MEK inhibitor), cisplatin (a platinum-based chemotherapeutic), BKM120 (a *PI3K* inhibitor), and BEZ235 (a *PI3K/mTOR* dual inhibitor; see Materials and Methods) and compared their responses to those of drug-naïve populations of the same sublines. In all cases, the post-idling population exhibited significantly altered sensitivities relative to the drug-naïve populations (Figure 4.7).

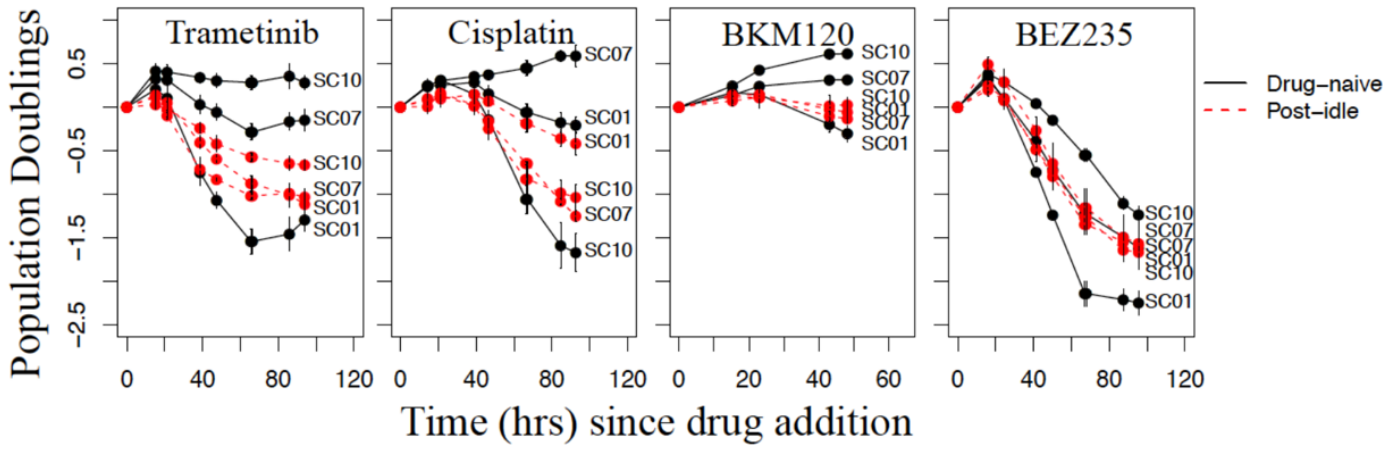

Figure 4.7: Idling melanoma cells show nearly uniform drug sensitivities regardless of their initial differences. Population growth curves (log_2 normalized) for drug-naïve and post-idling (one week of *BRAF*i treatment; *BRAF*i removed less than 24 h prior to subsequent drug addition) single cell-derived SKMEL5 sublines treated with saturating concentrations of trametinib, cisplatin, BKM120, and BEZ235 (error bars represent one standard deviation).

In particular, the least sensitive drug-naïve sublines (SC10 for trametinib, BKM120, and BEZ235; SC07 for cisplatin) were significantly more drug-sensitive after induction into idling. Furthermore, the responses of the post-idling populations were much more uniform across sublines (almost identical in BKM120 and BEZ235) than in the drug-naïve case, suggesting a homogenization of the cell population due to idling. Moreover, the least sensitive subline to three of the drugs (SC10 to trametinib, BKM120, and BEZ234) was the most sensitive to cisplatin, eliminating the possibility that this subline is intrinsically multi-drug resistant.

Since recent studies show melanoma cells undergo metabolic reprogramming in response to *BRAF*-inhibition [185,186,208,209], we characterized functional metabolic profiles of subclones at baseline and in idling state using the Seahorse extracellular flux analyzer platform. We quantified both the oxygen consumption rate (OCR) and extracellular acidification rate (ECAR) of isogenic SKMEL5 subclones (see Methods). At baseline, SC07 had higher oxygen consumption quantified in metrics such as basal mitochondrial respiration, ATP production, maximum mitochondrial respiration and spare capacity followed by SC10 and SC01 (Figure 4.8a). In idling state, we found that oxygen consumption rates of SC07 and SC10 are significantly reduced (Figure 4.8a, b), while SC01 exhibited little change from its already low initial metabolic profile (Figure 4.8). We also observed decreased glycolytic respiration, measured as extracellular acidification rate (ECAR) in subclones treated with PLX4720 (Figure 4.8c). Taken together, these results demonstrate that the short-term drug-response dynamics of single cell-derived clonal melanoma populations are drug- and subline-specific for drug-naïve populations and largely independent of initial clonal identity after induction into idling. Additionally, our results suggest that idling melanoma cells are not multi-drug resistant and represent a state of reduced metabolism.

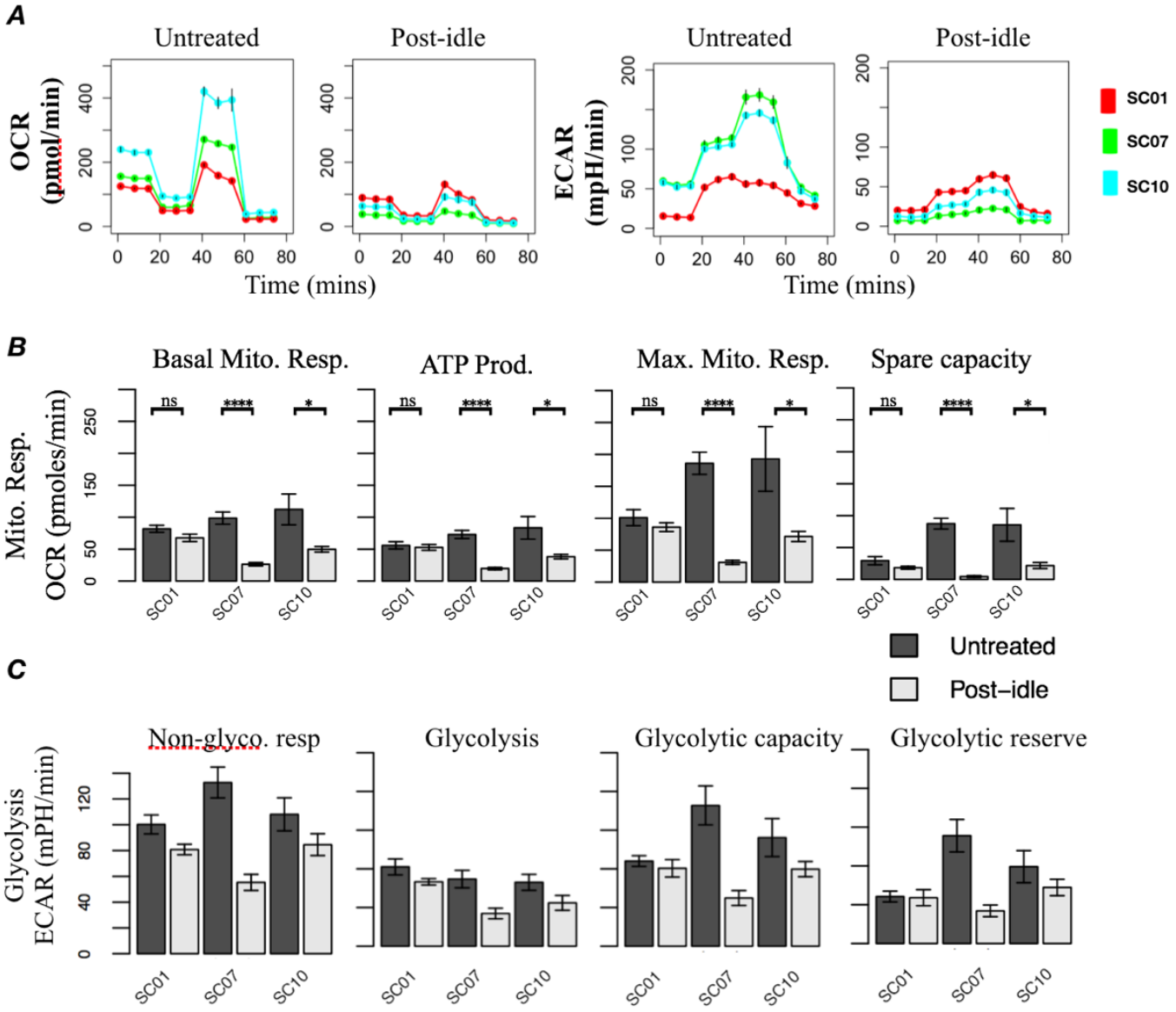

Figure 4.8: Sustained *BRAF*-inhibition leads to reduced metabolism in *BRAF*-mutated melanoma cells. (A) (left)Oxygen consumption profiles (OCR) of SKMEL5 sublines with sequential additions of oligomycin (1 μM), FCCP (1 μM) and Rotenone/Antimycin A (0.5 μM). (right) Extracellular pH (ECAR) profiles of cells with sequential additions of glucose (10 mM), oligomycin (1 μM), and 2-deoxyglucose (0.5 μM). (B) Various metabolic parameters calculated from OCR profiles (C) Various metabolic profiles calculated from ECAR profiles. (B) and (C) are estimated from 3+ replicates.

Mathematical modeling qualitatively reproduces complex, population-level drug-response dynamics

Our experimental observations can be summarized as follows: (i) *BRAF*-mutated melanoma cell populations are clonally heterogeneous, with initial clonal responses to *BRAF* inhibition varying over a wide range, from expanding to regressing (Figure 4.3, a and b); (ii) the short-term population level response is a composite of clonal responses (Figure 4.3d); (iii) all cell line and clonal subline populations eventually transition into a state of balanced death and division, termed idling, in the continued presence of drug (Figure 4.1a and Figure 4.6a); (iv) the idling state is reversible, with cell populations resuming normal exponential growth upon drug removal and responding like drug-naïve populations when re-challenged (Figure 4.1c); and (v) idling cells are not multi-drug resistant and exhibit near-uniform sensitivities to secondary drug treatment, regardless of initial drug-free response (Figure 4.7c). To mathematically formalize these observations, we constructed a simple kinetic model of cell proliferation that qualitatively captures the treatment responses of all *BRAF*-mutated melanoma cell lines considered here. Briefly, we defined three cell subpopulations: regressing (*R*), stable (*S*), and expanding (*E*), with negative, zero, and positive DIP rates, respectively (Figure 4.9a). We assume that cells in each subpopulation can die, divide or (reversibly) transition into "adjacent" subpopulations, thus changing the proportion of cells in each subpopulation over time (see Materials and Methods and Supplementary Information for further details). A similar formalism has been proposed to study cancer cell population dynamics [210]. With cells distributed across the three subpopulations, we expect a period of short-term, non-linear dynamics driven by differences in rates of death and division of each subpopulation (i.e., clonal competition), followed by phenotypic transitions of cells between subpopulations, resulting in idling. Intuitively, the nature of the short-term dynamics and the timescale for transition into idling will

depend upon the initial proportions of cells in each subpopulation and the values of the transition rate constants (Table 4.2).

Table 4.2: Model Variables and Parameters

Variable	Definition	
t	Time (h)	
N_R	Number of cells in state *R*	
N_S	Number of cells in state *S*	
N_E	Number of cells in state *E*	
T	Total number of cells	
Parameter	**Definition**	**Units**
k_{pR}	Net proliferation rate of cells in state *R*	h^{-1}
k_{pS}	Net proliferation rate of cells in state *S*	h^{-1}
k_{pE}	Net proliferation rate of cells in state E	h^{-1}
k_{rs}	Rate of transition of cells from state *R* to state *S*	h^{-1}
k_{sr}	Rate of transition of cells from state *S* to state *R*	h^{-1}
k_{se}	Rate of transition of cells from state *S* to state *E*	h^{-1}
k_{es}	Rate of transition of cells from state *E* to state *S*	h^{-1}
R_0	Initial proportion of cells in state *R*	unitless
S_0	Initial proportion of cells in state *S*	unitless
E_0	Initial proportion of cells in state *E*	unitless

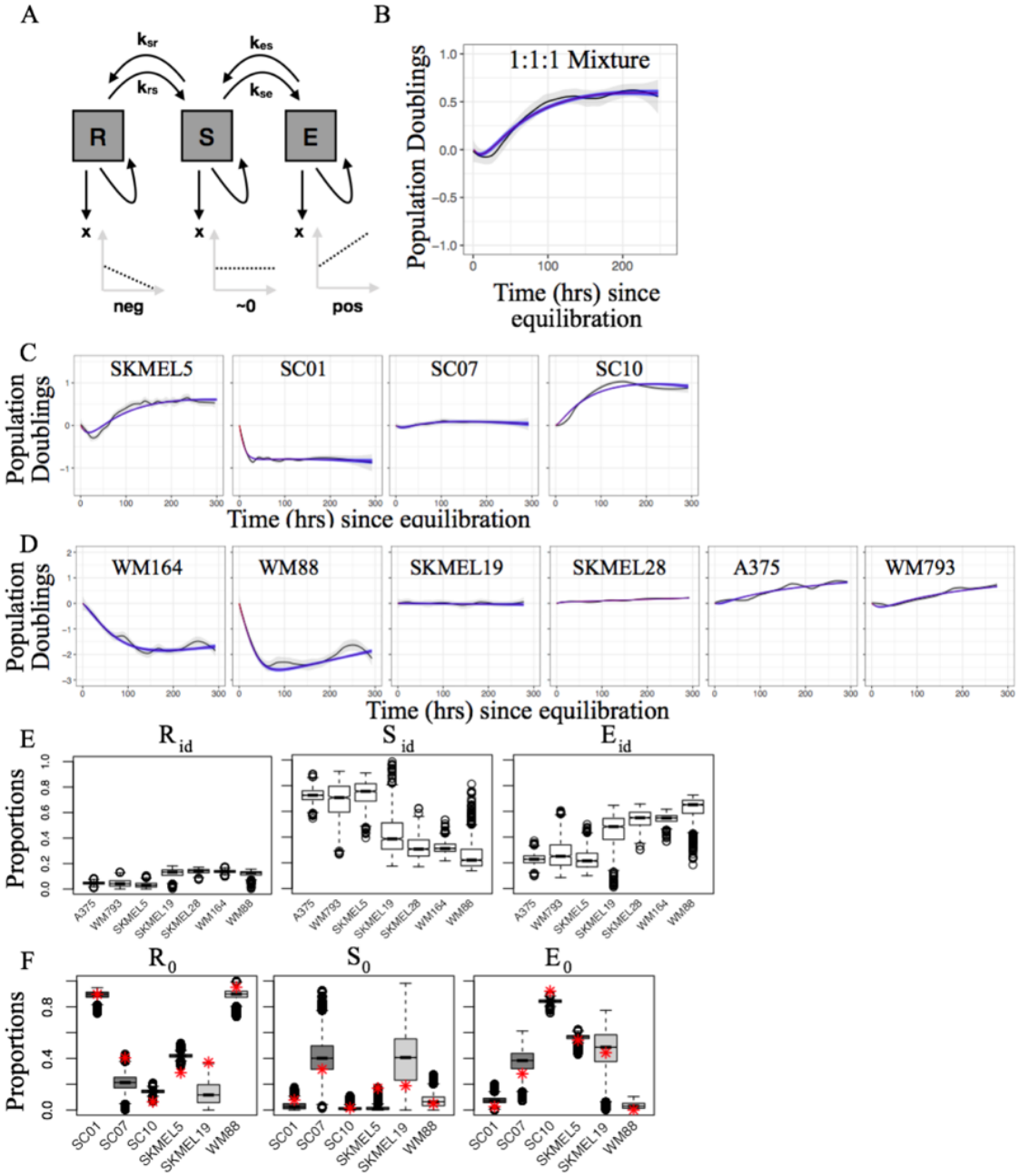

Figure 4.9: A three-state kinetic model qualitatively captures complex drug-response dynamics for numerous *BRAF*-mutated melanoma cell lines and sublines. (a) Graphical representation of the three-state model (arrows represent cell fates, i.e., death, division, and state transitions; growth dynamics for each subpopulation are illustrated in the lower plots). (b) *BRAF*i-induced response of a 1:1:1 clonal mixture of SKMEL5 sublines SC01, SC07, and SC10 used for model fitting (fit shown as a dark blue shaded region). (c) Model fits to the *BRAF*i-induced responses of the SKMEL5 SC01, SC07, and SC10 sublines (Fig. 3A) and the parental line (Fig. 1A) using the rate constants inferred from the fit to the 1:1:1 clonal mixture. (d) Model fits to the *BRAF*i-induced responses of six additional *BRAF*-mutated melanoma cell lines (Fig. 1A). (e) Model-predicted proportions of cells in the regressing (R_{id}), stable (S_{id}), and expanding (E_{id}) subpopulations in the idling state. (f) Comparison of model-predicted and experimentally-derived proportions of cells in the regressing (R_0), stable (S_0), and expanding (E_0) subpopulations at the time of drug addition (experimental estimates, based on cFP, are shown as red stars). For the box plots in E and F , the solid line is the median, the box spans the first and third quartiles, the whiskers extend to 1.5x the inter-quartile range, and outliers are shown as black circles.

For the SKMEL5 cell line, we estimated model parameters by fitting the mathematical model to experimental data for a 1:1:1 clonal mixture of the SC01, SC07, and SC10 sublines (Figure 4.9b) using Markov chain Monte Carlo (MCMC) sampling (see Materials and Methods). We then used the estimated transition rate constants (Figure 4.10a) to predict drug-response dynamics for individual SKMEL5 sublines as well as the parental line (allowing the initial cell proportions to vary). In each case, the model predictions match closely with the experimental time courses, capturing both the short-term dynamics and the transition into the idling state (Figure 4.9c). Importantly, the model cannot explain the observed dynamics if the transition rate constants are set to zero (Figure 4.10c). We also fit the model to experimental time courses for six additional melanoma cell lines (Figure 4.9d). In all cases, the model predicts that the idling state is comprised of very few cells in the *R* subpopulation but significant proportions of cells in both the *S* and *E* subpopulations, ranging between ~20–80% (Figure 4.9e and Figure 4.10c). This is a significant result because it demonstrates that the idling state is not a state of an individual cell, but rather a state of the population as a whole. To further validate the model, we compared the predicted initial cell proportions (R_0, S_0, and E_0=1-R_0-S_0) for the SKMEL5 parental line, sublines, and two additional *BRAF*-mutated melanoma cell lines to results of cFP assays (Figure 4.10d; see Materials and Methods). The cFP assay quantifies the short-term drug response and, therefore, is a reflection of the distribution of initial cell counts across subpopulations prior to drug exposure. In each case, the predicted proportions qualitatively match the experimental results (Figure 4.9f). In summary, our model, incorporating both clonal competition and phenotypic state transitions, captures the key features of the drug-response dynamics of several *BRAF*-mutated melanoma cell populations, which differ significantly in the shape and duration of their short-term response but all eventually converge into an idling state.

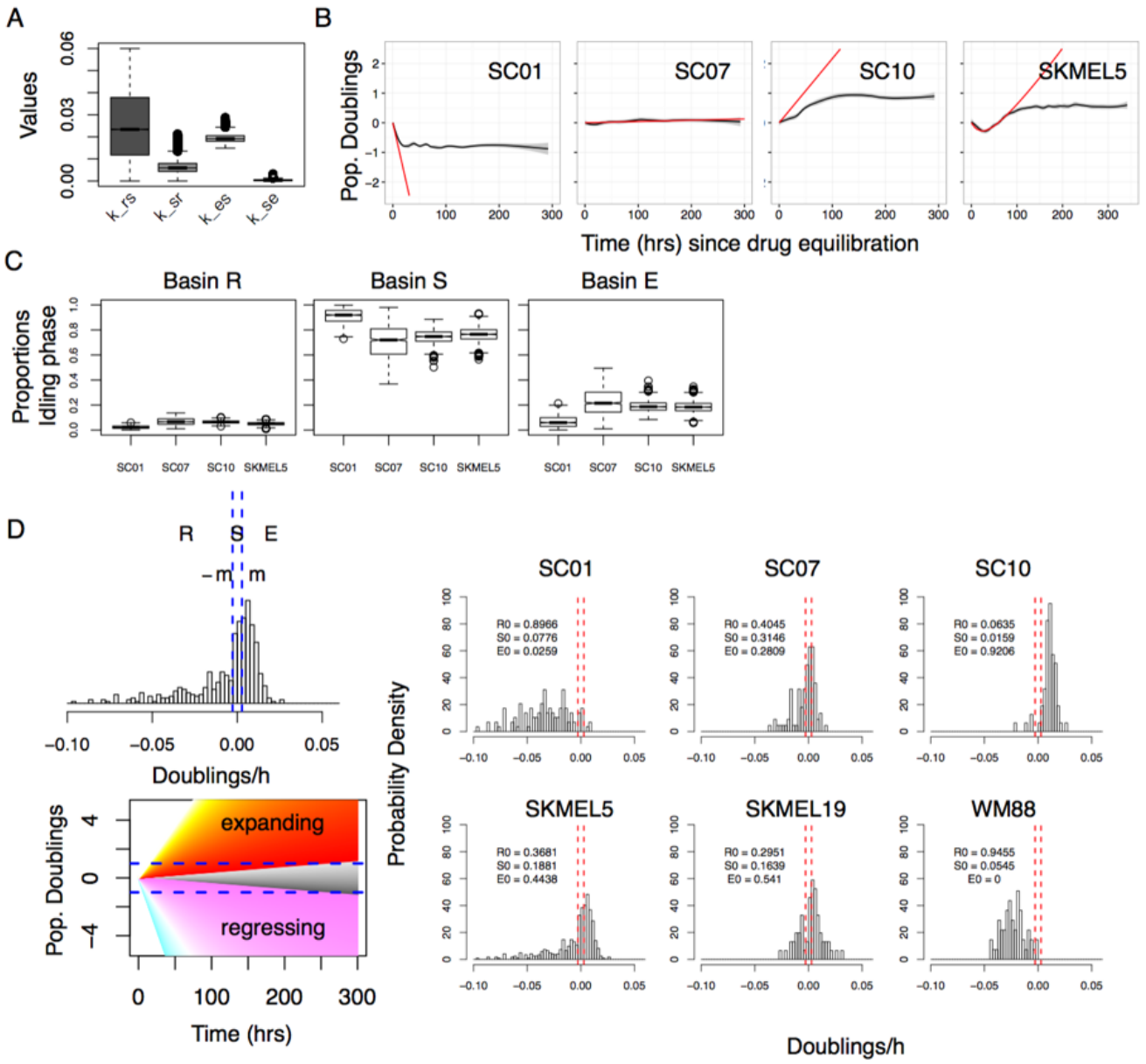

Figure 4.10: Model Predictions and State Discretization for Multiple *BRAF*-mutated Melanoma Cell Lines and Sublines (a) Distributions of transition rate constants (k_{rs}, k_{sr}, k_{se}, k_{es}) obtained by MCMC calibration of our three-state model to experimental data for a 1:1:1 clonal mixture of sublines SC01, SC07, and SC10 (boxes extend from the first to third quartile, solid horizontal line is the median, whiskers extend to 1.5x the interquartile range, outliers are shown as empty circles). (b) Experimental population growth curves (black solid line with 95% confidence envelope) for SKMEL5 parental and single cell-derived sublines SC01, SC07, and SC10 overlaid with model predictions (red) if all transition rate constants are set to zero. (c) Model-predicted proportions of cells in the regressing (R), stable (S), and expanding (E) subpopulations in the idling state for SKMEL5 parental and single cell-derived sublines SC01, SC07, SC10. (d) Discretizing cFP distributions into three states: (left) Cutoffs (± m) of one doubling every two weeks (± 1/360 doublings/h) defines the regressing state R, the zero-net-growth state S, and the expanding state E; (right) cFP distributions for multiple *BRAF*i-treated melanoma cell lines with quantified cell state proportions.

Drug-response dynamics as a reequilibration over a drug-modified quasi-potential energy landscape

Using the values of the transition rate constants from the MCMC-generated ensembles (Appendix 1), we inferred *BRAF*i-induced quasi-potential energy landscapes for all *BRAF*-mutated melanoma cell lines considered here (Figure 4.11; see Materials and Methods). Within this formalism, each subpopulation is associated with a basin of attraction and transitions between subpopulations amount to traversals of energy barriers separating basins [210]. Our results show that the basin associated with the expanding subpopulation (*E*) is consistently the shallowest across cell lines, i.e., has the smallest exit barrier (k_{es}). This makes intuitive sense, since for the cell population to reach the idling state (zero net growth) cells must rapidly evacuate the *E* basin (otherwise the cell population would continue expanding). However, at equilibrium a proportion of cells remain in this basin (Figure 4.9e and Figure 4.10c), providing a source to counterbalance cell depletion occurring in the regressing subpopulation. The depths of the basins associated with the regressing (k_{rs}) and stable (k_{sr}, k_{se}) subpopulations are more variable than for the *E* basin (across the MCMC-generated parameter ensemble) but generally show the *S* basin to be deeper than the *R* basin (Appendix). Notable exceptions are the WM164 and WM88 cell lines, which exhibit significant short-term cell loss. Again, this makes intuitive sense since within this framework the only way for this to occur is for the exit barrier from the *R* to the *S* basin to be large enough so as to abate escape of cells into the *S* basin after drug exposure. For comparison, we also inferred the *BRAF*i-induced epigenetic landscape for the A2058 cell line, which is known to be largely, but not entirely, insensitive to *BRAF* inhibition (Figure 4.12) [211]. Unsurprisingly, in this case the *E* basin is significantly deeper than the other basins and simulations show that the system cannot achieve a long-term dynamic equilibrium. Hence, we do not observe idling in this cell

line within the time frame of our experiment and we do not expect it to ever idle regardless of duration of drug exposure. Overall, the inferred epigenetic landscapes are powerful theoretical tools for understanding the basis of the complex population-level dynamics observed in *BRAF*-mutated melanoma cell populations and for reconciling differences seen across cell lines in terms of variations in landscape topography.

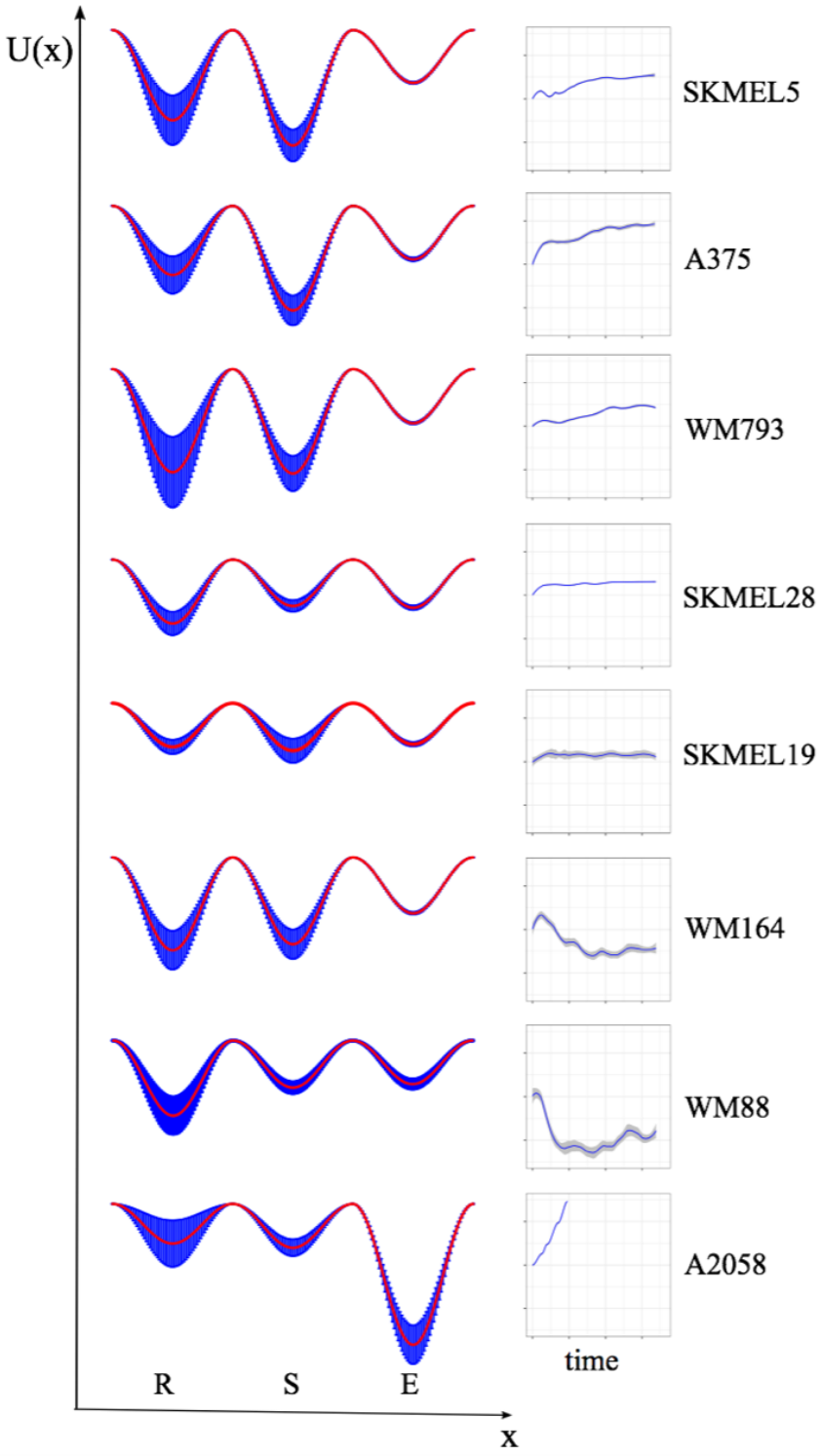

Figure 4.11: Inferred drug-modified quasi-potential energy landscapes provide insight into the drug-response dynamics. Quasi-potential energy landscapes for eight *BRAF*-mutated melanoma cell lines (seven from Fig. 1A, plus the largely *BRAF*i-insensitive A2058 cell line), inferred from model fits to the drug-response dynamics (shown to the right). U(x) is the quasi-potential energy, x is the "reaction coordinate." Landscapes are based on 2000 random samples of the MCMC-generated parameter ensemble. Mean basin depths and barrier heights are shown as red lines; the blue shaded regions correspond to one standard deviation around the mean. R, regressing; S, stable; E, expanding.

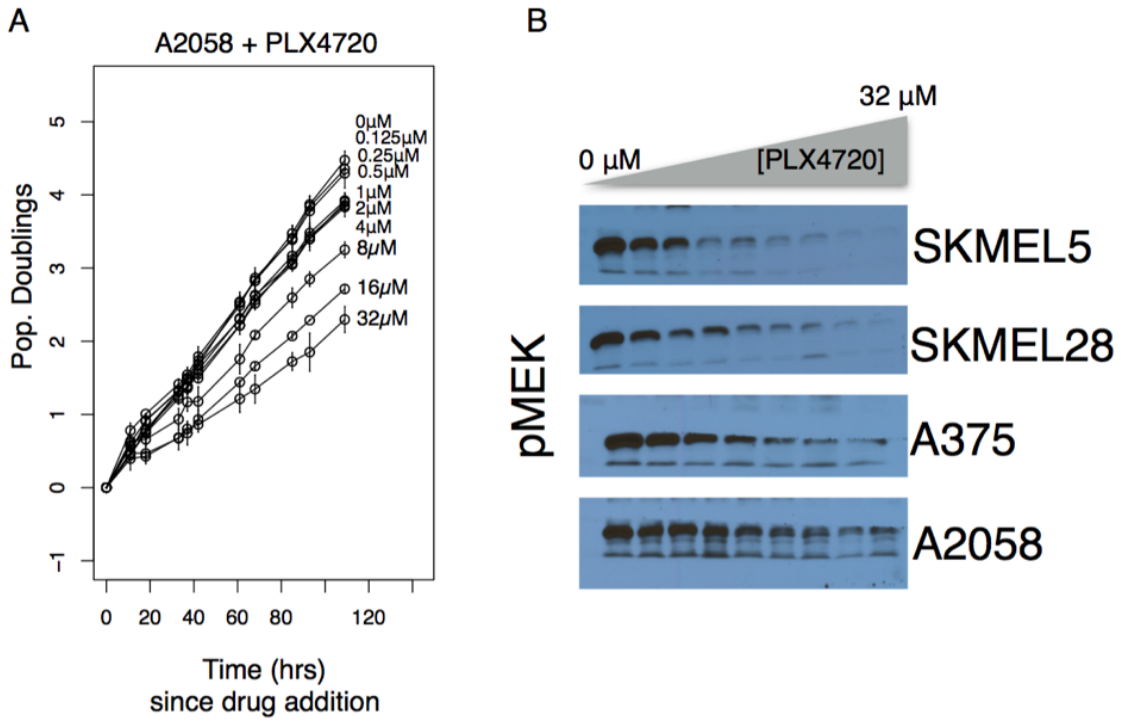

Figure 4.12: *BRAF*i-Induced Population Dynamics and Signaling Changes for the A2058 Cell Line. (a) Population growth curves (log_2 normalized) for varying concentrations of *BRAF*i. (b) Western blots comparing levels of phosphorylated *MEK* in A2058 cells and three other cell lines after 96 h exposure to *BRAF*i (lanes correspond to drug concentrations in for the population growth curves).

Discussion

We report here that sustained *BRAF* inhibition (>100 h *in vitro*) induces entry of *BRAF*-mutated melanoma cell populations into a non-quiescent idling state of balanced death and division, characterized by a near-zero proliferation rate. Idling occurs both at the population and clonal levels, independent of differences in initial short-term responses, and is both drug-induced and reversible, consistent with non-mutational drug tolerance described in earlier reports [105,212,213]. Cells in the idling state are not multi-drug resistant and respond to secondary drug treatments (nearly) uniformly, independent of initial clonal identity. To our knowledge, the idling state has not been previously reported, possibly because drug-response assays tend to be performed over short observation times (72–96 h) and proliferation rates are

not usually measured [92,147,150,159], as we do in this work. Taken together, these observations are not easily explained within the frameworks of existing models of drug resistance or tolerance [106,191,193,207,214–216]. In particular, cell populations that initially expand but then transition into the idling state (SKMEL5 and A375 in Figure 4.1a; SC10 in Figure 4.6a) cannot be the result of selection of a rare pre-existing resistant clone or due to the acquisition of a resistance-conferring genetic mutation; nor, as we show, is it due to confluence (Figure 4.2b and Figure 4.5d) or quiescence (Figure 4.1b, Figure 4.6b, and Figure 4.2c). This begs the question, why an apparently thriving cell population would cease expanding and enter into a state of balanced death and division.

To get a grasp on these confounding observations, we proposed a kinetic model (Figure 4.9a) in which a cell population is comprised of multiple discrete subpopulations that can interconvert and each of which is characterized by a DIP rate [150] that quantifies its net proliferation in drug. The model is most easily understood within the framework of epigenetic landscapes, where cell subpopulations are associated with basins of attraction and phenotypic state transitions with traversals of quasi-potential energy barriers. An implicit assumption of the model is that an epigenetic landscape exists in the *absence of drug*, which is set by the genetic background of the cell [128], over which cells within an isogenic population (e.g., a cell line) stochastically diffuse in time. This drug-naïve “phenotypic drift” sets the initial cellular occupancies of each basin in a *drug-modified* epigenetic landscape that is drug- and dose-dependent. The cFP assay [92] provides an experimental platform for quantifying these initial cell occupancies in terms of DIP rate distributions (Figure 4.3b and Figure 4.10d).

The central hypothesis of this work is that drug-treated cell populations re-equilibrate over this new, drug-modified landscape; the short-term population-level drug response is a

reflection of this re-equilibration process; and the idling state constitutes the final, equilibrated state. This theoretical framework explains why populations of single cell-derived sublines respond differently to drug in the short term (different initial numbers of cells in each basin) but identically in the long term (exposure to the same landscape topography), as we report here (Figure 4.6a). Convergence to a common drug-induced equilibrium state also explains the near uniform drug responses in post-idling populations of single cell-derived sublines (Figure 4.7). The reversibility of the idling phenotype for parental cell populations (Figure 4.1c) is explained by a return to the drug-naïve epigenetic landscape upon drug removal and a re-equilibration back to the original cell occupancies. Differential dynamics across cell lines is explained in terms of variations in the topographies of drug-modified landscapes (Figure 4.11) due to variations in the genetic backgrounds of the cell lines. An important consequence of this is that each cell line (with one exception, i.e., A2058) achieves idling in a slightly different way, with varying proportions of regressing, stable, and expanding subpopulations (Figure 4.9), despite harboring a common *BRAF*-activating mutation, i.e., driving addicting oncogene.

Cellular resistance to anticancer therapies is a complex, multi-faceted problem (CHAPTER 1) [204]. Genetic mutations obviously play a major role in the acquisition of irreversible drug resistance and ultimate treatment failure, but it is becoming increasingly clear that genetics is not the whole story [217]. We believe that the idling state presented here, and the relatively simple theoretical framework describing it, has potentially far-reaching implications for patient therapies. In particular, even in tumors with high therapeutic sensitivity, a minority of cells often survives and can persist for months or even years [217]. This “residual disease” is suspected to act as a reservoir from which resistance-conferring genetic mutations, and ultimately tumor recurrence, arises [106,207,214,215,218]. We speculate that idling

cancer cells may, in fact, constitute the bulk of the residual disease. Indeed, by continuing active progression through the cell cycle, idling cells are more prone to accumulate deleterious mutations and, hence, are a more fertile ground for acquiring resistance mutations, than quiescent [101,106,219,220] or senescent [221] cells. However, we have shown here that the idling state is not a property of individual cells but rather a property of the *population* as a whole. As such, idling cells cannot be eradicated by targeting one particular subpopulation. Rather, the landscape itself must be altered (e.g., using drugs) to favor regressing basins over stable and expanding basins. This is a significant departure from recent approaches that aim to identify and eliminate rare cell subtypes (e.g., cancer stem cells, drug-tolerant persisters) thought to be responsible for tumor progression and recurrence [106,204,216,222]. This type of cellular reprogramming will require deep knowledge of the molecular factors that shape and define the epigenetic landscapes and basins of attraction that cancer cells inhabit [223,224]. Future work will aim to identify the molecular actors that define the *BRAF*-mutated melanoma epigenetic landscape using, for example, single-cell RNA sequencing technologies [137–139]. Targeted landscaping, for example, therapeutic approaches that rationally modify the epigenetic landscape in order to suppress or eliminate the non-quiescent reservoir of idling cancer cells, could delay, perhaps indefinitely, tumor recurrence.

CHAPTER 5

NADPH OXIDASE INHIBITION SENSITIZES *BRAF*-MUTATED MELANOMA CELLS TO *BRAF*-INHIBITION

Adapted from:

Paudel BB, Hardeman KN, Meyer CM, Harris LA, Tyson DR, Fessel JP, & Quaranta, V. (2018). NADPH Oxidase Inhibition Sensitizes *BRAF*-mutated Melanoma Cells to *BRAF*-inhibition. (*in preparation; to be submitted Spring 2018*).

Summary

Identifying the molecular basis for intrinsic drug response variability of *BRAF*-mutated melanoma cells to *BRAF*-inhibition is an active area of research. In this chapter, I describe differences among single cell-derived isogenic sublines at the phenotypic and molecular level and identify the cumulative expression of *PGC1α* and *NOX5* as potential determinant of intrinsic drug insensitivity. This study uncovers a potential biomarker for identification of tumors which are likely to respond to existing therapy and therapeutic combination that could maximize cell killing in *BRAF*-mutant melanoma cells.

Abstract

BRAF-mutated melanoma cells exhibit varying drug sensitivities with *BRAF*-inhibition, which are associated with clonal heterogeneity, molecular basis to which is still poorly defined. We therefore utilized single-cell derived isogenic sublines to probe for molecular determinants of short-term drug response variability. We discovered that the cumulative expressions of *NOX5* and *PGC1α* show strong positive correlation to short-term drug sensitivity of melanoma

cells. We demonstrate that this could have direct clinical implications as we show that the high *NOX5* expression correlates with poor treatment outcome in melanoma patients undergoing MAPK pathway inhibition. Using both chemical and siRNA-mediated knockdown approaches, we identified that *NOX* inhibition sensitizes melanoma cells and enhances the anti-proliferative effects of *BRAF*i. We demonstrate that inhibiting *NOX5* in combination with *BRAF*i could improve current approaches to targeted melanoma therapy.

Introduction

Targeted small molecule inhibitors of *BRAF* [190] show remarkable, short-term efficacy in melanoma patients with tumors harboring $BRAF^{V600}$ mutations [26,44]. However, clinical responses are variable, short-lived, and tumor recurrence is almost universal within a few months of initiation of therapy [26,45]. Overcoming inherent and acquired resistance to targeted therapy is a major goal of current melanoma research, which uncovered two categories of resistance mechanisms: (i) re-activation of mitogen-activated protein kinase (MAPK) signaling cascades [64–66,70,72], and (ii) activation of MAPK-pathway independent signaling pathways [69,70,73,75,179]. This has led to the development of combination therapies of *BRAF* inhibitors with other targeted agents [52–55,225,226] or with immunotherapy [227]. While these therapies improve clinical responses, variation in treatment outcomes persists and benefits remain transient and unpredictable (CHAPTER 1) [52].

Most of our knowledge of melanoma tumor recurrence is derived from analysis of post-resistant tumors or cells [75]; the proliferation dynamics of drug-treated tumor cells prior to resistance is poorly understood [105]. Resistance is usually attributed to rare, resistance-conferring genetic alterations that either preexist [94,187,191] or develop during therapy [73,192]. However, there is accumulating evidence that non-mutational processes play a significant role in the response of cancer cells to drug treatment [102–105]. It has been

suggested that cancer cells employ a dynamic survival strategy involving phenotypic state transitions, governed by epigenetic alterations to evade lethal external cues [106,107]. These observations are consistent with preclinical and clinical evidence suggesting that cancer cells can become re-sensitized to therapy after a brief “drug holiday” [81,99,100]. It is likely, therefore, that both genetic and non-genetic processes are involved in the acquisition of drug resistance and/or relapse of melanoma tumors (CHAPTER 4).

The interplay between cancer cell metabolism and response to targeted therapies has gained considerable interest in recent years (CHAPTER 3). Recent studies have underscored the role of glycolysis and oxidative phosphorylation in melanoma cells responsiveness to *BRAF*-inhibition in different contexts [184,208,211,228–230]. Specifically, enhanced metabolic activity and metabolic switch have been implicated to affect treatment response outcomes via adaptive signaling within melanoma cells during therapy [231]. However, the relationship between metabolic states of cells and their therapeutic response still remains unclear. Recently, we reported a positive correlation between glucose utilization and sensitivity to *BRAF*-inhibition [211], sensitivities defined in terms of Drug-Induced Proliferation (DIP) rates [150]. Here, we extended our experimentation to quantify drug-response dynamics at the clonal and the single cell level, and show that drug sensitivity is linked to metabolic state of cells, defined with respect to their capacity to utilize both glycolysis and oxidative phosphorylation. Using single-cell derived isogenic clonal sublines, we identified PPARGC1A (or *PGC1α*) and NADPH Oxidase 5 (*NOX5*) as potential determinants of sensitivities to *BRAF*i. We show that NADPH Oxidase inhibition sensitizes melanoma cells to *BRAF* inhibition, including inherently resistant cell populations, using both genetic and chemical inhibition approaches. Our results suggest NADPH oxidase protects melanoma cells from anti-proliferative effects of *BRAF* inhibition and may represent a potential therapeutic opportunity.

Materials and Methods

Cell Culture and Reagents

BRAF-mutated melanoma cells (SKMEL5, A375, WM793, SKMEL19, SKMEL28, WM164, WM88, A2058) were grown and cultured in Dulbecco's modified Eagle's medium and Ham's F-12 medium (DMEM:F12, 1:1, Cat# 11330-032). Media were obtained from Gibco (Grand Island, NY) and supplemented with 10% FBS. All cells were cultured in CO_2, temperature-controlled (37°C), and humidified incubators. Cells were tested for mycoplasma before use and confirmed negative. Cells were passaged 1–2× per week and maintained as exponentially growing cultures for a maximum of less than 20 passages. Unless otherwise indicated, cells were seeded ~16–24 h prior to treatment to allow cells to adhere to culture plates. Reagents/drugs were prepared in complete medium immediately prior to adding to cells by replacement.

PLX4720 (Cat# S1152) and vemurafenib (Cat# S1267) were obtained from Selleckchem (Houston, TX) solubilized in dimethyl sulfoxide (DMSO) at a stock concentration of 10 mM. Diphenyleneiodonium chloride (DPI) (Cat# D2926) and Apocynin (Cat# 498-02-2) were obtained from Sigma-Aldrich and solubilized in DMSO at a stock concentration of 10 mM for DPI and at a stock concentration of 100 mM for Apocynin. GKT137831 (Cat# HY12298) was obtained from MedChemExpress (Monmouth Junction, NJ) and solubilized in DMSO at a stock concentration of 10 mM. All drugs were aliquoted and stored at -20°C until use.

Fluorescent Imaging

To facilitate automated image processing, cells were engineered to express fluorescent fusion proteins histone 2B monomeric red fluorescent protein (H2BmRFP; Addgene plasmid# 18982) and geminin1–110 monomeric azami green [164] using replication-incompetent recombinant lentiviral particles, as previously described [147,167]. Cells were seeded at 1000–

5000 cells per well in 96-well culture imaging plates (BD Biosciences, product# 353219). DMSO and PBS were used as vehicle controls, as appropriate. Images were acquired through a 10× or 20× objective with a Cellavista High End Bioimager (SynenTec Bio Services, Münster, Germany) every 6–12 hours as 3×3 or 5×5 montages. Media containing matching concentrations of drug or vehicle in each well were replaced every three days. Image processing to obtain counts of cell nuclei at each time point was performed as previously described [147,150].

Single-Cell Derived Sublines

Sixteen SKMEL5 sublines were derived from single cells by serial dilution. Briefly, cells were serially diluted to less than 1 cell per well in 96-well imaging plates and imaged to identify wells containing a single cell. Cells were expanded in complete growth medium (in the absence of *BRAF*i) and sequentially transferred to 48-, 24-, and 6-well plates until sufficient numbers of cells were available for cryopreservation. All sublines were tested for their sensitivity to *BRAF*i prior to cryopreservation.

RNASeq and Bioinformatics Analysis

Total RNA was isolated from untreated SKMEL5 single-cell derived sublines, each in triplicate, using Trizol isolation method (Invitrogen) according to the manufacturer's instructions [232]. RNA samples were submitted to Vanderbilt VANTAGE Core services for quality check, where mRNA enrichment and cDNA library preparation were done with Illumina Tru-Seq stranded mRNA sample prep kit. Sequencing was done at Paired-End 75 bp on the Illumina HiSeq 3000. Reads were aligned to the GRCh38 human reference genome using HISAT2 [233] and gene counts were obtained using featureCounts [234]. All downstream analyses were performed in R (https://www.r-project.org) using the Bioconductor framework (https://www.bioconductor.org). Differential gene expression analysis was performed on genes

(after low count genes were removed) using DESeq2 pipeline [235]. Differentially expressed genes (DEGs) were selected based on a statistical cutoff of FDR < 0.01 and fold change of 2. Pathway enrichment analysis was done using WebGestalt http://www.webgestalt.org/webgestalt_2013/). DESeq2 rlog-values were used for visualization of gene expression levels in heat maps. Clustering was performed using the default settings of the heatmap.2 function in the gplots R package.

RNA Isolation and Quantitative Real-Time PCR (qPCR)

Total RNA was extracted using Trizol isolation method (Invitrogen) according to the manufacturer's instructions [232]. cDNA synthesis was performed with QuantiTect Reverse Transcription Kit (Cat# 205311) from Qiagen. RT-qPCR was performed using the IQ^{TM} SYBR Green Supermix from BioRad (Cat# 1708880). Amplifications were performed in BioRad CFX96 Touch^{TM} Real-Time PCR Detection System. All experiments were done at least in 3+ technical replicates. Log_2 of the transcript expressions were normalized to their expressions to SKMEL5 subline SC01. HPRT was used as housekeeping gene in all the experiments. Primers used in RT-qPCR are listed in Table 5.1.

siRNA Transfection and Knockdown

For gene silencing experiments, ON-TARGETplus Human NOX5 siRNA SMARTPool (Cat# L-010195-00) was used. ON-TARGETplus Non-Targeting pool (Cat# D-001810-10-05) was used as scrambled control. Both were obtained from Dharmacon (Lafayette, CO) and stored at -20^{o}C until use. Transfection was carried out according to manufacturer's instructions using DharmaFECT1 Transfection Reagent (Cat# T-2001-02).

Clinical Gene Expression Analysis

Gene expression of drug-naïve patient samples were used from three published papers [75,107,236]. Gene expressions were quantile-normalized before comparison. RECIST criteria

reported in the papers were used as clinical outcomes, and are grouped into either Responders (partial and complete response) or Non-Responders (stable and progressive disease).

Seahorse Metabolic Assays

For measurement of Oxygen Consumption and Extracellular Acidification Rates, cells were plated onto 96-well plates (Seahorse Biosciences, Billerica, MA) at a density of 25,000-40,000 cells/well before analysis on the Seahorse XFe extracellular flux analyzer. Mitochondrial Oxygen Consumption was quantified using the Mito Stress Test kit, and glycolytic rate quantified using the Glycolysis Stress Test kit, each according to manufacturer's instructions. Briefly, assay medium was unbuffered DMEM containing either 10 mM Glucose, 2 mM Glutamine, and 1 mM Sodium Pyruvate (Mito Stress Test) or none of the aforementioned (Glyco Stress Kit). No FBS was used in assay medium.

Statistical Analysis

All statistical analyses were done in RStudio, Version 1.0.136. Two-sided Student's t-tests were used for pairwise comparisons for comparisons in gene expressions and metabolic differences.

Results

Identification of molecular determinants of short-term drug response variability using single-cell-derived isogenic sublines

We recently reported that *BRAF*-mutated melanoma cell lines exhibit varying drug sensitivities to small molecule *BRAF*i [211,237]. Briefly, we show that cell lines can be ordered on a continuum based on their drug sensitivities using Drug-Induced Proliferation (DIP) rates, an unbiased metric of anti-proliferative effects of drug [92,150]. Since there is a lot of inter-cell

line variation, we looked into each specific cell line and reported that the short-term population level response in each cell line comprises of a wide range of clonal behaviors [237]. In this study, we utilized single-cell derived isogenic sublines of a *BRAF*-mutated melanoma cell line, SKMEL5, and performed RNASeq analysis on three sublines with distinct drug responses in the short-term to probe for the molecular determinants of short-term response variability (Figure 5.1). Selected sublines had divergent drug responses in the short-term: SC01 (regressing), SC07 (stable) and SC10 (expanding). By performing pairwise comparisons between SC07 vs SC01, SC10 vs SC01, and SC10 vs SC07, we selected differentially expressed genes (DEGs) based on a statistical cutoff of FDR < 0.01. Among these genes, we focused on the subset differing in a degree of enrichment by twofold or more between the sublines (see Materials and Methods for details) (Figure 5.2a). The top KEGG pathways enriched in common set of upregulated DEGs included Metabolic pathways, Cell Adhesion Molecules, and Focal Adhesion (Figure 5.2b).

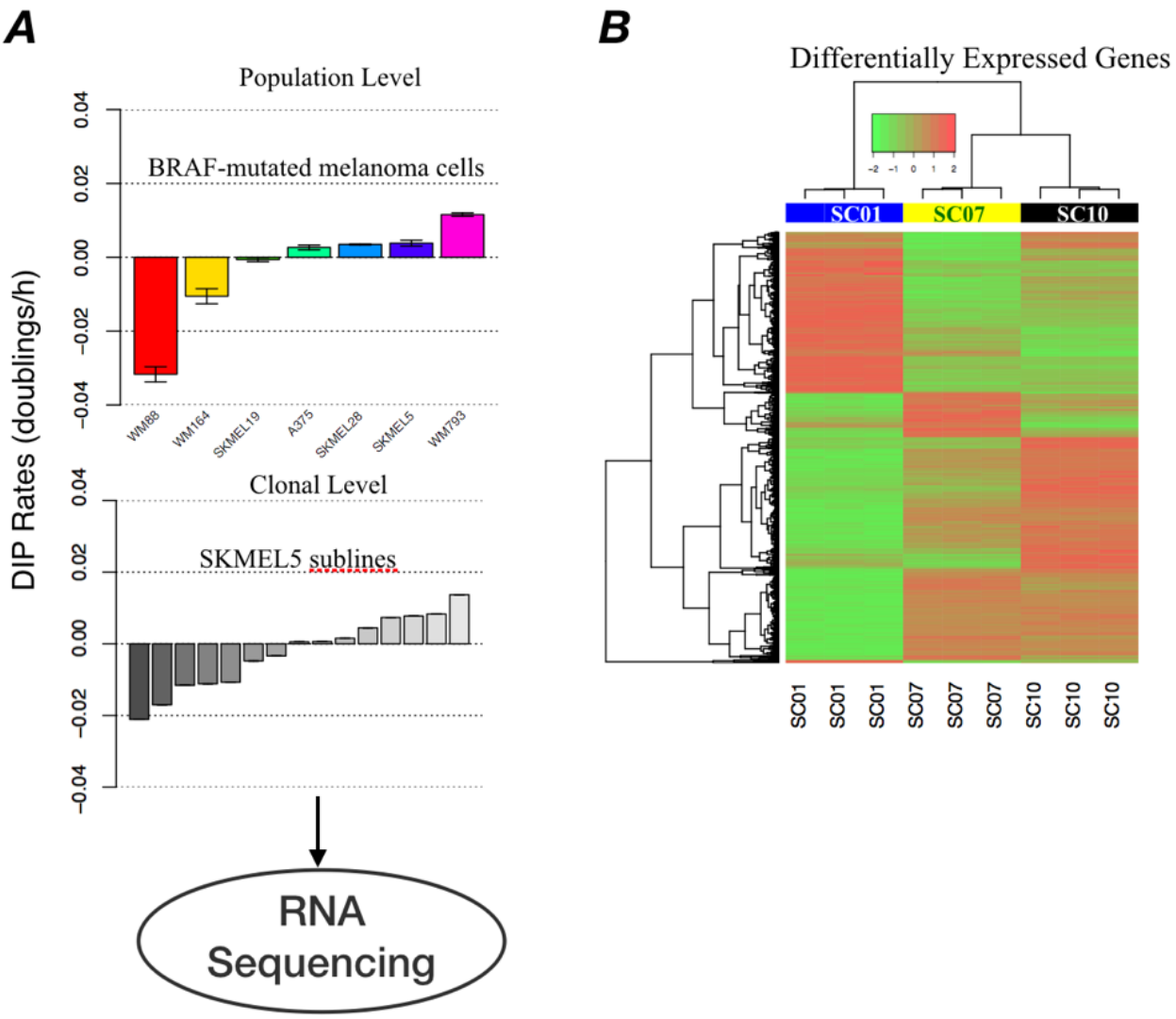

Figure 5.1: Identification of molecular determinants of short-term drug response variability using single-cell derived isogenic sublines. (A) Data from previous reports [211,237] showing drug-response variation among *BRAF*-mutated melanoma cells at the population level and among single-cell derived sublines of SKMEL5 cell line at the clonal level. For both population and clonal level, drug response is quantified as DIP rates (doublings/h) for cellular response at 8 μM PLX4720. (B) Heat map of differentially expressed genes determined after pairwise comparisons between SC07 vs SC01, SC10 vs SC01 and SC10 vs SC07. Three SKMEL5 sublines: SC01, SC07 and SC10 were chosen for RNASeq analysis based on their divergent drug responses.

We focused on genes involved in metabolic pathways, and identified *PGC1α*, a mitochondrial biogenesis transcriptional co-activator and NADPH Oxidase 5 (*NOX5*) as potentially important determinants of sensitivities to *BRAF*i. Based on our own results [211], and others [185,186,228], these are both plausible targets because of the metabolic and redox

regulatory functions that converge at the mitochondria. While the expression of *PGC1α* is significantly different in SC01 compared to SC07 and SC10, its expression in SC07 and SC10 is comparable. Similarly, the expression of *NOX5* is significantly different in SC10 compared to SC01 and SC07, while its expression in SC01 and SC07 is comparable (Figure 5.2c). Taken together, our results suggest metabolic differences between our isogenic sublines and identify *NOX5* and *PGC1α* as potential determinants of drug-response variability in the short-term.

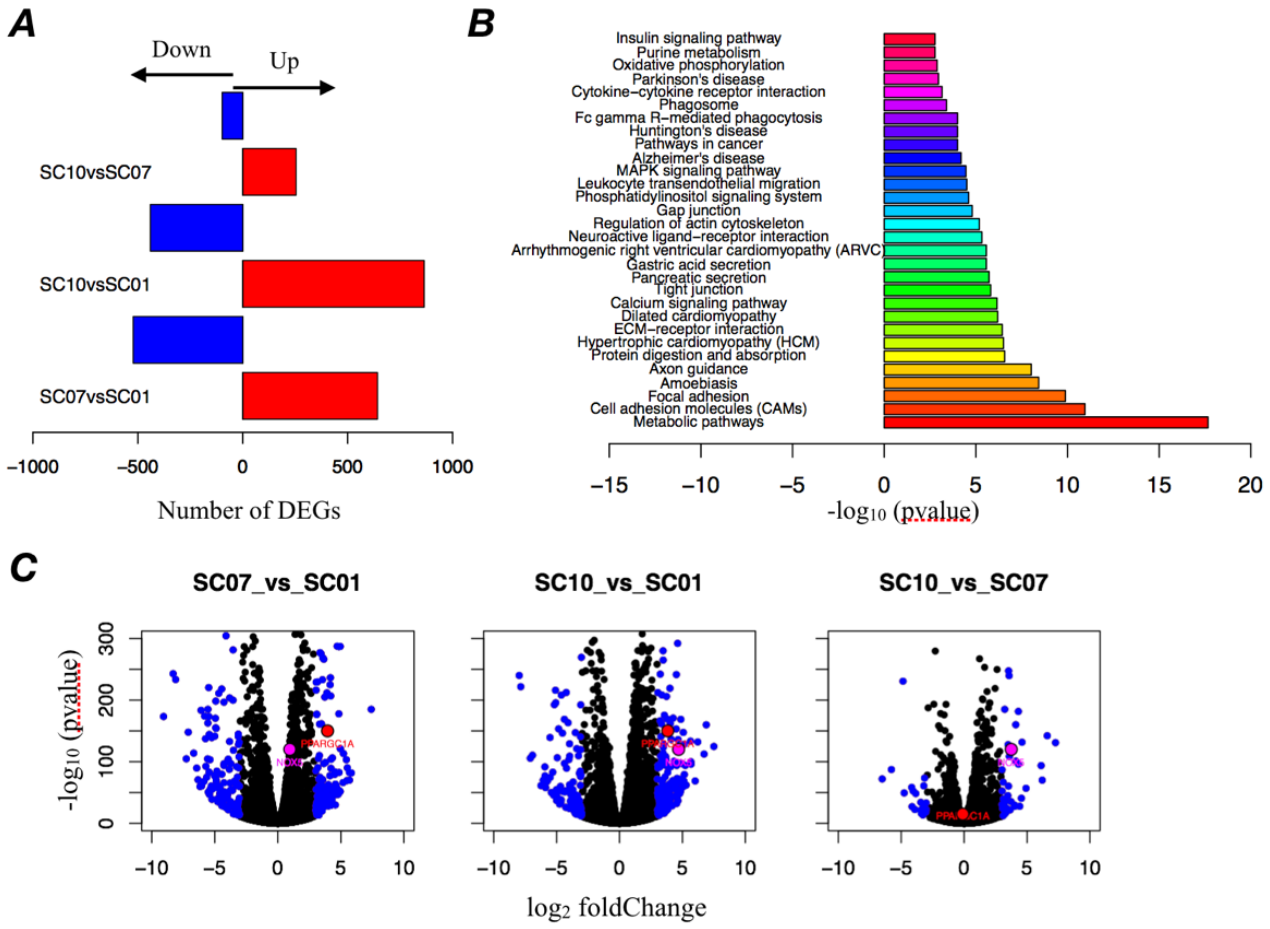

Figure 5.2: RNASeq analysis identifies *NOX5* and *PGC1α* as potential molecular determinants of short-term response variability. (A) Number of differentially expressed genes (DEGS) from pairwise comparisons between sublines; red represents upregulated, blue represents downregulated genes. (B) Top KEGG pathway enriched in common sets of upregulated genes among sublines. $-\log_{10}$ of adjusted p-valued is plotted along x-axis. (C) Volcano plots of differentially expressed genes from pairwise comparisons between sublines. Blue genes represent differentially expressed genes with FDR <0.001 and log fold change of 3 or higher. Indicated in magenta is *NOX5* and indicated in red is *PGC1α*. $\log_2$ of fold change in expression is plotted along x-axis and $-\log_{10}$ of adjusted p-value is plotted along y-axis.

Combined expression of PGC1α and NOX5 correlates to BRAFi DIP rates

We next probed the expression of *NOX5* and *PGC1α* in more detail in six of our isogenic sublines using quantitative PCR (qPCR). We observed heterogeneous expression of *NOX5* among clonal sublines, with SC10 having the highest and SC01 with the least expression. *NOX5* expression showed strong correlation (Corr: 0.754) with sensitivity of clonal sublines to *BRAF*-inhibition (Figure 5.3a). Similarly, we probed the expression of *PGC1α* among six of SKMEL5 sublines and observed heterogeneity in its expression among sublines (Fig. 3D). In contrast to *NOX5*, *PGC1α* expression showed moderate correlation (Corr: 0.526) with the DIP rates of clonal sublines (Figure 5.3b). Based on the results from volcano plots, we next wondered whether the combination of both *NOX5* and *PGC1α* expression improves the correlation to drug sensitivity. Indeed, we observed that a linear combination of *NOX5* and *PGC1α* expression showed best correlation (Corr: 0.824) to DIP rates among sublines, much higher than expression of *NOX5* (Corr: 0.754) or *PGC1α* (Corr: 0.526) alone (Figure 5.3c). In other words, higher the combined expression of *NOX5* and *PGC1α* in *BRAF*-mutated melanoma cell, the less sensitive the sublines are to *BRAF*i and vice-versa (Figure 5.3c).

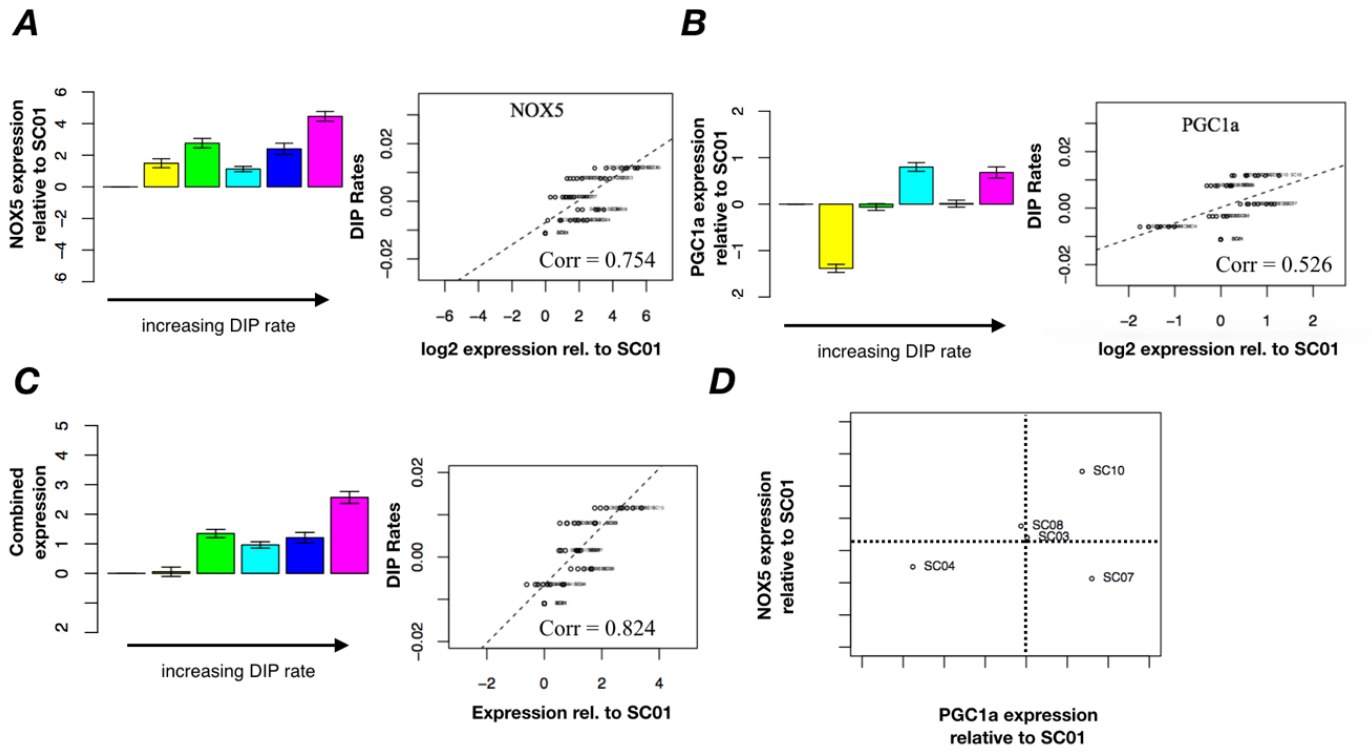

Figure 5.3: Combined expression of *NOX5* and *PGC1α* correlates with *BRAF*i DIP rates. (A) (left) Expression of *NOX5* in sublines relative to its expression in SC01; (right) Correlation of *NOX5* expression and DIP rates in SKMEL5 sublines. (B) (left) Expression of *PGC1α* in sublines relative to its expression in SC01; (right) Correlation of *PGC1α* expression and DIP rates in SKMEL5 sublines. (C) (left) Combined expression of *NOX5* and *PGC1α* in sublines relative to SC01; (right) Correlation of combined *NOX5* and *PGC1α* expression and DIP rates in SKMEL5 sublines. In all (A), (B) and (C), reported are the correlation coefficients from Pearson Correlation. Sublines are placed in order of their increasing DIP rates, from left to right. (D) Sublines are placed in 2D landscape based on expression of *NOX5* and *PGC1α*. All expressions reported are relative to SC01.

Additionally, examining the expression of both *NOX5* and *PGC1α* distinguishes sublines and categorizes them based on their *BRAF*i sensitivity quantified in terms of DIP rates (Figure 5.3d). Furthermore, to examine how the expression of these two genes (*NOX5* and *PGC1α*) vary among *BRAF*-mutated melanoma cell lines, we probed five *BRAF*-mutated melanoma cells: sensitive (WM88 and WM164), stable (A375) and insensitive (WM115 and A2058), selected based on their *BRAF*i sensitivities. We observed that *NOX5* but not *PGC1α* expression showed strong correlation (Corr: 0.92 vs Corr: 0.28) to *BRAF*i DIP rates. Similar to single-cell derived isogenic sublines, combined expression of *NOX5* and *PGC1α* showed best

correlation (Corr: 0.94) to *BRAF*i sensitivities among cell lines. Thus, these results suggest that cumulative expression of *NOX5* and *PGC1α* correlates with sensitivities of melanoma cell lines including isogenic sublines to *BRAF*i.

NADPH Oxidase (NOX) inhibition synergizes with BRAF-inhibition in BRAF-mutated melanoma cells

Because our data suggest that combined *NOX5* and *PGC1α* expression correlates with the sensitivity of melanoma cells to *BRAF*-inhibition, we evaluated the possibilities of combination therapies. We examined how the expressions of these two genes (*NOX5* and *PGC1α*) differ in normal skin compared to tumor skin tissues to examine whether targeting these genes in tumor is feasible. We observed that *NOX5* expression is significantly higher in tumor skin tissues compared to normal tissues, whereas *PGC1α* expression was higher in normal tissues (Figure 5.4). Since *PGC1α* expression is higher in normal tissues and therapeutic targeting of mitochondria is challenging [186,238], we evaluated the effects of *NOX* inhibitors in combination with *BRAF*i. For this, we tested three different *NOX* inhibitors (DPI, Apocynin and GKT137831).

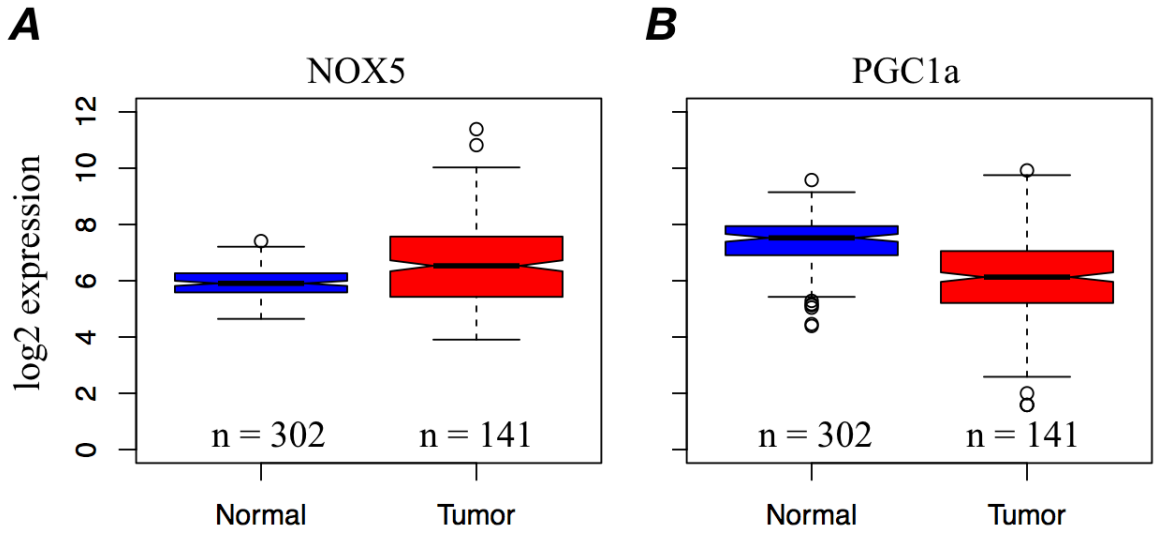

Figure 5.4: *NOX5* mRNA expression is higher in skin tumor compared to normal skin but not *PGC1α* expression. (A) *NOX5* mRNA expression levels were assessed in normal and cancer tissues of skin, (B) *PGC1α* mRNA expression levels were assessed in normal and cancer tissues of skin; both expression data retrieved from the Gene Expression Database of Normal and Tumor Tissues (GENT) database. Both expressions were significant, $p < 0.001$.

We examined the effects of this combination in cell lines that have higher expression of *NOX5* in our panel, including one isogenic sublines: SC10 and A2058. Interestingly, these two are also the cells with positive DIP rates under *BRAF*-inhibition (CHAPTER 3). While NADPH Oxidase (*NOX*) inhibitors exhibited concentration-dependent anti-proliferative effects, their combination with *BRAF*-inhibitor, PLX4720 enhanced the effects of *BRAF*i. In all three *NOX*-inhibitors used, we observed that the *NOX*-inhibition synergized with *BRAF*-inhibition and enhanced the anti-proliferative effects of *BRAF*-inhibition (Figure 5.5a, b). Since *NOX*-inhibitors we used are not only specific to *NOX5*, we examined whether *NOX5* knockdown enhances the effects of *BRAF*i in melanoma cells.

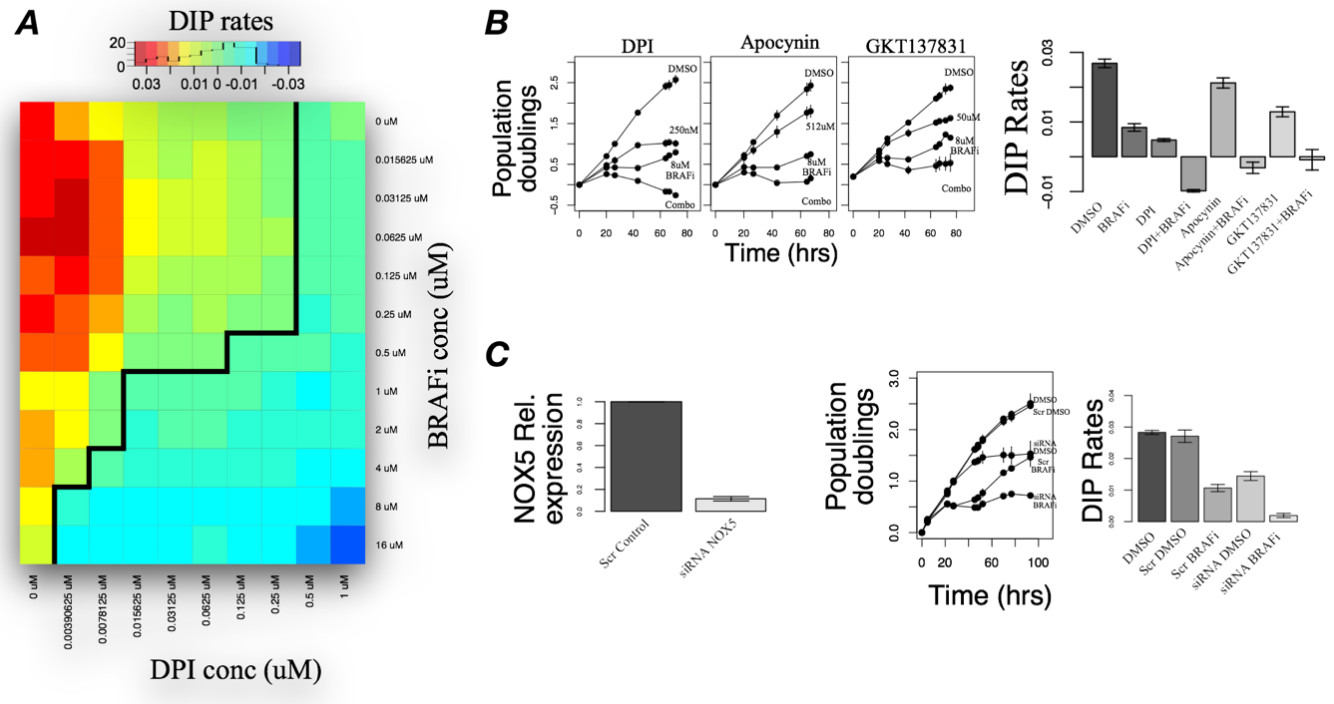

Figure 5.5: NADPH Oxidase (*NOX*) inhibition synergizes with *BRAF*-inhibition. (A) Heat map of DIP rates in various concentrations of DPI (*NOX*i) and PLX4720 (*BRAF*i). Black solid line separates drug-effects with positive DIP rates (top left) from negative DIP rates (bottom right). (B) (left) Population growth curves (log_2 normalized) for SC10 in three *NOX*i (DPI, Apocynin, and GKT137831) and *BRAF*i (PLX4720) and their combination; (right) DIP rates quantified from population growth curves shown for DMSO control, *BRAF*i, three *NOX*i and their combination with *BRAF*i. (C) (left) qPCR Quantification of NOX5 transcript expression in siRNA-mediated *NOX5* knockdown compared to Scrambled control. (right) Population growth curves (log_2 normalized) for SC10 in either DMSO, Scrambled control, siRNA, *BRAF*i and *BRAF*i+siRNA; Quantified DIP rates in corresponding conditions. In both (B) and (C) concentration of PLX4720 used was 8 µM.

For this, we used siRNA-mediated approach to knock down *NOX5* and validated the knockdown by qPCR. We observed more than 80% knockdown of *NOX5* and found that knockdown significantly slowed proliferation rates of cells compared to scrambled control (Figure 5.5c), consistent with previous studies that demonstrate the role of *NOX5* in supporting cell proliferation and growth in different cancers including melanoma [239–241]. Consistent with our drug combination studies, we our results show that siRNA-mediated knockdown enhanced the effects of *BRAF*i (Figure 5.5c). Similar results were observed for both drug combination and *NOX5* knockdown in A2058 cells (Figure 5.6). These results suggest,

therefore that NADPH Oxidase (*NOX*) inhibition, in combination with *BRAF*i, enhances the effects of anti-proliferative effects of *BRAF*-inhibition and may provide optimal outcomes in treatment of *BRAF*-mutated melanoma.

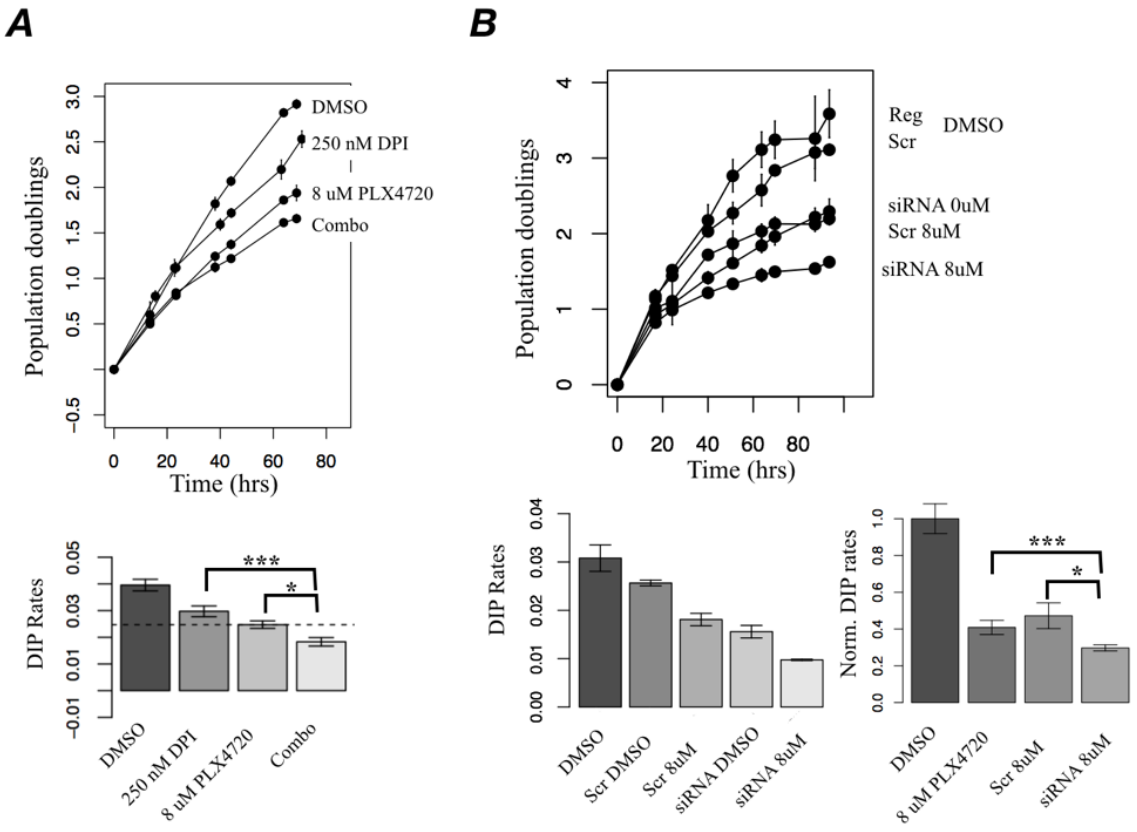

Figure 5.6: *NOX*-inhibition enhances the anti-proliferative effects of *BRAF*-inhibition. (A) (top) Population growth curves (log_2 normalized) for A2058 in either DPI (250 nM) or *BRAF*i (8 μM), or combination; (bottom) DIP rates quantified for corresponding conditions for respective growth curves. (B) (top) Population growth curves (log2 normalized) for A2058 in either DMSO, Scrambled control, siRNA, *BRAF*i and *BRAF*i+siRNA; (bottom) Quantified absolute DIP rates or normalized DIP rates (normalized to the control in respective controls) in corresponding conditions. * denotes $p < 0.05$ and *** denotes $p < 0.001$.

High NOX5 expression correlates with poor clinical outcome

To directly investigate *NOX5* expression and its correlation to patient treatment outcome, we analyzed three published papers [75,107,236] for which gene expression of drug-naïve patient samples and their clinical outcomes data were available. For this analysis, we

selected patients who underwent either *BRAF*i monotherapy or *BRAF*i combination with *MEK*i. We grouped clinical outcomes into two categories: Responders (includes complete and partial response) and Non-Responders (includes stable and progressive disease) using Response Evaluation Criteria in Solid Tumors (RECIST) categories reported in the papers. We observed that *NOX5* expression was higher in patients whose tumors under treatment were classified as Non-Responders (n = 28) than in patients whose tumors responded (n = 13) (t-test, p = 0.004). Although there is some overlap in *NOX5* expression between two groups, *NOX5* expression is significantly higher in Non-Responders than in Responders (Figure 5.7), suggesting the role of *NOX5* in limiting the therapeutic efficacy of MAPK-inhibitors. Overall, our analysis reveals that high *NOX5* expression correlate with poor clinical outcome in *BRAF*-mutated melanoma patients treated with MAPK-inhibitors. In other words, these results indicate that *NOX5* expression could identify *BRAF*-mutated melanoma patients that are less likely to respond to conventional *BRAF*-inhibition or combinational approaches that target MAPK pathway.

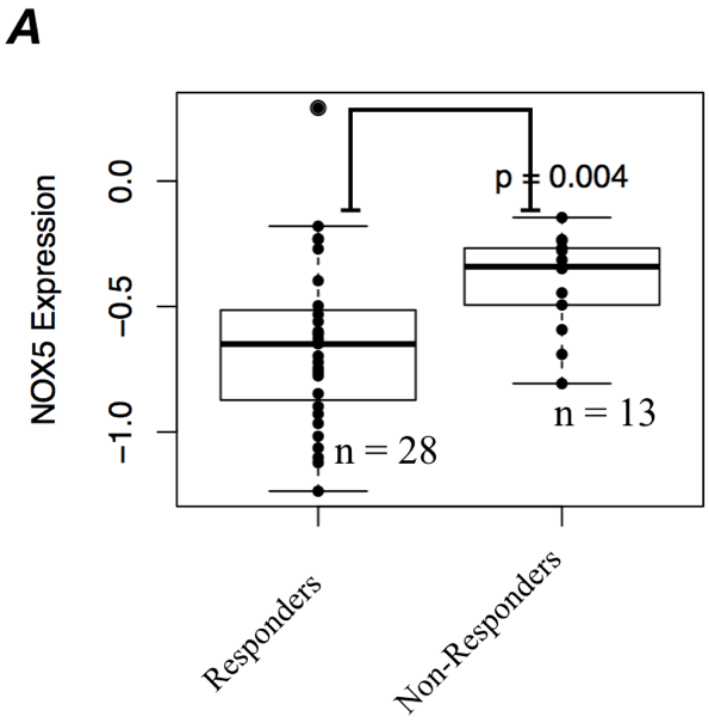

Figure 5.7: *NOX5* expression correlates with treatment outcome. Gene expression values from drug-naïve patient samples were obtained from three published reports and quantile normalized before comparison. Samples were placed in either Responders or Non-Responders category based on RECIST criteria reported in those papers. Responders included partial and complete response (PR, CR); and Non-Responders included stable and progressive disease (SD, SD). Two-sided t-test was performed for statistical comparison.

Expressions of NOX5 and PGC1α in melanoma cells correlate to glycolytic reserve and mitochondrial respiration respectively

To examine the metabolic roles of *NOX5* and *PGC1α* in melanoma cells, we quantified and measured extracellular acidification rate (ECAR) and oxygen consumption rate (OCR) in *BRAF*-mutated melanoma cells including isogenic sublines using Seahorse flux analyzer. From the metabolic parameters extracted from Seahorse assays, we observed that glycolytic reserve shows a strong correlation (Corr: 0.776) with *NOX5* expression in the melanoma cells we tested (Figure 5.8a). Given the recognized roles of NOXs in regulating redox signaling, these results are interesting, however, are in agreement with recent reports that have implicated the novel roles of NOXs in supporting aerobic glycolysis in cancer cells with

compromised mitochondria [242]. Not surprisingly, we also observed that cells with higher glycolytic reserve were mostly insensitive to *BRAF*-inhibition. We speculate that higher glycolytic reserve due to an elevated *NOX5* expression helps *BRAF*-mutated melanoma cells survive an initial *BRAF*-inhibition. Likewise, *PGC1α* expression showed moderate correlation (Corr: 0.638) with differences in mitochondrial function in melanoma cells quantified in terms of oxygen consumption rate (OCR) (Figure 5.8b). This is not surprising because induction of *PGC1α* has been shown to limit therapeutic efficacy of *BRAF*i in melanoma cells by redirecting metabolic program to mitochondrial respiration [185,186,208]. Because enhanced *NOX5* expression drives glucose utilization and *PGC1α* expression regulates mitochondrial respiration, collectively, our results suggest that *BRAF*-mutated melanoma cells may occupy distinct metabolic states defined by the combined expression of *NOX5* and *PGC1α*. We postulate that these expressions, which define how robust different metabolic programs are in melanoma cells, explain an initial drug response variability in *BRAF*-mutated melanoma cells.

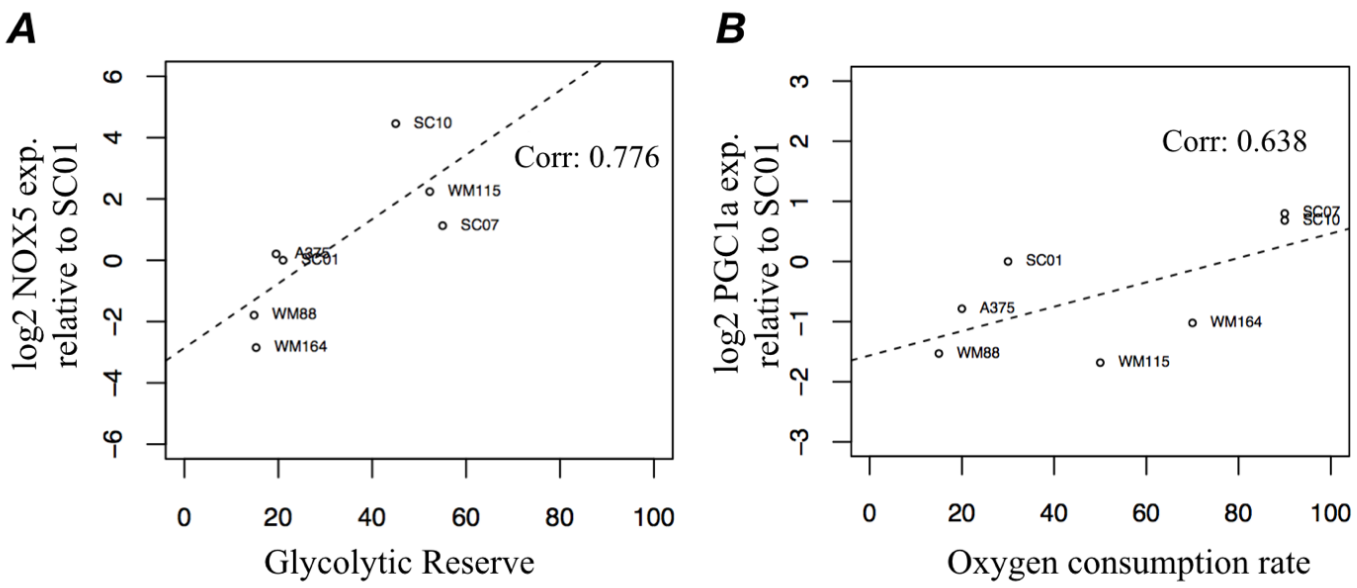

Figure 5.8: *NOX5* and *PGC1α* expression define metabolic states of melanoma cells. (A) Correlation between expression of *NOX5* in *BRAF*-mutated melanoma cells including isogenic sublines relative to SC01 and glycolytic reserve, indicative of glycolytic functions quantified from Seahorse assays. Pearson correlation coefficient: 0.776, p-value <0.05. (B) Correlation between expression of *PGC1α* in *BRAF*-mutated melanoma cells including isogenic sublines relative to SC01 and oxygen consumption rate, indicative of mitochondrial respiration quantified from Seahorse assays. Pearson correlation coefficient: 0.638, p-value not significant.

Table 5.1: Primers used for RT-qPCR.

Gene	Forward Primer	Reverse Primer
NOX5	GGCTCAAGTCCTACCACTGGA	GAACCGTGTACCCAGCCAAT
PGC1α	TGCCCTGGATTGTTGACATGA	TTTGTCAGGCTGGGGGTAGG
HPRT	TGCTCGAGATGTGATGAAGGAG	TGATGTAATCCAGCAGGTCAGC

Discussion

Here, we report that expressions of NADPH Oxidase 5 (*NOX5*) and *PGC1α* define distinct metabolic states in *BRAF*-mutated melanoma cells that correlate with their sensitivities to *BRAF*i. Extending our previous studies that show clonal heterogeneity within cell population [92,211], we utilized single-cell derived clonal lineages that presumably start from the same specific cancer genome (i.e. parental line) and identified *NOX5* and *PGC1α* as key regulators

of non-mutational drug response variability within *BRAF*-mutated melanoma cells. By characterizing metabolic features of cells, our study, therefore, links the metabolic state of melanoma cells, defined with respect to their ability to utilize glucose and mitochondrial respiration, to intrinsic drug insensitivity to *BRAF*i. Links between metabolism and therapeutic responses in *BRAF*-mutated melanoma cells have been previously implicated [182,184–186,211]; however, our results provide an overarching framework on how an overall metabolic phenotype of melanoma cells affects their sensitivities to *BRAF*i. Because targeting of mitochondrial respiration is challenging, we show that NADPH oxidase inhibition sensitizes *BRAF*-mutated melanoma cells to enhance anti-proliferative effects of *BRAF*-inhibition. Additionally, analyzing drug-naïve patient samples and their gene expression, we show that *NOX5* expression correlates with poor clinical outcome. Taken together, our results indicate that *NOX5* expression, which correlate with higher glycolytic reserve, protects melanoma cells from the effects of *BRAF*-inhibition and may represent a potential combination therapeutic opportunity in *BRAF*-mutated melanomas.

Both mutational and non-mutational factors have been implicated to contribute to drug response differences [73,105]. We have previously reported that cancer cells exhibit drug response variability, with clonal subpopulations responding differently to perturbations [92]. We and others have shown that drug-treated cells demonstrate the similar initial proliferation dynamics when re-challenged with drug after a brief drug holiday [99,101,211]. Collectively, these observations suggest that non-genomic factors, possibly at the transcriptional level, might regulate differential drug sensitivities within a cell population. To determine molecular determinants for short-term response variability, we utilized single-cell derived SKMEL5 sublines and performed RNASeq analysis. Single-cell derived sublines are ideal for examining non-genetic sources of response variability because they presumably start from the same

specific cancer genome, thus minimizing any genetic variation. Three representative sublines were selected based on short-term drug response to represent the wide range of response behaviors observed at the clonal level. Pathway enrichment analysis on differentially expressed genes (DEGs) highlighted the drug-naïve metabolic differences among the sublines. We identified *PGC1α*, a mitochondrial biogenesis transcriptional co-activator and *NOX5* as potentially important determinants of sensitivities to *BRAF*i, both of which are plausible targets because of their functional convergence at mitochondria. Our results are consistent with recent studies that have implicated *PGC1α* not only in defining melanomas with increased mitochondrial capacity [185], but also in modulating metabolic switch that help *BRAF*-mutated melanoma cells survive *BRAF*-inhibition [186,208]. Similarly, accumulating evidence indicate novel roles of *NOX*s in cancer cell metabolism [242,243]. Several other studies have revealed critical roles of *NOX*s in maintaining cell survival and proliferation [239–241,244,245]. Consistent with these reports, we established metabolic link between expressions of *NOX5* and *PGC1α* with respect to glucose utilization and mitochondrial respiration. We extended our findings from RNASeq analysis to probe the expressions of these genes in other single-cell-derived sublines and other *BRAF*-mutated melanoma cell lines and observed that their combined expression shows strong correlation to DIP rates in *BRAF*i, higher than correlation to expressions of single genes respectively.

Since the combined expression of *NOX5* and *PGC1α* was higher in cells with positive DIP rates, we reasoned whether therapeutic targeting of these targets sensitizes melanoma cells to *BRAF*-inhibition. Since targeting of mitochondria is challenging, we explored the possibility of inhibiting *NOX5* expression and examining the effects in combination with *BRAF*i. *NOX5* could be possible therapeutic target since a substantial overexpression of *NOX5* in several cancers including melanoma, prostate, ovarian has recently been reported [244,245].

Interestingly, *NOX* inhibition sensitized SC10 and A2058 cells and enhanced the anti-proliferative effects of *BRAF*i. Consistent with chemical inhibition, siRNA mediated knock down of *NOX5* also enhanced the effects of *BRAF*i in both SC10 and A2058, cells that have positive DIP rates in *BRAF*i. In addition, we also observed that *NOX5* knockdown alone also slowed cell proliferation rates, consistent with recent studies that highlight the roles of *NOX5* in controlling cell proliferation in different cancer cell types including melanoma[239–241,244,245]. Since the primary function of NADPH oxidases in cells is the production of intracellular Reactive Oxygen Species (ROS), we examined how the intracellular ROS levels changed in different conditions. Intriguingly, our preliminary data shows siRNA mediated knockdown of *NOX5* did not alter the ROS production in cells (Appendix 3b)—suggesting other sources might also contribute to intracellular ROS in melanoma cells. It is also possible that there is compensatory activation of other *NOX* informs when *NOX5* is inhibited. Intracellular ROS levels were also higher in combination of *NOX*i and *BRAF*i compared to *NOX*i alone but not different from *BRAF*i alone, suggesting that an increased oxidative stress in melanoma cells is due to *BRAF*i. Similarly, intensity of ROS inversely correlated with DIP rates in different treatment conditions (Appendix 3a), consistent with reports that suggest below a sub-toxic level, ROS can act as intracellular signals, while too much ROS is deleterious to cells [246]. These results, taken together, show that combination of *NOX*-inhibitors with *BRAF*i maximizes the anti-proliferative effects of *BRAF*-inhibition in *BRAF*-mutated melanoma cells. While further investigation is warranted, our preliminary studies also indicate that the effects of *NOX*-inhibition in melanoma cells are not due to its redox related signaling.

Mechanistically, we observed glycolytic reserve in melanoma cells strongly correlated with their *NOX5* expression and also with drug-induced proliferation (DIP) rates in *BRAF*i. Similarly, *PGC1α* expression strongly correlated with abilities of cells to utilize mitochondrial

respiration. Based on these results and earlier reports, we hypothesize that higher glycolytic reserve due to an elevated *NOX5* expression helps *BRAF*-mutated melanoma cells survive an initial *BRAF*-inhibition, while *PGC1α* expression reprograms cellular metabolism to support cells adapting in drug. Although needs to be validated, we speculate that higher glycolytic reserve in *NOX5*-high cells could be due to higher accumulation of intracellular NAD+, a by-product of NADPH oxidation. Furthermore, our clinical analysis on gene expression data from treatment-naïve patient samples undergoing MAPK-pathway inhibition (either *BRAF*i or *BRAF*i+*MEK*i) show significantly higher *NOX5* expression in non-responders compared to responders. This is consistent with our hypothesis that enhanced *NOX5* expression provides an initial survival advantage in *BRAF*-mutated melanoma cells, and also opens up clinical applications, with potential of using *NOX5* expression as a biomarker in identifying *BRAF*-mutated melanoma patients that are less likely to respond to MAPK pathway inhibition. Collectively, our results indicate that therapeutic approaches that reduce or suppress *NOX5*-high cell populations could thus maximize therapeutic efficacy of *BRAF*i or delay tumor recurrence. Our studies may represent a potential combination therapy that would maximize cell killing in *BRAF*-mutated melanoma cells. Future studies should focus, therefore, on identifying the mechanistic insights on the role of *NOX5* in melanoma cells and how the combination enhances the anti-proliferative effects in cells.

CHAPTER 6

CONCLUSIONS AND FUTURE DIRECTIONS

Conclusions

Despite significant progress in the treatment of melanoma in recent years, a majority of melanoma cases is still largely incurable. Even in patients with similar genomic classification (i.e. *BRAF*^{V600} mutations), treatment responses are highly variable and often unpredictable. Several intrinsic or adaptive resistance mechanisms have been proposed to describe tumor recurrence in melanoma. However, still a large portion of recurrent tumors remain unexplained. The premise of this work is to understand what happens to tumors especially during early phase of drug response leading up to resistance. This requires detailed understanding of drug-response variability that exists within melanoma tumors, and the quantification and characterization of the response dynamics under drug perturbations.

To this end, we used an integrative approach and combined both experimentation and mathematical modeling to understand complex drug response behaviors in *BRAF*-mutated melanoma cells. First part of this work focused on describing a novel metric and a high-throughput method to quantify drug response dynamics and its heterogeneity (CHAPTER 2). Utilizing Drug-Induced Proliferation (DIP) rates to measure drug sensitivity among cells, we addressed key problems that plague the traditional end-point assays (i.e. IC_{50})—biases due to exponential growth, differences due to drug effect stabilization, and inherent heterogeneity within cell population. DIP rate provides an unbiased metric to evaluate the anti-proliferative effects of drugs and also better resolves differences in drug sensitivity among cancer cells as opposed to metrics resulting from traditional end-point assays (i.e. IC_{50}, EC_{50} etc.) (Figure 6.1).

Although the practice of using growth rates to measure sensitivity to drugs among cancer cells is at its infancy [92,150,159,211], it will likely become a *de facto* metric to assess drug potencies, efficacies and responses in the future. It will most likely also facilitate identification of molecular signature of drug-response variability that existing drug-sensitivity metrics would otherwise miss out (Figure 6.2). For instance, we observed that expression of *NOX5* in *BRAF*-mutated melanoma cells shows strong correlation to their DIP rates, and not with IC_{50} values reported in CCLE database. This result laid the foundation for CHAPTER 5, where we present experimental evidence to highlight the application of *NOX5* as both biomarker and potential drug combination in *BRAF*-mutated melanomas.

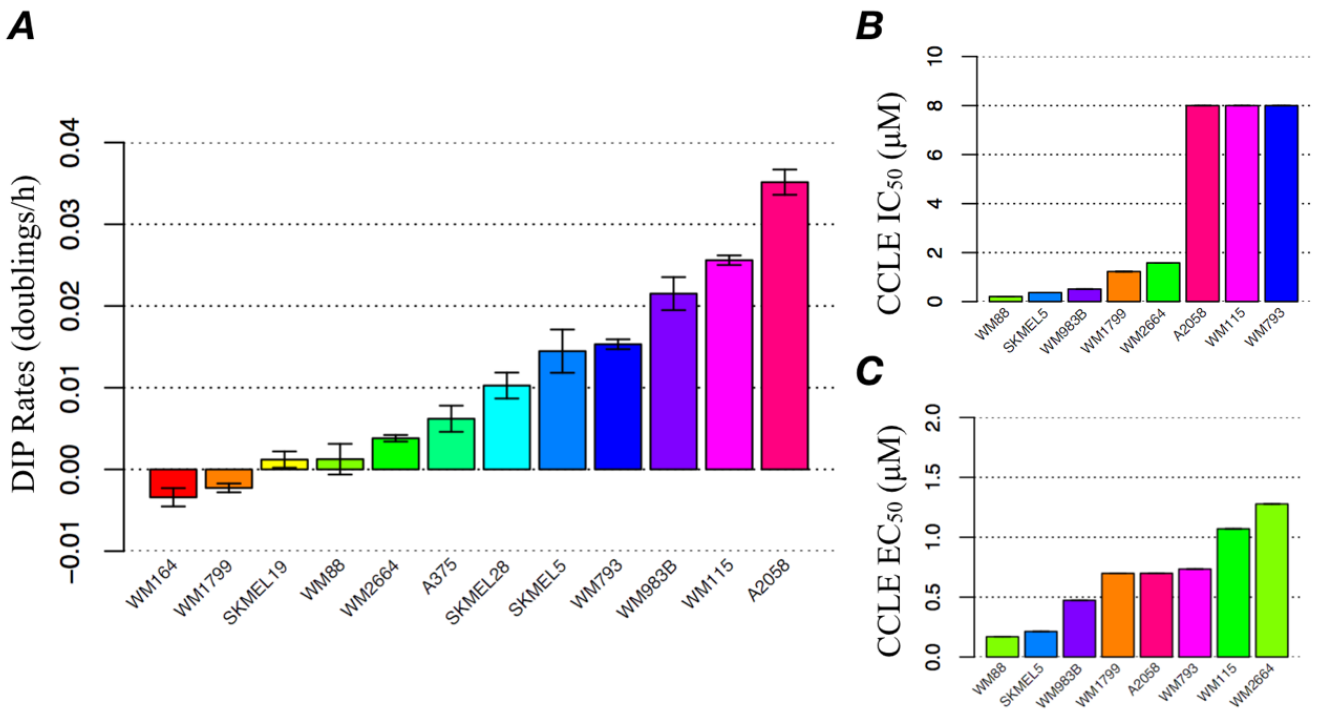

Figure 6.1: Drug-Induced Proliferation (DIP) rate is better metric to quantify drug sensitivity in cancer cells. *BRAF*-mutated melanoma cell lines ranked in order of: (A) quantified DIP rates in 8 μM PLX4720. (B) IC_{50} values (C) EC_{50} values; both IC_{50} and EC_{50} values are extracted from database maintained by Cancer Cell Line Encyclopedia (CCLE).

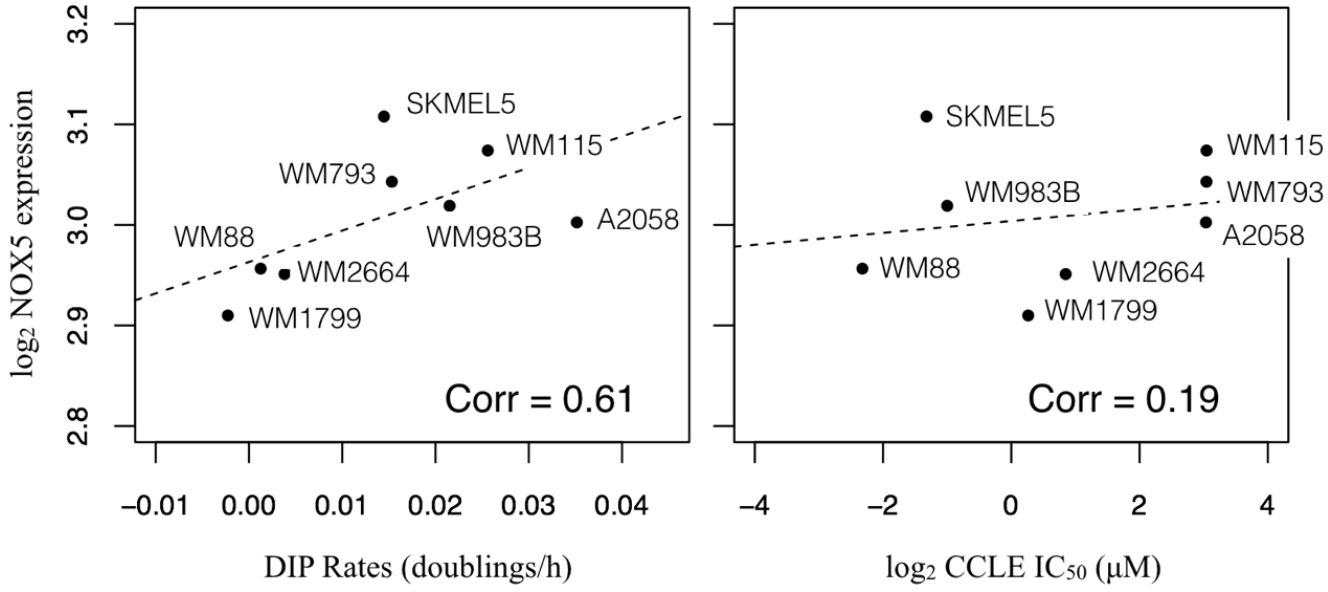

Figure 6.2: *NOX5* expression in CCLE Data correlates well with DIP rates and not with traditional IC_{50}. (left) *NOX5* expression extracted from CCLE database for *BRAF*-mutated melanoma cell lines for which we had quantified DIP rates, correlated with either their DIP rates (Corr: 0.61) or IC_{50} values reported in CCLE (Corr: 0.19). Correlation coefficient obtained from Pearson Correlation.

With the proposed DIP rate metric, we sought to determine the basis for drug-response variability among *BRAF*-mutated melanomas and established a mechanistic link between therapeutic response and cellular metabolism (CHAPTER 3). We identified that dependence on glycolysis sensitizes cells to *BRAF*-inhibition. Specifically, melanoma cells with higher glycolytic reserve were found to be less sensitive to *BRAF*i. In later chapters, we probed in more detail for molecular determinants of such metabolic differences in melanoma cells and provide a unifying framework to relate metabolic phenotype and therapeutic response.

Because there is a lot of inter-cell line variation, we isolated single-cell derived sublines to probe for molecular determinants of short-term drug response variability at the clonal level within a cell population (CHAPTER 4 and CHAPTER 5). Single-cell derived sublines originate from presumably the same cancer genome and are about as genetically similar as it can

possibly exist, thus providing an ideal experimental system to probe non-genetic sources of response variability. In CHAPTER 4, we provide a theoretical framework to account for short-term drug response sensitivity within the framework of multi-state epigenetic landscape and their relative occupancies. Our central hypothesis is that drug treatment alters the quasi-potential landscape and cell population re-equilibrate over new drug-modified epigenetic landscape, result of the process giving rise to differential short-term response dynamics in melanoma cell lines. Interestingly, the major findings of this work is that multiple melanoma cell lines under *BRAF*i treatment, including isogenic sublines converge into a non-quiescent 'idling' state of balanced death and division (~near-zero proliferation rate) which constitutes the final, equilibrated state.

The idling state represents a new dynamic equilibrium that is the property of the cell population, and not of individual cells. We show that idling state is drug-induced and reversible and is not necessarily multi-drug resistant—consistent with non-mutational drug tolerance reported in prior studies [105,212,213]. However, drug tolerant cells were reported to be quiescent [106] or slow dividers [212,214,215]. In contrast, by single-cell tracking, we show that idling cells continue to divide and die at moderate but balanced rates, leading to near zero-net-proliferation. To our knowledge, such drug-response phenotype has not been previously reported. Idling state may effectively model the clinical situation when residual disease persists for varying time-intervals prior to disease progression. Continued cell cycle progression without cell population expansion (i.e. idling state) make cancer cells more prone to accumulate deleterious mutations and, hence, a more fertile ground for acquired resistance than quiescent [101,106,219,220] or senescent cells [221].

The differential sensitivity of melanoma cells has remained puzzling over the years. Herein, we provide a unifying view and theoretical framework for short- and long-term

melanoma sensitivity to targeted drugs within the mathematical concepts of phenotypic landscape and state transitions (Figure 6.3)—which relate to the combined effects of clonal competitions and phenotype switching in biological terms. Apparent differences seen across cell lines and extreme variability in the length of response and durability or lack of durability of clinical response in patients can be reconciled in terms of the variations in drug-modified landscape topography unique to a melanoma tumor. We propose targeted landscaping, i.e. therapeutic approaches that rationally modify the epigenetic landscape in order to suppress or eliminate the non-quiescent reservoir of idling cancer cells, could delay, perhaps indefinitely, tumor recurrence.

In CHAPTER 5, through molecular and functional characterization (RNASeq analysis, PCR and Seahorse metabolic assays), we identified metabolic differences among isogenic sublines, and explored the possibility of defining distinct metabolic state that melanoma cells occupy. We constructed a two-dimensional landscape based on the expressions of *NOX5* and *PGC1α* in melanoma cells that correlate to ability of cells to utilize glucose and mitochondrial respiration respectively. The molecular characterization of melanoma cells and their correlation to drug sensitivity further substantiates the theoretical epigenetic landscape proposed in CHAPTER 4—which assumes the co-existence of multiple phenotypic states even within the same genome. Although the role of metabolism in differential therapeutic response has been extensively discussed [182–186,208,211], for the first time, we provide a general framework which combines the role of both glycolysis and oxidative phosphorylation to the response variability and dynamics in *BRAF*-mutated melanoma cells (Figure 6.4). While these two metabolic pathways are described in the context of *BRAF*i resistance to be mutually exclusive, we provide an explanation on how melanoma cells utilize two critical energy producing pathways to bypass *BRAF*-inhibition. With identification of *NOX5* and *PGC1α*, we provide

molecular links to differential metabolic profiles and ultimately therapeutic response variability in *BRAF*-mutated melanoma cells. We show that *NOX5* expression correlate to poor clinical outcome for *BRAF*-mutated melanoma patients treated with MAPK-pathway inhibitors. We believe that melanoma cells utilize glycolytic reserve to survive an initial exposure to *BRAF*i, and then reprogram their metabolism to favor oxidative phosphorylation upon continuous drug exposure. These findings might lead to the use of *NOX5* expression as a biomarker in identifying *BRAF*-mutated melanoma patients who are likely to respond to MAPK-pathway inhibition. In addition, *NOX5* could be a potential therapeutic target in combination with *BRAF*i to maximize the fraction of cell killing and increase treatment efficacy.

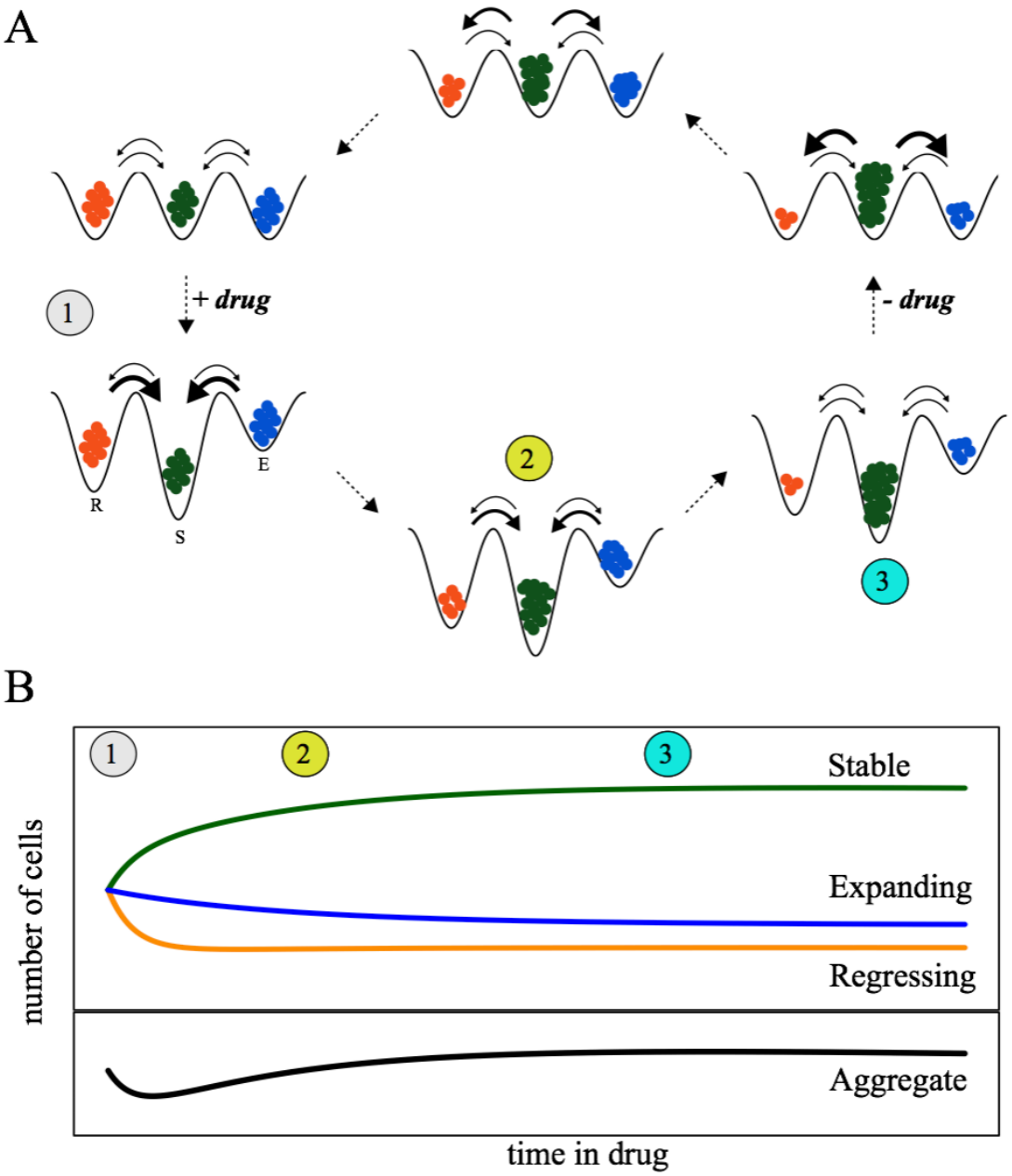

Figure 6.3: Drug-induced and drug-free population dynamics are explained as re-equilibrations over epigenetic landscapes. (a) A cartoon representation of a drug-addition/drug-removal cycle for a cancer cell population: (top-left) cells begin in complete growth medium and are in a dynamic equilibrium across basins of a drug-free epigenetic landscape; (top-left to bottom-left) exposure to drug modifies the landscape, taking the system out of equilibrium; (bottom-left to bottom-right) the population re-equilibrates over the new, drug-induced landscape by reducing cell proportions in the regressing (R) and expanding (E) basins and increasing the proportion in the stable (S) basin; (bottom-right) the idling state corresponds to the newly achieved dynamic equilibrium; (bottom-right to top-right) removal of drug reestablishes the drug-free epigenetic landscape and, again, takes the system out of equilibrium; (top-right to top-left) the population re-equilibrates over the drug-free landscape, returning the system to the original dynamic equilibrium. Arrow thicknesses represent relative transition rates at each stage of the re-equilibration process. (b) Clonal (top) and population-level (bottom) drug-response dynamics illustrating the connection to the different stages of the drug-induced re-equilibration process. Numbers and colors (orange, regressing; green, stable; blue, expanding) correspond to those in the cartoon schematic above.

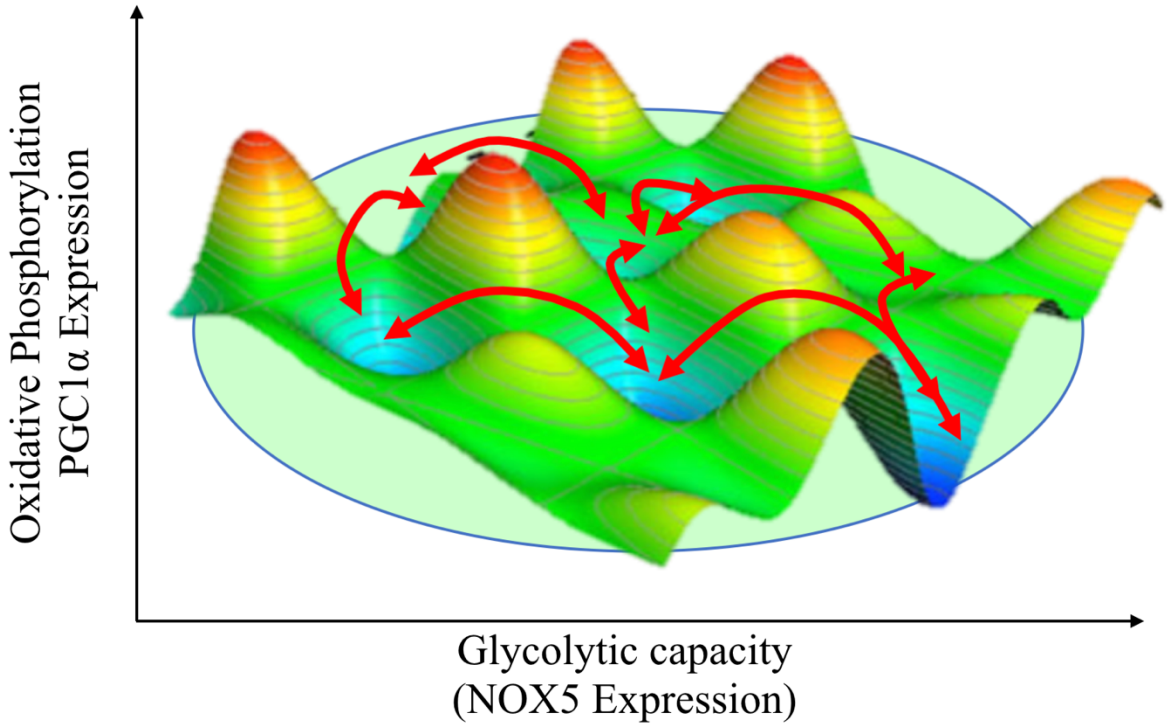

Figure 6.4: Metabolic 2-D landscape defined with respect to ability of cells to utilize glucose and mitochondrial respiration. Melanoma cells are hypothesized to occupy distinct metabolic state and undergo phenotypic state transitions under drug-treatment giving rise to differential short-term drug response.

Overall, the findings of this work add to the growing body of literature on the role of non-mutational sources of response variability and drug resistance in melanoma. The study contributes to our understanding of how seemingly identical melanoma cells might evade lethal drug exposure and ultimately lead to tumor recurrence. With drug response dynamics described in the context of isogenic quasi-potential landscape and phenotypic state transitions, our study is a significant departure from qualitative, mutation-centric thinking in cancer biology. Our quantitative approach integrating the cell-population, clonal and single-cell data captures the extent of cell-to-cell response variability while still explaining the cell population behavior. By linking phenotypic data with molecular signatures in a classical systems biology approach,

we identify novel regulators of initial drug response variation, which could lead to therapeutic combination for better clinical outcomes. Collectively, we provide an overarching framework to infer and quantify non-genetic clonal heterogeneity within cancer cell population, associate clonal drug sensitivity to molecular signals and link heterogeneity and dynamics to differential drug response outcomes. Through an appropriate combination of experimental and computational methods, in summary, we provide a powerful and a generalizable approach for analyzing response variability in cancer cells. We envision similar approaches could be applied in other systems beyond cancer.

Future Directions

Combination Therapy in BRAF-mutated Melanomas

One of the major findings of this work is the identification of *NOX5* as potential regulator of short-term drug response variability in *BRAF*-mutated melanomas. Recent studies suggest substantial *NOX5* overexpression in several human cancers including melanoma [244]—making it an attractive therapeutic target. Our *in vitro* data further corroborates the utility of targeting NADPH Oxidase in conjunction with *BRAF*i—as we show synergy in both potency and efficacy between *NOX*-inhibitors and *BRAF*i[*]. At the time of writing this dissertation, we are planning to carry out *in vivo* experiments with vemurafenib and GKT137831 in treatment-naïve *BRAF*-mutated melanoma PDXs and human melanoma cell lines in collaboration with Dr. Ann Richmond's Lab at Vanderbilt. Since *NOX5* is not expressed in the genome of rodents, it has significantly reduced our understanding of its involvement in the development and progression of cancer [244]. We will use both *NOX5*^{high} and *NOX5*^{low} human melanoma cell lines—from the panel of melanoma cell lines that we have at our disposal. Our use of patient-

[*] Synergy between NOX-inhibitors and BRAFi estimated in two terms: potency and efficacy using DIP rates. Manuscript detailing the mathematical basis for drug-synergy calculation and experimental evidence is currently in advanced stage to be submitted soon. (Meyer, C.M, Wooten, D.J. et. al.).

derived xenografts (PDXs) and human melanoma cells for *in vivo* studies will facilitate the examination on the role of *NOX*s in melanoma tumor maintenance, progression and intrinsic drug resistance. GKT137831 is a small molecule inhibitor of *NOX1/4/5* inhibitor, marketed by GenKyoTex SA, a biotechnology company located in France and has been in clinical trials Phase 2 for Type 2 Diabetes Mellitus with Diabetic Nephropathy (Clinical Trial# NCT02010242) and Primary Billiary Cirrhosis (Clinical Trial# NCT03226067). Four treatment groups (each n = 8) will be used for *in vivo* experiments: vehicle control, vemurafenib alone, GKT137831 alone, and vemurafenib + GKT137831 combination. Taken together, these experiments will provide a direct *in vivo* comparison to our *in vitro* results and further corroborate the benefits or lack of benefits of combination of *BRAF*i with *NOX*i in treatment of *BRAF*-mutated melanoma tumors.

Mechanistic Insight into Short-term Drug Response Variability

How does *NOX5* regulate glycolytic reserve in melanoma cells? Lu *et. al.* showed a critical role of NOXs in supporting increased glycolysis by generating NAD+, an important intermediate substrate for glycolysis [242]. Since we observed that enhanced NOX5 expression in our panel of melanoma cells correlated with higher glycolytic reserve, we hypothesize that increased glycolytic reserve in *NOX5*^{high} cells could be due to higher accumulation of NAD+. For this, the levels of NAD+ and its reduced form NADH could be examined in different cell lines. One could also examine how NAD+ levels change under *BRAF*i treatment. The role of NAD+ in *BRAF*i resistance is further supported by recent studies that indicate that *BRAF*i-resistant melanoma cells had higher NAD+ levels compared to sensitive cells [247]. The study points out higher expression of NAD+ biosynthetic enzyme nicotinamide phosphoribosyltransferase (*NAMPT*) in *BRAF*i resistant melanoma cells. To test whether *BRAF*i sensitivity could be enhanced by *NAMPT* inhibition, one could treat melanoma

cells with highly specific inhibitors of *NAMPT*, the rate-limiting enzyme of the NAD+ salvage pathway: FK866 and GMX1778. One should also examine whether the effects of *BRAF*i in sensitive melanoma cells (SC01, WM88 and WM164) can be rescued by supplementing additional NAD+ in the growth media. Supplementation could either be direct addition of NAD+ or nicotinamide mononucleotide (NMN), a precursor of NAD+, which bypasses NAMPT. To examine mechanistic roles of *NOX5* in maintaining high glycolytic reserve, one could test whether genetic knockdown or chemical inhibition of *NOX5* alters the glycolytic reserve in melanoma cells. Reciprocally, one could overexpress *NOX5* and examine how glycolytic reserve is altered.

Although our data suggest the effect of NOX5 inhibition in our melanoma panel is not due to levels of ROS (Appendix 3), it is very preliminary and warrants further investigation. It is possible that certain species of Reactive Oxygen Species (ROS) is modulated by differential activity of *NOX5*—as it is postulated to be involved in the production of superoxide (O_2^-). The use of ROS detection method could be improved, for instance distinguishing the subcellular compartment, as the dye we used stains all species of ROS, thereby, giving an incomplete information. It is also possible that there is compensatory activation of other isoforms of *NOX* when *NOX5* is inhibited, thus, maintaining a certain level of intracellular ROS. One could examine whether such compensatory mechanism exists in our system, by examining the levels of other isoforms of *NOX* when *NOX5* is inhibited. Antony et. al. demonstrated *NOX5*-generated ROS upregulates *HIF-1α* expression [245]. Specifically in cancer cells, *HIF-1α* induces increased activity of several glycolytic proteins including transporters (*GLUT1*, *GLUT3*) and enzymes [248]. In addition, *HIF-1α* may also modulate the mitochondrial respiration and oxygen consumption in cancer cells. It is possible that such mechanism could be at play in our panel of melanoma cells in their differential sensitivity to *BRAF*i.

Does mitochondrial phenotype correlate to differential short-term drug response? In recent years, there is considerable interest in evaluating the importance of oxidative phosphorylation in *BRAF*i resistance [105,182,185,208]. We have found *PGC1α* expression to be significantly different among single-cell-derived sublines at baseline. Consistent with earlier reports, our results confirm the differences in oxidative phosphorylation related genes among sublines (Figure 6.5). We also observed differences in mitochondrial physiology using MitoOrange and MitoGreen fluorescent probes. MitoGreen stains mitochondria of all live cells irrespective of mitochondrial membrane potential, while MitoOrange will only accumulate inside mitochondria with intact membrane potential. Although preliminary, we observed that SC01 to have consistently low mitochondrial mass compared to other sublines. Because mitochondria are dynamic organelles, constantly going through mitochondrial fission and fusion, one should evaluate further to determine whether fragmented, dysfunctional mitochondria predispose sensitive cells (i.e. SC01, WM88) for increased sensitivity to *BRAF*-inhibition. Similarly, one could examine whether knockdown/overexpression of *PGC1α* sensitizes or rescues our melanoma cells from the effects of *BRAF*-inhibition respectively.

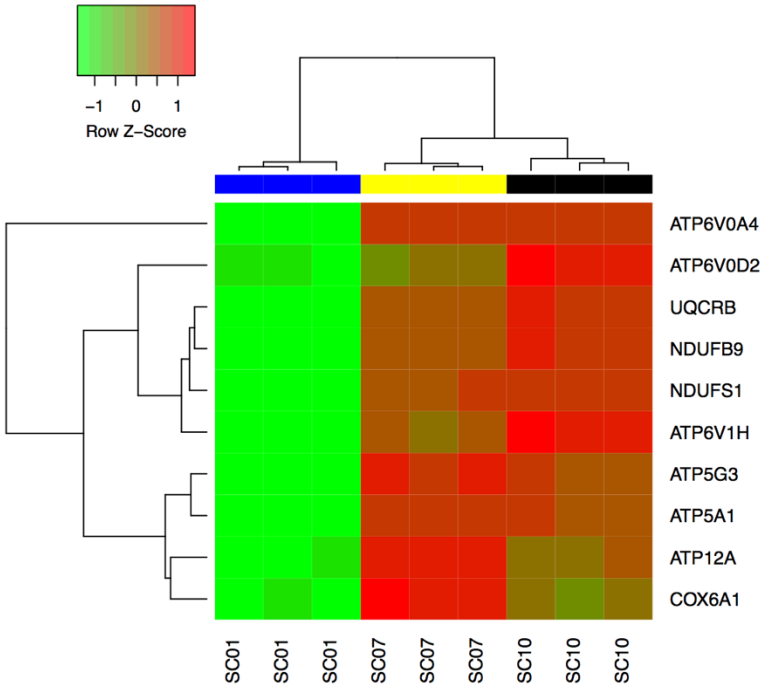

Figure 6.5: Heat map of differentially expressed genes related to oxidative phosphorylation among sublines. FDR of < 0.01 and fold-change of 2 is set to identify differentially expressed genes.

Molecular Mechanisms of Idling State

Idling state represents an interesting property of melanoma cell population under continuous *BRAF*i exposure. We speculate that residual disease observed in patients in clinic may comprise a significant number of idling cells, thus, determining the molecular determinants of the phenotypic landscape that idling cells occupy may lead to the development of novel therapies. The next obvious step to carry this project forward would to understand the molecular basis for the emergence of idling state in drug-treated *BRAF*-mutated melanoma cells. So far, we have investigated the changes in metabolic phenotype in cells under *BRAF*-inhibition. Surprisingly, we found that idling cells have reduced metabolic profiles (i.e. decrease in both oxygen consumption rate and glucose utilization) compared to their untreated counterparts. This is in contrast with other reports that suggest increased mitochondrial

respiration upon *BRAF*-inhibition due to induction of mitochondrial biogenesis and metabolic reprogramming to favor oxidative phosphorylation [186]. Since Haq *et. al*. evaluated the metabolic changes in melanoma cells treated with *BRAF*i within 96 hrs., we wondered whether idling state is representative of the changes seen in the short-term. For that, we examined the mRNA expression of *PGC1α* in SKMEL5 cells and its derivative clonal lineages. We observed a transient increase in the expression of *PGC1α* in all parental cell and sublines—particularly after 120 h, the induction of *PGC1α* under *BRAF*-inhibition plateaus (Figure 6.6).

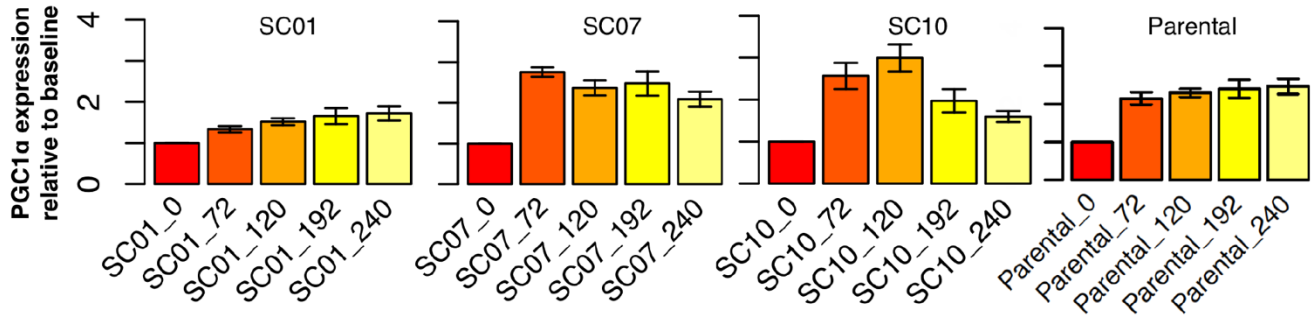

Figure 6.6: Induction of *PGC1α* upon *BRAF*-inhibition is transient and not sustained in idling cells. *PGC1α* expression normalized to its expression at time zero is plotted along y-axis, x-axis represents time lengths for drug exposure in hours. Error bar represents standard deviation from 3 technical replicates for each time point/cell line.

We also looked at other mitochondrial related genes to examine whether *BRAF*-inhibition induces mitochondrial biogenesis and its related genes. For that, we looked genes involved in oxidative phosphorylation and mitochondrial function in Subline SC07. The expressions of other oxphos-related genes exhibit similar trend as *PGC1α*—a transient induction and plateau effect. In some cases, (such as *ERRα*), there is no difference in drug treatment compared to its untreated control.

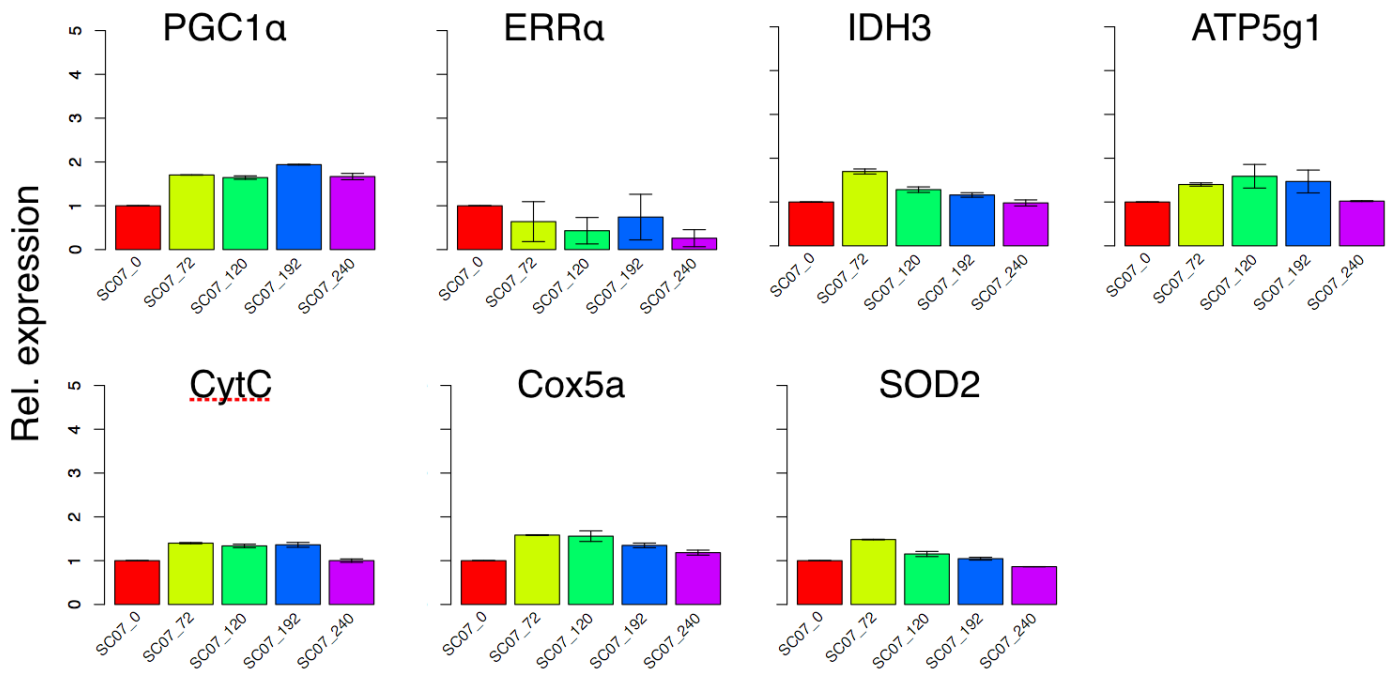

Figure 6.7: *BRAF*i-induced expression of Oxphos genes is not sustained in SC07. Relative expression of respective genes is quantified by RT-qPCR and normalized to its expression in time zero, untreated control. X-axis denotes the time lengths with different drug exposure. Error bar represents standard deviation from 3 technical replicates for each time point.

Similar analyses could be done in other sublines and *BRAF*-mutated melanoma cell lines. However, to examine global changes in the gene-expression in idling cells, one could also perform RNASeq analysis and analyze differentially expressed genes to identify key molecular drivers of idling phenotype. To this end, we performed RNASeq analysis in idling cells of three sublines, SC01, SC07 and SC10 (treated for 7 days in 8μM PLX4720). Analysis of this gene-expression data remains to be done. Differential gene expression analysis on the sublines between idling and untreated groups should be done to identify differentially expressed genes (DEGs). Because the metabolic profiles of idling melanoma cells are reduced, we speculate the shunting of metabolic intermediates into alternative metabolic pathways such as Pentose Phosphate Pathways (PPP), glutaminolysis, allows melanoma cells

to regenerate necessary substrates to survive continued drug exposure. Pentose phosphate pathway is involved in regeneration of reducing equivalents such as NADPH which helps cells to combat excessive oxidative stress. One could also examine whether prolonged *BRAF*i treatment induces oxidative stress in idling cells—if so, combating such stress is critical for cells to maintain their survival. Others have reported the transition of melanoma into similar drug-tolerant cells to be due to chromatin remodeling, enrichment in markers implicated in cancer stemness [106,207]. Drug-induced senescence, de-differentiation, enhanced expression of multi-drug transporters and phenotype switching such as Epithelial-Mesenchymal Transition (EMT) have also been proposed to describe drug-tolerant phenotype [101,212,249]. Since the drug-modified epigenetic landscape inferred from the population level data vary between cell lines, it is possible that several mechanisms could be at play to maintain a fine balance between cell division and death while sustaining prolonged *BRAF*i treatment. It is possible that melanoma cells achieve the idling state differently, as initial drug response vary among cell lines: some regress while others expand before converging to an idling state. Understanding the early drug-adaptation would be critical to maximize cell killing, and limit the number of cells that reach the idling state. It would be interesting to distinguish whether idling state is defined by common molecular signatures among *BRAF*-mutated melanoma cells, or unique to different cell lines. As all *BRAF*-mutated melanoma cells experience death in idling state, it would be exciting to determine the mode of cell death: apoptosis, necrosis or necroptosis. Collectively, these studies will deepen our understanding of how *BRAF*-mutated melanoma cells can survive sub-lethal concentrations of MAPK-pathway inhibitors. Combination therapies both simultaneous or sequential could be designed to deplete the reservoir of non-quiescent idling cells and potentially thwart the emergence of drug resistance in melanoma.

Single-Cell RNA Sequencing to Identify Distinct Cancer Subpopulations

In recent years, we have seen single-cell RNA Sequencing [137–139] become an indispensable tool to characterize intra-tumor heterogeneity within tumors or cell-to-cell heterogeneity within cancer cell population. Single-cell RNA Sequencing (scRNASeq) is a great tool to explore distinct genotypic and phenotypic states of tumors. We speculate that melanoma cells exist in distinct phenotypic states and they transition between states both as a result of phenotypic drift and under drug perturbations. To infer all possible phenotypic states within *BRAF*-mutated melanoma landscape and to characterize them molecularly, one could perform scRNASeq and evaluate genetic and transcriptional programs present in hundreds to thousands of individual cells. Through dimensionality reduction algorithms [250], one could identify the major subtypes of clonal subpopulations within *BRAF*-mutated melanoma cell population. These results will provide support to our theoretical framework and hypothesis of co-existing distinct phenotypic, functional states within melanoma. The identified signature of the subtypes would facilitate the study of phenotypic state transitions among cell subpopulations.

Clonal Sublines Mixture Experiments

Does cell-cell communication matter? To determine whether cell-cell communication regulate the differential responses of *BRAF*-mutated melanoma cells, one could mix clonal sublines and delineate how mixing affects the population dynamics at the cell population and clonal level. To be able to follow distinct clonal sublines and their response over time, sublines need to be fluorescently tagged with different colors, or defined with respect to some molecular signatures as in breast cancer subpopulations [194]. Taken together, results obtained from these experiments would form the basis for transition rate calibration and estimation in our model.

APPENDIX 1

Simple Three-State Model of Cell Proliferation

To better understand the complex dynamics exhibited by *BRAF*-mutated melanoma cells in response to *BRAF*i, including emergence of the idling phenotype, we devised a simple three-state model comprised of a regressing state *R*, a stable (zero net growth) state *S*, and an expanding state *E*. Cells in each state can experience two fates, division and death, with kinetic rate constants that are characteristic of the states. Additionally, drug induces transitions between "adjacent" states. The model can be expressed in kinetic terms as

$$Cell_R \xrightarrow{k_{gR}} Cell_R + Cell_R \quad \text{(A1)}$$

$$Cell_R \xrightarrow{k_{dR}} \varnothing \quad \text{(A2)}$$

$$Cell_S \xrightarrow{k_{gS}} Cell_S + Cell_S \quad \text{(A3)}$$

$$Cell_S \xrightarrow{k_{dS}} \varnothing \quad \text{(A4)}$$

$$Cell_E \xrightarrow{k_{gE}} Cell_E + Cel\therefore_E \quad \text{(A5)}$$

$$Cell_E \xrightarrow{k_{dE}} \varnothing \quad \text{(A6)}$$

$$Cell_R \underset{k_{sr}}{\overset{k_{rs}}{\rightleftarrows}} Cell_S \quad \text{(A7)}$$

$$Cell_S \underset{k_{es}}{\overset{k_{se}}{\rightleftarrows}} Cell_E \quad \text{(A8)}$$

Here, $Cell_X$ ($X \in \{R,S,E\}$) is the number of cells in state *X*, k_{gX} and k_{dX} are division (growth) and death rate constants for cells in state *X*, k_{XY} is the transition rate constant between states *X*

and Y ($R \Leftrightarrow S \Leftrightarrow E$), and $\varnothing$ represents cell death (the null state). A graphical representation of the model is provided in Figure 4.9a of the main text.

Given these reactions, and defining $k_{pX} \equiv k_{gX} - k_{dX}$ as the net proliferation rate for cells in state X, the coupled set of ordinary differential equations (ODEs) describing the state dynamics is

$$\frac{dN_R}{dt} = \left(k_{pR} - k_{rs}\right)N_R + k_{sr}N_S \quad \text{(A9)}$$

$$\frac{dN_S}{dt} = \left(k_{pS} - k_{sr} - k_{se}\right)N_S + k_{rs}N_R + k_{es}N_E \quad \text{(A10)}$$

$$\frac{dN_E}{dt} = \left(k_{pE} - k_{es}\right)N_E + k_{se}N_S \quad \text{(A11)}$$

Equations (A9)-(A11) are presented in the main text as Eqs. (1)-(3) in CHAPTER 4.

Model Simulation and Parameter Calibration

The model in Eqs. (A1)-(A8) consists of 10 parameters: three net proliferation rates (k_{pE}, k_{pS}, k_{pE}), four transition rate constants (k_{rs}, k_{sr}, k_{se}, k_{es}), and three initial cell counts ($N_R(t{=}0)$, $N_S(t{=}0)$, $N_E(t{=}0)$). We fixed the net proliferation rate for state S to zero and chose values for states R and E based on the range of responses seen for the SKMEL5 parental cell line (Figure 4.3a and Figure 4.4d). Specifically, we chose $k_{pR} = -0.055\ \text{h}^{-1}$, $k_{pS} = 0\ \text{h}^{-1}$, and $k_{pE} = 0.015\ \text{h}^{-1}$ based on the range of drug-induced proliferation rates (range: +0.03h^{-1} to -0.11 h^{-1}). We also set the total number of initial cells T_0 = 10,000. Altogether, this eliminates four free parameters, leaving a total of six free parameters in need of calibration: the four transition rate constants and the initial *proportions* of cells in states R and S (denoted R_0 and S_0, respectively; $R_0 = N_R(t{=}0)/T_0$, etc.). Model simulation was performed by numerically integrating Eqs. (A9)-(A11) using the LSODA algorithm [251] as implemented within the *ode*

function of the R package deSolve [196]. Model calibration was performed using the cost function (presented as Eq. (4) in the main text in CHAPTER 4)

$$Cost = \sum_{i=1}^{n} \frac{(M_i - O_i)^2}{\sigma_i} \quad \text{(A12)}$$

where n is the number of measured time points and M_i, O_i, and σ_i are the model prediction, experimentally observed value, and standard experimental error at time point i, respectively. We first identified the closest local minimum within the cost space using the Levenberg-Marquardt algorithm as implemented within the *modFit* function of the R package FME [199]. We then performed Markov chain Monte Carlo (MCMC) sampling, using the *modMCMC* function of the FME package, to sample the trough of the cost-space well and to confirm that it was, to our best estimate, the global minimum. A Gaussian prior was defined for all parameters[198] with variances obtained from *modFit*. A lower bound of 0 was imposed for all parameters. An upper bound of 0.06/h (the observed proliferation rate for SKMEL5 cells in dimethyl sulfoxide (DMSO) control) was imposed for the transition rate constants k_{rs}, k_{sr}, k_{se}, and k_{es}. For the initial cell proportions R_0 and S_0, an upper bound of 1 was imposed. In addition, we required that $R_0 + S_0 \leq 1$. Constraints such as this cannot be defined directly within the *modMCMC* function. Therefore, we modified our R script to impose an artificially large cost ($>10^6$) if an MCMC iteration returned values that violated this constraint.

In all cases, we performed 10^5 MCMC iterations starting from the parameter set obtained from *modFit.* Values of σ_i in Eq. (A12) were automatically determined in each case by *modMCMC* based on the input data set. The parameter covariance matrix was evaluated every 100 iterations (*updatecov* argument to *modMCMC*) and used to update the MCMC jumps. The maximum number of tries for the delayed rejection procedure was set to 2 (*ntrydr* argument to *modMCMC*). In some cases, three independent MCMC chains were run with

different initial parameter values (±25% around the best fit from *modFit*) and converged to the same distributions as per the Gelman-Rubin test [252,253]. Parameter distributions for numerous cell lines are shown in Appendix 1; associated MCMC trace plots are shown in Appendix 2.

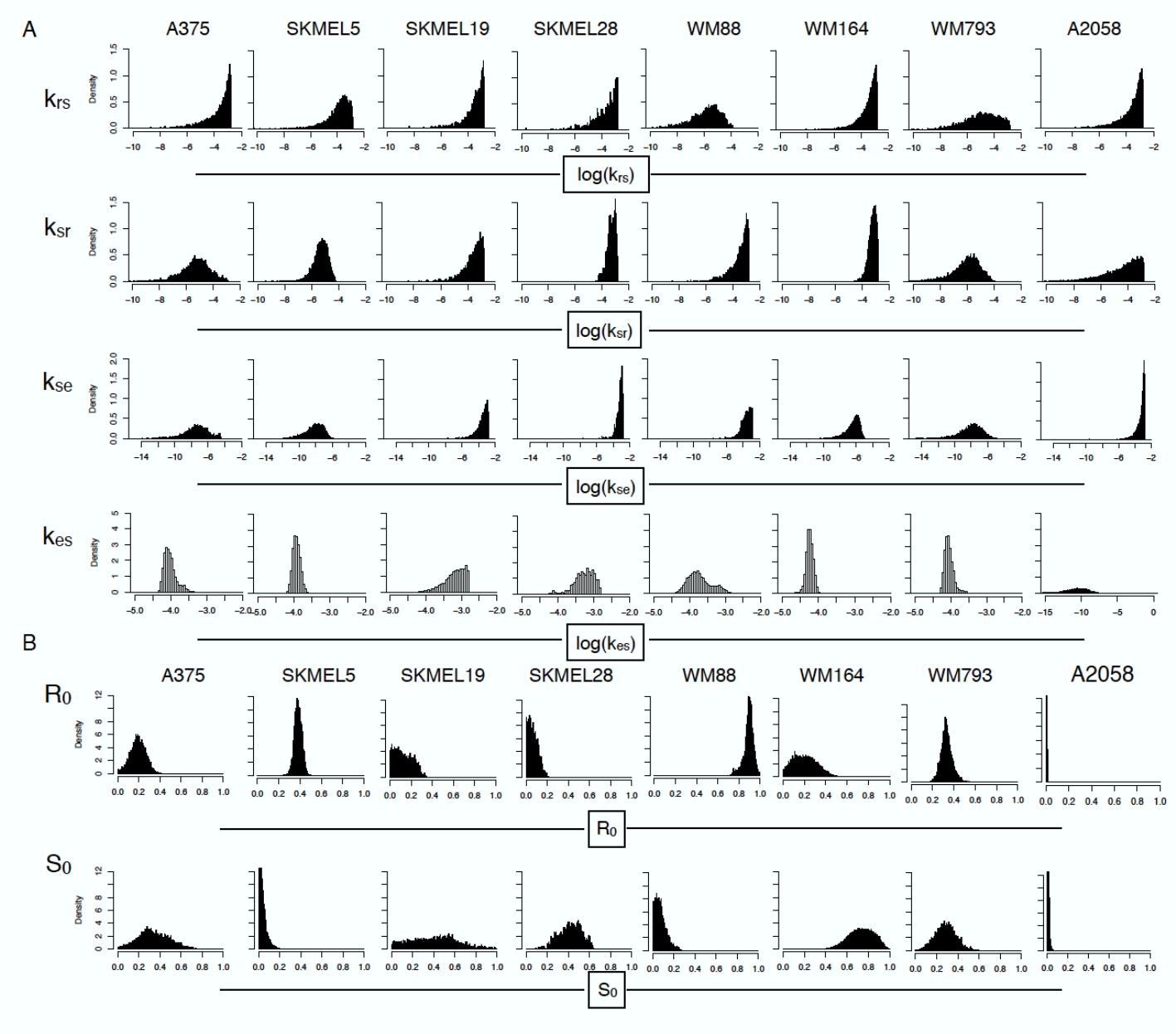

Appendix 1: Parameter estimation obtained by MCMC calibration against Experimental data for multiple *BRAF*-mutated melanoma cells. (A) Transition rate constants (log scale) (B) Proportions of initial cell counts.

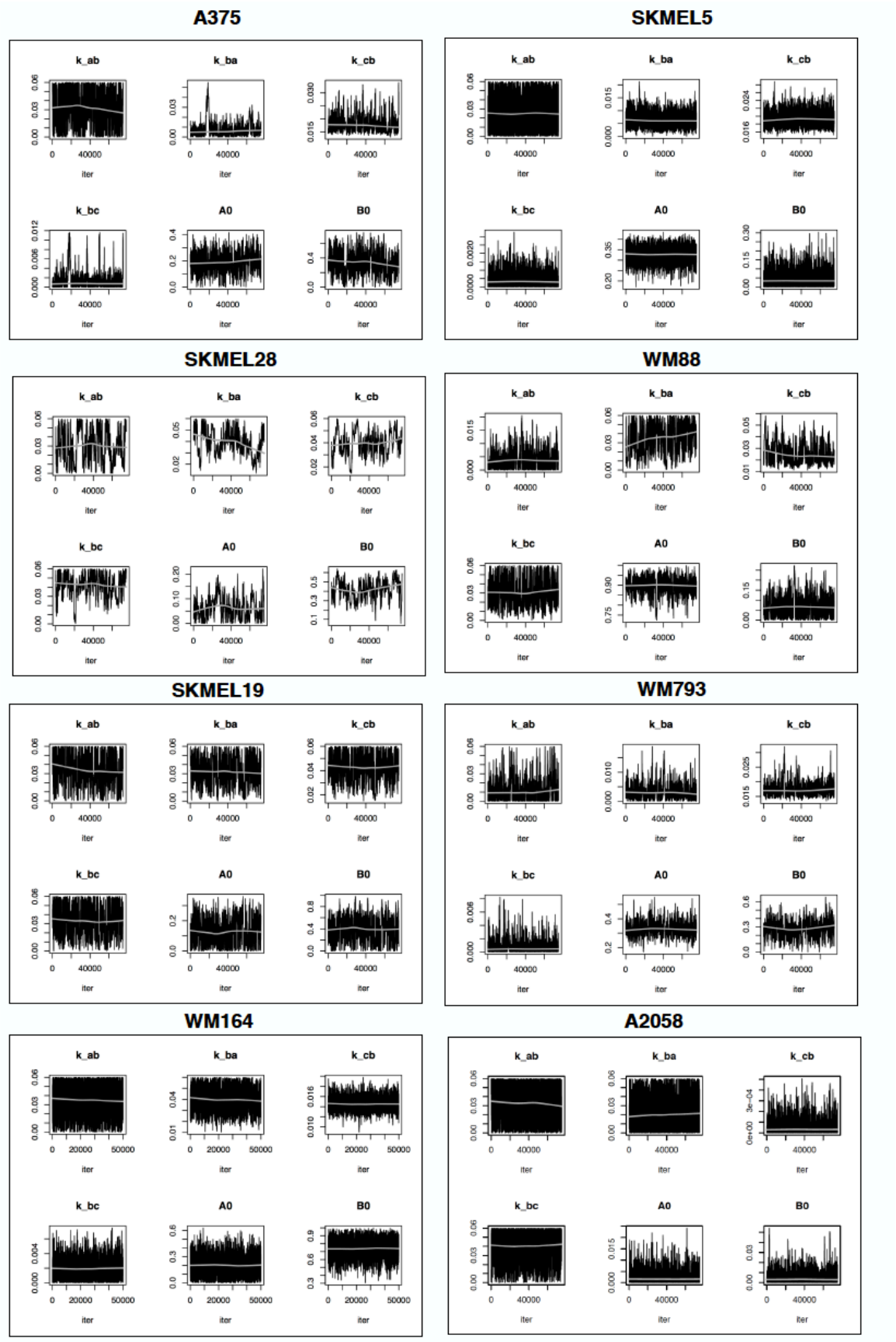

Appendix 2: MCMC traceplots for multiple *BRAF*-mutated melanoma cell lines. Last 50% (accounting for burn-in) of the total 10^5 iterations are shown.

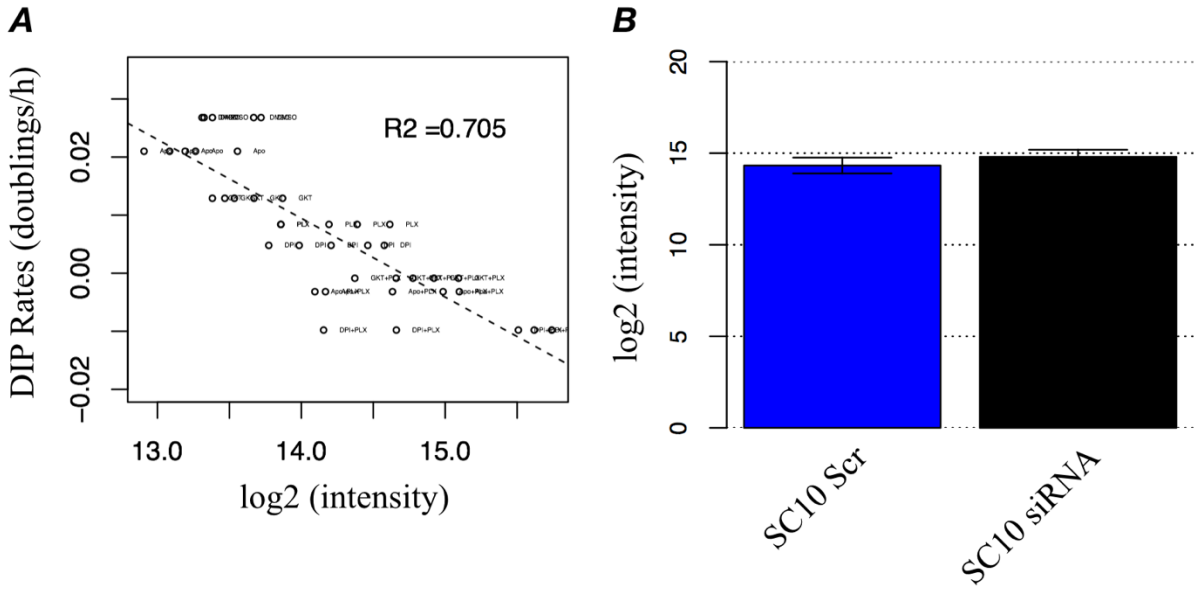

Appendix 3: Effect of *NOX*-inhibition on ROS signaling. (A) Correlation between Drug-induced proliferation (DIP) rates and ROS intensity (on $\log_2$ scale) from conditions described in Figure 5.5b. ROS is measured using CellRox™ Deep Red Reagent (Cat# C10422). Increased ROS signaling is inversely correlated with DIP rates (Corr: -0.705), Pearson Correlation used, p-value < 0.001. (B) Level of ROS signaling quantified on $\log_2$ scale for Scrambled control and siRNA knockdown of *NOX5* in SC10.

Model Selection

We additionally considered the possibility of: two-state models and three-state model with all possible phenotypic state transitions (triangle-model). For two-state model, we considered all possible combinations: (A) Two states with Regressing (R) and Stable (S) states; (B) Two states with Stable (S) and Expanding (E) states; (C) Two states with Regressing (R) and Expanding (E) states. Our three-state model tacitly assumes that the states are organized in a linear fashion—with zero possibility of transition between Regressing (R) to Expanding (E) states. Although biologically distant from each other, the transitions between States R and E are theoretically possible. Therefore, we also considered the "triangle" model where transitions between all three states are possible. Graphical representation of all possible combinations of the models we considered is shown in Appendix 4.

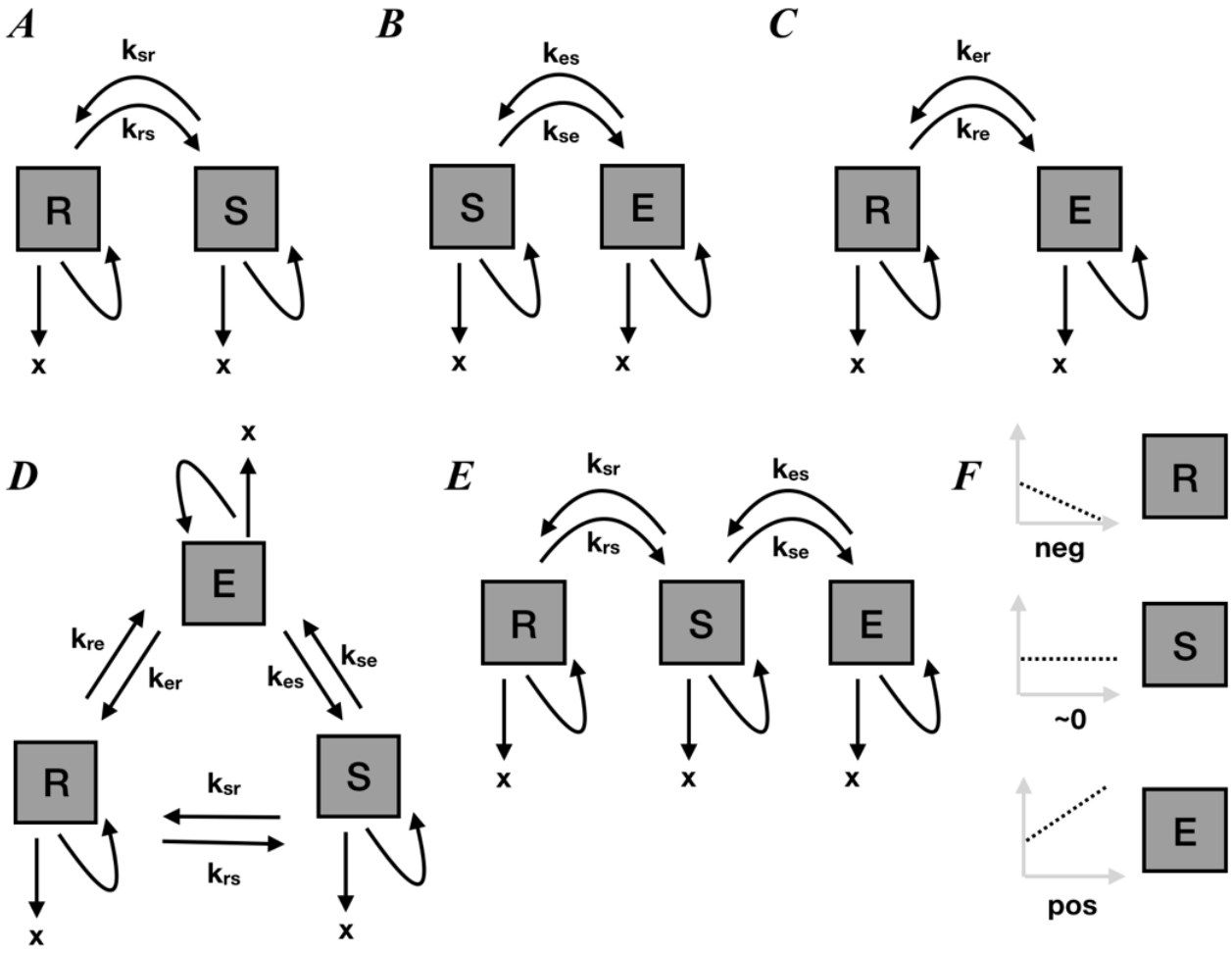

Appendix 4: Graphical representation of all possible model configurations. Two-state models with: (A) Regressing (R) and Stable (S) state; (B) Stable (S) and Expanding (E) states; (C) Regressing (R) and Expanding (E) states; (D) Three-state model with all possible state transitions among states, also called triangle model; (E) Three-state model organized in linear fashion. In all the states, cells can either divide/die or transition into another available states. (F) Population dynamics of the proposed three-states.

We calibrated the models against an experimental time course for a 1:1:1 clonal mixture of three single cell-derived sublines (SC01, SC07, and SC10). We inferred the Akaike information criteria (AIC) [254] for all the models we considered.

	Model A	Model B	Model C	Model D	Model E
Number of Parameters	4	4	4	8	6
AIC value	145.6585	-363.4001	-129.4709	-394.5141	-399.7858
Residual Std. Error	1.869	0.1965	0.5533	0.1677	0.1656

Appendix 5: Model fit and model selection statistics indicate three-state model linear model improves fit. Three-state model organized in linear fashion (Model E in Appendix 4) has the lowest AIC value and lowest residual standard error, indicating that the model E is both improved in terms of model selection and in terms of error minimization than the other possible models considered.

Definition of Quasi-Potential Landscape

It is a conceptual construct, with its basis on classical mechanics and captures the global behaviors of the complex Gene Regulatory Networks (GRN) [149]. A gene regulatory network (GRN) is specific to a cell type and regulates the expression of genes giving rise to distinct gene expression patterns. This network of genes can give rise to non-genetic heterogeneity due to multiple metastable phenotypes [127–131]. The mathematical basis for this idea relies on the concept of state space, where a phenotypic state of a cell at time *t*, *S(t)* is represented by quantity $x_i(t)$ of *N* interacting genes [127,133]. Given a network architecture, most random gene networks will ultimately settle into few stable basins of attraction called "attractors." [127]. This formalism is an extension to Waddington's epigenetic landscape [132], and links a multidimensional dynamical-systems framework to phenotypic variability. In the probabilistic view, not all attractors or states in the state space *S(t)* are equally likely to be occupied by cells. Hence, the probability for each state is assigned an 'elevation', *V(s)*, a quasi-potential energy ("potential") whose height or energy barrier is inversely related to its probability *P(s)*. A collection of the "potential" values *V(s)* over the entire state space gives rise to a quasi-potential landscape. The prefix "quasi" or "generalized" distinguishes this potential

from true energy potentials often used in physics. This framework allows for co-existence of multiple stable phenotypes within the same genome and has been used to describe phenotypic variability in cancer cells without genetic alterations [161,255]. With this view, distinct stable phenotypes in an epigenetic landscape can be visualized as attractors and their stability can be represented as a quasi-potential energy *U* of each state [195]. Thus, a quasi-potential energy surface defines an epigenetic landscape of a cancer where cells are hypothesized to reside in different attractors.

REFERENCES

1. Fitzmaurice C, Dicker D, Pain A, Hamavid H, Moradi-Lakeh M, MacIntyre MF, et al. The Global Burden of Cancer 2013. JAMA Oncol. 2015;1:505.

2. Siegel RL, Miller KD, Jemal A. Cancer statistics, 2017. CA. Cancer J. Clin. 2017;67:7–30.

3. NIH. Cancer Statistics [Internet]. Natl. Cancer Inst. 2017 [cited 2017 Jan 1]. Available from: https://www.cancer.gov/about-cancer/understanding/statistics

4. DeVita VT, Chu E. A history of cancer chemotherapy. Cancer Res. 2008. p. 8643–53.

5. Wolfe KH, Li W-H. Molecular evolution meets the genomics revolution. Nat. Genet. 2003;33:255–65.

6. Sawyers C. Targeted cancer therapy. Nature. 2004;432:294–7.

7. Weinstein IB. Addiction to Oncogenes — the Achilles Heal of Cancer. Science (80-.). 2002;297:63–4.

8. Hanahan D, Weinberg RA. Hallmarks of cancer: The next generation. Cell. 2011. p. 646–74.

9. Weinstein IB, Joe AK. Mechanisms of Disease: oncogene addiction—a rationale for molecular targeting in cancer therapy. Nat. Clin. Pract. Oncol. 2006;3:448–57.

10. Felsher DW, Bishop JM. Reversible tumorigenesis by MYC in hematopoietic lineages. Mol. Cell. 1999;4:199–207.

11. Colomer R, Lupu R, Bacus SS, Gelmann EP. erbB-2 antisense oligonucleotides inhibit the proliferation of breast carcinoma cells with erbB-2 oncogene amplification. Br. J. Cancer. 1994;70:819–25.

12. Slamon DJ, Leyland-Jones B, Shak S, Fuchs H, Paton V, Bajamonde A, et al. Use of Chemotherapy Plus a Monoclonal Antibody Against HER2 for Metastatic Breast Cancer That Overexpresses HER2. N. Engl. J. Med. 2001;344:783–92.

13. Bollag G, Hirth P, Tsai J, Zhang J, Ibrahim PN, Cho H, et al. Clinical efficacy of a RAF inhibitor needs broad target blockade in BRAF-mutant melanoma. Nature. 2010;467:596–9.

14. Pegram MD, Lipton A, Hayes DF, Weber BL, Baselga JM, Tripathy D, et al. Phase II study of receptor-enhanced chemosensitivity using recombinant humanized anti-p185(HER2/neu) monoclonal antibody plus cisplatin in patients with HER2/neu-overexpressing metastatic breast cancer refractory to chemotherapy treatment. J. Clin. Oncol. 1998;16:2659–71.

15. Cobleigh MA, Vogel CL, Tripathy D, Robert NJ, Scholl S, Fehrenbacher L, et al. Multinational study of the efficacy and safety of humanized anti-HER2 monoclonal antibody in

women who have HER2-overexpressing metastatic breast cancer that has progressed after chemotherapy for metastatic disease. J. Clin. Oncol. 1999;17:2639–48.

16. Baselga J, Tripathy D, Mendelsohn J, Baughman S, Benz CC, Dantis L, et al. Phase II Study of Weekly Intravenous Recombinant Humanized Anti-p185HER2 Monoclonal Antibody in Patients with HER2/neu-Overexpressing Metastatic Breast Cancer. J. Clin. Oncol. 1996;14:737–44.

17. Piccart-Gebhart MJ, Procter M, Leyland-Jones B, Goldhirsch A, Untch M, Smith I, et al. Trastuzumab after adjuvant chemotherapy in HER2-positive breast cancer. N. Engl. J. Med. 2005;353:1659–72.

18. Druker BJ, Tamura S, Buchdunger E, Ohno S, Segal GM, Fanning S, et al. Effects of a selective inhibitor of the Abl tyrosine kinase on the growth of Bcr–Abl positive cells. Nat. Med. 1996;2:561–6.

19. Druker BJ, Talpaz M, Resta DJ, Peng B, Buchdunger E, Ford JM, et al. Efficacy and safety of a specific inhibitor of the BCR-ABL tyrosine kinase in chronic myeloid leukemia. N Engl J Med. 2001;344:1031–7.

20. Druker BJ, Sawyers CL, Kantarjian H, Resta DJ, Reese SF, Ford JM, et al. Activity of a specific inhibitor of the BCR-ABL tyrosine kinase in the blast crisis of chronic myeloid leukemia and acute lymphoblastic leukemia with the Philadelphia chromosome. N Engl J Med. 2001;344:1038–42.

21. De Giorgi U, Verweij J. Imatinib and gastrointestinal stromal tumors: Where do we go from here? Mol. Cancer Ther. 2005;4:495–501.

22. Heinrich MC, Griffith DJ, Druker BJ, Wait CL, Ott K a, Zigler a J. Inhibition of c-kit receptor tyrosine kinase activity by STI 571, a selective tyrosine kinase inhibitor. Blood. 2000;96:925–32.

23. Shepherd FA, Rodrigues Pereira J, Ciuleanu T, Tan EH, Hirsh V, Thongprasert S, et al. Erlotinib in previously treated non-small-cell lung cancer. N. Engl. J. Med. 2005;353:123–32.

24. Fukuoka M. Multi-Institutional Randomized Phase II Trial of Gefitinib for Previously Treated Patients With Advanced Non-Small-Cell Lung Cancer. J. Clin. Oncol. 2003;21:2237–46.

25. Kris MG, Natale RB, Herbst RS, Lynch TJ, Prager D, Belani CP, et al. Efficacy of gefitinib, an inhibitor of the epidermal growth factor receptor tyrosine kinase, in symptomatic patients with non-small cell lung cancer: a randomized trial. JAMA. 2003;290:2149–58.

26. Chapman PB, Hauschild A, Robert C, Haanen JB, Ascierto P, Larkin J, et al. Improved Survival with Vemurafenib in Melanoma with BRAF V600E Mutation. N. Engl. J. Med. 2011;364:2507–16.

27. Flaherty KT, Yasothan U, Kirkpatrick P. Vemurafenib. Nat Rev Drug Discov. 2011;10:811–

2.

28. Kwak EL, Bang Y-J, Camidge DR, Shaw AT, Solomon B, Maki RG, et al. Anaplastic lymphoma kinase inhibition in non-small-cell lung cancer. N. Engl. J. Med. 2010;363:1693–703.

29. Shaw AT, Kim DW, Nakagawa K, Seto T, Crino L, Ahn MJ, et al. Crizotinib versus chemotherapy in advanced ALK-positive lung cancer. N Engl J Med. 2013;368:2385–94.

30. Garbe C, Leiter U. Epidemiology of melanoma and nonmelanoma skin cancer-the role of sunlight. Adv. Exp. Med. Biol. 2008. p. 89–103.

31. Gray-Schopfer V, Wellbrock C, Marais R. Melanoma biology and new targeted therapy. Nature. 2007;445:851–7.

32. Chang AE, Karnell LH, Menck HR. The National Cancer Data Base Report on Cutaneous and Noncutaneous Melanoma. Cancer. 1998;83:1664–78.

33. Jovanovic P, Mihajlovic M, Djordjevic-Jocic J, Vlajkovic S, Cekic S, Stefanovic V. Ocular melanoma: An overview of the current status. Int. J. Clin. Exp. Pathol. 2013. p. 1230–44.

34. Sandru A, Voinea S, Panaitescu E, Blidaru A. Survival rates of patients with malignant melanoma. J. Med. Life. 2014;7:572–6.

35. Smoller BR. Histologic criteria for diagnosing primary cutaneous malignant melanoma. Mod. Pathol. 2006;19 Suppl 2:S34–40.

36. Davies H, Bignell G, Cox C, Stephens P. Mutations of the BRAF gene in human cancer. Nature. 2002;417:949–54.

37. TCGA. Genomic Classification of Cutaneous Melanoma. Cell. 2015;161:1681–96.

38. Curtin JA, Fridlyand J, Kageshita T, Patel HN, Busam KJ, Kutzner H, et al. Distinct sets of genetic alterations in melanoma. N. Engl. J. Med. 2005;353:2135–47.

39. Lovly CM, Dahlman KB, Fohn LE, Su Z, Dias-Santagata D, Hicks DJ, et al. Routine multiplex mutational profiling of melanomas enables enrollment in genotype-driven therapeutic trials. PLoS One. 2012;7.

40. Sullivan RJ, Fisher DE. Understanding the Biology of Melanoma and Therapeutic Implications. Hematol. Oncol. Clin. North Am. 2014. p. 437–53.

41. Atkins MB, Lotze MT, Dutcher JP, Fisher RI, Weiss G, Margolin K, et al. High-dose recombinant interleukin 2 therapy for patients with metastatic melanoma: Analysis of 270 patients treated between 1985 and 1993. J. Clin. Oncol. 1999;17:2105–16.

42. Hoeflich KP, Gray DC, Eby MT, Tien JY, Wong L, Bower J, et al. Oncogenic BRAF is

required for tumor growth and maintenance in melanoma models. Cancer Res. 2006;66:999–1006.

43. Tsai J, Lee JT, Wang W, Zhang J, Cho H, Mamo S, et al. Discovery of a selective inhibitor of oncogenic B-Raf kinase with potent antimelanoma activity. Proc. Natl. Acad. Sci. U. S. A. 2008;105:3041–6.

44. Flaherty KT, Puzanov I, Kim KB, Ribas A, McArthur GA, Sosman JA, et al. Inhibition of Mutated, Activated BRAF in Metastatic Melanoma. N. Engl. J. Med. 2010;363:809–19.

45. Sosman JA, Kim KB, Schuchter L, Gonzalez R, Pavlick AC, Weber JS, et al. Survival in BRAF V600–Mutant Advanced Melanoma Treated with Vemurafenib. N. Engl. J. Med. 2012;366:707–14.

46. Hauschild A, Grob JJ, Demidov L V., Jouary T, Gutzmer R, Millward M, et al. Dabrafenib in BRAF-mutated metastatic melanoma: A multicentre, open-label, phase 3 randomised controlled trial. Lancet. 2012;380:358–65.

47. Medina T, Amaria MN, Jimeno a. Dabrafenib in the treatment of advanced melanoma. Drugs Today (Barc). 2013;49:377–85.

48. Gilmartin AG, Bleam MR, Groy A, Moss KG, Minthorn EA, Kulkarni SG, et al. GSK1120212 (JTP-74057) is an inhibitor of MEK activity and activation with favorable pharmacokinetic properties for sustained in vivo pathway inhibition. Clin. Cancer Res. 2011;17:989–1000.

49. Infante JR, Fecher LA, Falchook GS, Nallapareddy S, Gordon MS, Becerra C, et al. Safety, pharmacokinetic, pharmacodynamic, and efficacy data for the oral MEK inhibitor trametinib: A phase 1 dose-escalation trial. Lancet Oncol. 2012;13:773–81.

50. Flaherty KT, Robert C, Hersey P, Nathan P, Garbe C, Milhem M, et al. Improved Survival with MEK Inhibition in BRAF-Mutated Melanoma. N. Engl. J. Med. 2012;367:107–14.

51. Kim KB, Kefford R, Pavlick AC, Infante JR, Ribas A, Sosman JA, et al. Phase II study of the MEK1/MEK2 inhibitor trametinib in patients with metastatic BRAF-mutant cutaneous melanoma previously treated with or without a BRAF inhibitor. J. Clin. Oncol. 2013;31:482–9.

52. Long G V., Stroyakovskiy D, Gogas H, Levchenko E, de Braud F, Larkin J, et al. Combined BRAF and MEK Inhibition versus BRAF Inhibition Alone in Melanoma. N. Engl. J. Med. 2014;371:1877–88.

53. Larkin J, Ascierto P a., Dréno B, Atkinson V, Liszkay G, Maio M, et al. Combined Vemurafenib and Cobimetinib in BRAF -Mutated Melanoma. N. Engl. J. Med. 2014;371:1867–76.

54. Menzies AM, Long G V. Dabrafenib and Trametinib, alone and in combination for BRAF-Mutant metastatic melanoma. Clin. Cancer Res. 2014;20:2035–43.

55. Flaherty KT, Infante JR, Daud A, Gonzalez R, Kefford RF, Sosman J, et al. Combined BRAF and MEK Inhibition in Melanoma with BRAF V600 Mutations. N. Engl. J. Med. 2012. p. 1694–703.

56. Hodi FS, O'Day SJ, McDermott DF, Weber RW, Sosman JA, Haanen JB, et al. Improved survival with ipilimumab in patients with metastatic melanoma. N. Engl. J. Med. 2010;363:711–23.

57. Ribas A, Wolchok JD, Robert C, Kefford R, Hamid O, Daud A, et al. P0116 Updated clinical efficacy of the anti-PD-1 monoclonal antibody pembrolizumab (MK-3475) in 411 patients with melanoma. Eur. J. Cancer. 2015;51:e24.

58. Robert C, Ribas A, Wolchok JD, Hodi FS, Hamid O, Kefford R, et al. Anti-programmed-death-receptor-1 treatment with pembrolizumab in ipilimumab-refractory advanced melanoma: A randomised dose-comparison cohort of a phase 1 trial. Lancet. 2014;384:1109–17.

59. Robert C, Schachter J, Long G V., Arance A, Grob JJ, Mortier L, et al. Pembrolizumab versus Ipilimumab in Advanced Melanoma. N. Engl. J. Med. 2015;372:2521–32.

60. Devji T, Levine O, Neupane B, Beyene J, Xie F. Systemic Therapy for Previously Untreated Advanced *BRAF* -Mutated Melanoma. JAMA Oncol. 2017;3:366.

61. Gorre ME. Clinical Resistance to STI-571 Cancer Therapy Caused by BCR-ABL Gene Mutation or Amplification. Science (80-.). 2001;293:876–80.

62. Pao W, Miller VA, Politi KA, Riely GJ, Somwar R, Zakowski MF, et al. Acquired resistance of lung adenocarcinomas to gefitinib or erlotinib is associated with a second mutation in the EGFR kinase domain. PLoS Med. 2005;2:0225–35.

63. Villanueva J, Infante JR, Krepler C, Reyes-Uribe P, Samanta M, Chen HY, et al. Concurrent MEK2 Mutation and BRAF Amplification Confer Resistance to BRAF and MEK Inhibitors in Melanoma. Cell Rep. 2013;4:1090–9.

64. Poulikakos PI, Persaud Y, Janakiraman M, Kong X, Ng C, Moriceau G, et al. RAF inhibitor resistance is mediated by dimerization of aberrantly spliced BRAF(V600E). Nature. 2011. p. 387–90.

65. Montagut C, Sharma S V., Shioda T, McDermott U, Ulman M, Ulkus LE, et al. Elevated CRAF as a potential mechanism of acquired resistance to BRAF inhibition in melanoma. Cancer Res. 2008;68:4853–61.

66. Shi H, Moriceau G, Kong X, Lee M-K, Lee H, Koya RC, et al. Melanoma whole-exome sequencing identifies V600EB-RAF amplification-mediated acquired B-RAF inhibitor resistance. Nat. Commun. Nature Publishing Group; 2012;3:724.

67. Kemper K, Krijgsman O, Kong X, Cornelissen-Steijger P, Shahrabi A, Weeber F, et al. BRAFV600E Kinase Domain Duplication Identified in Therapy-Refractory Melanoma Patient-

Derived Xenografts. Cell Rep. 2016;16:263–77.

68. Johannessen CM, Boehm JS, Kim SY, Thomas SR, Wardwell L, Johnson LA, et al. COT drives resistance to RAF inhibition through MAP kinase pathway reactivation. Nature. Nature Publishing Group, a division of Macmillan Publishers Limited. All Rights Reserved.; 2010;468:968–72.

69. Nazarian R, Shi H, Wang Q, Kong X, Koya RC, Lee H, et al. Melanomas acquire resistance to B-RAF(V600E) inhibition by RTK or N-RAS upregulation. Nature. 2010;468:973–7.

70. Wagle N, Emery C, Berger MF, Davis MJ, Sawyer A, Pochanard P, et al. Dissecting therapeutic resistance to RAF inhibition in melanoma by tumor genomic profiling. J. Clin. Oncol. 2011;29:3085–96.

71. Wagle N, Van Allen EM, Treacy DJ, Frederick DT, Cooper ZA, Taylor-Weiner A, et al. MAP kinase pathway alterations in BRAF-mutant melanoma patients with acquired resistance to combined RAF/MEK inhibition. Cancer Discov. 2014;4:61–8.

72. Villanueva J, Vultur A, Lee JT, Somasundaram R, Fukunaga-Kalabis M, Cipolla AK, et al. Acquired Resistance to BRAF Inhibitors Mediated by a RAF Kinase Switch in Melanoma Can Be Overcome by Cotargeting MEK and IGF-1R/PI3K. Cancer Cell. 2010;18:683–95.

73. Shi H, Hugo W, Kong X, Hong A, Koya RC, Moriceau G, et al. Acquired resistance and clonal evolution in melanoma during BRAF inhibitor therapy. Cancer Discov. 2013;4:08–93.

74. Shi H, Hong A, Kong X, Koya RC, Song C, Moriceau G, et al. A novel AKT1 mutant amplifies an adaptive melanoma response to BRAF inhibition. Cancer Discov. 2014;4:69–79.

75. Rizos H, Menzies AM, Pupo GM, Carlino MS, Fung C, Hyman J, et al. BRAF inhibitor resistance mechanisms in metastatic melanoma: Spectrum and clinical impact. Clin. Cancer Res. 2014;20:1965–77.

76. Tap WD, Gong K-W, Dering J, Tseng Y, Ginther C, Pauletti G, et al. Pharmacodynamic Characterization of the Efficacy Signals Due to Selective BRAF Inhibition with PLX4032 in Malignant Melanoma 1,2. Neoplasia. 2010;12:637–649.

77. Straussman R, Morikawa T, Shee K, Barzily-Rokni M, Qian ZR, Du J, et al. Tumour micro-environment elicits innate resistance to RAF inhibitors through HGF secretion. Nature. 2012;487:500–4.

78. Hirata E, Girotti MR, Viros A, Hooper S, Spencer-Dene B, Matsuda M, et al. Intravital imaging reveals how BRAF inhibition generates drug-tolerant microenvironments with high integrin β1/FAK Signaling. Cancer Cell. 2015;27:574–88.

79. Fedorenko I V., Wargo JA, Flaherty KT, Messina JL, Smalley KSM. BRAF Inhibition Generates a Host–Tumor Niche that Mediates Therapeutic Escape. J. Invest. Dermatol.

2015;135:3115–24.

80. Fedorenko I V, Abel E V, Koomen JM, Fang B, Wood ER, Chen YA, et al. Fibronectin induction abrogates the BRAF inhibitor response of BRAF V600E/PTEN-null melanoma cells. Oncogene. 2016;35:1225–35.

81. Sun C, Wang L, Huang S, Heynen GJJE, Prahallad A, Robert C, et al. Reversible and adaptive resistance to BRAF(V600E) inhibition in melanoma. Nature. 2014;508:118–22.

82. Burrell RA, McGranahan N, Bartek J, Swanton C. The causes and consequences of genetic heterogeneity in cancer evolution. Nature. 2013;501:338–45.

83. Prahallad A, Heynen GJJE, Germano G, Willems SM, Evers B, Vecchione L, et al. PTPN11 Is a Central Node in Intrinsic and Acquired Resistance to Targeted Cancer Drugs. Cell Rep. 2015;12:1978–85.

84. Corcoran RB, Ebi H, Turke AB, Coffee EM, Nishino M, Cogdill AP, et al. EGFR-mediated reactivation of MAPK signaling contributes to insensitivity of BRAF-mutant colorectal cancers to RAF inhibition with vemurafenib. Cancer Discov. 2012;2:227–35.

85. Prahallad A, Sun C, Huang S, Di Nicolantonio F, Salazar R, Zecchin D, et al. Unresponsiveness of colon cancer to BRAF(V600E) inhibition through feedback activation of EGFR. Nature. 2012;483:100–3.

86. Holderfield M, Deuker MM, McCormick F, McMahon M. Targeting RAF kinases for cancer therapy: BRAF-mutated melanoma and beyond. Nat. Rev. Cancer. 2014;14:455–67.

87. Vogelstein B, Papadopoulos N, Velculescu VE, Zhou S, Diaz LA, Kinzler KW. Cancer Genome Landscapes. Science (80-.). 2013;339:1546–58.

88. Yancovitz M, Litterman A, Yoon J, Ng E, Shapiro RL, Berman RS, et al. Intra- and Inter-Tumor Heterogeneity of BRAFV600EMutations in Primary and Metastatic Melanoma. PLoS One. 2012;7:e29336.

89. Sensi M, Nicolini G, Petti C, Bersani I, Lozupone F, Molla a, et al. Mutually exclusive NRASQ61R and BRAFV600E mutations at the single-cell level in the same human melanoma. Oncogene. 2006;25:3357–64.

90. Altschuler SJ, Wu LF. Cellular Heterogeneity: Do Differences Make a Difference? Cell. 2010. p. 559–63.

91. Gascoigne KE, Taylor SS. Cancer Cells Display Profound Intra- and Interline Variation following Prolonged Exposure to Antimitotic Drugs. Cancer Cell. 2008;14:111–22.

92. Frick PL, Paudel BB, Tyson DR, Quaranta V. Quantifying heterogeneity and dynamics of clonal fitness in response to perturbation. J. Cell. Physiol. 2015;230:1403–12.

93. Kreso A, O'Brien CA, van Galen P, Gan OI, Notta F, Brown AMK, et al. Variable Clonal Repopulation Dynamics Influence Chemotherapy Response in Colorectal Cancer. Science (80-.). 2013;339:543–8.

94. Nowell PC. The clonal evolution of tumor cell populations. Science (80-.). 1976;194:23–8.

95. Gerlinger M, Rowan AJ, Horswell S, Larkin J, Endesfelder D, Gronroos E, et al. Intratumor Heterogeneity and Branched Evolution Revealed by Multiregion Sequencing. N. Engl. J. Med. 2012;366:883–92.

96. Dugo M, Nicolini G, Tragni G, Bersani I, Tomassetti A, Colonna V, et al. A melanoma subtype with intrinsic resistance to BRAF inhibition identified by receptor tyrosine kinases gene-driven classification. Oncotarget. 2015;6:5118–33.

97. Krauthammer M, Kong Y, Ha BH, Evans P, Bacchiocchi A, McCusker JP, et al. Exome sequencing identifies recurrent somatic RAC1 mutations in melanoma. Nat. Genet. 2012;44:1006–14.

98. Van Allen EM, Wagle N, Sucker A, Treacy DJ, Johannessen CM, Goetz EM, et al. The genetic landscape of clinical resistance to RAF inhibition in metastatic melanoma. Cancer Discov. 2014;4:94–109.

99. Cara S, Tannock IF. Retreatment of patients with the same chemotherapy: implications for clinical mechanisms of drug resistance. Ann. Oncol. 2001;12:23–7.

100. Das Thakur M, Salangsang F, Landman AS, Sellers WR, Pryer NK, Levesque MP, et al. Modelling vemurafenib resistance in melanoma reveals a strategy to forestall drug resistance. Nature. 2013;494:251–5.

101. Rowdo, Madorsky, Florencia Paula, Antonela Barón, Erika María von Euw and JM. In vitro long-term treatment with MAPK inhibitors induces melanoma cells with resistance plasticity to inhibitors while retaining sensitivity to CD8 T cells. Oncol. Rep. 2017;37:1367–78.

102. Raj A, van Oudenaarden A. Nature, Nurture, or Chance: Stochastic Gene Expression and Its Consequences. Cell. 2008;135:216–26.

103. Niepel M, Spencer SL, Sorger PK. Non-genetic cell-to-cell variability and the consequences for pharmacology. Curr. Opin. Chem. Biol. 2009;13:556–61.

104. Vandamme N, Berx G. Melanoma cells revive an embryonic transcriptional network to dictate phenotypic heterogeneity. Front. Oncol. 2014;4:352.

105. Smith MPP, Brunton H, Rowling EJJ, Ferguson J, Arozarena I, Miskolczi Z, et al. Inhibiting Drivers of Non-mutational Drug Tolerance Is a Salvage Strategy for Targeted Melanoma Therapy. Cancer Cell. 2016;29:270–84.

106. Sharma S V., Lee DY, Li B, Quinlan MP, Takahashi F, Maheswaran S, et al. A

Chromatin-Mediated Reversible Drug-Tolerant State in Cancer Cell Subpopulations. Cell. 2010;141:69–80.

107. Hugo W, Shi H, Sun L, Piva M, Song C, Kong X, et al. Non-genomic and Immune Evolution of Melanoma Acquiring MAPKi Resistance. Cell. 2015;162:1271–85.

108. Goldman A, Majumder B, Dhawan A, Ravi S, Goldman D, Kohandel M, et al. Temporally sequenced anticancer drugs overcome adaptive resistance by targeting a vulnerable chemotherapy-induced phenotypic transition. Nat. Commun. 2015;6:6139.

109. Hayashi-Takanaka Y, Yamagata K, Wakayama T, Stasevich TJ, Kainuma T, Tsurimoto T, et al. Tracking epigenetic histone modifications in single cells using Fab-based live endogenous modification labeling. Nucleic Acids Res. 2011;39:6475–88.

110. Przybilla J, Rohlf T, Loeffler M, Galle J. Understanding epigenetic changes in aging stem cells - a computational model approach. Aging Cell. 2014;13:320–8.

111. Balaban NQ, Merrin J, Chait R, Kowalik L, Leibler S. Bacterial Persistenceas a Phenotypic Switch. Science (80-.). 2004;305:1622–5.

112. Balaban NQ. Persistence: Mechanisms for triggering and enhancing phenotypic variability. Curr. Opin. Genet. Dev. 2011;21:768–75.

113. Navin N, Kendall J, Troge J, Andrews P, Rodgers L, McIndoo J, et al. Tumour evolution inferred by single-cell sequencing. Nature. 2011;472:90–4.

114. Melchor L, Brioli A, Wardell CP, Murison A, Potter NE, Kaiser MF, et al. Single-cell genetic analysis reveals the composition of initiating clones and phylogenetic patterns of branching and parallel evolution in myeloma. Leukemia. 2014;28:1705–15.

115. Potter NE, Ermini L, Papaemmanuil E, Cazzaniga G, Vijayaraghavan G, Titley I, et al. Single-Cell mutational profiling and clonal phylogeny in cancer. Genome Res. 2013;23:2115–25.

116. Wang W, Quan Y, Fu Q, Liu Y, Liang Y, Wu J, et al. Dynamics between cancer cell subpopulations reveals a model coordinating with both hierarchical and stochastic concepts. PLoS One. 2014;9.

117. Elowitz MB, Levine AJ, Siggia ED, Swain PS, Guptasarma P, Spudich JL, et al. Stochastic gene expression in a single cell. Science. 2002;297:1183–6.

118. Spencer SL, Gaudet S, Albeck JG, Burke JM, Sorger PK. Non-genetic origins of cell-to-cell variability in TRAIL-induced apoptosis. Nature. 2009;459:428–32.

119. Marusyk A, Almendro V, Polyak K. Intra-tumour heterogeneity: a looking glass for cancer? Nat. Rev. Cancer. 2012;12:323–34.

120. Reya T, Morrison SJ, Clarke MF, Weissman IL. Stem cells, cancer, and cancer stem cells. Nature. 2001;414:105–11.

121. Dick JE. Stem cell concepts renew cancer research. Blood. 2008;112:4793–807.

122. Fletcher JI, Haber M, Henderson MJ, Norris MD. ABC transporters in cancer: more than just drug efflux pumps. Nat. Rev. Cancer. 2010;10:147–56.

123. Storms RW, Trujillo AP, Springer JB, Shah L, Colvin OM, Ludeman SM, et al. Isolation of primitive human hematopoietic progenitors on the basis of aldehyde dehydrogenase activity. Proc. Natl. Acad. Sci. U. S. A. 1999;96:9118–23.

124. Ginestier C, Hur MH, Charafe-Jauffret E, Monville F, Dutcher J, Brown M, et al. ALDH1 Is a Marker of Normal and Malignant Human Mammary Stem Cells and a Predictor of Poor Clinical Outcome. Cell Stem Cell. 2007;1:555–67.

125. Boiko AD, Razorenova O V., van de Rijn M, Swetter SM, Johnson DL, Ly DP, et al. Human melanoma-initiating cells express neural crest nerve growth factor receptor CD271. Nature. 2010;466:133–7.

126. Civenni G, Walter A, Kobert N, Mihic-Probst D, Zipser M, Belloni B, et al. Human CD271-positive melanoma stem cells associated with metastasis establish tumor heterogeneity and long-term growth. Cancer Res. 2011;71:3098–109.

127. Kauffman SA. Homeostasis and Differentiation in Random Genetic Control Networks. Nature. 1969;224:177–8.

128. Huang S. Genetic and non-genetic instability in tumor progression: Link between the fitness landscape and the epigenetic landscape of cancer cells. Cancer Metastasis Rev. 2013;32:423–48.

129. Mack SC, Witt H, Piro RM, Gu L, Zuyderduyn S, Stütz AM, et al. Epigenomic alterations define lethal CIMP-positive ependymomas of infancy. Nature. 2014;506:445–50.

130. Ohnishi K, Semi K, Yamamoto T, Shimizu M, Tanaka A, Mitsunaga K, et al. Premature termination of reprogramming in vivo leads to cancer development through altered epigenetic regulation. Cell. 2014;156:663–77.

131. Li Q, Wennborg A, Aurell E, Dekel E, Zou J-Z, Xu Y, et al. Dynamics inside the cancer cell attractor reveal cell heterogeneity, limits of stability, and escape. Proc. Natl. Acad. Sci. 2016;113:2672–7.

132. Waddington CH. Canalization of Development and the Inheritance of Acquired Characters. Nature. 1942;150:563–5.

133. Huang S, Eichler G, Bar-Yam Y, Ingber DE. Cell fates as high-dimensional attractor states of a complex gene regulatory network. - PubMed - NCBI. Phys. Rev. Lett.

2005;94:128701.

134. Wales DJ, Bogdan T V. Potential energy and free energy landscapes. J. Phys. Chem. B. 2006;110:20765–76.

135. Wang J, Zhang K, Xu L, Wang E. Quantifying the Waddington landscape and biological paths for development and differentiation. Proc. Natl. Acad. Sci. 2011;108:8257–62.

136. Cai S, Fu XB, Sheng ZY. Dedifferentiation: A new approach in stem cell research. Bioscience. 2007;57:655–62.

137. Tang F, Barbacioru C, Wang Y, Nordman E, Lee C, Xu N, et al. mRNA-Seq whole-transcriptome analysis of a single cell. Nat. Methods. 2009;6:377–82.

138. Patel AP, Tirosh I, Trombetta JJ, Shalek AK, Gillespie SM, Wakimoto H, et al. Single-cell RNA-seq highlights intratumoral heterogeneity in primary glioblastoma. Science (80-.). 2014;344:1396–401.

139. Tirosh I, Izar B, Prakadan SM, Wadsworth MH, Treacy D, Trombetta JJ, et al. Dissecting the multicellular ecosystem of metastatic melanoma by single-cell RNA-seq. Science (80-.). 2016;352:189–96.

140. Femino a M, Fay FS, Fogarty K, Singer RH. Visualization of single RNA transcripts in situ. Science. 1998;280:585–90.

141. Raj A, van den Bogaard P, Rifkin SA, van Oudenaarden A, Tyagi S. Imaging individual mRNA molecules using multiple singly labeled probes. Nat. Methods. 2008;5:877–9.

142. Lubeck E, Cai L. Single-cell systems biology by super-resolution imaging and combinatorial labeling. Nat. Methods. 2012;9:743–8.

143. Lubeck E, Coskun AF, Zhiyentayev T, Ahmad M, Cai L. Single-cell in situ RNA profiling by sequential hybridization. Nat. Methods. 2014;11:360–1.

144. Moffitt JR, Hao J, Wang G, Chen KH, Babcock HP, Zhuang X. High-throughput single-cell gene-expression profiling with multiplexed error-robust fluorescence in situ hybridization. Proc. Natl. Acad. Sci. 2016;113:11046–51.

145. Kwon S. Single-molecule fluorescence in situ hybridization: Quantitative imaging of single RNA molecules. BMB Rep. 2013. p. 65–72.

146. Albeck JG, Mills GB, Brugge JS. Frequency-Modulated Pulses of ERK Activity Transmit Quantitative Proliferation Signals. Mol. Cell. 2013;49:249–61.

147. Tyson DR, Garbett SP, Frick PL, Quaranta V. Fractional proliferation: a method to deconvolve cell population dynamics from single-cell data. Nat. Methods. 2012;9:923–8.

148. Buckingham ME, Meilhac SM. Tracing cells for tracking cell lineage and clonal behavior. Dev. Cell. 2011. p. 394–409.

149. Huang S. Non-genetic heterogeneity of cells in development: more than just noise. Development. 2009;136:3853–62.

150. Harris LA, Frick PL, Garbett SP, Hardeman KN, Paudel BB, Lopez CF, et al. An unbiased metric of antiproliferative drug effect in vitro. Nat. Methods. 2016;13:497–500.

151. Zuber J, McJunkin K, Fellmann C, Dow LE, Taylor MJ, Hannon GJ, et al. Toolkit for evaluating genes required for proliferation and survival using tetracycline-regulated RNAi. Nat Biotechnol. 2011;29:79–83.

152. Berns K, Hijmans EM, Mullenders J, Brummelkamp TR, Velds A, Heimerikx M, et al. A large-scale RNAi screen in human cells identifies new components of the p53 pathway. Nature. 2004;428:431–7.

153. Bonnans C, Chou J, Werb Z. Remodelling the extracellular matrix in development and disease. Nat. Rev. Mol. Cell Biol. 2014;15:786–801.

154. Garnett MJ, Edelman EJ, Heidorn SJ, Greenman CD, Dastur A, Lau KW, et al. Systematic identification of genomic markers of drug sensitivity in cancer cells. Nature. 2012;483:570–5.

155. Feero WG, Guttmacher AE, Wang L, McLeod HL, Weinshilboum RM. Genomics and Drug Response. N. Engl. J. Med. 2011;364:1144–53.

156. Barretina J, Caponigro G, Stransky N, Venkatesan K, Margolin A a, Kim S, et al. The Cancer Cell Line Encyclopedia enables predictive modelling of anticancer drug sensitivity Supp. Nature. 2012;483:603–7.

157. Fallahi-Sichani M, Honarnejad S, Heiser LM, Gray JW, Sorger PK. Metrics other than potency reveal systematic variation in responses to cancer drugs. Nat. Chem. Biol. 2013;9:708–14.

158. Barlow R, Blake JF. Hill coefficients and the logistic equation. Trends Pharmacol. Sci. 1989;10:440–1.

159. Hafner M, Niepel M, Chung M, Sorger PK. Growth rate inhibition metrics correct for confounders in measuring sensitivity to cancer drugs. Nat. Methods. 2016;13:521–7.

160. Dexter DL, Kowalski HM, Blazar BA, Fligiel Z, Vogel R, Heppner GH. Heterogeneity of tumor cells from a single mouse mammary tumor. Cancer Res. 1978;38:3174–81.

161. Brock A, Chang H, Huang S. Non-genetic heterogeneity--a mutation-independent driving force for the somatic evolution of tumours. Nat. Rev. Genet. Nature Publishing Group; 2009;10:336–42.

162. Balaban NQ, Merrin J, Chait R, Kowalik L, Leibler S. Bacterial Persistence as a Phenotypic Switch. Science (80-.). 2004;305:1622–5.

163. Rein M. The partial-equilibrium approximation in reacting flows. Phys. Fluids A Fluid Dyn. 1992;4:873–86.

164. Sakaue-Sawano A, Kurokawa H, Morimura T, Hanyu A, Hama H, Osawa H, et al. Visualizing Spatiotemporal Dynamics of Multicellular Cell-Cycle Progression. Cell. 2008;132:487–98.

165. Rasband W. ImageJ. U. S. Natl. Institutes Heal. Bethesda, Maryland, USA. 2012;//imagej.nih.gov/ij/.

166. Shoemaker RH. The NCI60 human tumour cell line anticancer drug screen. Nat. Rev. Cancer. 2006;6:813–23.

167. Quaranta V, Tyson DR, Garbett SP, Weidow B, Harris MP, Georgescu W. Trait Variability of Cancer Cells Quantified by High-Content Automated Microscopy of Single Cells. Methods Enzymol. 2009;467:23–57.

168. Gong Y, Somwar R, Politi K, Balak M, Chmielecki J, Jiang X, et al. Induction of BIM is essential for apoptosis triggered by EGFR kinase inhibitors in mutant EGFR-dependent lung adenocarcinomas. PLoS Med. 2007;4:1655–68.

169. Yang W, Soares J, Greninger P, Edelman EJ, Lightfoot H, Forbes S, et al. Genomics of Drug Sensitivity in Cancer (GDSC): A resource for therapeutic biomarker discovery in cancer cells. Nucleic Acids Res. 2013;41.

170. Gray JW, Mills GB. Large-scale drug screens support precision medicine. Cancer Discov. 2015;5:1130–2.

171. Rees MG, Seashore-Ludlow B, Cheah JH, Adams DJ, Price E V, Gill S, et al. Correlating chemical sensitivity and basal gene expression reveals mechanism of action. Nat. Chem. Biol. 2016;12:109–16.

172. Rooswinkel RW, van de Kooij B, Verheij M, Borst J. Bcl-2 is a better ABT-737 target than Bcl-xL or Bcl-w and only Noxa overcomes resistance mediated by Mcl-1, Bfl-1, or Bcl-B. Cell Death Dis. 2012;3:e366.

173. Sporn MB, Harris ED. Proliferative Diseases. Am. J. Med. 1981;70:1231–6.

174. Michor F, Hughes TP, Iwasa Y, Branford S, Shah NP, Sawyers CL, et al. Dynamics of chronic myeloid leukaemia. Nature. 2005;435:1267–70.

175. Ribas A, Flaherty KT. BRAF targeted therapy changes the treatment paradigm in melanoma. Nat. Rev. Clin. Oncol. 2011;8:426–33.

176. Ascierto PA, Kirkwood JM, Grob J-J, Simeone E, Grimaldi AM, Maio M, et al. The role of BRAF V600 mutation in melanoma. J. Transl. Med. 2012;10:85.

177. Chan MMK, Haydu LE, Menzies AM, Azer MWF, Klein O, Lyle M, et al. The nature and management of metastatic melanoma after progression on braf inhibitors: Effects of extended BRAF inhibition. Cancer. 2014;120:3142–53.

178. Hodis E, Watson IR, Kryukov G V., Arold ST, Imielinski M, Theurillat JP, et al. A landscape of driver mutations in melanoma. Cell. 2012;150:251–63.

179. Whittaker SR, Theurillat JP, Van Allen E, Wagle N, Hsiao J, Cowley GS, et al. A genome-scale RNA interference screen implicates NF1 loss in resistance to RAF inhibition. Cancer Discov. 2013;3:350–62.

180. Villanueva J, Vultur A, Herlyn M. Resistance to BRAF inhibitors: Unraveling mechanisms and future treatment options. Cancer Res. 2011. p. 7137–40.

181. Zhao Y, Butler EB, Tan M. Targeting cellular metabolism to improve cancer therapeutics. Cell Death Dis. 2013;4:e532.

182. Baenke F, Chaneton B, Smith M, Van Den Broek N, Hogan K, Tang H, et al. Resistance to BRAF inhibitors induces glutamine dependency in melanoma cells. Mol. Oncol. 2016;10:73–84.

183. Hernandez-Davies JE, Tran TQ, Reid MA, Rosales KR, Lowman XH, Pan M, et al. Vemurafenib resistance reprograms melanoma cells towards glutamine dependence. J. Transl. Med. 2015;13:210.

184. Parmenter TJ, Kleinschmidt M, Kinross KM, Bond ST, Li J, Kaadige MR, et al. Response of BRAF-mutant melanoma to BRAF inhibition is mediated by a network of transcriptional regulators of glycolysis. Cancer Discov. 2014;4:423–33.

185. Vazquez F, Lim JH, Chim H, Bhalla K, Girnun G, Pierce K, et al. PGC1?? Expression Defines a Subset of Human Melanoma Tumors with Increased Mitochondrial Capacity and Resistance to Oxidative Stress. Cancer Cell. 2013;23:287–301.

186. Haq R, Shoag J, Andreu-Perez P, Yokoyama S, Edelman H, Rowe GC, et al. Oncogenic BRAF regulates oxidative metabolism via PGC1α and MITF. Cancer Cell. 2013;23:302–15.

187. Greaves M, Maley CC. Clonal evolution in cancer. Nature. 2012;481:306–13.

188. Warburg O. The Metabolism of Carcinoma Cells. J. Cancer Res. 1925;9:148–63.

189. McArthur GA, Puzanov I, Amaravadi R, Ribas A, Chapman P, Kim KB, et al. Marked, homogeneous, and early [18F]fluorodeoxyglucose-positron emission tomography responses to vemurafenib in BRAF-mutant advanced melanoma. J. Clin. Oncol. 2012;30:1628–34.

190. Flaherty KT, Yasothan U, Kirkpatrick P. Vemurafenib. Nat. Rev. Drug Discov. 2011;10:811–2.

191. Shackleton M, Quintana E, Fearon ER, Morrison SJ. Heterogeneity in Cancer: Cancer Stem Cells versus Clonal Evolution. Cell. 2009;138:822–9.

192. Johnson DB, Menzies AM, Zimmer L, Eroglu Z, Ye F, Zhao S, et al. Acquired BRAF inhibitor resistance: A multicenter meta-analysis of the spectrum and frequencies, clinical behaviour, and phenotypic associations of resistance mechanisms. Eur. J. Cancer. 2015;51:2792–9.

193. Visvader JE, Lindeman GJ. Cancer stem cells: Current status and evolving complexities. Cell Stem Cell. 2012;10:717–28.

194. Gupta PB, Fillmore CM, Jiang G, Shapira SD, Tao K, Kuperwasser C, et al. Stochastic state transitions give rise to phenotypic equilibrium in populations of cancer cells. Cell. 2011;146:633–44.

195. Huang S. The molecular and mathematical basis of Waddington's epigenetic landscape: A framework for post-Darwinian biology? BioEssays. 2012;34:149–57.

196. Soetaert K, Petzoldt T, Setzer RW. Package deSolve : Solving Initial Value Differential Equations in R. J. Stat. Softw. 2010;33:1–25.

197. Gutenkunst RN, Waterfall JJ, Casey FP, Brown KS, Myers CR, Sethna JP. Universally sloppy parameter sensitivities in systems biology models. PLoS Comput. Biol. 2007;3:1871–8.

198. Eydgahi H, Chen WW, Muhlich JL, Vitkup D, Tsitsiklis JN, Sorger PK. Properties of cell death models calibrated and compared using Bayesian approaches. Mol. Syst. Biol. 2014;9:644.

199. Soetaert K, Petzoldt T. Inverse Modelling , Sensitivity and Monte Carlo Analysis in R Using Package FME. J. Stat. Softw. 2010;33:1–28.

200. Hänggi P, Talkner P, Borkovec M. Reaction-rate theory: Fifty years after Kramers. Rev. Mod. Phys. 1990;62:251–341.

201. Zhou JXX, Aliyu MDS, Aurell E, Huang S. Quasi-potential landscape in complex multi-stable systems. J. R. Soc. Interface. 2012;9:3539–53.

202. Ziegler U, Groscurth P. Morphological Features of Cell Death. News Physiol. Sci. 2004;19:124–8.

203. Sottoriva A, Kang H, Ma Z, Graham TA, Salomon MP, Zhao J, et al. A Big Bang model of human colorectal tumor growth. Nat. Genet. 2015;47:209–16.

204. Mellor HR, Callaghan R. Resistance to chemotherapy in cancer: A complex and

integrated cellular response. Pharmacology. 2008;81:275–300.

205. Saraswathy M, Gong S. Different strategies to overcome multidrug resistance in cancer. Biotechnol. Adv. 2013;31:1397–407.

206. Lage H. An overview of cancer multidrug resistance: A still unsolved problem. Cell. Mol. Life Sci. 2008;65:3145–67.

207. Menon DR, Das S, Krepler C, Vultur a, Rinner B, Schauer S, et al. A stress-induced early innate response causes multidrug tolerance in melanoma. Oncogene. 2015;34:4545–4545.

208. Haq R, Fisher DE, Widlund HR. Molecular pathways: BRAF induces bioenergetic adaptation by attenuating oxidative phosphorylation. Clin. Cancer Res. 2014;20:2257–63.

209. Abildgaard C, Guldberg P. Molecular drivers of cellular metabolic reprogramming in melanoma. Trends Mol. Med. 2015. p. 164–71.

210. Zhou JX, Pisco AO, Qian H, Huang S. Nonequilibrium population dynamics of phenotype conversion of cancer cells. PLoS One. 2014;9.

211. Hardeman KN, Peng C, Paudel BB, Meyer CT, Luong T, Tyson DR, et al. Dependence On Glycolysis Sensitizes BRAF-mutated Melanomas For Increased Response To Targeted BRAF Inhibition. Sci. Rep. 2017;7:42604.

212. Fallahi-Sichani M, Becker V, Izar B, Baker GJ, Lin J-RJ, Boswell SA, et al. Adaptive resistance of melanoma cells to RAF inhibition via reversible induction of a slowly dividing de-differentiated state. Mol. Syst. Biol. 2017;13:1–24.

213. Shaffer SM, Dunagin MC, Torborg SR, Torre EA, Emert B, Krepler C, et al. Rare cell variability and drug-induced reprogramming as a mode of cancer drug resistance. Nature. 2017;546:431–5.

214. Hata AN, Niederst MJ, Archibald HL, Gomez-Caraballo M, Siddiqui FM, Mulvey HE, et al. Tumor cells can follow distinct evolutionary paths to become resistant to epidermal growth factor receptor inhibition. Nat. Med. 2016;22:262–9.

215. Ramirez M, Rajaram S, Steininger RJ, Osipchuk D, Roth MA, Morinishi LS, et al. Diverse drug-resistance mechanisms can emerge from drug-tolerant cancer persister cells. Nat. Commun. Nature Publishing Group; 2016;7:10690.

216. Holohan C, Van Schaeybroeck S, Longley DB, Johnston PG. Cancer drug resistance: an evolving paradigm. Nat. Rev. Cancer. 2013;13:714–26.

217. Blatter S, Rottenberg S. Minimal residual disease in cancer therapy - Small things make all the difference. Drug Resist. Updat. 2015;21–22:1–10.

218. Lito P, Rosen N, Solit DB. Tumor adaptation and resistance to RAF inhibitors. Nat. Med.

2013;19:1401–9.

219. Haass NK, Sproesser K, Nguyen TK, Contractor R, Medina CA, Nathanson KL, et al. The mitogen-activated protein/extracellular signal-regulated kinase kinase inhibitor AZD6244 (ARRY-142886) induces growth arrest in melanoma cells and tumor regression when combined with docetaxel. Clin. Cancer Res. 2008;14:230–9.

220. Haass NK, Beaumont KA, Hill DS, Anfosso A, Mrass P, Munoz MA, et al. Real-time cell cycle imaging during melanoma growth, invasion, and drug response. Pigment Cell Melanoma Res. 2014;27:764–76.

221. Haferkamp S, Borst A, Adam C, Becker TM, Motschenbacher S, Windhövel S, et al. Vemurafenib Induces Senescence Features in Melanoma Cells. J. Invest. Dermatol. 2013;133:1601–9.

222. Szakacs G, Paterson JK, Ludwig JA, Booth-Genthe C, Gottesman MM. Targeting multidrug resistance in cancer. Nat Rev Drug Discov. 2006;5:219–34.

223. Zhou JX, Huang S. Understanding gene circuits at cell-fate branch points for rational cell reprogramming. Trends Genet. 2011;27:55–62.

224. Macarthur BD, Ma'ayan A, Lemischka IR. Systems biology of stem cell fate and cellular reprogramming. Nat Rev Mol Cell Biol. 2009;10:672–81.

225. Greger JG, Eastman SD, Zhang V, Bleam MR, Hughes AM, Smitheman KN, et al. Combinations of BRAF, MEK, and PI3K/mTOR Inhibitors Overcome Acquired Resistance to the BRAF Inhibitor GSK2118436 Dabrafenib, Mediated by NRAS or MEK Mutations. Mol. Cancer Ther. 2012. p. 909–20.

226. Whittaker SR, Cowley GS, Wagner S, Luo F, Root DE, Garraway L a. Combined Pan-RAF and MEK Inhibition Overcomes Multiple Resistance Mechanisms to Selective RAF Inhibitors. Mol. Cancer Ther. 2015;14:2700–11.

227. Hu-Lieskovan S, Robert L, Moreno BH, Ribas A. Combining targeted therapy with immunotherapy in BRAF-mutant melanoma: Promise and challenges. J. Clin. Oncol. 2014;32:2248–54.

228. Delgado-Goni T, Miniotis MF, Wantuch S, Parkes HG, Marais R, Workman P, et al. The BRAF Inhibitor Vemurafenib Activates Mitochondrial Metabolism and Inhibits Hyperpolarized Pyruvate–Lactate Exchange in BRAF-Mutant Human Melanoma Cells. Mol. Cancer Ther. 2016;15:2987–99.

229. Hall A, Meyle KD, Lange MK, Klima M, Sanderhoff M, Dahl C, et al. Dysfunctional oxidative phosphorylation makes malignant melanoma cells addicted to glycolysis driven by the (V600E)BRAF oncogene. Oncotarget. 2013;4:584–99.

230. Ferguson J, Smith M, Zudaire I, Wellbrock C, Arozarena I. Glucose availability controls

ATF4-mediated MITF suppression to drive melanoma cell growth. Oncotarget. 2017;8:32946–59.

231. Hanahan D, Weinberg RA. Ha1. Hanahan D, Weinberg RA. Hallmarks of cancer: The next generation. Vol. 144, Cell. 2011. p. 646–74. llmarks of cancer: The next generation. Cell. 2011. p. 646–74.

232. Life Technologies. TRIzol ® Reagent. Prod. Data Sheet. 2014.

233. Sirén J, Välimäki N, Mäkinen V. HISAT2 - Fast and sensitive alignment against general human population. IEEE/ACM Trans. Comput. Biol. Bioinforma. 2014;11:375–88.

234. Liao Y, Smyth GK, Shi W. FeatureCounts: An efficient general purpose program for assigning sequence reads to genomic features. Bioinformatics. 2014;30:923–30.

235. Love MI, Huber W, Anders S. Moderated estimation of fold change and dispersion for RNA-seq data with DESeq2. Genome Biol. 2014;15:550.

236. Long G V., Fung C, Menzies AM, Pupo GM, Carlino MS, Hyman J, et al. Increased MAPK reactivation in early resistance to dabrafenib/trametinib combination therapy of BRAF-mutant metastatic melanoma. Nat. Commun. 2014;5:5694.

237. Paudel BB, Harris LA, Hardeman KN, Abugable AA, Hayford CE, Tyson DR. Title : A Non-Quiescent " Idling " State in Drug-Treated BRAF -Mutated Melanoma Cell Populations. Biophys. J. in revision.

238. Mcquade JL, Gopal YV, Mcquade JL, Gopal YNV. Counteracting oxidative phosphorylation- mediated resistance of melanomas to MAPK pathway inhibition Counteracting oxidative phosphorylation- mediated resistance of melanomas to MAPK pathway inhibition. Mol. Cell. Oncol. 2015;3556:2–4.

239. Brar SS, Corbin Z, Kennedy TP, Hemendinger R, Thornton L, Bommarius B, et al. NOX5 NAD(P)H oxidase regulates growth and apoptosis in DU 145 prostate cancer cells. Am. J. Physiol. Cell Physiol. 2003;285:C353–69.

240. Brar SS, Kennedy TP, Sturrock AB, Huecksteadt TP, Quinn MT, Whorton a R, et al. An NAD(P)H oxidase regulates growth and transcription in melanoma cells. Am. J. Physiol. Cell Physiol. 2002;282:C1212–24.

241. Dho SH, Kim JY, Lee K-P, Kwon E-S, Lim JC, Kim C-J, et al. STAT5A-mediated NOX5-L expression promotes the proliferation and metastasis of breast cancer cells. Exp. Cell Res. 2016;1–8.

242. Lu W, Hu Y, Chen G, Chen Z, Zhang H, Wang F, et al. Novel role of NOX in supporting aerobic glycolysis in cancer cells with mitochondrial dysfunction and as a potential target for cancer therapy. PLoS Biol. 2012;10.

243. Zeng C, Wu Q, Wang J, Yao B, Ma L, Yang Z, et al. NOX4 supports glycolysis and promotes glutamine metabolism in non-small cell lung cancer cells. Free Radic. Biol. Med. 2016;101:236–48.

244. Antony S, Wu Y, Hewitt SM, Anver MR, Butcher D, Jiang G, et al. Characterization of NADPH oxidase 5 expression in human tumors and tumor cell lines with a novel mouse monoclonal antibody. Free Radic. Biol. Med. 2013;65:497–508.

245. Antony S, Jiang G, Wu Y, Meitzler JL, Makhlouf HR, Haines DC, et al. NADPH oxidase 5 (NOX5) - induced reactive oxygen signaling modulates normoxic HIF-1α and p27 ^{Kip1} expression in malignant melanoma and other human tumors. Mol. Carcinog. 2017;

246. Circu ML, Aw TY. Reactive oxygen species, cellular redox systems, and apoptosis. Free Radic. Biol. Med. 2010. p. 749–62.

247. Audrito V, Managò A, La Vecchia S, Zamporlini F, Vitale N, Baroni G, et al. Nicotinamide Phosphoribosyltransferase (nampt) as a Therapeutic Target in Braf-mutated Metastatic Melanoma. Jnci J. Natl. Cancer Inst. JNCI: Journal of the National Cancer Institute; 2018;110.

248. Marín-Hernández A, Gallardo-Pérez JC, Ralph SJ, Rodríguez-Enríquez S, Moreno-Sánchez R. HIF-1alpha modulates energy metabolism in cancer cells by inducing over-expression of specific glycolytic isoforms. Mini Rev. Med. Chem. 2009;9:1084–101.

249. Ramsdale R, Jorissen RN, Li FZ, Al-Obaidi S, Ward T, Sheppard KE, et al. The transcription cofactor c-JUN mediates phenotype switching and BRAF inhibitor resistance in melanoma. Sci Signal. 2015;8:ra82.

250. Perraudeau F, Risso D, Street K, Purdom E, Dudoit S. Bioconductor workflow for single-cell RNA sequencing: Normalization, dimensionality reduction, clustering, and lineage inference. F1000Research. 2017;6:1158.

251. Petzold L. Automatic Selection of Methods for Solving Stiff and Nonstiff Systems of Ordinary Differential Equations. SIAM J. Sci. Stat. Comput. 1983;4:136–48.

252. Gelman A, Rubin DB. Inference from Iterative Simulation Using Multiple Sequences. Stat. Sci. 1992;7:457–511.

253. Brooks SPB, Gelman AG. General methods for monitoring convergence of iterative simulations. J. Comput. Graph. Stat. 1998;7:434–55.

254. Akaike H. A new look at the statistical model identification. IEEE Trans. Autom. Control. 1974;19:716–23.

255. Pisco AO, Brock A, Zhou J, Moor A, Mojtahedi M, Jackson D, et al. Non-Darwinian dynamics in therapy-induced cancer drug resistance. Nat. Commun. 2013;4:2467.